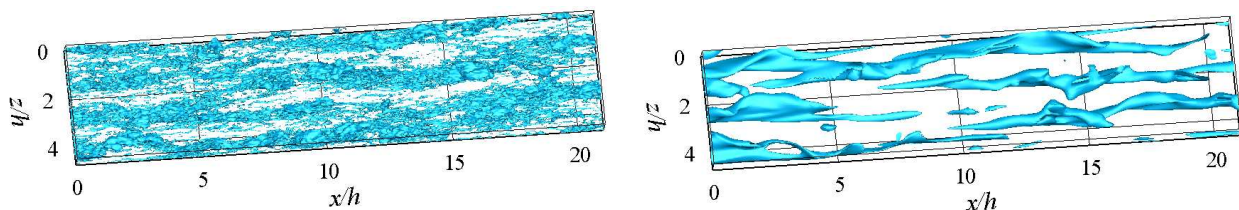**École Polytechnique**

Laboratoire d'Hydrodynamique (LadHyX)

Thèse présentée pour obtenir le grade de

DOCTEUR DE L'ÉCOLE POLYTECHNIQUE

spécialité : mécanique

par

YONGYUN HWANG

Large-scale streaks in wall-bounded turbulent flows: amplification, instability, self-sustaining process and control

Soutenue le 17 décembre 2010 devant le jury composé de:

M. Carlo Cossu	Directeur de thèse	École Polytechnique & IMFT, Toulouse
M. Bruno Eckhardt	Examinateur	Université de Marburg, Germany
M. Uwe Ehrenstein	Rapporteur	Universités de Provence, Marseille
M. Stéphan Fauve	Examinateur	École Normale Supérieure, Paris
M. Patrick Huerre	Examinateur industriel	École Polytechnique, Palaiseau
M. Jean-Christophe Robinet	Examinateur	ENSAM, Paris
M. Pierre Sagaut	Rapporteur	UPMC, Paris

Yongyun Hwang

Large-scale streaks in wall-bounded turbulent flows: amplification, instability, self-sustaining process and control

Acknowledgement

Contents

Chapter 1

Introduction

1 Streaky motions in laminar and transitional flows

Transition to turbulence in wall-bounded flows such as plane Couette, pressure-driven channel, pipe and boundary layer flows has been an elusive problem for a long time. Traditionally, the fist step is linear stability analysis, which seeks exponentially growing modes in time or space. However, the critical Reynolds numbers for linear instability do not agree with those at which transition is observed. For example, the pressure-driven channel flow is stable for $Re_h < 5772$ (Orszag, 1971) and plane Couette flow is stable for all Reynolds numbers (Romanov, 1973). However, experiments have shown that the channel flow undergoes transition to turbulence for Re_h as low as 1000 (e.g. Patel & Head, 1969) and for the plane Couette flow the transitional Reynolds number is in the range $325 < Re_h < 370$ (e.g. Lundbladh *et al.*, 1992). This discrepancy between the experimental observations and linear stability analysis has led to numerous efforts to explain transition without a primary linear modal instability.
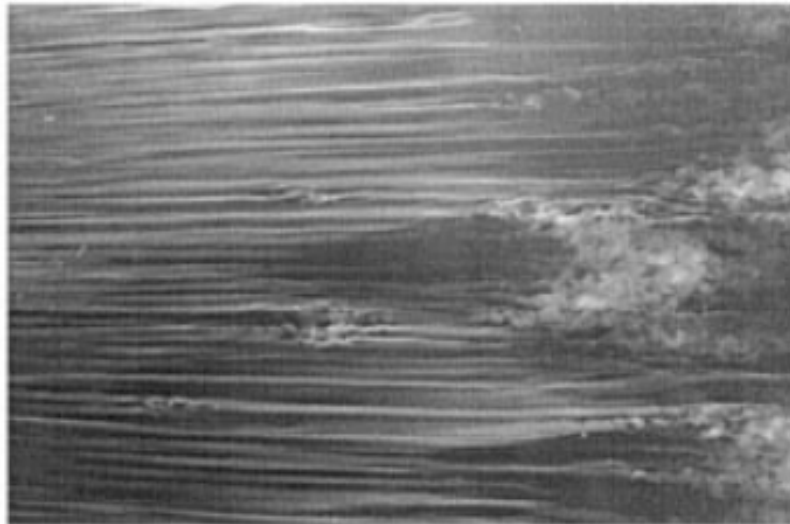

Figure 1.1. Smoke visualization of streaks in transition under the high-level free-stream turbulence in a boundary layer (from Matsubara & Alfredsson, 2001).

Flow	$\lambda_{z,opt}/\delta$		
	$G_{\max}$	$R_{\max}$	V
Couette	$3.9^{(a)}$	$5.3^{(a)}$	$4.5^{(b)}$
Channel flow	$3.1^{(a)}$	$3.9^{(a)}$	$3.5^{(b)}$
Pipe flow	$6.3^{(c)}$	–	–
Boundary layer	$3.3^{(d)}$	–	–

Table 1.1. Optimal spanwise wavelengths of the maximum responses to initial perturbation $G_{\max}$, harmonic forcing $R_{\max}$, and stochastic excitation V in laminar wall-bounded flows. Results from (a) Trefethen et al. (1993), (b) Jovanović & Bamieh (2005), (c) Schmid & Henningson (1994), (d) Butler & Farrell (1992). Here, δ is half of the channel height for Couette and channel flows, the radius for pipe flow, and the boundary-layer thickness for boundary layer.

Under high-level free-stream noise, transition often occurs without the linear instability waves (bypass transition). In such an environment, the streaks are often observed as a prominent feature (Kendall, 1985; Matsubara & Alfredsson, 2001), and they are shown in Fig. 1.1. The streaks consist of a spanwise alternating pattern of high and low streamwise velocity which is elongated in the streamwise direction. The appearance of streaks is now understood with the 'lift-up' effect which transforms streamwise vortices into streaks by taking energy from the base flow, and it is an important process leading the large energy growth in the stable laminar flows (Moffatt, 1967; Ellingsen & Palm, 1975; Landahl, 1980, 1990). This mechanism is essentially associated with the nonnormal nature of linearized Navier-Stokes operator, and the growth of the streaks has been extensively investigated in most of the canonical wall-bounded laminar flows by optimizing three types of perturbations: initial conditions (Butler & Farrell, 1992; Reddy & Henningson, 1993; Trefethen et al., 1993; Schmid & Henningson, 1994), harmonic forcing (Reddy & Henningson, 1993; Reddy et al., 1993; Trefethen et al., 1993) and stochastic excitation (Farrell & Ioannou, 1993a,b, 1996; Bamieh & Dahleh, 2001; Jovanović & Bamieh, 2005). The optimal perturbations leading the largest growth of the streaks are found to be almost uniform in the streamwise direction with a well-defined band of amplified spanwise wavelengths. Table 1 reports the spanwise wavelengths of the optimal streaks, which have been shown to correspond well to the ones observed in transitional flows (Matsubara & Alfredsson, 2001).

When the streaks reach sufficiently large amplitudes via the lift-up effect, they can sustain the growth of secondary perturbations. This secondary growth appears through inflectional modal instability (Waleffe, 1995; Reddy et al., 1998; Andersson et al., 2001) or secondary transient growth (Schoppa & Hussain, 2002; Hœpffner et al., 2005; Cossu et al., 2007), and is often dominated by the sinuous mode originated from the spanwise shear of the streaks. The secondary growth leads the breakdown of the amplified streaks and the flow eventually develops into the turbulent state.

The development of streaks is a crucial element for the bypass transition, but well-controlled streaks are also found to be useful for delaying transition. Cossu & Brandt (2002, 2004) have shown that moderate amplitude streaks stabilize Tollmien-Schlichting waves in laminar boundary layers. This theoretical prediction was recently confirmed by the experiment of Fransson et al. (2004, 2005), and Fransson et al. (2006) have shown that the transition via the Tollmien-Schlichting wave can be delayed by artificially driven streaky flows.

2 Streaky motions in wall-bounded turbulent flows

Turbulent flows are phenomenologically much more complicated than transitional flows due to their multi-scale nature, and wall-bounded turbulent flow are even less understood than the other important canonical flows such as free shear flows or isotropic turbulence (Jiménez, 2007). The main reason essentially stems from the presence of the wall, which confines the size of the energy-containing large eddies to their wall-normal locations. Therefore, the length scale of those large eddies varies with the wall-normal location, and this lays at the core of the complexity of wall-bounded turbulent flows.

2.1 Length scales and mean flow

The length scales in wall-bounded turbulent flow are typically reflected in the mean-velocity profile. The first analytical description on the mean-velocity profile is probably found in 1930's (e.g. von Kármán, 1930; Millikan, 1938). In the near-wall region, the effect of wall-shear stress and molecular viscosity dominates over the inertia. Therefore, a proper choice of the length scale is the viscous length $\delta_v \equiv \nu/u_\tau$, where ν is the kinematic viscosity and $u_\tau \equiv (\tau_w/\rho)^{1/2}$ is the friction velocity formed by the wall-shear stress τ_w and density ρ. With these length and velocity scales, a dimensionless equation for the mean flow, so called *law of the wall*, is given as follows:

$$U^+ = f(y^+), \tag{1.1}$$

where a superscript $^+$ denotes the variables made dimensionless by u_τ and δ_v: $U^+ \equiv U/u_\tau$ and $y^+ \equiv y/\delta_v$.

In the outer region, the equation for the mean flow has been used in terms of the defect from the centerline velocity of the channel or the free-stream velocity of boundary layer denoted as U_e (Tennekes & Lumley, 1967): $U - U_e = g'(y)$. In this region, the relevant length scale is the outer length δ such as the half of channel height h or the thickness of the boundary layer. According to the classical theory by Townsend (1976), u_τ can also be used as the relevant outer velocity scale (but this is currently subject of debate). Then, the *defect law* of the mean flow is non-dimensionalized by the outer scales as follows:

$$\frac{U_e - U}{u_\tau} = g(y/\delta). \tag{1.2}$$

In the region where the influences of the inner and outer scales overlap, (1.1) and (1.2) can be asymptotically matched, with the distance from the wall y becoming the relevant length scale. By also choosing the velocity scale as u_τ, the logarithmic law is obtained:

$$U^+ = \frac{1}{\kappa} \ln y^+ + B, \tag{1.3}$$

where κ is called the Kármán constant whose value is around 0.4, and B is a value depending on the geometry, pressure gradient and so on.

A typical mean-velocity profile of wall-bounded turbulent flow is reported in Fig. 1.2. The region where the law of the wall (1.1) applies is defined as the viscous sublayer ($y^+ \lesssim 5$). The buffer layer is located right above the viscous sublayer at $5 \lesssim y^+ \lesssim 30$, and it is an important place where the near-wall turbulent production reaches its maximum. The logarithmic layer, also called the overlap layer, is typically located between $y^+ \simeq 30$ and $y/\delta \simeq 0.2 - 0.3$. The region $y/\delta > 0.2 - 0.3$ is the wake region where the velocity defect law (1.2) is valid. For
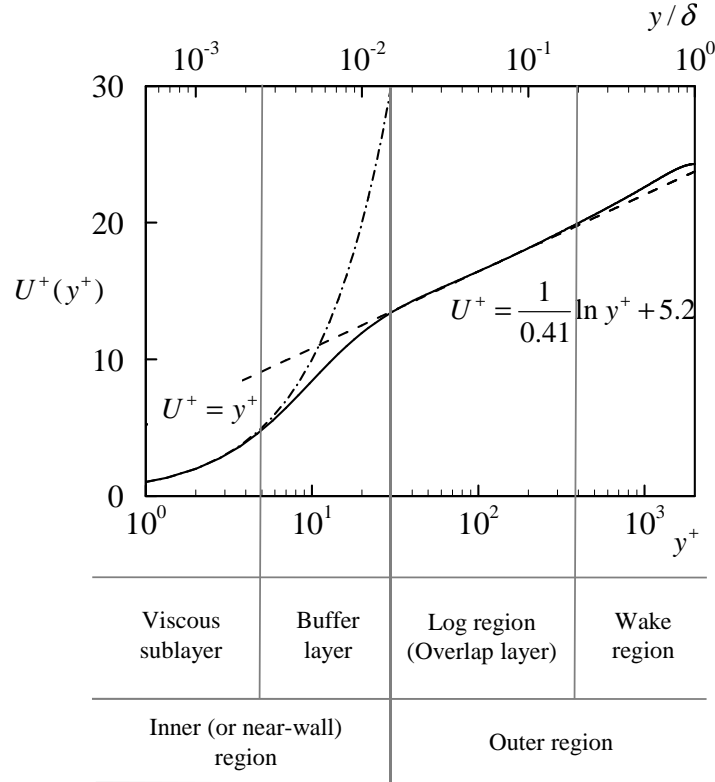
Figure 1.2. Profile of mean flow in turbulent channel at $Re_\tau = 2000$ (from Hoyas & Jiménez, 2006): ———, $U^+(y^+)$; —·—·—, law of the wall ($U^+ = y^+$); ----, logarithmic law ($U^+ = 1/0.41 \ln y^+ + 5.2$).

convenience, both the viscous sublayer and buffer layer will be called the inner (or near-wall) region, and the log layer and wake region will be denoted as the outer region hereafter.

The friction Reynolds number (or Kármán number) is defined as the ratio of the outer length scale δ to the inner length scale δ_v:

$$Re_\tau \equiv \frac{\delta}{\delta_v} = \frac{u_\tau \delta}{\nu}. \tag{1.4}$$

At sufficiently high Re_τ, the typical size of energy-containing eddies in the near-wall region is scaled by the inner length scale δ_v, thus it is much smaller than that of the outer-region eddies. In the logarithmic region, the relevant length scale is the distance from the wall y, thus the size of eddies is determined by their wall-normal location: the further from the wall the eddies live, the larger their size can be. The gradual increase of the eddy size with the increasing wall-normal distance stops when the eddy size becomes of the order of the outer length scale δ. The largest eddies are found in the outer region, and they are scaled by the outer-length scale δ. This growth of the length scales from the inner to outer unit is a core feature of wall-bounded turbulent flows, and it has been observed in many laboratory and numerical experiments (Morrison & Kronauer, 1969; Bullock et al., 1978; Tomkins & Adrian, 2003; del Álamo et al., 2004). This idea is also the basic skeleton of the classical theory by
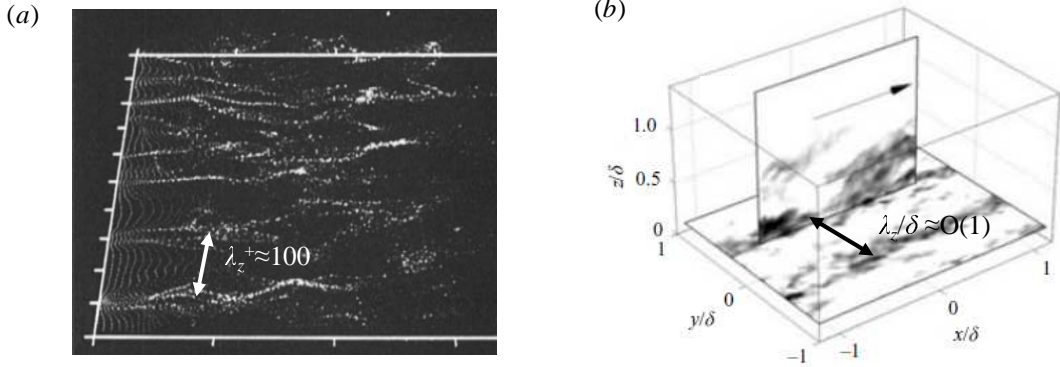
Figure 1.3. Streaky structures in wall-bounded turbulent flows: (*a*) particle tracing in the near-wall region (from Kim *et al.*, 1987); (*b*) PIV measurement in the outer region (from Hutchins & Marusic, 2007*a*).

Townsend (1976), who suggested the concept of 'attached eddy' to explain the behavior of turbulent velocity fluctuations and the Reynolds stress. Later, Perry and coworkers further extended this idea by considering more specific forms of the eddies such as 'Λ-vortices' (Perry & Chong, 1982; Perry *et al.*, 1986; Perry & Marusic, 1995).

2.2 Streaky motions

The presence of the streaky motions in wall-bounded turbulent flows has been constantly observed for the last five decades. Relevant streaky motions exist at least with two different length scales: the inner and outer length scales. The evidences are presented in Fig. 1.3 (*a*) and (*b*) where the streaky motions in the near-wall and outer regions are visualized respectively.

Streaks in the near-wall region

The near-wall region is the place where the coherent streaky structures were first found (Kline *et al.*, 1967; Smith & Metzler, 1983; Kim *et al.*, 1987). There, streaky motions have the mean spanwise spacing of $\lambda_z^+ \simeq 100$ (Fig. 1.3*a*), and their mean streamwise length extends up to $\lambda_x^+ \simeq 1000$. The streaky structures propagate downstream with phase speed $c^+ \simeq 10$ while they are slightly lifted from the wall. The lifted streaks abruptly oscillate with violent ejection of fluid outward from the wall, followed by sweeping fluid motions toward the wall. These motions form an internal shear layer and give the birth of streamwise vortices that develop into new streaky motions. This process, called 'bursting', is believed to be at the core of near-wall turbulence generation (Robinson, 1991).

There have been numerous efforts to explain the bursting and regeneration of the near-wall coherent structures (for further details, see e.g. the review by Panton, 2001). Hamilton *et al.* (1995) and Waleffe (1995, 1997) suggested a self-sustaining cycle of the near-wall turbulence using the minimal computational box approach by Jiménez & Moin (1991). Fig. 1.4 (*a*) shows a schematic diagram of the self-sustaining cycle. The mean advection amplifies the streamwise vortices into the streaks through lift-up effect. Then, the amplified streaks break down through inflectional instability, and the subsequent nonlinear interaction of instability waves regenerates the streamwise vortices. Schoppa & Hussain (2002) suggested that the
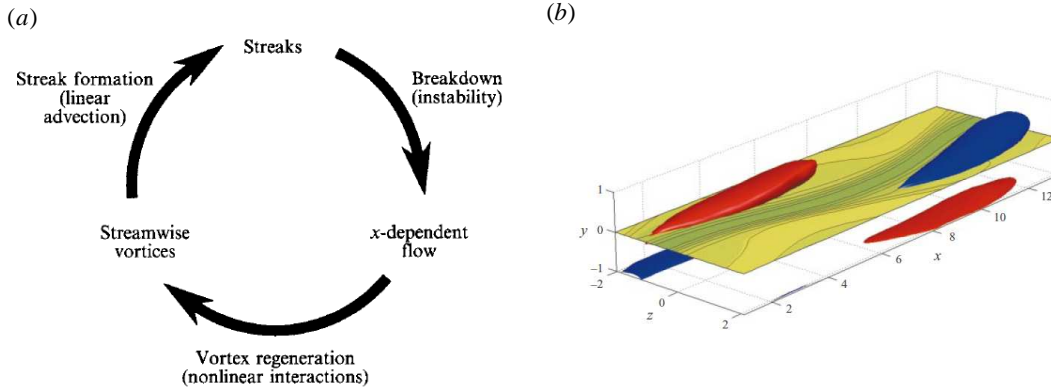
Figure 1.4. Self-sustaining process of near-wall turbulence: (*a*) schematic illustration (from Hamilton *et al.*, 1995); (*b*) A traveling wave solution embedded into the self-sustaining process (from Waleffe, 2001). In (*b*), the *x*-*z* plane velocity contour denotes the streamwise velocity fluctuation, and the red and blue three-dimensional iso-surfaces are positive and negative streamwise vorticity respectively.

breakdown of streaks can also occur via secondary transient growth instead of the modal instability of the streaks. The existence of such a self-sustaining mechanism was also supported by the numerical experiment of Jiménez & Pinelli (1999) where the near-wall structures are shown to be sustaining even if the outer motions are artificially quenched.

The discovery of the self-sustaining cycle has fostered attempts to describe the near-wall turbulence in terms of 'exact' nonlinear solutions of the Navier-Stokes equation such as saddles and unstable periodic orbits (Nagata, 1990; Waleffe, 1998, 2001; Kawahara & Kida, 2001; Jiménez & Simens, 2001; Waleffe, 2003; Faisst & Eckhardt, 2003; Wedin & Kerswell, 2004; Viswanath, 2007; Gibson *et al.*, 2009; Viswanath, 2009). Many unstable nonlinear saddle solutions have been found, and their typical spatial structure is shown in Fig. 1.4 (*b*). They consist of a streak sinuously oscillating in the streamwise direction and aligned vortices at its flank. Some of these solutions sit on the boundary between laminar and turbulent states (e.g. Schneider *et al.*, 2007; Duguet *et al.*, 2008), and the others are embedded into the trajectory of turbulent solution (for the further details, refer to a recent review by Eckhardt *et al.*, 2007).

Large-scale and very-large-scale motions in the outer region

The outer region of wall-bounded turbulent flows is characterized by spatial intermittency of turbulence. Fig. 1.5 shows a smoke visualization of a turbulent boundary layer. The near-wall region where the buffer-layer streaks reside is very thin, and it is fully filled by the smoke. On the other hand, the outer region is dominated by spatially intermittent smoke filled areas, and each of them are separated by deep penetration of non-turbulent fluid. These δ-scale structures are called 'large-scale motions (LSM)' or 'bulges', and they have streamwise extent of $2 \sim 3\delta$ and spanwise extent of $1 \sim 1.5\delta$ (Corrsin & Kistler, 1954; Kovasznay *et al.*, 1970; Balckwelder & Kovasznay, 1972; Murlis *et al.*, 1982). The large-scale motions have been shown to contain finer-scale structures. Falco (1977) called these structures 'typical eddies' (see also fig. 1.5) and Head & Bandyopadhay (1981) suggested that they are hairpin or Λ-vortices inclined at $45°$. Zhou *et al.* (1999) and Adrian *et al.* (2000) suggested that these
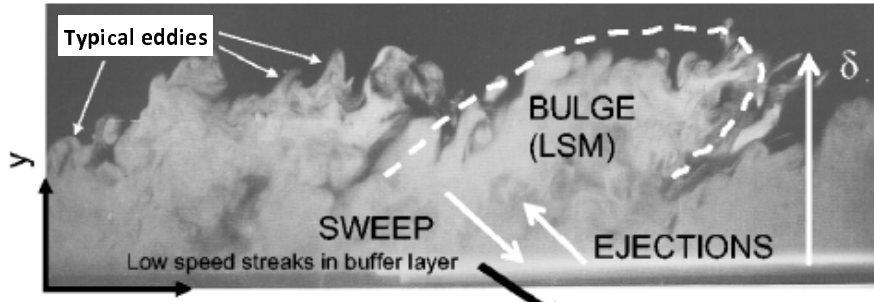
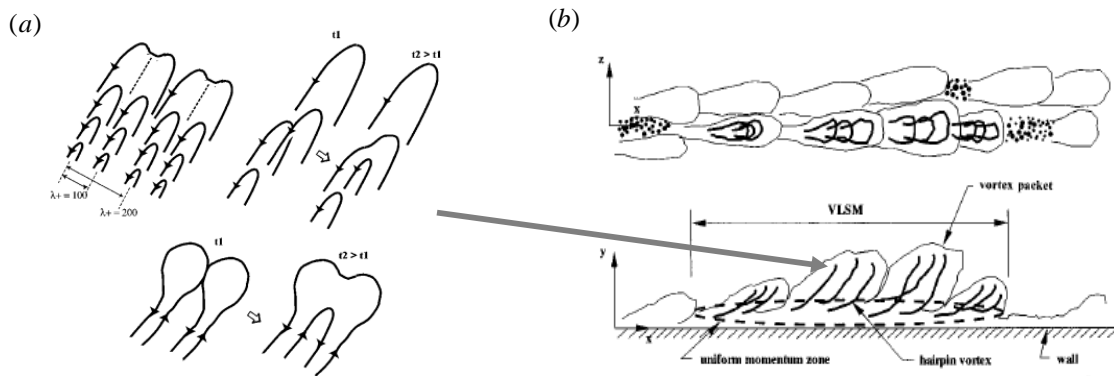Figure 1.5. Smoke visualization of turbulent boundary layer (from Adrian, 2007).

Figure 1.6. Schematic diagram on the formation of (*a*) large-scale and (*b*) very-large-scale motions (streaky motions): (*a*) formation of a large-scale motion by the self-similar merger and/or growth of individual hairpin vortices (from Adrian, 2007); (*b*) formation of the large-scale streaky motions by the concatenation of individual large-scale motions (bulges) (from Kim & Adrian, 1999); .

hairpin vortices are generated by the mutual vortical induction, and more recently Tomkins & Adrian (2003) and Adrian (2007) insisted that the large-scale motions are the vortex packets formed by the merger and growth of individual hairpin vortices as shown in Fig. 1.6(*a*). They also argued that this merger and growth process occurs in the logarithmic layer where the length-scale growth is observed.

While the existence of large-scale motions has been known for a long time, it is only in recent years that the existence of long streaky motions extending up to $\lambda_x \simeq O(10h)$ has been recognized in boundary layers (Tomkins & Adrian, 2005; Hutchins & Marusic, 2007*a*,*b*), Couette (Komminaho *et al.*, 1996; Kitoh *et al.*, 2005; Kitoh & Umeki, 2008), plane channel (Jiménez, 1998; del Álamo & Jiménez, 2003; del Álamo *et al.*, 2004) and pipe flows (Kim & Adrian, 1999; Guala *et al.*, 2006). These very long streaky motions, also called 'very-large-scale motions (VLSM)' or 'superstructures' or 'global modes', are very energetic and active: they carry a significant amount of the turbulent kinetic energy and Reynolds stress in the outer region. These features are persistent even in the buffer layer, thus they modulate the near-wall cycles (Hunt & Morrison, 2000; Hutchins & Marusic, 2007*b*; Mathis *et al.*, 2009). A

first attempt to explain the origin of the very large-scale streaks was made by Kim & Adrian (1999) and Guala *et al.* (2006). They found that several large-scale motions (or bulges) are coherently aligned as shown in Fig. 1.6(*b*). They conjectured that the long streaky motion is the low-momentum region formed by the concatenation of individual large-scale motions through vortex induction. Note that the energy transfer from small-scale near-wall cycles to large-scale outer motions is a key element of this type of the explanations, where the long outer streaky motions would not exist in the absence of the near-wall cycles. However, the recent numerical experiments by Flores & Jiménez (2006) and Flores *et al.* (2007) have shown that the outer motions are not significantly influenced even if the near-wall region is completely disturbed by the roughness of the wall. Also, del Álamo *et al.* (2006) insists that the life time of the individual vortex packets aligned along the streaks are considerably shorter than that of the streaky motions, thus the concatenation is not likely to be the process generating the streaky motions.

Coherent lift-up effect

An alternative viewpoint on the origin of the long-streaky structures is emerging from recent findings that extend hydrodynamic stability methodologies to fully developed turbulent flows. By using the Reynolds & Hussain (1972) linear model for small coherent motions, del Álamo & Jiménez (2006), Pujals *et al.* (2009) and Cossu *et al.* (2009) have computed the optimal transient growth sustained by fully-developed turbulent flows. They found that there exist strong amplification of streaks by the lift-up effect with two locally optimal spanwise wavelengths scaled by the outer and inner units respectively. The dominant optimal wavelengths have shown to be in good agreement with the spanwise spacing of the large-scale streaky structures in the outer region, and the secondary optimal wavelength corresponds to typical spanwise spacing of the near-wall streaks. This theoretical prediction on the large amplification of the streaky structures has also been experimentally confirmed. Kitoh & Umeki (2008) and Pujals *et al.* (2010*a*) carried out experiments in which they installed passive devices such as vortex generator and roughness elements designed to induce streamwise vortices in the flow field. They found that such passive devices generate amplified long streaky structures, indicating that the large-scale streaky motions could be a consequence of 'coherent lift-up' effect.

3   Motivations and objectives of this work

The main goal of this thesis is to understand the origin of large-scale coherent streaky motions in wall-bounded turbulent flows. We have decided to follow the work hypothesis that a self-sustaining cycle similar to the near-wall process exists at large scale (Guala *et al.*, 2006; Jiménez, 2007; Cossu *et al.*, 2009). To verify this conjecture we have first investigated if such large-scale streaky structures can be continuously amplified by *forcing* via the coherent lift-up effect. Then, we have investigated the existence of the secondary instabilities able to regenerate the vortices. Finally, we have made sure that those large-scale structures sustain even if the absence of smaller-scale structures in the near-wall and logarithmic regions. Finally, we have verified if artificially forced large-scale streaks can be used to reduce the turbulent skin friction.

Amplification of streaks by optimal harmonic and stochastic forcing

Previous investigations by del Álamo & Jiménez (2006), Pujals *et al.* (2009) and Cossu *et al.* (2009) have shown that the large-scale streaky motions can be amplified via a coherent lift-up effect, but they have considered only optimal temporal transient energy growth of initial conditions. The present study extends the previous investigations to the responses to optimal harmonic and stochastic forcing. Computation of the response to optimal harmonic forcing is of a fundamental interest for flow control application. Also, in turbulent flows, structures of a given scale are permanently forced by structures of different scales via nonlinear interactions. In this respect, a modeling of the streaks amplification based on the response to stochastic forcing would seem more relevant than the transient growth of initial growth considered in previous studies. By computing the responses to harmonic and stochastic forcing, we will provide answers to the following questions: What are the most amplified spanwise length scales? Are the optimal amplifications scaled by the outer and inner units as in optimal transient growth? How is amplification characteristics related to logarithmic layer? Is the response to stochastic forcing relevant to describe the fully turbulent flow?

Secondary instability of large-scale streaks

Natural streaky motions observed in laboratory and numerical experiments have the streamwise lengths of $O(10h)$ and also sinuously oscillate. The large-scale motions (bulges) are found to be coherently aligned along the streaky motions. The questions addressed here are: Why do the very-large-scale motions sinuously oscillate in the streamwise direction? Why are the large-scale motions aligned? In order to answer these questions, we conduct a stability analysis of the amplified large-scale streaks using an eddy-viscosity model. We focus particularly on the streamwise wavelength related to the most unstable mode. Also, the role of the eddy viscosity on the onset of streak instability are investigated.

Self-sustaining process at large scale

As discussed in section 2.2, coherent structures in the outer region of turbulent boundary layer have often been understood as formed by the active near-wall cycle via a 'bottom-up' process. Several previous investigations have insisted that the large-scale motions are formed by merger and/or growth of hairpin vortices (Adrian, 2007). Even from a different perspective, the numerical experiment by Toh & Itano (2005) have also supported the idea that large-scale motions can be directly forced via a 'co-supporting' cycle. On the other hand, the recent numerical experiments by Flores & Jiménez (2006) and Flores *et al.* (2007) have reported that the characteristics of turbulent motions in the outer region do not change significantly when the near-wall region is completely disturbed by the roughness of the wall. While the latter result give credit to the existence of an independent self-sustaining process at the outer length scales, the eddies in the logarithmic-layer length scale are still present in their simulations. Therefore, the role of the logarithmic length-scale eddies are not clear in those studies. In this perspective, the outstanding questions are probably: Can the large-scale coherent structures sustain without the presence of the near-wall and logarithmic-layer eddies? Do they sustain similarly to the near-wall process? The answers to these questions are investigated by conducting a numerical experiment in which we attempt to suppress the small-scale eddies in the near-wall and logarithmic regions.

Turbulent skin-friction drag reduction by forcing large-scale streaks

From the viewpoint of flow control, the large amplification of streak is a fruitful feature providing a high-amplitude actuation only with a small amount of the energy input. For laminar flows, this feature has been used to delay transition in boundary layer. Recently, the strong amplification of large-scale streaks predicted by the non-modal stability theories has been confirmed by Kitoh *et al.* (2005), Kitoh & Umeki (2008) and Pujals *et al.* (2010*a*), where the large-scale streaks are shown to be highly amplified by the roughness element installed in upstream. Furthermore, Pujals *et al.* (2010*b*) showed that the artificially forced streaks on the roof of an Ahmed body can suppress separation occurring in its rear side. Motivated by these studies, we examine the relevance of artificially driven streaks for turbulent skin-friction drag reduction by answering the following questions: Can artificially driven streaks reduce turbulent skin-friction drag? If yes, how do they reduce the skin friction? Is the effective length of the streak forcing scaled by the outer unit or inner unit? Does this kind of approach also provide a net saving of power when the control energy is considered?

4   Organization of the dissertation

The present dissertation is organized as follows: In chapter 2, optimal perturbations for initial condition, deterministic forcing and stochastic forcing are computed to study the amplification of the streaks in turbulent Couette and pressure-driven channel flows. In chapter 3, the instability of amplified streaks is investigated using the Floquet theory, and its physical implications are discussed with the streamwise length scales of the large-scale motions and long streaky structures. In chapter 4, we prove the existence of a self-sustaining process supported only at large scale. The statistics related to the large-scale self-sustaining process are intensively studied with the physical features of large-scale motion and streaky structures. Also, the nature of the self-sustaining process is studied by minimizing the size of the computational box. In chapter 5, the amplification of the large-scale streaks is examined using direct numerical simulation. The artificially driven large-scale streaks are found to reduce the skin-friction drag by quenching the the near-wall streamwise vortices. Finally, conclusion and outlook are given in chapter 6.

Chapter 2

Linear non-normal amplification of coherent streaks

As stated in the introduction, the linear non-normal amplification of coherent streaks sustained by a turbulent mean flow has been investigated by del Álamo & Jiménez (2006), Pujals *et al.* (2009) and Cossu *et al.* (2009) following the early linear formulation for the small coherent perturbations (Reynolds & Hussain, 1972). However, in these studies, only the optimal temporal transient growth has been considered. The scope of this chapter is to extend these analyses to the responses to optimal harmonic and stochastic forcing. We begin by recalling the model of Reynolds & Hussain (1972). The standard definitions of the optimal amplifications is then introduced. The main results are presented for Couette flow at a low Reynolds number (Hwang & Cossu, 2010*a*), pressure-driven channel flow (Hwang & Cossu, 2010*b*) and pipe flow (Willis *et al.*, 2010). Finally, a comprehensive discussion on the relevance of the linear amplifications is given by comparing the results of the linear analysis with the features of streaky structures in wall-bounded turbulent flows. The results for the turbulent pipe flow have been obtained in collaboration with A. P. Willis.

1   Equations for small coherent motions

Following Reynolds & Hussain (1972), the equation of coherent motions is derived here. We begin from the incompressible Navier-Stokes equation with the continuity:

$$\frac{\partial u_i}{\partial x_i} = 0,\tag{2.1a}$$

$$\frac{\partial u_i}{\partial t} + u_j \frac{\partial u_i}{\partial x_j} = -\frac{1}{\rho}\frac{\partial p}{\partial x_i} + \nu \frac{\partial^2 u_i}{\partial x_j \partial x_j},\tag{2.1b}$$

where u_i is the velocity, p is the pressure and x_i denotes the coordinate. First, we imagine a situation where the turbulent flow field is perturbed in a statistically correlated way by external devices (e.g. a vibrating ribbon, or roughness elements). Under such circumstance, it is convenient to describe flow field by decomposing the velocity signal as

$$u_i = \bar{u}_i + \tilde{u}_i + u_i',\tag{2.2}$$

where $\bar{u}_i$ the time-averaged velocity, $\tilde{u}_i$ the coherent motion induced by the driven perturbation and u_i' is the random part of the motion. Here, $\tilde{u}_i$ is precisely defined as the velocity field

captured by the *ensemble average*: i.e. the field averaged by numerous repetition of the same experiment. From this definition, the ensemble average (denoted by $\langle \cdot \rangle$) of (2.2) gives $\langle u_i \rangle = \bar{u}_i + \tilde{u}_i$. An equation for $\bar{u}_i$ is obtained by averaging (2.1b) in time:

$$\bar{u}_j \frac{\partial \overline{u}_i}{\partial x_j} = -\frac{1}{\rho} \frac{\partial \overline{p}}{\partial x_i} + \nu \frac{\partial^2 \overline{u}_i}{\partial x_j \partial x_j} + \frac{\partial \overline{r}_{ij}}{\partial x_j}, \tag{2.3a}$$

where

$$\overline{r}_{ij} \equiv -\overline{u_i' u_j'} - \overline{\tilde{u}_i \tilde{u}_j}. \tag{2.3b}$$

Here, the first term in $\overline{r}_{ij}$ is the Reynolds stress term originated by the random-velocity field and the second term $-\overline{\tilde{u}_i \tilde{u}_j}$ represents the stress induced by the coherent motions. If we assume that the amplitude of the coherent motions is sufficiently small, the term $-\overline{\tilde{u}_i \tilde{u}_j}$ can be neglected, and the equation for small coherent perturbations is derived by subtracting (2.3) from the ensemble-averaged equation of (2.1b):

$$\frac{\partial \tilde{u}_i}{\partial t} + \bar{u}_j \frac{\partial \tilde{u}_i}{\partial x_j} + \tilde{u}_j \frac{\partial \overline{u}_i}{\partial x_j} = -\frac{1}{\rho} \frac{\partial \tilde{p}}{\partial x_i} + \nu \frac{\partial^2 \tilde{u}_i}{\partial x_j \partial x_j} + \frac{\partial \tilde{r}_{ij}}{\partial x_j}, \tag{2.4a}$$

where

$$\tilde{r}_{ij} \equiv -\langle u_i' u_j' \rangle + \overline{u_i' u_j'}. \tag{2.4b}$$

Note that (2.4a) has an additional unknown stress term $\tilde{r}_{ij}$ consisting of $\langle u_i' u_j' \rangle$ and the Reynolds stress $\overline{u_i' u_j'}$, and this term essentially stems from the effect of background turbulence on the coherent motions.

Reynolds & Hussain (1972) suggested to model this term with a Newtonian eddy viscosity:

$$\tilde{r}_{ij} = -2\nu_t \tilde{S}_{ij}, \tag{2.5}$$

where ν_t is the eddy viscosity corresponding to the mean-velocity field without any perturbations and $\tilde{S}_{ij} \equiv 1/2(\partial \tilde{u}_i / \partial x_j + \partial \tilde{u}_j / \partial x_i)$. This model is simple and crude, but Reynolds & Hussain (1972) have demonstrated that it provides a qualitatively good description on the dynamics of small coherent perturbations.

2   Optimal perturbations

2.1   The generalized Orr-Sommerfeld-Squire equations

For convenience, the tensor form of notation is changed into the vector form hereafter. We consider the turbulent flow in a channel with the upper and bottom walls located at $\pm h$. The streamwise, wall-normal and spanwise directions are denoted as x, y and z respectively. The vector form of equation (2.4) around the mean flow $\bar{\mathbf{u}} = (U(y), 0, 0)$ is written as follows:

$$\frac{\partial \tilde{\mathbf{u}}}{\partial t} + \nabla \tilde{\mathbf{u}} \cdot \bar{\mathbf{u}} + \nabla \bar{\mathbf{u}} \cdot \tilde{\mathbf{u}} = -\frac{1}{\rho} \nabla \tilde{p} + \nabla \cdot \left[\nu_T \left(\nabla \tilde{\mathbf{u}} + \nabla \tilde{\mathbf{u}}^T \right) \right] + \tilde{\mathbf{f}}, \tag{2.6}$$

Here, $\nu_T \equiv \nu + \nu_t$ is the total eddy viscosity and $\tilde{\mathbf{f}}$ is a body forcing term added to study the response of (2.6) to 'external' forcing. The homogeneity of the mean flow in the streamwise

and spanwise directions allows to consider the Fourier mode decomposition in the horizontal plane:

$$
\begin{array}{rcl}
\tilde{\mathbf{u}}(x,y,z,t) & = & \hat{\mathbf{u}}(y,t;\alpha,\beta)e^{i(\alpha x+\beta z)}, \\
\tilde{\mathbf{f}}(x,y,z,t) & = & \hat{\mathbf{f}}(y,t;\alpha,\beta)e^{i(\alpha x+\beta z)},
\end{array}
\tag{2.7}
$$

where α and β are the streamwise and spanwise wavenumbers respectively. Then, using standard manipulations, the generalized Orr-Sommerfeld-Squire system (Pujals *et al.*, 2009; Hwang & Cossu, 2010*a*) is obtained from (2.6) as follows:

$$
\frac{\partial}{\partial t}\underbrace{\begin{bmatrix} \hat{v} \\ \hat{\eta} \end{bmatrix}}_{\hat{\mathbf{q}}} = \underbrace{\begin{bmatrix} \Delta^{-1}\mathcal{L}_{\mathcal{OS}} & 0 \\ -i\beta U' & \mathcal{L}_{\mathcal{SQ}} \end{bmatrix}}_{\mathbf{A}} \begin{bmatrix} \hat{v} \\ \hat{\eta} \end{bmatrix}
$$

$$
+ \underbrace{\begin{bmatrix} -i\alpha\Delta^{-1}\mathcal{D} & -k^2\Delta^{-1} & -i\beta\Delta^{-1}\mathcal{D} \\ i\beta & 0 & -i\alpha \end{bmatrix}}_{\mathbf{B}} \underbrace{\begin{bmatrix} \hat{f_u} \\ \hat{f_v} \\ \hat{f_w} \end{bmatrix}}_{\hat{\mathbf{f}}},
\tag{2.8a}
$$

where

$$
\begin{array}{rcl}
\mathcal{L}_{\mathcal{OS}} & = & -i\alpha(U\Delta - U") + \nu_T\Delta^2 + 2\nu_T'\Delta\mathcal{D} + \nu_T"(\mathcal{D}^2 + k^2), \\
\mathcal{L}_{\mathcal{SQ}} & = & -i\alpha U + \nu_T\Delta + \nu_T'\mathcal{D}.
\end{array}
\tag{2.8b}
$$

Here, $\mathcal{D}$ and $'$ denote $\partial/\partial y$, $\Delta = \mathcal{D}^2 - k^2$, $k^2 = \alpha^2 + \beta^2$, and $\hat{\eta}$ is Fourier mode of the wall-normal vorticity. The initial condition is given as $\hat{\mathbf{u}}|_{t=0} = \hat{\mathbf{u}}_0$ and no-slip boundary conditions of the velocity are applied on the walls: $\hat{v}(y = \pm h) = 0$, $\mathcal{D}\hat{v}(\pm h) = 0$, and $\hat{\eta}(\pm h) = 0$. The velocity components $\hat{\mathbf{u}}$ are retrieved from the wall-normal variables with

$$
\underbrace{\begin{bmatrix} \hat{u} \\ \hat{v} \\ \hat{w} \end{bmatrix}}_{\hat{\mathbf{u}}} = \frac{1}{k^2}\underbrace{\begin{bmatrix} i\alpha\mathcal{D} & -i\beta \\ k^2 & 0 \\ i\beta\mathcal{D} & i\alpha \end{bmatrix}}_{\mathbf{C}} \begin{bmatrix} \hat{v} \\ \hat{\eta} \end{bmatrix},
\tag{2.9}
$$

and vice-versa

$$
\begin{bmatrix} \hat{v} \\ \hat{\eta} \end{bmatrix} = \underbrace{\begin{bmatrix} 0 & 1 & 0 \\ i\beta & 0 & -i\alpha \end{bmatrix}}_{\mathbf{D}} \begin{bmatrix} \hat{u} \\ \hat{v} \\ \hat{w} \end{bmatrix}.
\tag{2.10}
$$

A slightly different formulation has been used in the case of the pipe flow. (for further details, refer to Willis *et al.*, 2010).

2.2   Optimal perturbations

To examine the amplification by the given linear system, the optimal responses to initial conditions, harmonic forcing and stochastic forcing are studied. The standard definitions of these responses are found in the reviews by Farrell & Ioannou (1996), Schmid & Henningson (2001) and Schmid (2007)[1].

---

[1]A small error is found in this paper where $\hat{\mathbf{q}} = \mathbf{B}\hat{\mathbf{u}}$ is used instead of $\hat{\mathbf{q}} = \mathbf{D}\hat{\mathbf{u}}$.

The optimal temporal energy growth of a Fourier mode is defined as the energy ratio of the response at a given time t to the initial condition:

$$G(t; \alpha, \beta) \equiv \max_{\hat{\mathbf{u}}_0 \neq \mathbf{0}} \frac{\|\hat{\mathbf{u}}(t; \alpha, \beta)\|^2}{\|\hat{\mathbf{u}}_0(\alpha, \beta)\|^2} = \|\boldsymbol{\Phi}(t; \alpha, \beta)\|^2, \qquad (2.11)$$

where $\|\hat{\mathbf{u}}\|^2 = \int_{-h}^{h} |\hat{u}|^2 + |\hat{v}|^2 + |\hat{w}|^2 dy$, and $\boldsymbol{\Phi}(t; \alpha, \beta) = \mathbf{C}e^{t\mathbf{A}}\mathbf{D}$ is the state-transition matrix (also called propagator). The maximum transient energy growth $G_{\max}$ is then defined by maximizing $G(t)$ for all the admissible t: $G_{\max}(\alpha, \beta) \equiv \max_t G(t; \alpha, \beta)$.

If a harmonic forcing $\hat{\mathbf{f}}(y, t) = \check{\mathbf{f}}(y)e^{i\omega_f t}$ with a frequency ω_f is driven into the linearly stable system, its response is also tuned by the same forcing frequency after the switch-on transient decays: $\hat{\mathbf{u}}(y, t) = \check{\mathbf{u}}(y)e^{i\omega_f t}$. The optimal response is then obtained by maximizing the energy ratio of the response to the forcing:

$$R(\omega_f; \alpha, \beta) = \max_{\check{\mathbf{f}} \neq \mathbf{0}} \frac{\|\check{\mathbf{u}}(\omega_f; \alpha, \beta)\|^2}{\|\check{\mathbf{f}}(\omega_f; \alpha, \beta)\|^2} = \|\mathbf{H}(\omega_f; \alpha, \beta)\|^2, \qquad (2.12)$$

where $\mathbf{H}(\omega_f; \alpha, \beta) \equiv \mathbf{C}(i\omega_f \mathbf{I} - \mathbf{A})^{-1}\mathbf{B}$ is the transfer function. The maximum possible response $R_{\max}(\alpha, \beta) = \max_{\omega_f} R(\omega_f; \alpha, \beta)$ is obtained with $\omega_{f,max}$, and it is also referred to as H_∞-norm of the transfer function (Zhou *et al.*, 1996).

Finally, the response to stochastic forcing is studied. The forcing is assumed to have a zero-mean ($\langle \hat{\mathbf{f}} \rangle = \mathbf{0}$) and Gaussian probability density distribution, and its covariance is assumed to be delta-correlated in time and space with spatially uniform distribution ($\langle \hat{\mathbf{f}}(t)\hat{\mathbf{f}}^H(t') \rangle = \hat{\mathbf{I}}\delta(t - t')$). The amplification of the stochastic forcing is measured by the variance $V = \langle \|\hat{\mathbf{u}}\|^2 \rangle$, and it can be computed by the trace of the covariance matrix $\langle \hat{\mathbf{u}}\hat{\mathbf{u}}^H \rangle$, where the superscript ^{H} denotes the complex conjugate transpose. The variance, also referred to as the H_2-norm of the transfer function (Zhou *et al.*, 1996), is then given in the frequency or in the temporal domain as follows:

$$V(\alpha, \beta) = \frac{1}{2\pi} \int_{-\infty}^{\infty} trace\left(\mathbf{H}\mathbf{H}^\dagger\right) d\omega = trace(\mathbf{C}\mathbf{X}_\infty \mathbf{C}^\dagger), \qquad (2.13)$$

where the superscript † denotes the adjoint operator based on the inner product $(\hat{\mathbf{u}}, \hat{\mathbf{v}}) = \int_{-h}^{h} \hat{\mathbf{u}}^H \hat{\mathbf{v}} dy$, and $\mathbf{X}_\infty$ is the solution of the following algebraic Lyapunov equation:

$$\mathbf{A}\mathbf{X}_\infty + \mathbf{X}_\infty \mathbf{A}^\dagger + \mathbf{B}\mathbf{B}^\dagger = 0. \qquad (2.14)$$

The covariance matrix of the response is self-adjoint by its definition. Therefore, it has real eigenvalues σ_j with $V = \sum \sigma_j$ and a set of mutually orthogonal eigenfunctions referred to as 'empirical orthogonal functions' (EOF) or Karhunen-Loève (KL) or 'proper orthogonal decomposition' (POD) modes. The ratio σ_j/V represents the contribution of the j-th mode to the variance, and the corresponding eigenfunction provides the associated spatial structure in the response. The eigenfunction corresponding to the largest σ_j is the optimal mode in the sense that it contributes most to the variance. The forcing profiles associated with each Karhunen-Loève mode are obtained by solving the dual Lyapunov problem. For further details, the reader is referred to Farrell & Ioannou (1993a), Farrell & Ioannou (1993b), Zhou *et al.* (1996), Bamieh & Dahleh (2001), Jovanović & Bamieh (2005) and Schmid (2007).
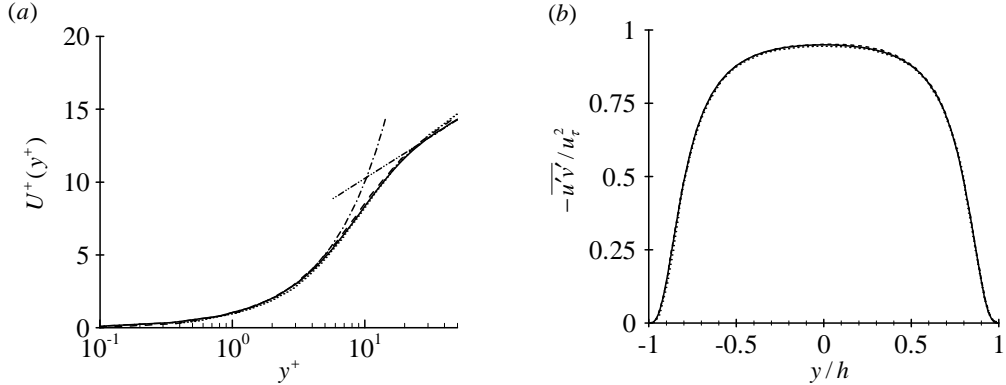
Figure 2.1. Mean flow and the Reynolds stress in turbulent Couette flow at $Re_\tau = 52$: (a) $U^+(y^+)$; (b) $-\overline{u'v'}/u_\tau^2$. Here, ———, the present DNS; - - - -, Komminaho et $al.$ (1996); ⋯⋯⋯, Tsukahara et $al.$ (2006). In (a), —·—·—, $U^+ = y^+$; —··—··—, $U^+ = 1/0.4\log y^+ 4.5$.

3 Base flows

From (2.3a), both the turbulent mean flow and the Reynolds stress are related each other. In parallel flows with small coherent perturbations, the following equation is obtained by integrating (2.3a) in wall-normal direction with the eddy viscosity $-\overline{u'v'} = \nu_t dU/dy$:

$$\frac{\tau_w}{\rho} = \nu_T \frac{dU}{dy} = u_\tau^2 + \frac{y+h}{\rho}\frac{d\bar{p}}{dx}. \tag{2.15}$$

Here, the left-hand side represents the total shear stress due to molecular and turbulent diffusion. For turbulent Couette flow, $d\bar{p}/dx$ is zero, thus the total shear stress is constant across the channel. On the other hand, the pressure-driven channel flow has constant $d\bar{p}/dx$, leading the linear dependence of total shear stress on the distance from the wall y.

3.1 Turbulent Couette flow at $Re_\tau = 52$

First, we consider the turbulent Couette flow where the upper and lower walls move in opposite directions with the same velocity U_w. The turbulent mean flow is computed by direct numerical simulation. Once the simulation is carried out, the total eddy viscosity ν_T can be computed from either the mean-velocity profile or the Reynolds stress. Since $d\bar{p}/dx = 0$ in the Couette flow, the eddy viscosity is easily obtained from (2.15) as

$$\nu_T(y) = \frac{u_\tau^2}{dU/dy}. \tag{2.16}$$

The direct numerical simulation is performed using the `channelflow` code (Gibson et $al.$, 2008) at $Re_h = U_w h/\nu = 750$ (for further details, see Appendix). The friction Reynolds number is found to be $Re_\tau = 52$, the same value found in Komminaho et $al.$ (1996) and in good agreement with the experimental value $Re_\tau = 50$ by Kitoh et $al.$ (2005). Fig. 2.1 shows the computed turbulent mean flow and the associated Reynolds shear stress, almost undistinguishable from those in Komminaho et $al.$ (1996) and Tsukahara et $al.$ (2006). In this mean flow, the logarithmic layer is almost absent due to the low Reynolds number considered.
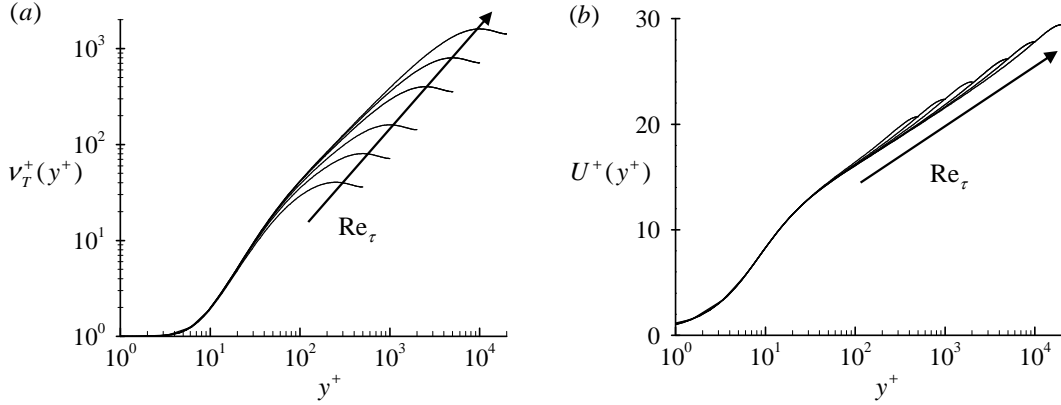
Figure 2.2. The Cess expression of the total eddy viscosity and the corresponding mean flow at $Re_\tau = 500, 1000, 2000, 5000, 10000, 20000$: (a) $\nu_T(y^+)$; (b) $U^+(y^+)$.

3.2   Turbulent channel and pipe flows

In turbulent channel flow, the mean-velocity profile can be retrieved using the following semi-empirical expression for the total eddy viscosity ν_T (Cess, 1958; Reynolds & Tiederman, 1967):

$$\nu_T(\eta) = \frac{\nu}{2}\Big\{1 + \frac{\kappa^2 Re_\tau^2}{9}(1-\eta^2)^2(1+2\eta^2)^2 \times \{1 - exp[(|\eta|-1)Re_\tau/A]\}^2\Big\}^{1/2} + \frac{\nu}{2}, \quad (2.17)$$

with $\eta = y/h$. Here, the constants are set to be $\kappa = 0.426$ and $A = 25.4$ according to del Álamo & Jiménez (2006) and Pujals et al. (2009). Note that these values were obtained from fits based on a direct numerical simulations result at $Re_\tau = 2000$ (Hoyas & Jiménez, 2006). Therefore, they may not be reliable for the Reynolds numbers far from $Re_\tau = 2000$.

For the turbulent channel flow, the pressure gradient is constant across the channel and it is directly related to the friction velocity: $(h/\rho)d\bar{p}/dx = -u_\tau^2$. Using this relation and (2.15), the equation for the mean-velocity profile is obtained with the analytic profile of ν_T:

$$\frac{dU}{d\eta} = -u_\tau^2 \frac{\eta}{\nu_T(\eta)}. \quad (2.18)$$

Then, integration in the wall-normal direction of 2.18 gives the mean-velocity profile. Fig. 2.2 shows the profiles of the total eddy viscosity ν_T and the corresponding mean flow obtained from (2.18) for several large Reynolds numbers. Contrary to the mean flow in the Couette flow at the low Reynolds number, the logarithmic region is now clearly developed due to the considered large Reynolds numbers. Also, the size of the logarithmic region increases as the Reynolds number becomes larger.

Essentially the same base flow is found for the turbulent pipe flows, in which the centerline velocity and the radius of the pipe are denoted as U_e and δ respectively. The mean-velocity profile is also obtained from the semi-empirical expression (2.17) by replacing $\eta = (\delta - r)/\delta$ where $r \in [0, \delta]$ is the radial direction of pipe. The constants in (2.17) are chosen as $\kappa = 0.42$ and $A = 27$ to improve the match with recent observations in McKeon et al. (2005).
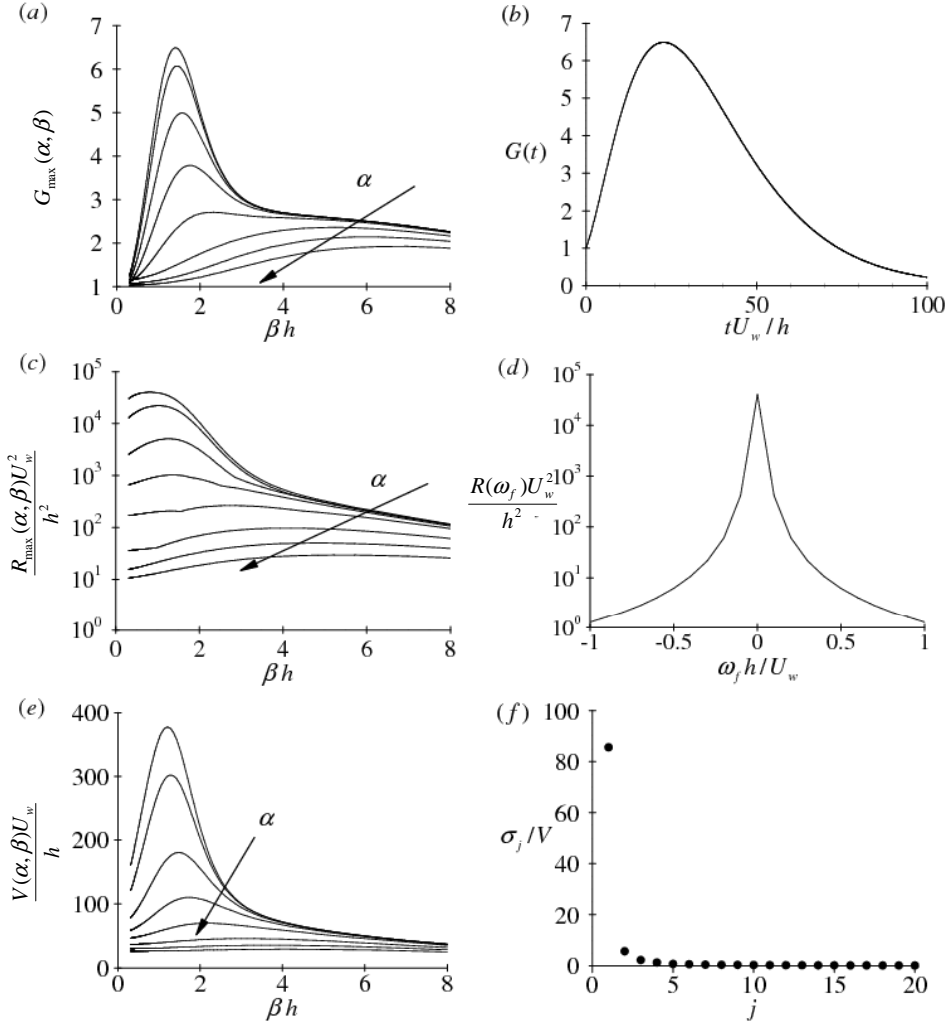
Figure 2.3. Optimal amplification by (a, b) initial condition, (c, d) harmonic, and (e, f) stochastic forcing in turbulent Couette flow at $Re_\tau = 52$: (a) $G_{\max}(\alpha, \beta)$; (b) $G(t)$ for the most amplified wavenumbers $(\alpha, \beta) = (0, 1.46/h)$; (c) $R_{\max}(\alpha, \beta)$; (d) $R_{\max}(\omega_f)$ for the most amplified wavenumbers $(\alpha, \beta) = (0, 0.82/h)$; (e) $V(\alpha, \beta)$; (f) σ_j/V for the most amplified wavenumbers $(\alpha, \beta) = (0, 1.21/h)$. Here, $\alpha h = 0, 0.1, 0.2, 0.5, 1, 2, 5, 10$.

4   Optimal amplifications and associated perturbation

The computation of the eigenvalues of the Orr-Sommerfeld-Squire system (2.8) reveals that all the considered turbulent mean flows are linearly stable. Therefore, the input-output analysis of the stable linear system is carried out by computing the optimal perturbations. The optimal transient growth and optimal harmonic response are computed using standard methods described in Schmid & Henningson (2001), and the stochastic response is computed by solving (2.14) using the `lyap` function in `matlab` (for more details on the numerical method for computation of optimal perturbations, see also Appendix).

4.1   Turbulent Couette flow at $Re_\tau = 52$

Optimal amplifications

Figs. 2.3 (*a*) and (*b*) show the optimal temporal energy growth $G_{\max}(\alpha, \beta)$ and $G(t)$ for the wavenumbers with the largest amplification, respectively. Only streamiwse elongated structures ($\alpha \lesssim \beta$) are significantly amplified, and the maximum amplification is observed for streamwise uniform structures ($\alpha = 0$). For the streamwise uniform perturbations, the spanwise wavelength with the largest amplification corresponds to the $\lambda_z = 4.4h$. As the streamwise wavenumber α increases, the most amplified spanwise wavenumber β slightly increases.

The optimal response to harmonic forcing $R_{\max}(\alpha, \beta)$ is reported in Fig. 2.3 (*c*). Similarly to the optimal transient growth, only elongated structures are amplified. For streamwise uniform structures, the largest response ($R_{\max} = 40269$) is obtained with $\lambda_z = 7.7h$. The dependence of the optimal response on the forcing frequency is shown in 2.3 (*d*) for the most amplified wavenumbers. The frequency response of the system is strongly concentrated around $\omega_f = 0$ and the largest response is found with the steady forcing ($\omega_{f,\max} = 0$), indicating that the system behaves as a strongly selective low-pass frequency filter.

Finally, the variance $V(\alpha, \beta)$ of the response to the stochastic forcing is shown in Fig. 2.3 (*e*). The selection of elongated structures also appears in this case. The maximum amplification of the variance ($V = 377$) have been obtained for streamwise uniform structures with $\lambda_{z\max} = 5.2h$. The structures with the largest contribution to the variance are also identified using the the Karhunen-Loève decomposition. Fig. 2.3 (*f*) shows the twenty largest contributions to the total variance σ_j/V for the wavenumbers of the largest variance ($\alpha=0$, $\beta = 1.21/h$). The most energetic mode contributes to 85% of the total variance, implying that a unique coherent structure strongly dominates the stochastic response.

Optimal perturbations

Figs. 2.4 (*a*) and (*b*) show the spatial structures of the leading Karhunen-Loève modes of the stochastic forcing problem. The forcing contains most of the energy in the cross-stream components and consists of a pair of streamwise vortices. While the response is dominated by the streamwise velocity component and the related structures are streaks. This spatial structure of the optimal streaks is also found to be strikingly similar to that of the most energetic POD mode computed using DNS by Tsukahara *et al.* (2007) (see figs. 2.4*b* and *c*). The optimal transient growth and harmonic forcing problem reveals the same features of those found in the stochastic forcing case (Hwang & Cossu, 2010*a*).
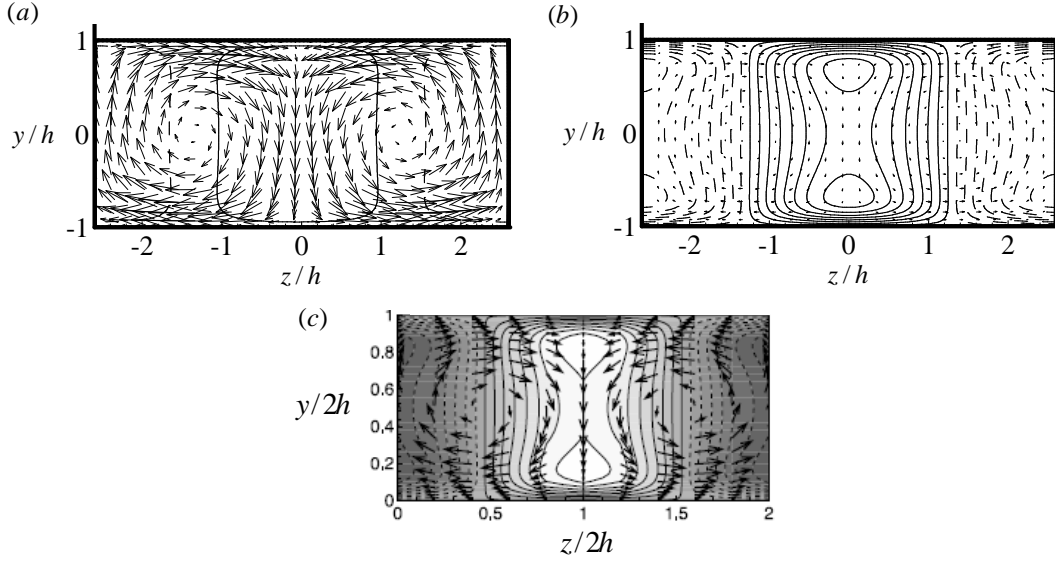
Figure 2.4. Cross-streamwise view of the normalized leading Karhunen-Loève modes of the stochastic forcing and corresponding response for the most amplified wavenumbers: (a) forcing ; (b) response. Here, the solid and dashed contours denote positive and negative values of the streamwise component respectively with the increment of 0.1 from -0.95 to 0.95, and the the cross-stream components are represented as vectors. In (c), the most energetic POD mode in turbulent Coutte flow (Tsukahara et al., 2007) is drawn together for the comparison.

4.2 Turbulent plane channel flow at large Reynolds numbers

The turbulent Couette flow reveals the well-defined nonmodal amplification of streaks for the spanwise spacing $\lambda_z = 4 \sim 7h$. However, the computation of optimal perturbations is limited to low Reynolds numbers ($Re_\tau \lesssim 128$) because the mean-velocity profile must be computed by DNS in very large domain to achieve convergence. For such low Reynolds numbers, the length-scale separation between the inner and outer units is almost non-existent, and this prevents the identification of the two peaks revealed in del Álamo & Jiménez (2006), Pujals et al. (2009) and Cossu et al. (2009). For this reason, we consider the turbulent channel flow in which the profile of the mean flow is available for sufficiently high Reynolds numbers based on the analytical expression by Cess (1958) and Reynolds & Tiederman (1967). We pay particular attention to seek a relation between nonmodal amplification and the spanwise length scales of the amplified streaks at high Reynolds numbers.

Optimal amplification

Let us first consider a sufficiently high Reynolds number $Re_\tau = 10000$. At this Reynolds number, $R_{\max}$ and V are computed for a set of selected streamwise and spanwise wavenumbers, and they are reported in Fig. 2.5 with the $G_{\max}$ data of Pujals et al. (2009). In all the cases, the largest amplifications are reached for streamwise uniform perturbations ($\alpha = 0$), and only streamwise elongated perturbations ($\alpha \leq \beta$) are significantly amplified. $G_{\max}$, $R_{\max}$ and V have a peak for $\lambda_z = 4.0h$, $\lambda_z = 5.0h$ and $\lambda_z = 5.5h$ respectively. While $G_{\max}$ reveals the secondary peak at $\lambda_z^+ \simeq 92$, both $R_{\max}$ and V monotonously decrease as β increases with a noticeable change of slope around $\lambda_z^+ \approx 80$. Particularly in the range $15 < \beta h < 400$, both
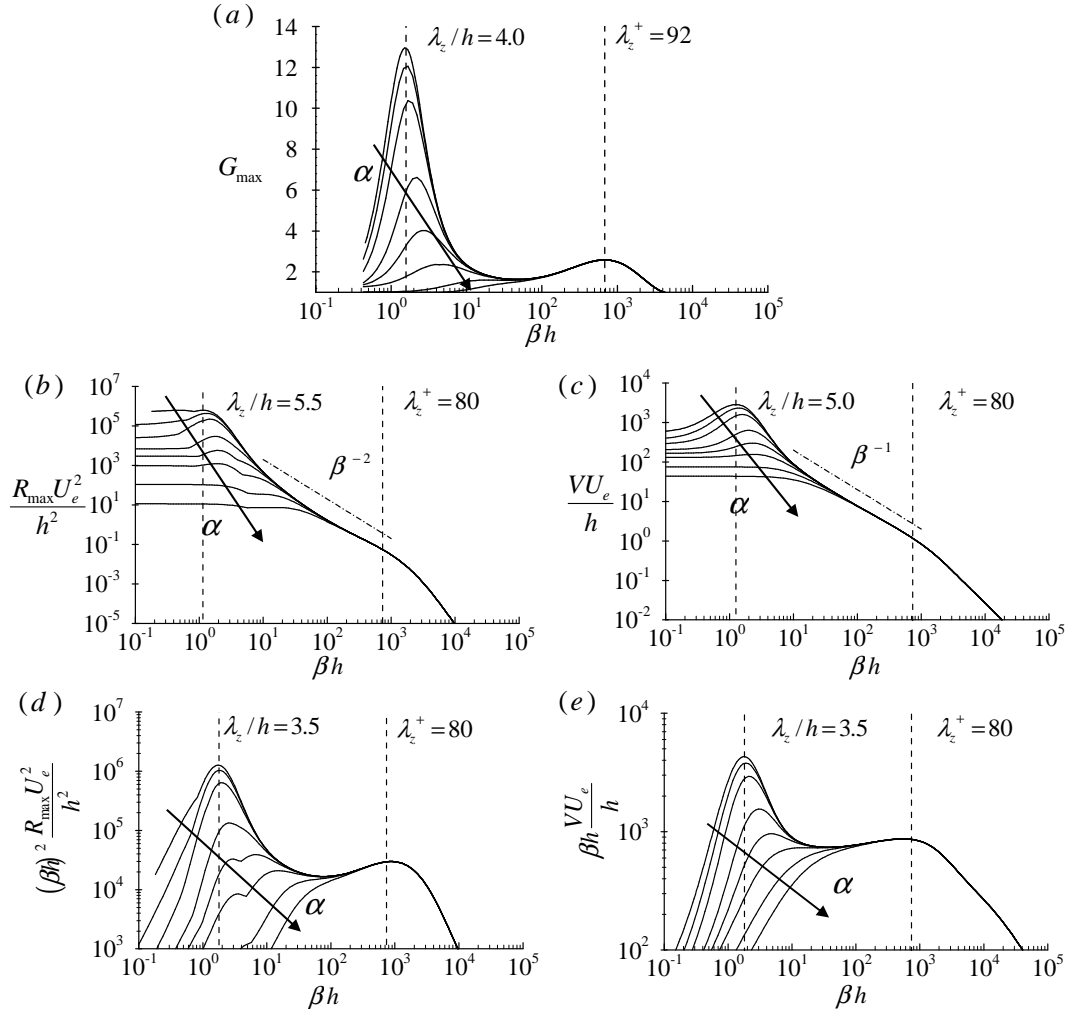
Figure 2.5. Energy amplifications of initial condition, optimal harmonic forcing and stochastic excitation with respect to spatial wavenumbers at $Re_\tau = 10000$: (a) $G_{\max}(\alpha, \beta)$; (b) $R_{\max}(\alpha, \beta)$; (c) $V(\alpha, \beta)$; (d) $\beta^2 R_{\max}(\alpha, \beta)$; (e) $\beta V(\alpha, \beta)$. Here, $\alpha h = 0.0, 0.1, 0.2, 0.5, 1.0, 2.0, 5.0, 10.0$, outer to inner curves.
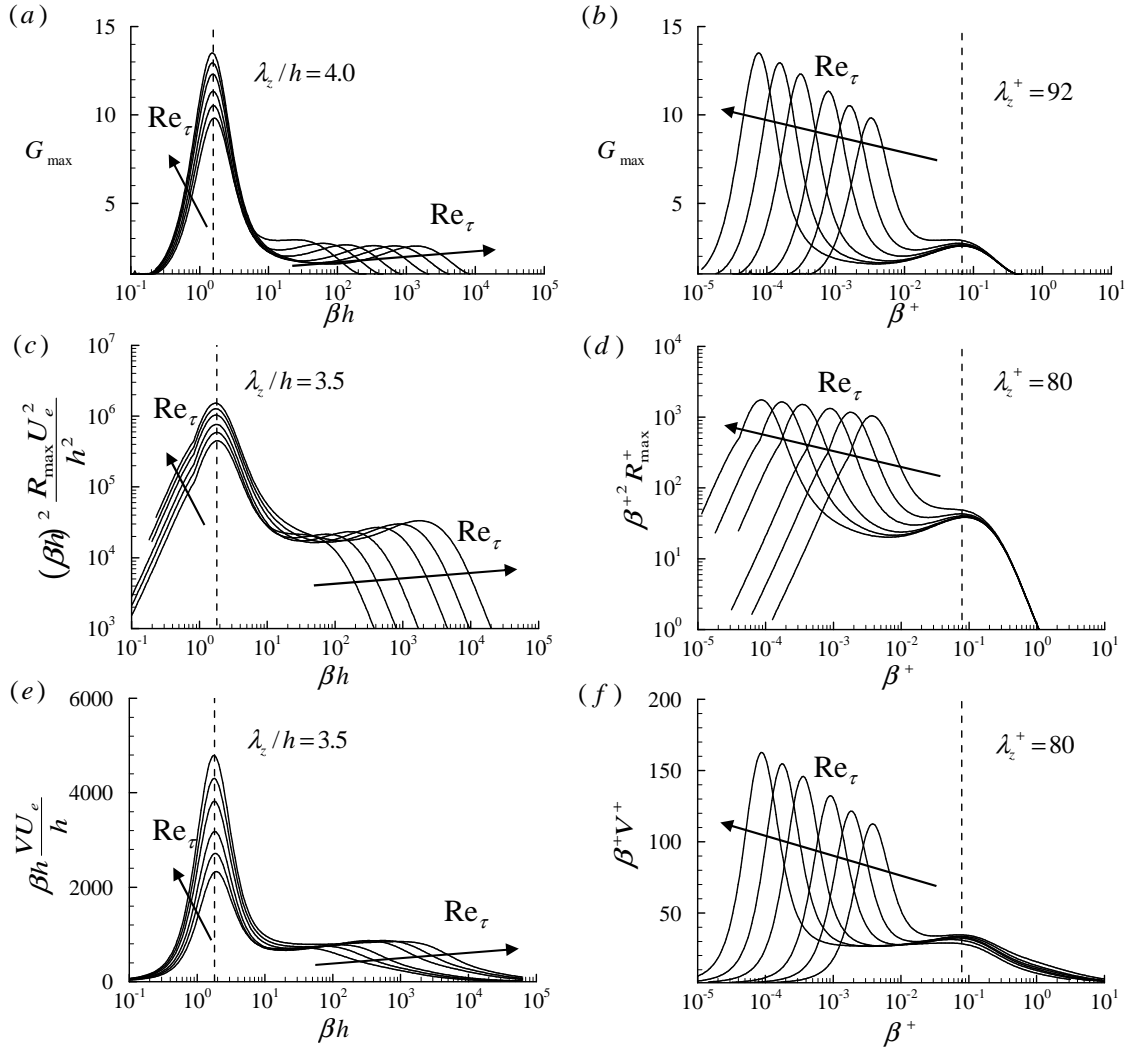
Figure 2.6. Premultiplied amplification of (a, b) optimal initial condition (c, d) optimal harmonic forcing and (e, f) stochastic excitation with respect to the spanwise wavenumber β for $\alpha = 0$ and for the Reynolds numbers $Re_\tau = 500, 1000, 2000, 5000, 10000$, and 20000: (a, c, d) scaling in the outer units; (b, d, f) scaling in the inner units.
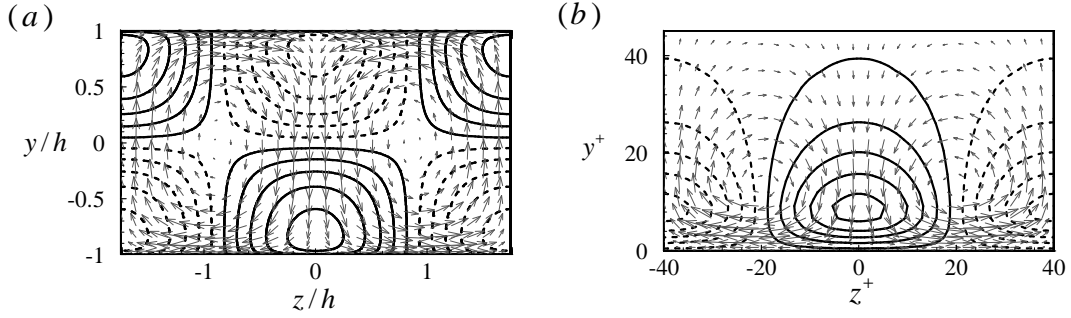
Figure 2.7. Cross-stream (y-z plane) view of the normalized leading Karhunen-Loève modes of stochastic forcing and the corresponding response for spanwise wavenumbers corresponding to (a) the outer peak ($\lambda_z = 3.5h$) and (b) inner peak ($\lambda_z^+ = 80$). The solid and dashed contours denote the positive and negative streamwise velocity of the responses with increment of 0.2 from -0.9 to 0.9 respectively, and the vectors represent the cross-streamwise fields of the forcing. Here, the perturbations are streamwise uniform ($\alpha = 0$).
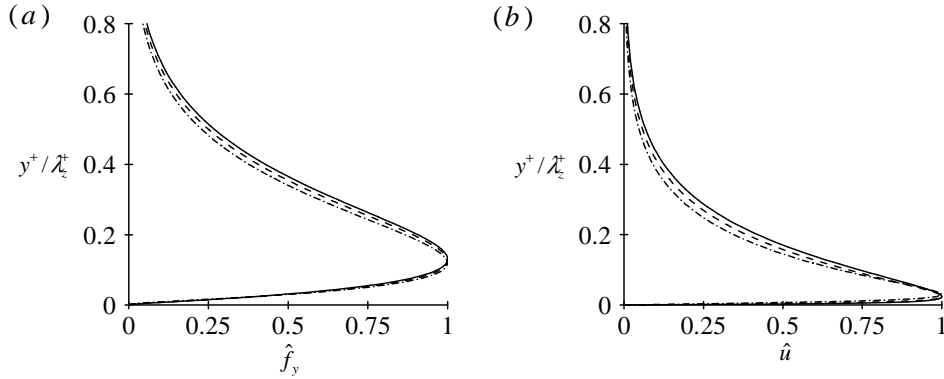

Figure 2.8. Self-similarity of the wall-normal profiles of the leading Karhunen-Loève modes in the stochastic forcing: (a) $\hat{f}_y(y^+/\lambda_z^+)$; (b) $\hat{u}(y^+/\lambda_z^+)$. Here, ———, $\beta^+ = 0.01$ ($\lambda_z^+ = 628$); - - - -, $\beta^+ = 0.005$ ($\lambda_z^+ = 1257$); - - - - -, $\beta^+ = 0.003$ ($\lambda_z^+ = 2094$).

$R_{\max}$ and V for small streamwise wavenumber α reveal an approximate power-law dependence on β, and their best fits are found β^{-2} scaling for $R_{\max}$ and β^{-1} scaling for V. The details on the emergence of these scaling will be discussed in section 4.3, where the power-law dependence is related to geometrical similarity of optimal structures in the logarithmic layer.

In order to analyze their deviations from the power-law dependence, $R_{\max}$ and V are premultiplied by β^2 and β respectively, and are reported in Fig. 2.5 (d) and (e) respectively. The premultiplied amplification curves now reveal the double-peak structure similar to the optimal transient growth in Fig. 2.5 (a). In both cases, the peak associated with the streamwise uniform large-scale structures is found for $\lambda_z \simeq 3.5h$, while the one associated with near-wall streaks is found for $\lambda_z^+ \simeq 80$. These two wavelengths seem to delimit the range where the approximate power law can apply. However, note that both $\beta^2 R_{\max}$ and βV do not display an exact 'plateau' in the approximate power-law range of the spanwise wavenumbers. This indicates that the influence of the inner and outer length scales is appreciable in this range even at this large Re_τ.

The computations have been repeated for several Reynolds numbers. The premultiplied

amplifications scaled by the outer and inner units are reported in Fig. 2.6. In all the cases, the global maxima of the premultiplied amplification curves are scaled by the outer unit and they are found near $\lambda_z = 3.5 \sim 4h$. The corresponding maximum amplifications gradually increase as Re_τ increases (figs. 2.6a, c and e). On the other hand, the secondary peaks are scaled by the inner units, and are located at $\lambda_z^+ \simeq 80 \sim 100$. The amplifications related to the inner peak do not sensibly change with Re_τ contrary to the outer peaks.

Optimal perturbations

The leading Karhunen-Loève modes of stochastic forcing corresponding to the outer ($\lambda_z = 3.5h$) and inner ($\lambda_z^+ = 80$) amplification peaks at $Re_\tau = 10000$ are reported in Figs. 2.7 (a) and (b) respectively. Similarly to the turbulent Couette flow, the structures of the optimal perturbations for the transient growth and harmonic forcing are essentially the same as those found for the stochastic forcing case. The structures related to the outer peak occupy the whole wall-normal domain (fig. 2.7a). The forcing consists of a pair of the streamwise vortices while the response reveals the streak with its maxima at a distance of $0.2h$ from the wall. On the other hand, the structures of the forcing and its response associated with the inner peak are strongly concentrated in the near-wall region: The core of the streamwise vortices is located at $y^+ \simeq 15$, and the maximum value of the streaks is found at $y^+ \simeq 10$.

In the intermediate range of spanwise wavenumbers between the outer and inner peaks, the optimal perturbations and the corresponding responses are found to be mainly concentrated in the logarithmic layer and have negligibly small amplitude above the logarithmic layer (i.e. at a distance from the wall larger than $0.2h$). More importantly, they are found to be scaled by the spanwise wavelength λ_z. Fig. 2.8 shows the wall-normal profiles of the optimal perturbations and their responses normalized by the spanwise wavelength λ_z for three different spanwise wavenumbers. All the wall-normal profiles normalized by λ_z are almost identical, and this suggests that the wall-normal size of optimal perturbations in this range self-similarly grows as the spanwise wavelength λ_z increases. This geometrical similarity is compatible with the concept of 'attached' eddies proposed by Townsend (1976).

Power-law behavior and geometrically similar optimal perturbations in the logarithmic layer

The premultiplied amplification in the previous section clearly suggests that there exist well-defined amplifications scaled by the outer and inner units and that $G_{\max} \sim \beta^0$, $R_{\max} \sim \beta^{-2}$ and $V \sim \beta^{-1}$ in some range of intermediate spanwise wavernumbers between the outer and inner peaks. In the same intermediate range, the optimal perturbations exhibit a geometrical similarity in the logarithmic layer, which provides a way to track the origin of the power-law dependence.

We begin by considering a channel with the location of wall at $y = \pm h$. Then, the logarithmic dependence of the mean-velocity profile on the distance from the wall and the constant Reynolds stress in the logarithmic layer gives the following relations: $U'(y) = u_\tau/[\kappa(y+h)]$, $\nu_T(y) = u_\tau\kappa(y+h)$. Since only elongated structures are strongly amplified, we consider streamwise uniform perturbations ($\alpha = 0$). The self-similarity allows to define the rescaled wall-normal coordinate by the spanwise wavelength λ_z, and the time is also scaled by λ_z as a consequence of the rescaled wall-normal coordinate:

$$y^{(\lambda)} \equiv \beta/\beta_0(y+h), \ t^{(\lambda)} \equiv \beta/\beta_0 t, \tag{2.19}$$

where β_0 is the reference spanwise wavenumber arbitrarily chosen in the intermediate range. Then, defining the rescaled state vector, $\hat{\mathbf{q}}^{(\lambda)} \equiv [\hat{v}, i\beta_0\hat{u}]^T$, gives the following rescaled governing system:

$$\frac{\partial \hat{\mathbf{q}}^{(\lambda)}}{\partial t^{(\lambda)}} = \mathbf{A}_0\hat{\mathbf{q}}^{(\lambda)} + \frac{\beta_0}{\beta}\mathbf{B}_0\hat{\mathbf{f}} \tag{2.20a}$$

with

$$\hat{\mathbf{u}} = \mathbf{C}_0\hat{\mathbf{q}}^{(\lambda)}, \tag{2.20b}$$

$$\hat{\mathbf{q}}^{(\lambda)} = \mathbf{D}_0\hat{\mathbf{u}}. \tag{2.20c}$$

Here, $\mathbf{A}_0$, $\mathbf{B}_0$, $\mathbf{C}_0$ and $\mathbf{D}_0$ are obtained by evaluating $\mathbf{A}$, $\mathbf{B}$, $\mathbf{C}$ and $\mathbf{D}$ at $\beta = \beta_0$ and $\alpha = 0$ with the mean-velocity profile and the constant Reynolds stress in the logarithmic layer. In (2.20a), the dependence of the system on β now appears only in the forcing term.

Using the rescaled system (2.20), the optimal energy growth by the initial condition is easily found to be

$$G(\beta, t) = G(\beta_0, t^{(\lambda)}). \tag{2.21}$$

Equation (2.21) implies that the optimal growth $G(\beta, t)$ remains almost the same as the one computed for the reference β_0 and that the time for growth is rescaled by $t = (\beta_0/\beta)t^{(\lambda)}$. Therefore, G_{max} is almost constant in the range of spanwise wavenumbers associated with logarithmic-layer structures as confirmed in Fig 2.5 (a), and the time attaining the maximum growth becomes proportional to the spanwise wavelength λ_z: $t_{max} \sim \lambda_z t_{max}^{(\lambda)}$. This is exactly what has been found by del Álamo & Jiménez (2006), Pujals et $al.$ (2009) and Cossu et $al.$ (2009).

In the case of harmonic forcing, the rescaled forcing frequency is defined as $\omega_f^{(\lambda)} \equiv (\beta_0/\beta)\omega_f$ rescaled so that $\omega_f t = \omega_f^{(\lambda)} t^{(\lambda)}$. In the rescaled system, the harmonic response is given as

$$R(\beta, \omega_f) = \left(\frac{\beta}{\beta_0}\right)^{-2} R(\beta_0, \omega_f^{(\lambda)}). \tag{2.22}$$

Therefore, the optimal harmonic response is proportional to β^{-2}, consistently with results in Fig 2.5 (b). Moreover, the forcing frequency related to the maximum response is found to be inversely proportional to the spanwise wavelength λ_z: $\omega_{f,max} \sim \lambda_z^{-1}\omega_{f,max}^{(\lambda)}$.

Finally, from the definition of the covariance matrix in the frequency domain (2.13), the variance of the stochastic response is found to be

$$V(\beta) = \left(\frac{\beta}{\beta_0}\right)^{-1} V(\beta_0), \tag{2.23}$$

implying that the variance is proportional to β^{-1} as shown in Fig 2.5 (c).

These results therefore suggest that the origin of the power-law dependence of the optimal amplifications is basically associated with the self-similar nature of optimal perturbations in the logarithmic region.

4.3   Turbulent pipe flow

The optimal amplifications have been also computed in the turbulent pipe flow at the large $Re_\tau = 19200$. We pay a particular attention to the power-law dependence of the optimal amplification in order to validate the results in turbulent channel flows.
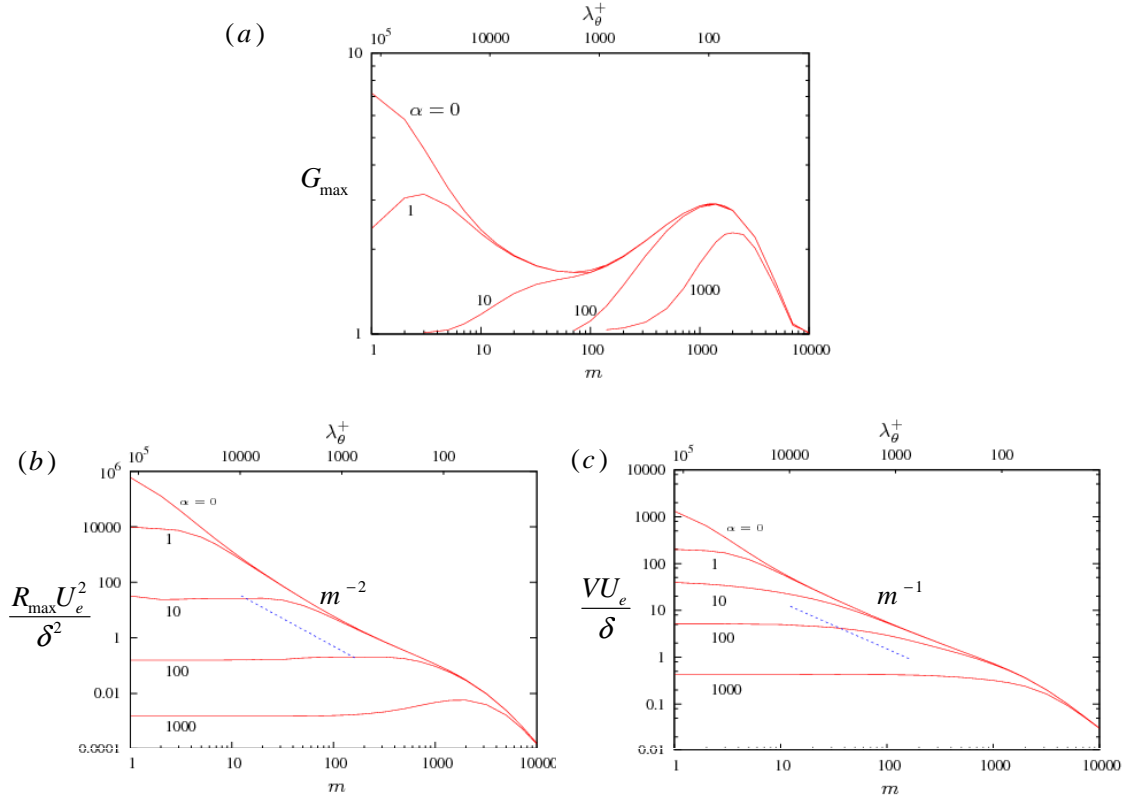
Figure 2.9. Energy amplifications by initial condition, optimal harmonic forcing and stochastic excitation with respect to spatial wavenumbers at $Re_\tau = 19200$: (a) $G_{\max}(\alpha, m)$; (b) $R_{\max}(\alpha, m)$; (c) $V(\alpha, \beta)$. Here, $\alpha h = 0.0, 1, 10, 100, 1000$, outer to inner curves.

Fig. 2.9 shows the dependence of G_{max}, R_{max} and V on the azimuthal wavenumber m for the selected streamwise wavenumbers $\alpha = 0, 1, 10, 100, 1000$. Only the streamwise elongated structures ($\alpha \lesssim m$) are significantly amplified similarly to turbulent Couette and channel flows. The largest growths are found for axially-independent modes ($\alpha = 0$), for which the curve provides an envelope over the results for non-zero α, and the maxima on the $\alpha = 0$ curves are for $m = 1$ azimuthal symmetry. In the optimal transient growth G_{max}, a secondary peak occurs at a larger m corresponding to an azimuthal wavelength of $\lambda_\theta^+ = 92$. However, no secondary peak is found in the responses to optimal harmonic and stochastic forcing just as in the plane channel flow cas. A closer examination of Figs. 2.9(b) and 2.9(c) reveals that the R_{max} and V curves corresponding to $\alpha = 0$ scale approximatively like m^{-2} and m^{-1} respectively for intermediate values of m, and a noticeable change of slope is observed for values of m corresponding to $\lambda_\theta^+ \approx 100$. These features are essentially the same as those observed in turbulent channel, implying that these are the common features stemming from the logarithmic layer of the mean flows.

In Fig. 2.10, we report the leading Karhunen-Loève modes for $m = 1, 2, 4$. Similarly to the Couette and plane channel, the spatial structures of the most energetic forcing and response consist of large-scale streamwise vortices and streaks respectively. Note that in this geometry, only $m = 1$ modes can exhibit flow across the mid-plane. The structures corresponding to the
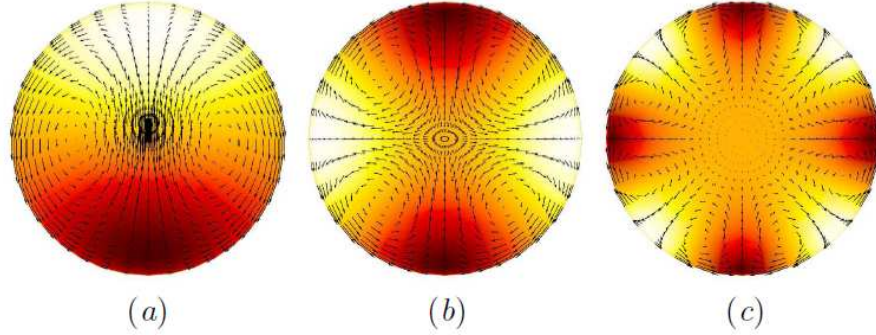
Figure 2.10. Cross-streamwise view of the normalized leading Karhunen-Loève modes of the stochastic forcing for $\alpha = 0$ at $Re_\tau = 19200$: (a) $m = 1$; (b) $m = 2$; (c) $m = 4$. Here, the vectors represent the cross-streamwise components of the optimal forcing, and color contour is the streamwise component of the corresponding response (white: $\hat{u} > 0$, red/dark: $\hat{u} < 0$).

secondary peak, scaled by the inner units, are almost indistinguishable from those found in the channel and the boundary layer (Pujals *et al.*, 2009; Cossu *et al.*, 2009; Hwang & Cossu, 2010*b*) and are therefore not reported here.

5   Discussion

5.1   The lift-up effect and the spanwise spacing of natural streaky motions

It has long been known that the streaky motions in the near-wall region have spanwise spacing $\lambda_z^+ \simeq 100$. This spacing has been understood as an important element for the existence of near-wall streaky motions. For example, Jiménez & Moin (1991) and Hamilton *et al.* (1995) showed that numerical simulation with the spanwise computational domain smaller than this spanwise spacing does not provide self-sustaining turbulence. However, the nature of the selection mechanism for the observed $\lambda_z^+ \simeq 100$ has long been elusive. The findings of del Álamo & Jiménez (2006), Pujals *et al.* (2009) and Cossu *et al.* (2009) are important because the value $\lambda_z^+ \simeq 80 \sim 90$ is naturally obtained as a secondary peak value of $G_{\max}$. The present results are the extension of these previous studies to the responses to optimal harmonic and stochastic forcing. Contrary to the case of initial perturbations, no secondary peak is found in the 'raw' amplification curves. However, the secondary peak at $\lambda_z^+ \simeq 100$ is recovered in the amplifications premultiplied by the proper spanwise wavenumbers associated with the power-law behavior in the logarithmic-layer regime.

The emergence of the global maximum with the specific spanwise spacing scaled by the outer units is also found as in previous studied for the optimal transient growth, and it is an interesting feature related to the large-scale streaky motions. In table 2.1, we summarize the optimal spanwise spacings obtained from the previous investigations and the present study, and compare them with the spanwise spacings of the large-scale streaky structures found in the laboratory or numerical experiments. The predicted spanwise spacings show a fair agreement with those observed in natural turbulent flows, suggesting that the lift-up effect at the outer scales is related to the emergence of the large-scale streaky motions. However, the linear analysis generally predicts slightly larger spanwise spacings. The crudeness of the

Flow				$\lambda_{z,opt}/\delta$		
	DNS/Exp	$G_{\max}$	$R_{\max}$	V	$\beta^2 R_{\max}$	βV
Couette	$4 \sim 5^{(c)}$	$4.4^{(*)}$	$7.7^{(*)}$	$5.2^{(*)}$	$4.2^{(*)}$	$4.2^{(*)}$
Channel flow	$1.5 \sim 2^{(d)}$	$4.0^{(a)}$	$5.5^{(*)}$	$5.0^{(*)}$	$3.5^{(*)}$	$3.5^{(*)}$
Pipe flow	$1.4 \sim 2.1^{(e)}$	$6.3^{(*)}$	$6.3^{(*)}$	$6.3^{(*)}$	$6.3^{(*)}$	$6.3^{(*)}$
Boundary layer	$0.5 \sim 1.0^{(f)}$	$7.2^{(b)}$	—	—	—	—

Table 2.1. Optimal spanwise wavenumbers of the maximum responses to initial perturbation, harmonic forcing, and stochastic excitation. Results from: (*) the present study, (a) Pujals et al. (2009), (b) Cossu et al. (2009), (c) Tsukahara et al. (2006), (d) del Álamo & Jiménez (2003), (e) Bailey & Smits (2010), and (f) Hutchins & Marusic (2007a). Here, δ is half of the channel height for Couette and channel flows, the radius for pipe flow, and the boundary-layer thickness for boundary layer.

present eddy-viscosity modeling can partially explain this discrepancy, but a second plausible explanation could also reside in the nonlinear terms neglected in this linear analysis.

In the intermediate range of spanwise wavenumbers between the outer and inner peaks, the optimal perturbations mainly populate the logarithmic layer and reveal an approximate geometrical similarity. These findings are reminiscent of the concept of 'attached' eddies proposed by Townsend (1976) and the further developed theories by Perry and coworkers (Perry & Chong, 1982; Perry et al., 1986; Perry & Marusic, 1995), all based on a continuum of geometrically similar structures.

5.2 The similarity of all the optimal perturbations

In Fig. 2.11, we report the wall-normal profiles of all the optimal perturbations and their responses corresponding to the outer peak (fig. 2.11 a and b), the intermediate wavenumber range (fig. 2.11 c and d), and the inner peak (fig. 2.11 e and f) for the plane channel flow at $Re_\tau = 10000$. All the optimal perturbations issued from the three different analyses (optimal transient growth, harmonic and stochastic forcing) are found to be almost identical, and this is not originally expected. At this time of writing, no simple explanation is available for these results, and this should be in the future investigation.

5.3 Stochastic response and the spanwise spectra of turbulent flows

For the comparison of the present analysis to the experimental observations in natural turbulent flows, the response to stochastic forcing may be the most relevant among the three framework considered. Following the approaches by Farrell & Ioannou (1994) and Farrell & Ioannou (1998), the stochastic forcing can be interpreted as a surrogate for the nonlinear terms neglected in the linearized model (2.6). The stochastic response would then represent the linear amplification of the nonlinear terms related to turbulent fluctuation. It is important to note that these nonlinear terms in reality are neither Gaussian nor isotopic, thus the stochastic forcing considered here is basically unrealistic. However, the response to such forcing shares important features with natural self-sustaining turbulent flows. For example, the stochastic response is highly anisotropic: the large response is obtained only for the streamwise elon-
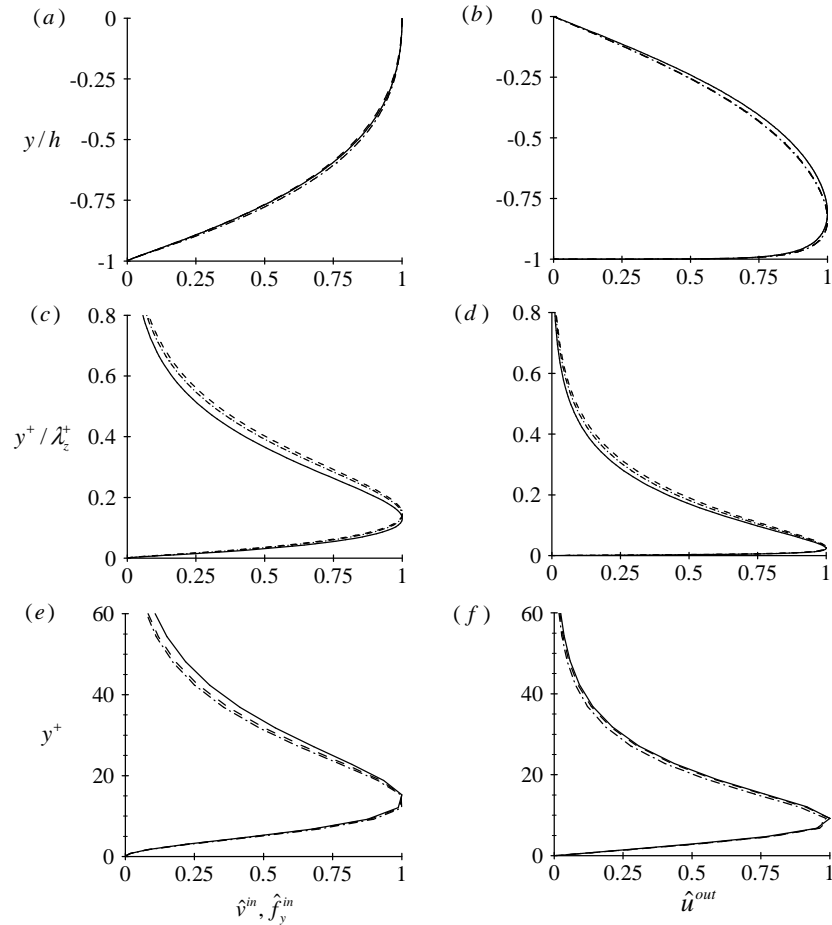
Figure 2.11. Profiles of streamwise uniform ($\alpha = 0$) optimal modes corresponding to (a, b) the outer peak, (c, d) the intermediate wavenumber range ($\beta^+ = 0.003/h$; $\lambda_z^+ = 2094$) and (e, f) the inner peak in the premultiplied amplifications: (a, c, e) wall-normal components of the input (initial condition $\hat{v}^{\mathrm{in}}(y)$ for transient growth and forcing $\hat{f}_y^{\mathrm{in}}(y)$ for harmonic and stochastic forcing); (b, d, f) streamwise components of the corresponding outputs $\hat{u}^{\mathrm{out}}(y)$. Here, ———, optimal transient growth; – – – –, optimal harmonic forcing; —·—·—, stochastic excitation. The results are from the plane channel flow at $Re_\tau = 10000$.

Figure 2.12. Premultiplied spectral density of the streamwise velocity at each wall-normal location for the streamwise uniform case $\beta\hat{u}\hat{u}^*(y;\alpha = 0,\beta)$ based on the stochastic response (a) without wall-damping function and (b) with wall-damping function $f_d(y) = 1 - exp(-(y^+/A^+)^3)$ where $A^+ = 25$. The same data from DNS by del Álamo & Jiménez (2003) are shown in (c) for the comparison. Here, the wall-normal location is chosen as $y^+ = 5, 9, 15, 20, 30, 39, 61, 104, 165, 2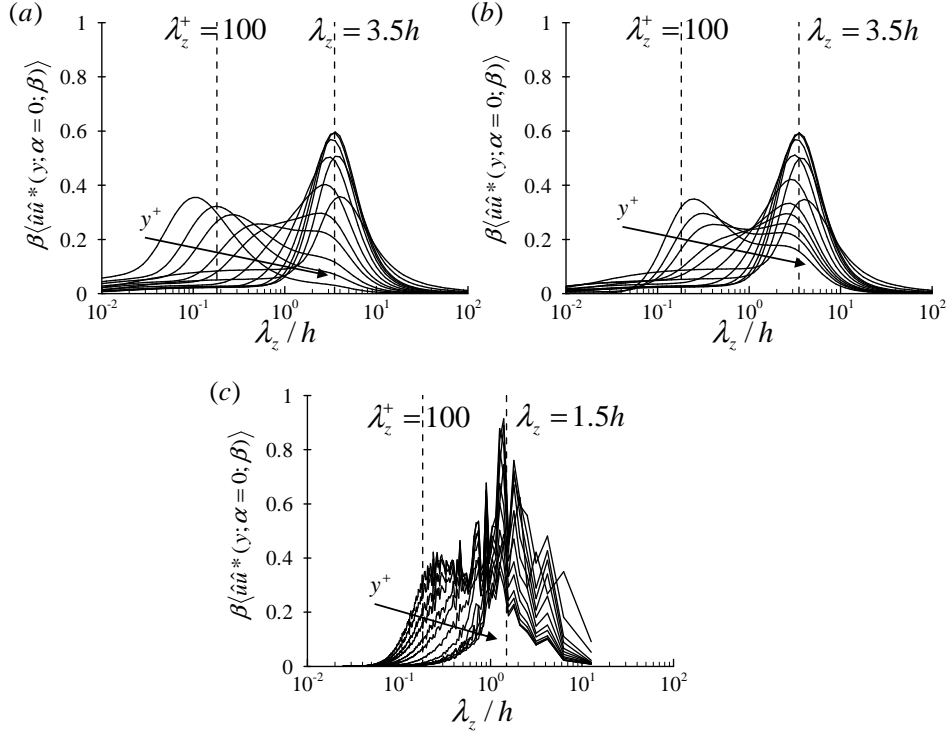21, 277, 414, 547$ and each premultiplied spectral density is normalized by its energy to emphasize the contents of spanwise wavenumber.

gated structures (i.e. $\alpha < \beta$), and it mainly consists of the streamwise velocity. This feature is commonly observed in the spectra of all the wall-bounded turbulence (del Álamo & Jiménez, 2003; del Álamo et al., 2004; Hoyas & Jiménez, 2006), suggesting that the linear process plays an important role in the generation of wall turbulence.

More quantitative information on the stochastic response can be extracted by examining the velocity covariance operator $\mathbf{C}\mathbf{X}_\infty\mathbf{C}^\dagger$ whose diagonal terms give the spatial spectral density $\langle\hat{u}_i^*(y,t)\hat{u}_i(y,t)\rangle$. Fig. 2.12(a) reports the premultiplied spanwise spectral density of the streamwise velocity $\beta\langle\hat{u}_1^*(y,t)\hat{u}_1(y,t)\rangle$ for several distances from the wall y for $Re_\tau = 550$. To compare this with real turbulent flows, the spectra in direct numerical simulation data at $Re_\tau = 550$ are also shown in Fig. 2.12(c) (del Álamo & Jiménez, 2003). A qualitative agreement is found between the two sets of data: the spectral peak scaled by the outer length scale is found in the outer region, while the near-wall region displays the peak around $\lambda_z^+ \simeq O(100)$. The slight difference of the peak location in the outer region is probably because of the crudeness of the eddy viscosity or the different length-scale selection mechanism embedded in the nonlinear term. However, the difference in the near-wall region seems to be induced by the unrealistic assumption that the wall-normal distribution of the forcing is uniform in y. In the viscous sublayer, the turbulence is not strongly active due to the large molecular dissipation near the wall, thus it is reasonable to assume that the nonlinear terms are negligible at $y^+ \lesssim 5$.

Therefore, we recompute $\mathbf{C}\mathbf{X}_\infty\mathbf{C}^\dagger$ with a wall-damping function $f_d(y) = 1 - exp(-(y^+/A^+)^3)$ in the wall-normal distribution of the stochastic forcing. As a result, the spatial spectral density below $y^+ = 5$ are greatly improved as in Fig. 2.12(b), showing a better agreement with that of real turbulent flow in Fig. 2.12(c): in the near-wall region there is a energetic peak at $\lambda_z^+ \simeq 100$, whereas in the outer region a energetic peak at $\lambda_z = 3.5h$ is found.

Chapter 3

Instability of large-scale coherent streaks

In chapter 2, we have studied the amplification of streaks by computing the linear optimal perturbations. Although linear theories provide a good explanation of how the vortices convert into the streaks, they do not explain how such vortices are formed. If the large-scale streaky structures in the outer region self-sustain with a process similar to the one at work for the near-wall streaky structures, the formation of the vortices is probably associated with instability of the amplified streaks (Hamilton *et al.*, 1995) or secondary transient growth (Schoppa & Hussain, 2002). The importance of studying streak instability also lays in the understanding how the streamwise length scales of the experimentally observed streaky structures are selected. Although the nonmodal stability theories predicts the spanwise spacings comparable with those observed in the experiments, streaks maximally amplified are always found to be streamwise uniform. Note that this feature is observed not only in the present turbulent case but also in the laminar case. However, the observed streaky motions are neither infinitely long nor streamwise uniform: They have streamwise length of $O(10\delta)$ and also oscillate in the streamwise direction. Moreover, the large-scale motions (the bulges) are found to be coherently aligned along the streaky motions as also shown in Fig. 1.5 (*a*) (Kim & Adrian, 1999; Guala *et al.*, 2006; Hutchins & Marusic, 2007*a*). It is interesting to note that these properties resemble to the typical features of the traveling waves embedded into the self-sustaining process (Waleffe, 1998, 2001, 2003). However, there is no sound explanation for these features yet, and only recently it has been conjectured that vortex packets may be related to the instability of large-scale streaks (Guala *et al.*, 2006).

The goal of this chapter is to analyze the stability of finite-amplitude large-scale streaks and to seek a relationship between the streamwise wavelengths of the instability and the length-scales of the coherent structures in the outer region. In order to theoretically track this issue, we consider the same eddy-viscosity model used in chapter 2, and conduct a secondary stability analysis of the most amplified streaks in the turbulent Couette and Poiseulle flows. The results reported in this chapter have been obtained in collaboration with J. Park and are reported in the paper by Park *et al.* (2010)

1   The streaky base flows

Let us rewrite the equation for finite amplitude coherent motions supported by the mean flow ($\bar{u}_i = (U(y), 0, 0)$):

$$\frac{\partial \tilde{u}_i}{\partial t} + \tilde{u}_j \frac{\partial \bar{u}_i}{\partial x_j} + \bar{u}_j \frac{\partial \tilde{u}_i}{\partial x_j} + \tilde{u}_j \frac{\partial \tilde{u}_i}{\partial x_j} = -\frac{1}{\rho} \frac{\partial \tilde{p}}{\partial x_i} + \frac{\partial}{\partial x_j} [\nu_T(y)(\frac{\partial \tilde{u}_i}{\partial x_j} + \frac{\partial \tilde{u}_j}{\partial x_i})]. \qquad (3.1)$$

The streaky base flow is computed by solving (3.1) with assumption that the flow is uniform in the streamwise direction. Here, it should be mentioned that the use of the spanwise-homogeneous eddy viscosity $\nu_T(y)$ is a potentially inappropriate assumption because $-\widetilde{\tilde{u}_i \tilde{u}_j}$ in (2.3b) may not be negligible. An alternative solution could be to conduct direct numerical simulation with external forcing and retrieve the steady mean flow by averaging. However, in this case, as the amplitude of streaks increases, the flow field in direct numerical simulation is presumably contaminated by the streaky instability and does not provide physically relevant streak mean flows for the cases of interest, which are unstable. For these reasons, here we keep using the spanwise-homogeneous eddy viscosity $\nu_T(y)$ even if this is a very crude approximation. Once the streaky base flow $\tilde{u}_s(y, z)$ is computed, the secondary base flow is defined as $U_i^b = (U^b(y, z), 0, 0)$ where $U^b(y, z) \equiv U(y) + \tilde{u}_s(y, z)$.

Equation (3.1) is discretized using Chebyshev polynomials and Fourier series in the wall-normal and spanwise directions respectively. The time integration used to compute the streaky base flow is conducted using the Runge-Kutta third-order method. The computations of the base flow are carried out with $N_y \times N_z = 65 \times 32$ points in the cross-streamwise plane.

We consider the turbulent Couette flow at $Re_\tau = 52$ and the Poiseulle flow at $Re_\tau = 300$. The computation of the streaky base flows is carried out by using the optimal initial conditions, that consist of pairs of counter-rotating streamwise vortices computed in chapter 2 (see also Fig. 3.2). The spanwise spacing is chosen as $\lambda_z = 4h$ ($\beta_0 h = \pi/2$), which is near the optimal value. The spanwise size of the computational box is set to $L_z = \lambda_z$, so that a single pair of optimal initial vortices is driven in the box. The amplitude of the initial vortices is defined as

$$A_v = [(2/V) \int_V (u^2 + v^2 + w^2) dv]^{1/2}. \qquad (3.2)$$

The amplitude of the streaks induced by these vortices is defined as in Andersson *et al.* (2001)

$$A_s = \frac{[max_{y,z} \triangle U(y, z) - min_{y,z} \triangle U(y, z)]}{2\, U_{ref}}, \qquad (3.3)$$

where $\triangle U(y, z) \equiv u_s(y, z)$. Here, $U_{ref} = 2U_w$ and $U_{ref} = U_e$ for Couette and Poiseulle flows respectively.

Fig. 3.1 shows the temporal evolution of the streak amplitude for several amplitudes A_v of the optimal initial vortices. Both Couette and Poiseulle flows exhibit large transient amplifications of the streaks through the coherent lift-up effect. As A_v increases, the amplitude of the streaks also increases. However, the ratio of the amplification slightly decays with increasing A_v, and the time for A_s to reach its maximum (t_{max}) also becomes shorter. Typical cross-stream views of the initial vortices and streaks at $t = t_{max}$ are reported in Fig. 3.2. It is seen that the low-momentum regions where the fluid is ejected from the wall by the vortices (($y > 0, z \simeq \pm 2$) and ($y < 0, z \simeq 0$) in fig. 3.2) are narrow and intense, and this tendency generally becomes stronger for larger streak amplitudes (see also chapter 5).
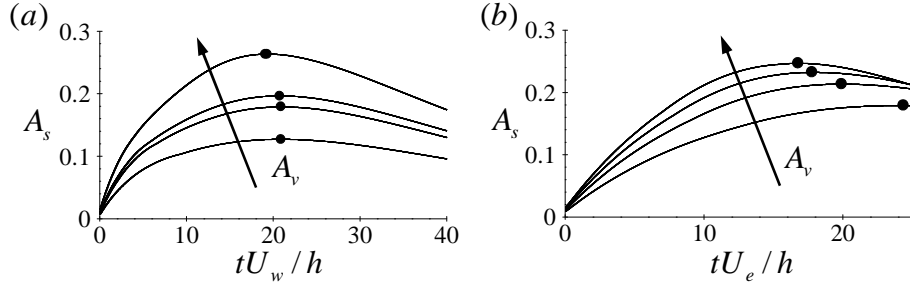
Figure 3.1. Evolution of the streak amplitude in time: (a) Couette flow with $A_v = 0.08, 0.11, 0.12, 0.16$; (b) Poiseulle flow with $A_v = 0.06, 0.078, 0.09, 0.1$. Here, • denotes the maximum of A_s at $t = t_{max}$.
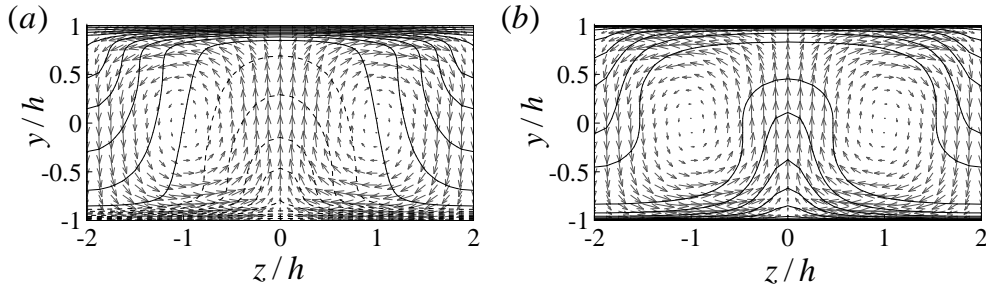

Figure 3.2. Cross-stream (y-z) view of streaky base flow extracted at $t = t_{max}$ and optimal initial vortices: (a) Couette flow with $A_s = 26\%$ and (b) Poiseulle flow with $A_s = 25\%$. Here, the solid and dashed contour lines respectively denote positive and negative parts of the streaky base flow with the increment 0.1 of its maximum, and the vectors represent the initial vortices.

2 Stability of secondary perturbations

The stability of the streaky base flow is then studied by linearizing (3.1) around U_i^b with the secondary perturbations $u_i'(x, y, z, t)$:

$$\frac{\partial \breve{u}_i}{\partial t} + \breve{u}_j \frac{\partial U_i^b}{\partial x_j} + U_j^b \frac{\partial \breve{u}_i}{\partial x_j} = -\frac{1}{\rho}\frac{\partial \breve{p}}{\partial x_i} + \frac{\partial}{\partial x_j}[\nu_T(y)(\frac{\partial \breve{u}_i}{\partial x_j} + \frac{\partial \breve{u}_j}{\partial x_i})]. \tag{3.4}$$

Here, we also keep using the same eddy viscosity as in the base flow. Under the assumption that the streaky base flow $U_b(y, z)$ is periodic in the spanwise direction, the Floquet theory allows (3.4) to have the following normal-mode solution:

$$\breve{u}_i'(x, y, z, t) = e^{i\alpha x - i\omega t} \sum_{n=-\infty}^{\infty} \hat{u}_i^n(y)e^{i(n+\epsilon)\beta_0 z} + c.c, \tag{3.5}$$

where α is the streamwise wavenumber, ω the complex frequency, β_0 the spanwise wavenumber related to the fundamental period of the base flow, and $0 \leq \epsilon \leq 1/2$ is the detuning parameter. According to the values of ϵ, the solutions (3.5) are classified into 'fundamental' ($\epsilon = 0$) and 'subharmonic' ($\epsilon = 1/2$) modes. Also, the modes with even and odd symmetries about base flows are called 'sinuous' and 'varicose' respectively. For further details on the classification of the modes, the readers are referred to Andersson *et al.* (2001) and Cossu & Brandt (2004). In
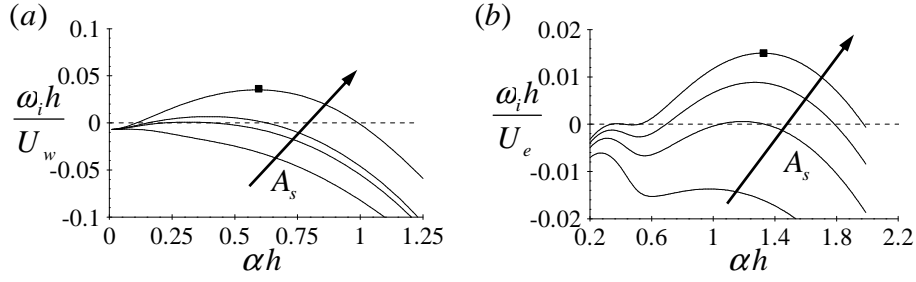
Figure 3.3. Growth rate of fundamental sinuous mode with the streamwise wavenumber α for streaky base flows corresponding to • in Fig. 3.1: (a) Couette flow with $A_s = 13, 18, 20, 26\%$; (b) Poiseulle flow with $A_s = 18, 21, 23, 25\%$. Here, ■ indicates the location of maximum ω_i of the largest amplitude of streaks considered.

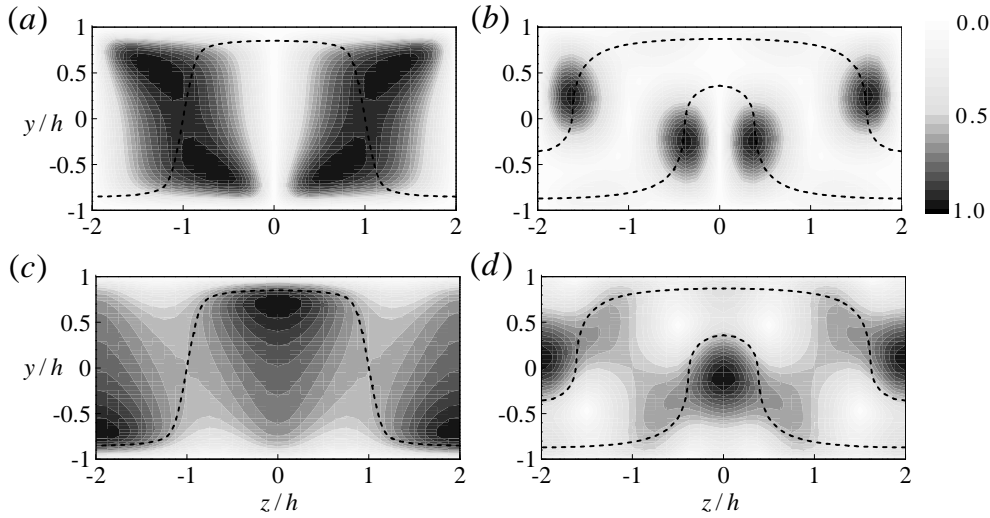Figure 3.4.   Cross-stream $(y\text{-}z)$ view of the absolute value of (a, b) the streamwie and (c, d) spanwise velocity eigenfunction corresponding to ■ in Fig. 3.3: (a, c) Couette flow; (b, d) Poiseulle flow. Here, the contour is normalized by its maximum and the thick dashed line denotes the velocity of streaky base flow which is the same with the phase speed of the streak instability.

the present study, we focus only on the fundamental sinuous mode, found as the most unstable one for all the cases considered.

For the Floquet analysis, the code used in Cossu & Brandt (2004) has been adapted to the turbulent case. In this code, the same spatial discretization of the code used to compare the base flow is applied to the linear operators, and the resulting eigenvalue problem is then solved using the implicitly restarted Arnoldi method. For the computation of the stability of streaks, the same number of grid points of the base-flow computation is also used.

The Floquet stability analysis is performed for the fundamental modes using the streaky base flows extracted at $t = t_{\max}$. Fig. 3.3 shows the growth rate ω_i of sinuous modes versus the streamwise wavenuber α for several A_s. Both Couette and Poiseulle flows are stable ($\omega_i < 0$) for sufficiently low amplitudes of the streaks. As the amplitude of streak A_s increases, the growth rate gradually increases. Then, instability begins to appear ($\omega_i > 0$) when A_s reaches the value: $A_{s,c} = 18\%$ at $\alpha_c h = 0.3$ for Couette flow (Fig. 3.3a) and $A_{s,c} = 21\%$ at $\alpha_c h = 1.2$ for Poiseulle flow (Fig. 3b). When $A_s > A_{s,c}$, a finite interval of the streamwise wavenumbers is

unstable with maximum growth at $\alpha_{max}h \simeq 0.6$ in Couette flow (Fig. 3.3a) and $\alpha_{max}h \simeq 1.4$ in Poiseulle flow (Fig. 3.3b). We have verified that varicose modes are less unstable than sinuous modes in this range of $A_v - A_s$.

Fig. 3.4 shows the streamwise and spanwise velocity components of the streak-instability eigenfunction and the line where the mean velocity is the same as the phase speed c_r of instability wave ($c_r = 0$ in Couette flow while $c_r = 0.87U_e$ in Poiseulle flow). The streamwise component of the eigenfunction has the large value in the flank of the streaks, where the spanwise shear of base flow is expected to be large (fig. 3.4 a and b). The spanwise component of the eigenfunction is concentrated in the lifted low-momentum region for both Couette and Poiseulle flows. Therefore, in Couette flow the amplitude of the eigenfunction is appreciable even close to the opposite wall, whereas in Poiseulle flow it is mainly concentrated on the center of the channel (fig. 3.4 c and d).

3 Discussion

3.1 Comparison with the instability of laminar streaks

The instability of finite amplitude streaks in the framework of an eddy viscosity of turbulent Couette and Poiseulle flows has been investigated. The nature of the secondary streak instability in the turbulent case bears same similarity to the one observed in the laminar case: the instability appears for high amplitude streaks and it is dominated by the fundamental sinuous mode. An interesting point is that the critical streak amplitudes in the present model are lower than those in laminar flows: for example, our own computations in laminar Couette and Poiseulle flows at $Re_h = 500$ give $A_{s,c} \simeq 23\%$ and $A_{s,c} \simeq 28\%$ respectively (see also Reddy et $al.$, 1998), whereas for the turbulent Couette and Poiseulle flows it is found $A_{s,c} \simeq 18\%$ and $A_{s,c} \simeq 21\%$ respectively at $Re_\tau = 52$ and $Re_\tau = 300$. However, this does not mean that the streak instability in turbulent flows can be more easily triggered than in laminar flows because as the optimal turbulent transient growth is smaller than the laminar one (Pujals et $al.$, 2009; Hwang & Cossu, 2010a), initial vortices in turbulent flows should be more energetic to drive streak instability than those in laminar flows. For example, in the laminar Poiseulle flow, $A_{v,c} \sim O(10^{-3})$ is required to trigger streak instability Reddy et $al.$ (1998), but the amplitude of initial vortices in the present model of Poiseulle flow is almost two order of magnitude larger (i.e. $A_{v,c} \simeq 0.08$).

3.2 The relation with the streamwise length scales embedded in the large-scale streaky motions

In the outer region of the turbulent Poiseulle flow, the streamwise length scale of the large-scale motions has been associated with the peak near the high wavenumber boundary of the α^{-1} regime in the spectra of the outer region at $\alpha h = 1 \sim 2$ ($\lambda_x = 3.1 \sim 6.3h$), and that is clearly visible for $0 < |y| < 0.6h$ (Balakumar & Adrian, 2007; Monty et $al.$, 2009). The range of unstable streamwise wavenumbers in the present study is also obtained for $\alpha h = 0.8 \sim 1.8$ ($\lambda_x = 3.5 \sim 7.9h$; see Fig. 3.3$b$), showing good agreement with the location of the peak in the streamwise turbulent spectra. Moreover, the eigenfunctions obtained here have significant values in $0 < |y| < 0.6h$, which also compares well to the spectra. For the turbulent Couette flow, the streamwise wavenumber having the maximum growth rate ($\alpha h \simeq 0.6$; $\lambda_x \simeq 10.5h$; see Fig. 3.3a) also corresponds well to the location of the peak in the streamwise spectra at

the channel center ($\alpha h \simeq 0.63$; $\lambda_x \simeq 10h$) (Tsukahara *et al.*, 2006). This good correlation in the length-scale comparison implies that the large-scale motions could be formed by instability of large-scale streaks in the outer region, and also explains why the large-scale motions are aligned along the streaky motions.

It is also interesting to note that the low-wavenumber boundary of instability for the largely amplified streaks. The wavenumbers smaller than the low-wavenumber boundary do not have the streak instability, thus there could be no nonlinear feedback of vortices for these wavenumbers. This implies that the low-wave number boundary could be a rough indicator of the maximum length of streaky motions. This rationale can be for instance applied to the near-wall cycle: Schoppa & Hussain (2002) have shown that the low-wavenumber boundary of the sufficiently amplified streamwise uniform streaks is $\lambda_x^+ \simeq 1000 \sim 2000$, comparable to the average length of the near-wall streaky structures $\lambda_x^+ \simeq 1000$, and numerical simulations by Jiménez *et al.* (2004) indeed confirmed that the streamwise wavelengths larger than $\lambda_x^+ \simeq 1200$ do not have the nonlinear feedback for the near-wall streaky structures. If the same rationale is applied to the present results, the low-wavenumber boundaries for Poiseulle and Couette flows are found $\alpha h \simeq 0.3 \sim 0.5$ ($\lambda_x/h \simeq 13 \sim 21$) and $\alpha h \simeq 0.1 \sim 0.15$ ($\lambda_x/h \simeq 42 \sim 62$). These lengths are comparable to the lengths of the very large-scale streaky motions: $\lambda_x/h \simeq 10 \sim 20$ for Poiseulle flow (Balakumar & Adrian, 2007; Monty *et al.*, 2009) and $\lambda_x/h \simeq 42 \sim 64$ for Couette flow Tsukahara *et al.* (2006).

Despite the many promising results, the present computations remain, however, to be confirmed by the more 'realistic' models for the eddy viscosity and at larger Reynolds numbers.

Chapter 4

The existence of self-sustaining process at large scale

In previous investigations, the near-wall region of wall-bounded turbulent flows has been understood as the place where an independent self-sustaining cycle exists, while in the outer region turbulent motions have often been thought to be produced from the near-wall cycles via so called the 'bottom-up' process. However, the results from the stability analyses in the previous chapters suggest that a self-sustaining cycle at large scale may exist independently from the near-wall process. The scope of this chapter is to verify whether such a self-sustaining process exists or not. For this purpose, we conduct a numerical experiment, which is designed to remove energy production of the small-scale eddies in the near-wall and logarithmic regions. The results described in this chapter are summarized in Hwang & Cossu (2010c), and a second paper that is in preparation.

1   Background

To understand if large-scale outer motions can survive without 'fueling' from the motions at smaller scale in the near-wall and logarithmic regions, we design a 'conceptual' numerical experiment where the eddies smaller than the outer-length scale are gradually quenched. An ideal tool to perform such a kind of experiment is the large eddy simulation (LES) (Sagaut, 1998). From the perspective of this chapter, it is important to avoid any backward spectral energy transfer from the small to the larger scales. Therefore, we consider the 'static' Smagorinsky model (Smagorinsky, 1963), which provides purely dissipative subgrid-scale stresses. The subgrid-scale stress tensor $\bar{\tau}_{ij}$ of this model is given as

$$\bar{\tau}_{ij} - \frac{\delta_{ij}}{3}\bar{\tau}_{kk} = -2\nu_t \bar{S}_{ij}, \tag{4.1a}$$

where

$$\nu_t = D(C_S \bar{\Delta})^2 \bar{S}. \tag{4.1b}$$

Here, the overbar denotes the filtering action, $\bar{S} = (2\bar{S}_{ij}\bar{S}_{ij})^{1/2}$, $\bar{\Delta} = (\bar{\Delta}_1 \bar{\Delta}_2 \bar{\Delta}_3)^{1/3}$ is the average length scale of the filter and C_S is the Smagorinsky constant. The van Driest damping function $D = 1 - e^{-(y^+/A^+)^3}$ is also enforced to describe the proper physical behavior near the wall (Härtel & Kleiser, 1998).

Re_m	L_x/h	L_z/h	Δ_x^+	$\Delta_{y,\mathrm{min}}^+$	$\Delta_{y,\mathrm{max}}^+$	Δ_z^+	$T_{\mathrm{avg}}u_\tau/h$
20133	18π	6	81	1.8	40	34	$15.6 \sim 33$
38133	12π	6	93	1.8	59	45	$13.4 \sim 36$

Table 4.1. Computational parameters for the present large eddy simulation. Note the choice of very long computational domains

The simulations with the static Smagorinsky model are carried out using the public domain code `diablo` (Bewley *et al.*, 2001), and its details are in appendix. Table 4.1 summarizes the simulation parameters in the present simulations. The simulations are performed at two relatively high Reynolds numbers by enforcing the constant mass flux, and very large computational boxes are considered to include several large-scale streaky structures. The grid filter is implicitly applied as the LES filter: the cut-off filter in the streamwise and spanwise directions and the box filter in the wall-normal direction. The filter widths are also chosen to be sufficiently small so that the near-wall streaky structure can be properly resolved (Zang, 1991). The time intervals to obtain the statistics are also considered little larger than those in DNS by Hoyas & Jiménez (2006). In the present study, we mainly focus on the results at $Re_m = 38133$ where $Re_m \equiv U_m 2h/\nu$ with the mass flux $U_m = (1/2h)\int_{-h}^{h} U dy$, and they do not reveal essential difference from those at $Re_m = 20133$ (see also Hwang & Cossu, 2010*c*).

During the simulation, the mean velocity and turbulent fluctuations are accumulated, and the following one-dimensional streamwise and spanwise spectra at each wall-normal location y are also computed to be identified with the statistical information on the flow structures:

$$\Phi_{ij}(k_x; y) = \frac{1}{L_x}\int_0^{L_x} R_{ij}(\Delta x, y)e^{-ik_x\Delta x}\, d\Delta x, \tag{4.2a}$$

$$\Phi_{ij}(k_z; y) = \frac{1}{L_z}\int_0^{L_z} R_{ij}(\Delta z, y)e^{-ik_z\Delta z}\, d\Delta z, \tag{4.2b}$$

where

$$R_{ij}(\Delta x, y) = \langle u_i(x, y, z, t)u_j(x + \Delta x, y, z, t)\rangle_{x,z,t}, \tag{4.2c}$$

$$R_{ij}(\Delta z, y) = \langle u_i(x, y, z, t)u_j(x, y, z + \Delta z, t)\rangle_{x,z,t}. \tag{4.2d}$$

Here, k_x and k_z denotes the streamwise and spanwise wavenumbers respectively, and $\langle \cdot \rangle_{x,z,t}$ is the average in time and in the streamwise and spanwise directions. Once the spatial spectra are computed, we plot the spectra premultiplied by the spatial wavenumber in the logarithmic coordinate of the wavelength (or the wavelength): $k_x\Phi_{ij}(k_x; y)$ and $k_z\Phi_{ij}(k_x; y)$. The use of the premultiplied spectra is to be identified with the energy containing length scales because the area under the premultiplied spectra in the logarithmic coordinate represents the energy of the corresponding length scales.

2   The reference simulation

To begin with, a reference simulation is carried out by choosing $C_s = 0.05$. According to (Härtel & Kleiser, 1998), this value of the Smagorinsky constant provides the statistics in the
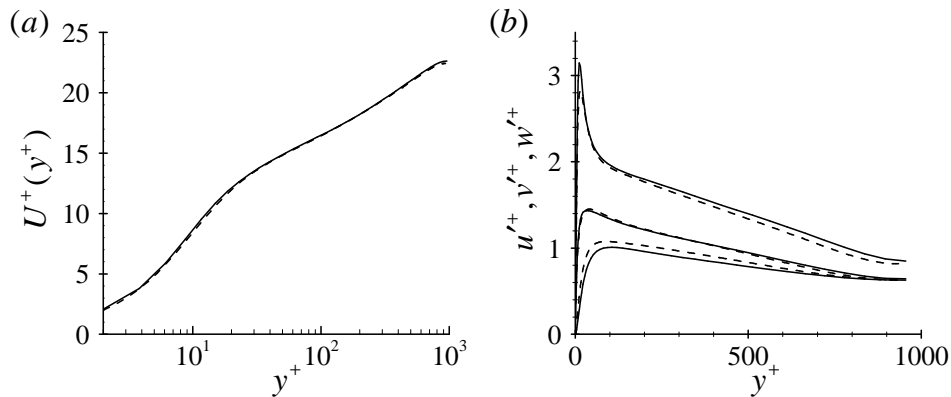
Figure 4.1. The mean flow and velocity fluctuations at $Re_\tau = 955$: (a) $U^+(y^+)$; (b) $u'^+(y^+)$, $v'^+(y^+)$, $w'^+(y^+)$. Here, ———, the present LES (reference case); - - - -, DNS of Hoyas & Jiménez (2006).

best agreement with direct numerical simulations. In the reference simulation at $Re_m = 38133$, the friction Reynolds number is obtained as $Re_\tau = 955$. Fig. 4.1 (a) and (b) report the mean-velocity profile and turbulent fluctuations from the reference simulation respectively, and both of them show the good agreement with direct numerical simulation by Hoyas & Jiménez (2006). An instantaneous flow field of the streamwise velocity fluctuation for the reference case is also presented in 4.2 (a). The structures in the flow field is very similar to those from direct numerical simulations (see e.g. Jiménez, 2007): the large-scale streaks embedded in clouds of smaller-scale eddies are found with $\lambda_z = 1.5 \sim 2h$ and they are highly elongated in the streamwise direction. The premultiplied spanwise spectra for the reference case are also computed and reported in 4.3 (a). The spectra shows the peak in the buffer layer ($y^+ \lesssim 30$ or $y/h \lesssim 0.03$) with $\lambda_z^+ \simeq 100$ corresponding to the spanwise spacing of the near-wall streaky structures (fig. 4.3 a). In the outer region around $y/h \simeq 0.2$, there is an another peak with $\lambda_z \simeq 1.5h$, and this spanwise spacing is also in good agreement with the one corresponding to the bulge and the large-scale streaky motions (del Álamo & Jiménez, 2003). The streamwise spectra for the reference case are also reported in 4.3 (b). Similarly to the spanwise spectra, two spectral peaks are clearly visible at $\lambda_x^+ \simeq 1000$ and $\lambda_x/h \simeq 3 \sim 4$ respectively (fig. 4.3 b). The peak at $\lambda_x^+ \simeq 1000$ is located in the buffer layer, and it corresponds to the mean streamwise length of the near-wall streaky structures. On the other hand, the outer region for $y/h > 0.2$ shows the peak around $\lambda_x/h \simeq 3h$ corresponding to the large-scale motion (Kim & Adrian, 1999; Guala *et al.*, 2006; Monty *et al.*, 2009), but it also has the long tail in streamwise spectra extending up to $\lambda_x \simeq 10 \sim 20h$ at $y/h \simeq 0.2$. This long tail has been understood as the reflection of the long outer streaky structures (del Álamo *et al.*, 2004; Monty *et al.*, 2009).

3   The numerical experiment with increased Smagorinsky constant

3.1   Instantaneous flow field

To quench the small-scale structures from the flow field, the Smagorinsky constant C_s is gradually increased from the reference value $C_s = 0.05$. Five higher Smagorinsky constants
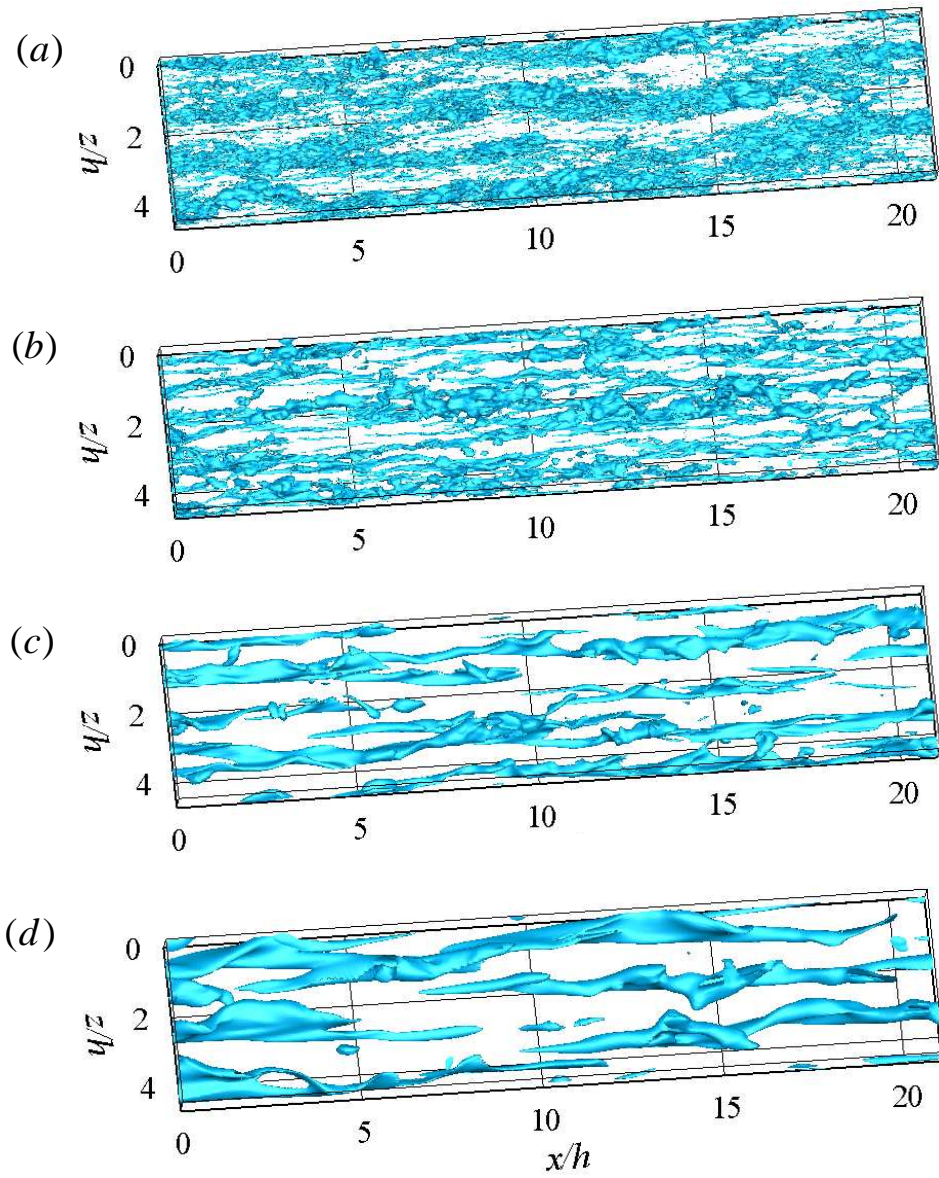
Figure 4.2. Iso-surface of instantaneous streamwise velocity fluctuation ($u^+ = -2$) at $Re_m = 38133$: (a) $C_s = 0.05$ (reference case); (b) $C_s = 0.10$; (c) $C_s = 0.20$; (d) $C_s = 0.30$.
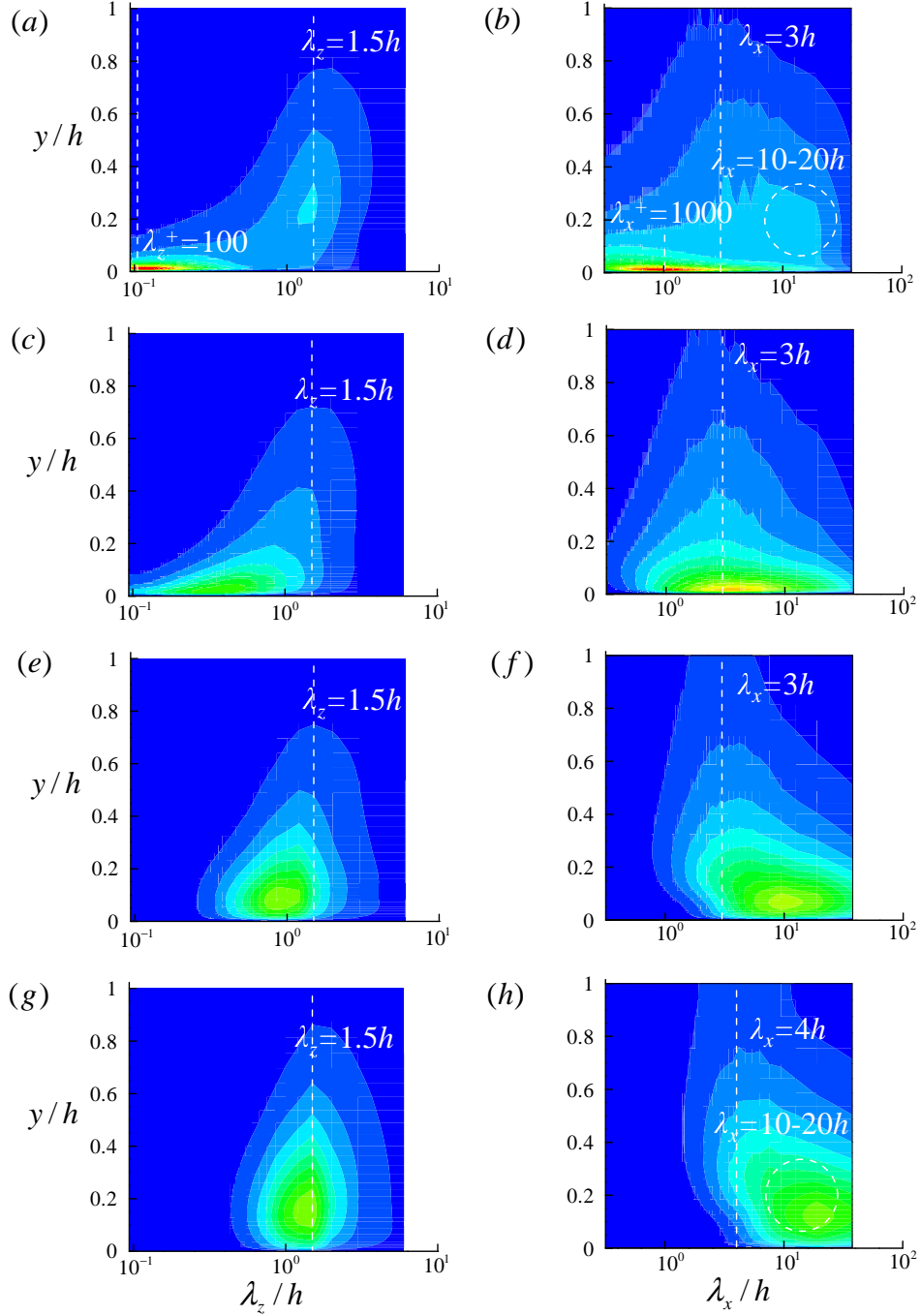
Figure 4.3. One-dimensional premultiplied spanwise and streamwise spectra of the streamwise velocity for (a,b) $C_s = 0.05$, (c,d) $C_s = 0.10$, (e,f) $C_s = 0.20$ and (g,h) $C_s = 0.30$: (a,c,e,g) $k_z \Phi_{uu}(k_z; y)/u_\tau^2$, (b,d,f,h) $k_x \Phi_{uu}(k_x; y)/u_\tau^2$.

Figure 4.4. The dependence of one-dimensional premultiplied spectra of the streamwise velocity on the increase of the Smagorinsky constant C_s : (a) $k_z\Phi_{uu}(k_z;y)/u_\tau^2$, (b) $k_x\Phi_{uu}(k_x;y)/u_\tau^2$. Here, the contour lines are the isoline of 0.8 times the maximum of the spectra for $C_s = 0.05, 0.1, 0.2, 0.3$.

$C_s = 0.1, 0.2, 0.3, 0.4$ and 0.5 are considered. All the coherent motions are completely stabilized when $C_s = 0.5$. While C_s is increased, the friction Reynolds number does not change signif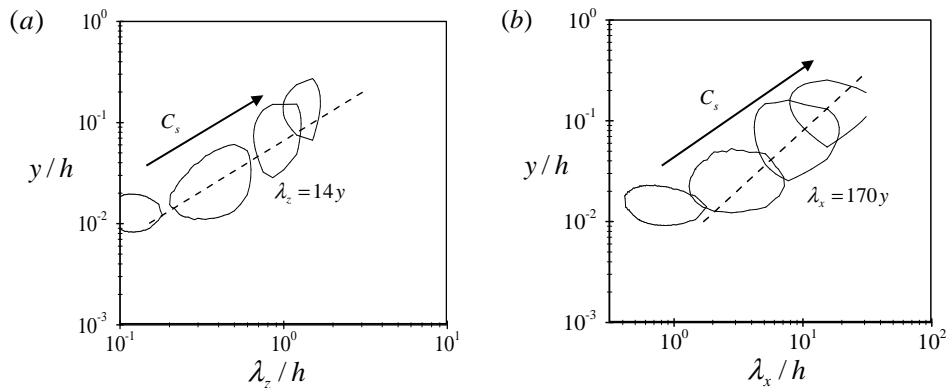icantly: e.g. $Re_\tau = 887$ for $C_s = 0.1$, $Re_\tau = 953$ for $C_s = 0.2$, $Re_\tau = 1051$ for $C_s = 0.3$, and $Re_\tau = 1137$ for $C_s = 0.4$. Figs 4.2 (b), (c) and (d) report the instantaneous flow fields of the streamwise velocity fluctuation for several larger C_s. It is clearly seen that the small-scale turbulent motions are gradually quenched as C_s is increased (figs. 4.2a, b and c), and only the long large-scale streaky motions are left for $C_s = 0.3$ (fig. 4.2d). Interestingly, the size and shape of the surviving large-scale streaky structures for the large C_s are extremely similar to the ones in the reference simulation (compare figs. 4.2a and d).

3.2   Premultiplied one-dimensional spectra

Figs. 4.3 (c), (e) and (g) show one-dimensional premultiplied spanwise spectra of the streamwise velocity for several large C_s. As C_s is increased, a significant change in the spectra is observed at $y/h < 0.2$. For $C_s = 0.1$, the spectral peak of the near-wall streaky structure has almost disappeared (fig. 4.3c), but the outer part of the spectra still remains almost unchanged. This is consistent with the recent numerical experiments by Flores & Jiménez (2006) and Flores *et al.* (2007) where the large-scale outer structures are found to be independent of the presence of the rough wall disturbing the buffer-layer cycles. We further increase C_s, and the corresponding changes of the spectra in the logarithmic region are reported in 4.4. With constantly increasing C_s, the spectra in the logarithmic region also gradually diminish along the $\lambda_z \simeq 14y$ (4.4a), whereas the remaining part does not change significantly. For $C_s = 0.30$, only a spanwise peak remains at $\lambda_z \simeq 1.5h$, implying that the outer mode is sustaining by itself in this case.

The streamwise spectra reveal a tendency similar to the spanwise spectra, but some interesting differences are also found. The streamwise spectra for several C_s are reported in Figs. 4.3 (d), (f) and (h). Similarly to the spanwise spectra, a significant change is observed below $y/h \simeq 0.2$ while no significant difference is found in the outer region. The near-wall streaky structure seems to completely disappear for $C_s = 0.1$ (fig. 4.3 d), and the spectra diminish along $\lambda_x \simeq 170y$ in the logarithmic region as C_s is further increased (4.4b). The streamwise spectra for $C_s = 0.3$ shows two peaks. The first one corresponding to the large-scale motion
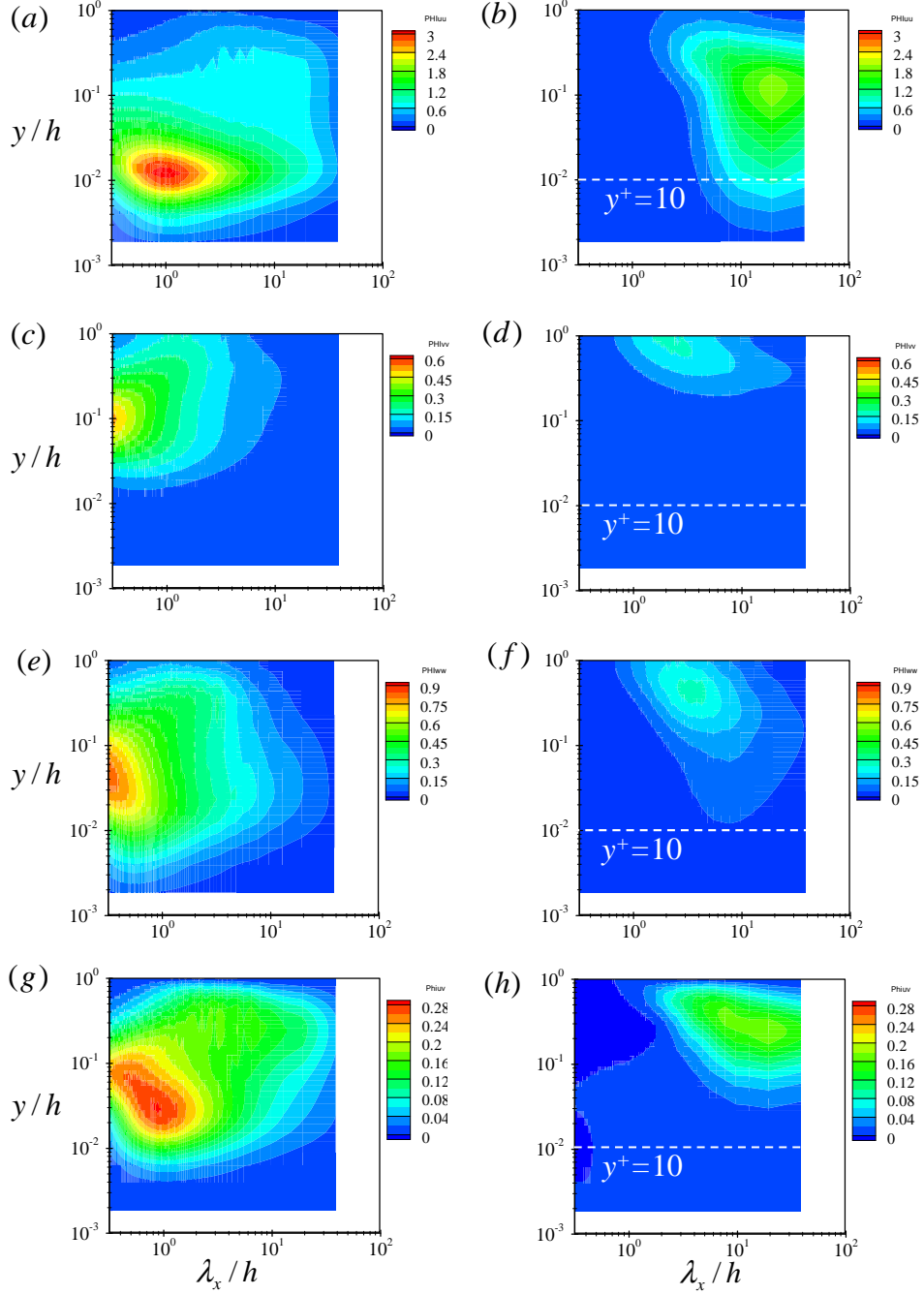
Figure 4.5. Premultiplied streamwise spectra for (a, c, e, g) $C_s = 0.05$ and (b, d, e, f) $C_s = 0.30$ in the logarithmic wall-normal coordinate: (a, b) $k_x h \Phi_{uu}(k_x; y)/u_\tau^2$; (c, d) $k_x h \Phi_{vv}(k_x; y)/u_\tau^2$; (e, f) $k_x h \Phi_{ww}(k_x; y)/u_\tau^2$; (g, h) $-k_x h \Phi_{uv}(k_x; y)/u_\tau^2$.

is located at $\lambda_x/h \simeq 4h$ without significant amplitude for $y/h < 0.2$. The second peak at $\lambda_x \simeq 10 \sim 20h$ is found near $y/h \simeq 0.1 \sim 0.2$; in the reference simulation this is masked by peak related to the near-wall and logarithmic layer structures. The location of the second peak is similar to the average length of the very large-scale streaky structure experimentally observed, implying that it is statistical reflection of the large-scale streaks.

It is also worth mentioning that two curves $\lambda_z \simeq 14y$ and $\lambda_x \simeq 170y$ found in the logarithmic region (see fig. 4.4) characterize the spanwise and streamwise length scales of the streamwise-velocity eddies in the logarithmic region. These two curves roughly satisfy the spectral relation of the logarithmic region $\lambda_z^2 = 2\kappa\lambda_x y$ in del Álamo et $al.$ (2004): for instance, at $y/h = 0.1$, $\lambda_z^2 \simeq (14y)^2 = 1.96h^2$ and this is comparable to $2\kappa\lambda_x y = 1.4h^2$ with $\kappa = 0.41$ at the leading order. Note that this level of agreement is not obtained using $\lambda_x \simeq 12y$ suggested by Jiménez & Hoyas (2008), where the linear scaling in the logarithmic layer is performed based on the outer peak $\lambda_x \simeq 3h$.

3.3   The spectra and flow structure of the large-scale outer mode

The premultiplied streamwise spectra of all the velocity fluctuations (uu, vv, ww) and the Reynolds stress (uv) for $C_s = 0.3$ are also compared with those for $C_s = 0.05$ in Fig. 4.5. All the spectra for $C_s = 0.3$ seem to well represent the contribution of the outer modes comparing to those in the outer region for $C_s = 0.05$, although they tend to be slightly longer in the streamwise direction and carry slightly more energy than those for $C_s = 0.05$ due to the artificial over-diffusion. For $C_s = 0.3$, while the streamwise velocity reveals two peaks as also indicated in Fig. 4.3 (b), the energy peaks of the wall-normal and spanwise velocities are found for $\lambda_x \simeq 2 \sim 4h$ at $y/h > 0.2$ corresponding to the large-scale motion. This implies that the large-scale motion contains the significant fraction of vortical structures being able to drive the streaks according to the linear analysis in chapter 2 and 3. It is also interesting to note that the streamwise and spanwise components of the outer modes carry appreciable energy even at $y^+ = 10$ (figs. 4.5b and f), consistently with the results of chapter 2 and those in Pujals et $al.$ (2009) where it was shown that optimal large-scale streaks strongly penetrate to the near-wall region. Contrary to these two components, the wall-normal components reveal little energy in the near-wall region (figs. 4.5d). For this reason, the Reynolds stress related to the outer modes gives very little influence to the near-wall region because the streamwise and wall-normal velocities are hardly correlated due to the very small wall-normal velocity. This suggests that in the near-wall region the outer modes are essentially 'inactive' in the sense that they do not carry the Reynolds stress. However, the penetration of the streamwise and spanwise velocity structures to the near-wall region can affect the dynamics in there, and this kind of the effect has been indeed observed by Hutchins & Marusic (2007a) and Hutchins & Marusic (2007b) where the large-scale streaky structures are shown to modulate the near-wall cycles. Finally, it is worth mentioning that the near-wall contribution of each velocity component and the Reynolds stress of the outer modes enable to distinguish whether they are 'attached' or 'detached' eddies in the sense of Townsend (1976). According to the spectra in Fig. 4.6, the streamwise and spanwise velocities are attached because they have appreciable values in the near-wall region, whereas the wall-normal velocity and Reynolds stress are detached or more precisely 'floated'. Note that this classification is also consistent with the findings of Jiménez & Hoyas (2008).

The presence of two peaks in the streamwise spectra is now investigated by inspecting the instantaneous flow field for $C_s = 0.3$. Figs. 4.6 (a) and (b) show side and top views of a
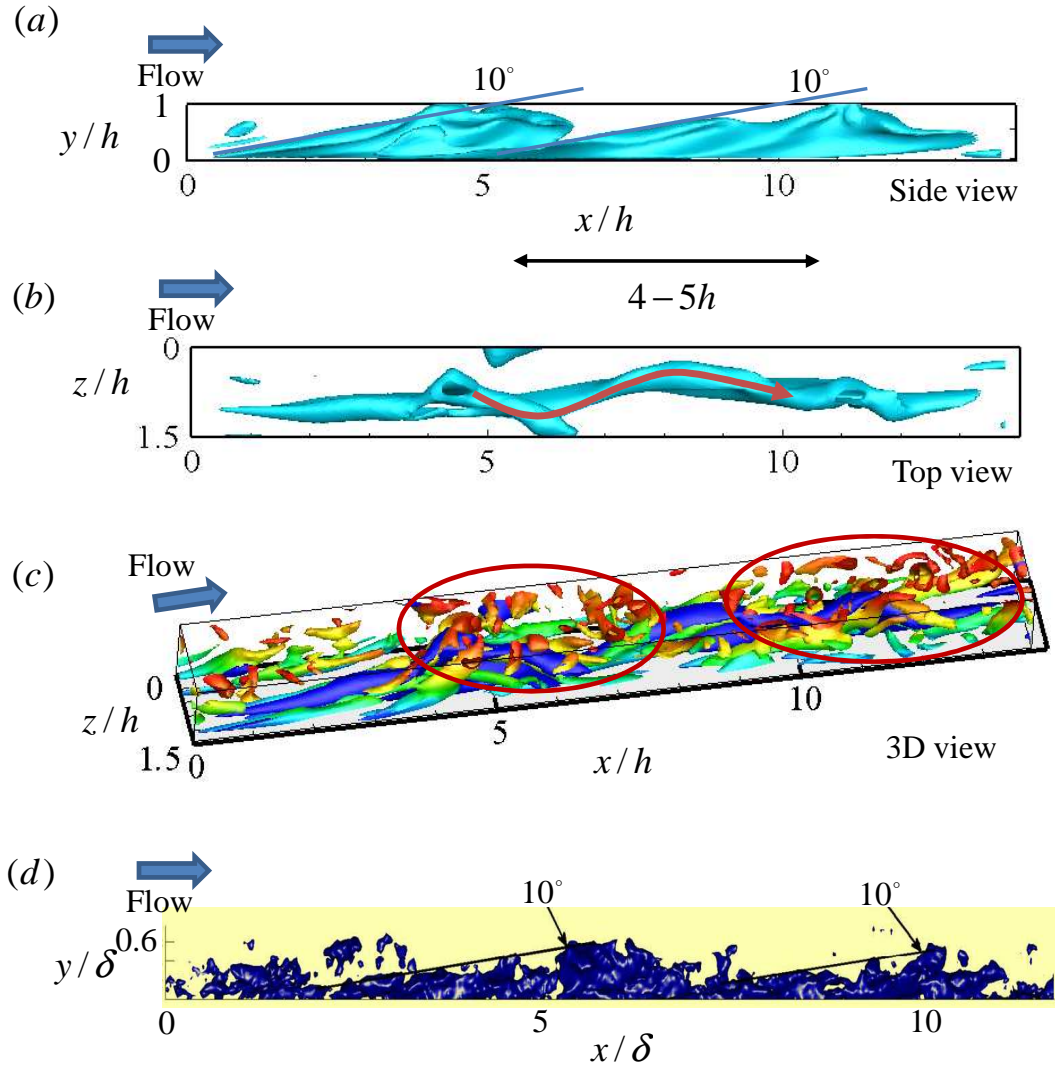
Figure 4.6. Iso-surface of instantaneous streamwise velocity fluctuation ($u^+ = -2.45$) of an isolated large-scale streak for $C_s = 0.30$: (a) side view (x-y plane); (b) top view (x-z plane); (c) 3D view. In (c), iso-surface of the second invariant of the velocity gradient tensor ($Q = 0.071U_e^2/h^2$) is also drawn together with colors indicating its wall-normal distance (the more red is, the further the wall-normal distance is from the wall). In (d), experimental data by PIV measurement for the streamwise velocity fluctuation is also presented for the comparison (from Nickels, 2010).

large-scale streak for $C_s = 0.3$, respectively. The side view shows that the streak is connected through the region below $y/h \simeq 0.2$ and that its length is approximately $\lambda_x \simeq 13 \sim 14h$, that corresponds well to the peak in the streamwise spectra at $y/h < 0.2$ (see also fig. 4.3 h). At $y/h > 0.2$, the streak is found to be inclined to the wall with 10°, and this angle is strikingly similar to the experimental results in turbulent boundary layer (see e.g. Adrian *et al.*, 2000; Nickels, 2010). The streamwise spacing of these outer-layer structures in a streak is roughly $\lambda_x = 4 \sim 5h$ (fig. 4.6a), and the top view clearly shows that it is closely associated with the sinuous oscillation of the streak (fig. 4.6b). Note that this spacing is comparable to the peak at $y/h > 0.2$ in the streamwise spectra (fig. 4.3h), thus this peak can be interpreted as a signature of the streak sinuous mode. More interesting feature related to this inclination is also found in Fig. 4.6 (c), where the vortical structures along this streak are drawn together. It is seen that compact vortex packets are intensively aligned at the top of the streak reaching to the channel center. This suggests that the vortex packets are closely related to the streak sinuous mode. This coherent alignment of the vortex packets along the streaky motions is consistent with the experimental observation by Kim & Adrian (1999) and Guala *et al.* (2006). However, in this case, it does not require the small-scale hairpin vortices in the near-wall and logarithmic regions because all the energy containing eddies in the scales of those regions have been completely removed. Therefore, we show that large-scale motions (bulges) located at least above $y/h \simeq 0.2$ are not necessary formed by the growth and/or merger of the small-scale vortices from the wall, but are probably originated by the sinuous motions of large-scale streaks.

4   Dynamics in the minimal box

Although tuning the Smagorinsky constant in the subgrid-scale stress model of LES makes the outer modes isolated from the smaller-scale structures in the near-wall and logarithmic regions, their dynamics is still complicated due to the interaction of the two outer modes. In this section, we try to understand the detailed dynamics between the large-scale motions ($\lambda_x \simeq 3 \sim 5h$) and the very large-scale motions ($\lambda_x \simeq 10 \sim 20h$). The main question addressed here is: does one of these motions force the other one? or do they mutually support each other? In order to answer to this question, we follow the box minimization approach that has also been used for the near-wall streaky structure (Jiménez & Moin, 1991; Hamilton *et al.*, 1995). The box minimization is conducted for $C_s = 0.4$ which is the highest Smagorinsky constant sustaining turbulence in the large box. Note that the spectra obtained in the large box with $C_s = 0.4$ are not significantly different from those with $C_s = 0.3$. Also, the simulation for $C_s = 0.4$ has a benefit that the vortical structures in instantaneous flow field are observed in a well-organized form due to the higher diffusion. For $C_s = 0.4$, the minimal box size is found approximately $L_x \times L_z \simeq 3h \times 1.5h$. In computational boxes smaller than this size either in the streamwise or spanwise directions, coherent motions do not sustain. It is interesting to note that this box size well corresponds to the size of the large-scale motion with $\lambda_x \simeq 3 \sim 5h$ (see also figs. 4.3a and b). This implies that the length scale of the large-scale motion with $\lambda_x \simeq 3 \sim 5h$ are the fundamental element of the outer mode.

The energies of the streamwise velocity fluctuation E_u and the wall-normal and spanwise velocity fluctuations E_{v+w} integrated over the lower half of the computational box are introduced as

$$E_u \equiv \frac{1}{2V_h U_e^2} \int_{V_h} |u'|^2 \, dV, \tag{4.3a}$$
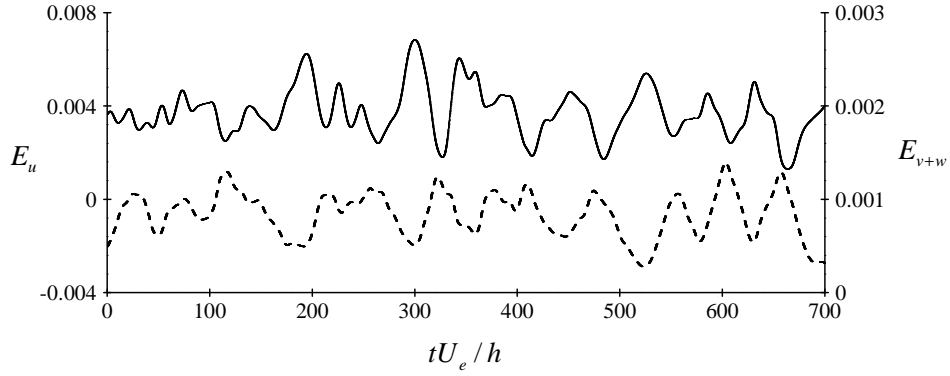
Figure 4.7. Time trace of E_u and E_{v+w} for $C_s = 0.4$ in the minimal box. Here, ———, E_u; $----$, E_{v+w}.
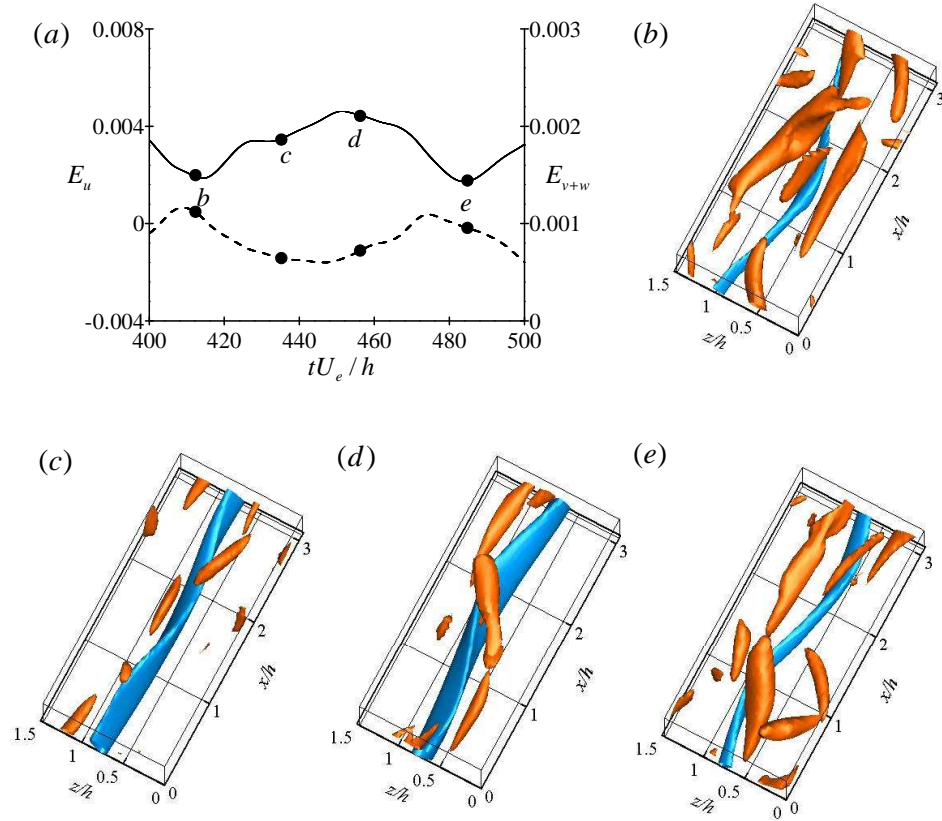
Figure 4.8. Time trace of the energies and the corresponding flow visualizations in the minimal box: (a) E_u and E_{v+w} for $tU_e/h \in [400, 500]$; flow visualization at (b) $tU_e/h = 412.3$, (c) $tU_e/h = 435.2$, (d) $tU_e/h = 456.2$, and (e) $tU_e/h = 484.8$. In (b-d), the blue and red iso-surfaces denote $u^+ = -2.6$ and $Q = 0.064U_e^2/h^2$ respectively.

$$E_{v+w} \equiv \frac{1}{2V_h U_e^2} \int_{V_h} |v'|^2 + |w'|^2 \, dV, \qquad (4.3b)$$

where V_h denotes the volume of the lower half of the computational domain, and the superscript $'$ is the fluctuation of the variables. The energy of the wall-normal velocity is found to be highly correlated to that of the spanwise velocity, consistent with the spectra in Fig. 4.5. Therefore, they are considered together as in (4.3b). From these quantities, the amplitude of streaky motion is roughly represented by E_u, while that of the related streamwise vortical structures is approximated by E_{v+w}.

Fig. 4.7 shows the time trace of E_u and E_{v+w} for $C_s = 0.4$ in the minimal box $L_x \times L_z = \pi h \times 1.5h$. Both of them oscillate quasi-periodically with $TU_e/h \simeq 50 \sim 70$, and they are clearly seen to be anti-correlated. When E_u reaches the highest value, E_{v+w} almost becomes the lowest. Inversely, when E_u becomes the lowest value, E_{v+w} is almost the highest. This anti-correlation between E_u and E_{v+w} implies that the outer modes sustains in the form of a cycle consisting of 'vortices-streaks-vortices'. This cycle is very similar to the observations in the minimal Couette flow by Hamilton *et al.* (1995), suggesting that the outer mode sustains with a process the bears some similarity to the one of the near-wall cycle.

The nature of the self-sustaining process at large scale is also seen from a series of the instantaneous snapshots of the streak and vortical structures in Fig. 4.8. When E_{v+w} reaches the highes value (fig. 4.8 *b*), the strong quasi-streamwise vortices are found extending roughly up to the half of the streamwise computational domain. The vortical structures are gradually damped as the time passes by, and they are transformed to the streak (fig. 4.8*c*). When the streak reaches a sufficiently large amplitude, it begins to oscillate as shown in Fig. 4.8 (*d*). At this moment, the streak has very similar to the traveling waves computed in Waleffe (1998), Waleffe (2001) and Waleffe (2003): i.e. the sinuously oscillating streak with the streamwise vortices at its flank. After the streak breakdown, the streamwise vortices are regenerated (fig. 4.8*e*). In the minimal box, this whole process repeats permanently and individual process forms the large-scale 'bursting', suggesting that the outer mode self-sustains with a similar process to the near-wall cycle.

Chapter 5

Artificial forcing of streaks: application to turbulent drag reduction

The amplification of streaks is a crucial element in the self-sustaining cycle, and through this process the turbulent kinetic energy is directly extracted from the mean shear. From the viewpoint of flow control, this amplification is a fruitful feature providing high-amplitude actuation with small amounts of energy input. For laminar flows, artificially forced streaks have been shown to stabilize Tollmien-Schlichting waves (Cossu & Brandt, 2002, 2004) and delay transition in the boundary layer (Fransson *et al.*, 2006). Recently, Pujals *et al.* (2010*a*) have experimentally proved that streaks are also highly amplified in turbulent boundary layers, and Pujals *et al.* (2010*b*) have used this feature to suppress separation on an Ahmed body. The possible usefulness of the amplified streaks to reduce turbulent skin-friction drag has, however, not yet been explored. The purpose of this chapter is to track this issue.

1   Motivation

Reducing turbulent skin-friction drag is an important issue promising a wide range of engineering application. An important contribution to the high turbulent skin friction has been firmly established in the presence of near-wall streamwise vortices (Kravchenko *et al.*, 1993; Choi *et al.*, 1994), which are also important elements of the near-wall self-sustaining process. Therefore, many efforts have been oriented to directly tackle the near-wall streamwise vortices at their characteristic length scales (i.e. $l^+ = O(10 \sim 10^2)$). Fig. 5.1 (*a*) and (*b*) show two well-known examples, the 'opposition control' and the 'riblet', respectively. The opposition control is a way to modify boundary conditions at the wall to suppress the near-wall streamwise vortices using the flow-field information at $y^+ = 10 \sim 20$ (Choi *et al.*, 1994). This method has been reported to reduce the turbulent skin friction up to $20 \sim 30\%$, but it is difficult to implement in practical situations because the information inside the flow field is necessary. On the other hand, riblets are practical passive devices, which do not require active energy input (Walsh, 1983). The performance of the riblets is known to be dependent on its tip-to-tip spanwise size. The riblets having the large tip-to-tip size (left in Fig. 5.1*b*) increase the skin fiction because the contact area with the streamwise vortices is increased. However, riblets with sufficiently small tip-to-tip spanwise size reduce the contact area (right in Fig. 5.1*b*). In
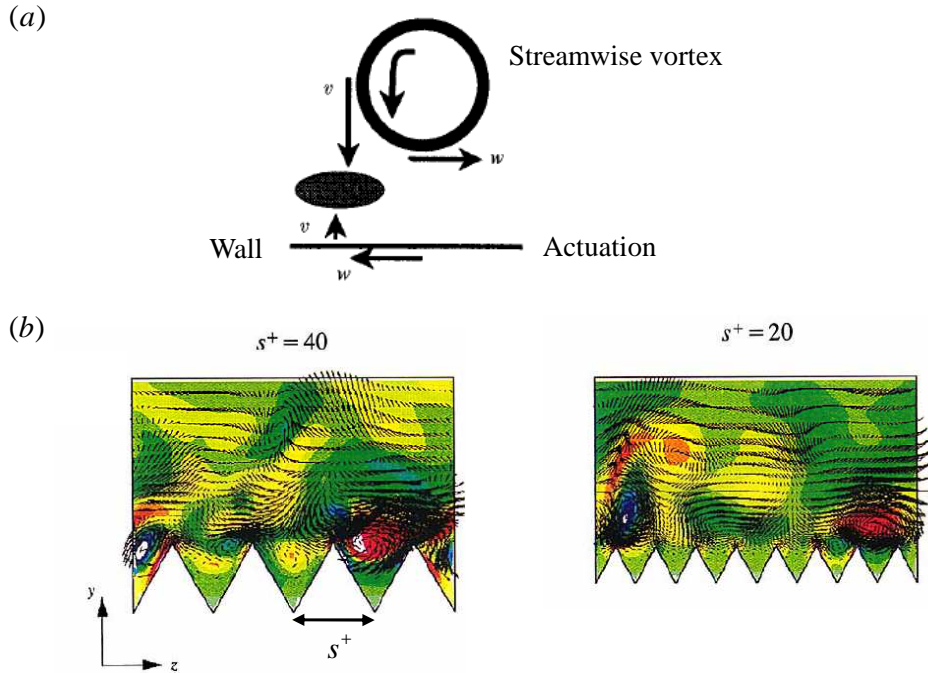
(*a*)

(*b*)

Figure 5.1. Control of the near-wall streamwise vortices for the turbulent skin-friction reduction: (*a*) the opposition control strategy (from Choi *et al.*, 1994); (*b*) flows over drag increasing (left) and reducing (right) riblets (from Choi *et al.*, 1993)

this case, skin friction is reduced up to 8%. Nevertheless, the practical implementation of the riblet is hampered due to its small size. For example, the relevant tip-to-tip spanwise spacing of riblet is $O(10\mu m)$ for commercial airplanes. With this small size, the riblet valley is easily filled by dust in the air, resulting in very little drag reduction.

To overcome these difficulties, it has been suggested to act 'indirectly' on the near-wall cycle via large-scale control. A representative example of this approach has been suggested by Schoppa & Hussain (1998) who showed that a pair of large-scale streamwise vortices spanning $L_z^+ \approx 400$ in the flow field reduces the skin-friction drag by quenching the near-wall streamwise vortices. This method has been implemented in laboratory experiments using wall jets (Iuso *et al.*, 2002).

Motivated by these studies, the scope of our investigation is to examine the feasibility, using optimal perturbations, to implement control at large scale. The shape of optimal perturbations corresponding to the outer peak is almost independent of the Reynolds numbers, and their amplification increases with the Reynolds number. In this respect, they are ideal candidates to use for controlling wall-bounded flows at large Reynolds numbers.

First, the amplification of streak is tested in turbulent flows using direct numerical simulation, and the reduction of skin friction is then studied. Significant amount of skin-friction drag is achieved by forced streaks. We also investigate the power consumption of the present control strategy, which was not examined in Schoppa & Hussain (1998). This chapter mainly focuses on the results in turbulent channel flow. Basically the same results are also found for turbulent pipe flow in Willis *et al.* (2010) as also discussed in section 5.

Re_m	Re_τ	L_x/h	L_z/h	Δx^+	$\Delta y^+_{\max}$	Δz^+	$T_{\mathrm{avg}}U_m/h$
2867	100	12π	4π	29.2	3.2	9.74	1267
5600	180	6π	$4\pi/3$	17.7	5.8	5.9	800
5300	180	15	–	9.4	4.4	5.9	1400

Table 5.1. Computational parameters used in the direct numerical simulation of the turbulent channel (first two rows) and pipe (the last rows). For pipe flows, h the radius of pipe, Δy^+ the grid spacing in the radial direction and Δz^+ is the grid spacing in the azimuthal direction at the wall.

2   Direct numerical simulation

For the plane channel flow, direct numerical simulations are performed using the `channelflow` code (Gibson *et al.*, 2008) (the main features of this code are summarized in appendix). A constant mass flux is imposed during the simulations, and two Reynolds numbers are considered ($Re_\tau = 100$ and 180). The simulation parameters are summarized in table 5.1. To reduce computational cost, extensive parametric studies are conducted at $Re_\tau = 100$, and only several important cases are validated at $Re_\tau = 180$. The large spanwise computational domain is chosen so that the effect of spanwise wavelength of optimal forcing can be tested. A long streamwise domain is also considered to resolve at least one wavelength of the natural very large-scale streaky structures.

For the turbulent pipe flow, the code described in Willis & Kerswell (2008) has been used for direct numerical simulations. In this code, the Fourier-Galerkin method is applied to the axial (x) and azimuthal (θ) directions, and a finite difference scheme with 9-point stencil is used. Time integration is conducted using a second-order predictor-corrector method (for further details, refer to Willis & Kerswell, 2008). The streaks are also driven by the same method with channel case. The simulation parameters are summarized in table 5.2. Similarly to turbulent channel flow, a sufficiently long streamwise domain is considered.

3   Response to finite amplitude optimal forcing

A reference simulation has first been conducted without any forcing. The mean flow in the reference case is denoted as $U_0(y)$ with its centerline velocity U_{e0}. Then, a steady body force has been added to the right-hand side of the Navier-Stokes equation. The body force consists of optimal linear forcing computed in chapter 2[1]. The amplitude of forcing is defined as its L_2-norm:

$$\|\mathbf{f}\| \equiv \left[\frac{1}{V} \int_V \mathbf{f} \cdot \mathbf{f} \, dV \right]^{1/2}, \tag{5.1}$$

where V is the volume of the computational box. The forcing term induces large-scale streaks in the flow. The forced large-scale streaks can be characterized with $U(y, z) = \langle u(x, y, z, t) \rangle_{x,t}$.

---

[1]Since the Cess expression for $Re_\tau < 200$ is not differentiable at the channel center, the optimal forcing is computed at a higher Reynolds number. However, this is not a severe approximation since the spatial structure of optimal perturbations is almost independent of the Reynolds number.
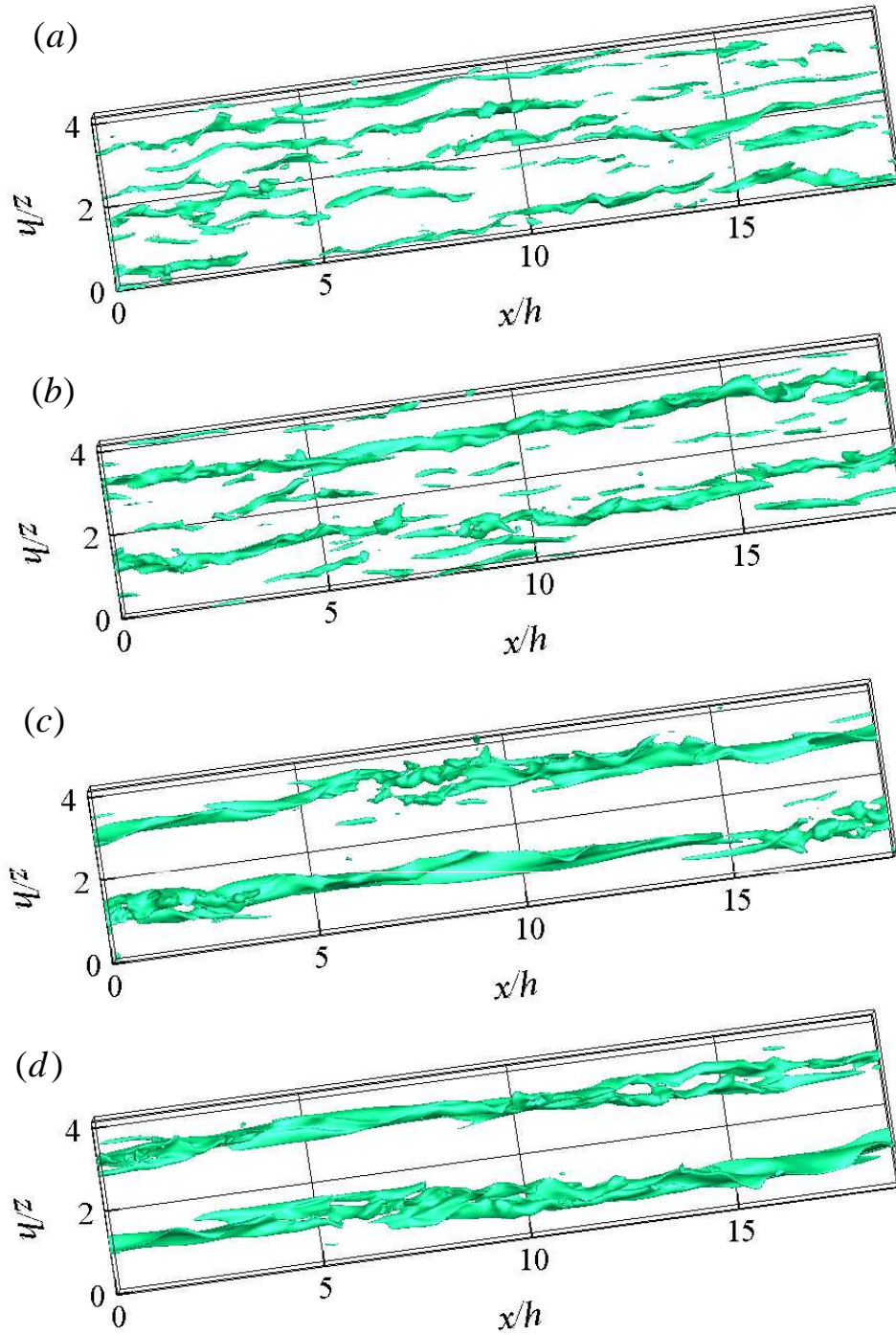
Figure 5.2. Instantaneous iso-surface of the streamwise velocity $(u'/U_m = -0.11)$ at $Re_\tau = 180$: (a) $\|\mathbf{f}h/U_{e0}^2\| = 0$; (b) $\|\mathbf{f}h/U_{e0}^2\| = 6.4 \times 10^{-4}$; (c) $\|\mathbf{f}h/U_{e0}^2\| = 1.5 \times 10^{-3}$; (d) $\|\mathbf{f}h/U_{e0}^2\| = 2.1 \times 10^{-3}$.
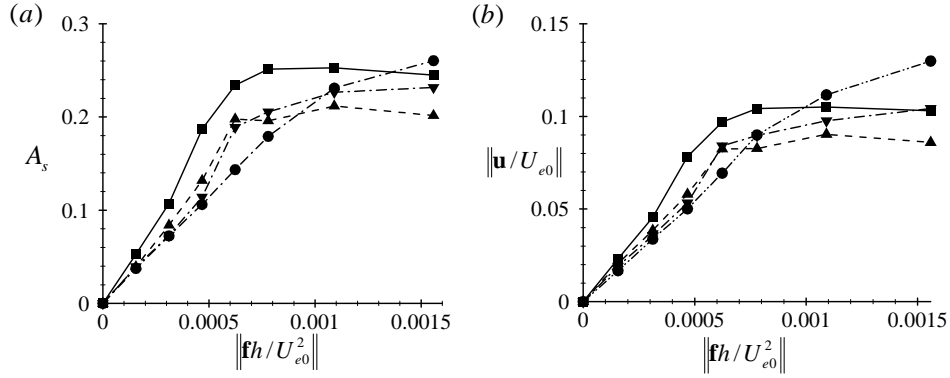
Figure 5.3. The amplification of streaks by the optimal forcing in turbulent channel at $Re_\tau = 100$: (a) A_s; (b) $\|\mathbf{u}\|$. Here, ———, $\lambda_z = 2.1h$; - - - -, $\lambda_z = 3.14h$; —·—·—, $\lambda_z = 4.2h$; —··—··—, $\lambda_z = 6.3h$.

Fig. 5.1 shows the instantaneous streamwise velocity fluctuation for several amplitudes of the forcing with the spanwise spacing $\lambda_z = 2.1h$ in the plane channel. In the reference flow field (fig. 5.6a), the near-wall streaky structures are clearly visible with $\lambda_z^+ \simeq 100$ ($\lambda_z \simeq 0.5 \sim 0.6$), while the large-scale streaky motions are difficult to identify due to the low Reynolds number. As the forcing amplitude is gradually increased, the flow field clearly reveals the streaks with $\lambda_z = 2.1h$ amplified by the forcing (fig. 5.1b, c and d). For sufficiently large amplitudes of the forcing (e.g. fig. 5.1c and d), the forced streaks become the most prominent feature of the flow.

The influence of the optimal forcing is measured by the variation of the averaged streaky mean flow by $\Delta U(y, z) \equiv U(y, z) - U_0(y)$. The mean amplitude of the forced streaks is defined as (Andersson *et al.*, 2001)

$$A_s = \frac{[max_{y,z}\Delta U(y, z) - min_{y,z}\Delta U(y, z)]}{2\,U_{e0}}. \tag{5.2}$$

The response to the forcing can also be defined as the norm of the difference between unforced and forced mean flows: $\|\mathbf{u_s}\|$ where $\mathbf{u_s} \equiv (U(y, z) - U_0(y), V(y, z), W(y, z))$.

Fig. 5.2 reports the streak amplitudes A_s and the corresponding responses to forcing $\|\mathbf{u}\|$ for several spanwise wavelengths as the forcing amplitude is increased. For small forcing amplitudes ($\|\mathbf{f}h/U_{e0}^2\| \lesssim 2.0 \times 10^{-4}$), both of them almost linearly grow as the forcing amplitude is increased. When the forcing amplitude is sufficiently large ($\|\mathbf{f}h/U_{e0}^2\| \gtrsim 5.0 \times 10^{-4}$), they begin to saturate due to nonlinear effect. The streak amplitudes are almost saturated at $A_s \simeq 20 \sim 30\%$, and the responses to forcing also stay approximately at $\|\mathbf{u}/U_{e0}\| \simeq 0.05 \sim 0.1$.

The dependence of the amplification in the range of linear growth on the spanwise wavenumbers is reported in Fig. 5.4 based on the responses to the smallest considered forcing amplitude. Here, the results from two Reynolds numbers are reported for the plane channel together to check the role of the Reynolds number. Large amplifications are found for all the considered spanwise wavelengths, and the maximum amplification by direct numerical simulation is observed at $\lambda_z \simeq 2.1h$. Interestingly, this spanwise spacing from direct numerical simulation agrees well with that of the natural large-scale streaky motion ($\lambda_z \simeq 1.5 \sim 2h$). However, this spanwise spacing is slightly different from the value $\lambda_z \simeq 5.5h$ obtained from the eddy-viscosity model in chapter 2. This suggests that the prediction of larger amplifications for $\lambda_z \gtrsim 4h$ is
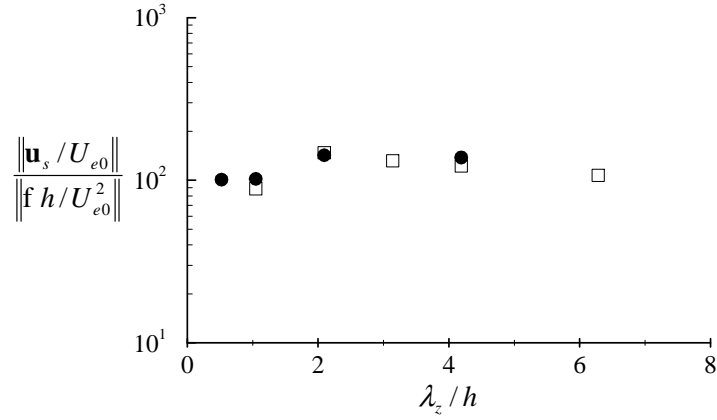
Figure 5.4. The dependence of amplification ratio $\|\mathbf{u}\|/\|\mathbf{f}\|$ on the spanwise wavelength for the small-amplitude forcing: $\square$, $Re_\tau = 100$; $\bullet$, $Re_\tau = 180$.
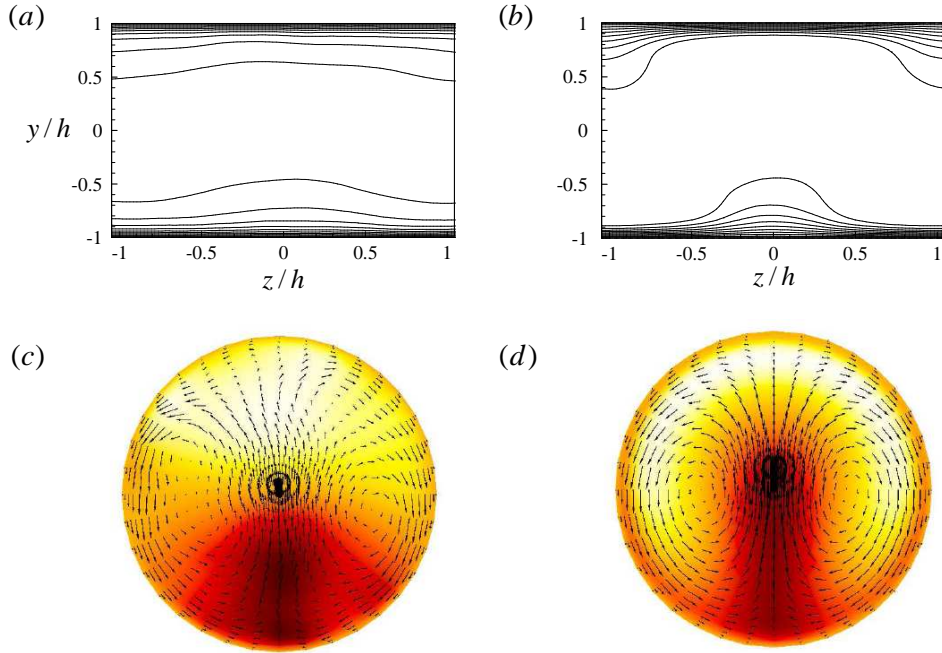
Figure 5.5. Cross-streamwise view of the streaky mean flow $U(y,z)$ $(U(r,\theta))$ in turbulent (a,b) channel and (c,d) pipe flows at $Re_\tau = 180$ with respect to the forcing amplitude: (a) $\|\mathbf{f}h/U_{e0}^2\| = 2.1 \times 10^{-4}$; (b) $\|\mathbf{f}h/U_{e0}^2\| = 1.5 \times 10^{-3}$; (c) $\|\mathbf{f}h/U_{e0}^2\| = 8.0 \times 10^{-5}$; (d) $\|\mathbf{f}h/U_{e0}^2\| = 8.0 \times 10^{-4}$. In (a,b), the contour lines denote isoline of the streamwise velocity with increment of 0.1 of its maximum. In (c,d), vectors are the cross-stream components of the forced field, and colored contour denotes the the streamwise velocity (white, fast-streaks; red/dark, slow-streaks).

probably due to the crudeness of the eddy viscosity model. The amplification ratio $\|\mathbf{u}\|/\|\mathbf{f}\|$ computed in the present direct numerical simulations are found to be comparable to the ones predicted by the linear model: for example, the amplification ratio computed with the linear model in chapter 2 is typically $\|\mathbf{u}/U_{e0}\|/\|\mathbf{f}h/U_{e0}^2\| \simeq O(10^2)$ at similar Reynolds numbers, and this is comparable to the present result. However, if we recompute the amplification ratio using the linear model without eddy viscosity (e.g. Butler & Farrell, 1993), two order of magnitude larger values are found than those from the present simulation. This confirms that the use of the eddy viscosity is essential to describe dynamics of the small perturbations in turbulent flows. Very similar results are found for the pipe flow.

Fig. 5.5 shows the forced streaky profiles $U(y,z)$ for both the plane channel and the pipe. For sufficiently small forcing amplitudes, the low- and high-momentum regions in both turbulent channel and pipe flows occupy the almost same spanwise spacing (fig. 5.5a and c), consistently with the results in chapter 2. However, as the forcing amplitude increases, the low-momentum region becomes narrower and more intense than the high momentum region (fig. 5.5 b and d). This feature, typical of turbulent flows, is also observed in laminar flows, thus it is presumably originated from the nonlinearity related to the large amplitude of the streaks.

4 Skin-friction drag reduction

In this section, we examine whether the streak forcing reduces the skin-friction drag. Note that the large-scale streamwise vortices used by Schoppa & Hussain (1998) are quite similar to the optimal forcing we use, and therefore we also expect the certain amount of the drag reduction. Fig. 5.6 (a) compares the time trace of the ratio of the total wall-shear stress to the mean reference case value in two forced simulations with the one for the reference case for the plane channel. After some initial transient, the skin-friction drag is sustained at lower values than that in the reference case.

The dependence of the mean drag on forcing amplitude is reported in Fig. 5.6 (b). For small forcing amplitudes, the skin-friction drag is gradually reduced as the forcing amplitude is increased. The minimum drag is achieved when $\|\mathbf{f}h/U_{e0}^2\| \simeq 1 \times 10^{-3}$, and the corresponding drag reduction is approximately 10.3%. As the forcing amplitude is further increased, the skin-friction drag slowly increases. These results agree well with those in Schoppa & Hussain (1998). Essentially the same tendency is found for the pipe flow (Willis $et\ al.$, 2010).

For this control strategy to be interesting for applications, the net-power saving should be considered as well as the drag reduction. The net power consumption per unit volume is

$$P_{net} = \frac{1}{V}\int_V -\nabla\mathbf{p}\cdot\mathbf{u}dV + \frac{1}{V}\int_V \mathbf{f}\cdot\mathbf{u}dV. \tag{5.3}$$

Here, the first term in the right-hand side is the power consumption to maintain the constant mass flux by the pressure gradient. This term is easily found to correspond to the total skin friction. The second term represents the power consumption by the forcing, necessary to drive streaks into the flow field. The net-power saving is reported in Fig. 5.6 (b). Even for the largest amplitude of the forcing, the power consumption by the forcing is only 1.4% of $P_{net,0}$. The maximum net power saving is is 9.9% where the maximum skin friction reduction is obtained, and the corresponding power consumption to drive the streaks is only 0.4% of $P_{net,0}$. This suggests that driving optimally large-scale streaks can become a promising strategy to reduce the skin-friction drag. Similar conclusion apply to the pipe flow case.
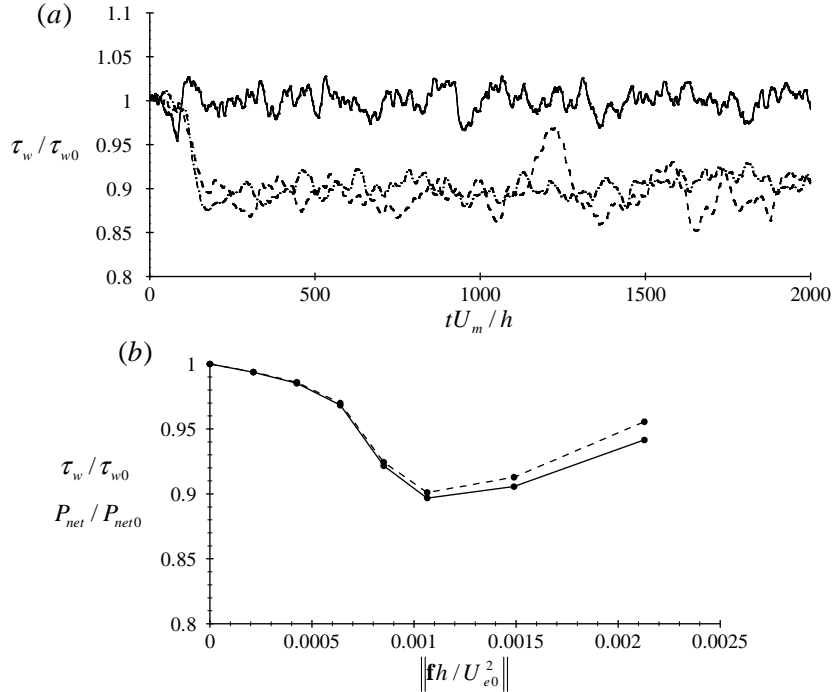
(a)

(b)

Figure 5.6. Drag and net power consumption reduction by streak forcing in turbulent channel flow at $Re_\tau = 180$. (a) time trace of the normalized skin friction τ_w/τ_{w0} by the value in the reference case: ———, $\|\mathbf{f}h/U_{e0}^2\| = 0$ (the reference case); - - - -, $\|\mathbf{f}h/U_{e0}^2\| = 8.5\times10^{-4}$; —·—·—, $\|\mathbf{f}h/U_{e0}^2\| = 1.06 \times 10^{-3}$. ($b$) normalized wall-shear stress and net power spent with respect to the forcing amplitude: ———, τ_w/τ_{w0}; - - - -, P_{net}/P_{net0}.

We now consider the mechanism explaining the observed drag reduction. Fig. 5.7 shows the instantaneous streamwise vorticity fields of unforced and forced cases in both plane channel and pipe flows. In the unforced flow field (fig. 5.6a and c), the near-wall streaky structures and the streamwise vortices are clearly visible with $\lambda_z^+ \simeq 100$. For the forced cases, most of the streamwise vortices in the high-speed regions of the streaks are quenched, and streamwise vortices are found only low-speed regions in the form of localized packets of smaller intensity. This suggests that the present drag reduction is directly associated with disappearance of the streamwise vortices, consistently with the explanation by Schoppa & Hussain (1998).

5   Discussion

The direct numerical simulations discussed in this chapter clearly show that small amplitude steady optimal forcing computed by the linear theory strongly is amplified into the large-scale streaks. It is also found that the use of proper eddy viscosity is essential to describe the dynamics of the driven small perturbations in turbulent flows. This large sensitivity to steady forcing has also been observed in recent experiments on Couette and boundary layer flows (Kitoh *et al.*, 2005; Kitoh & Umeki, 2008; Pujals *et al.*, 2010a).

The drag reduction observed in the present study can be attributed to the mechanism reported by Schoppa & Hussain (1998). In fact, the large-scale vortices driven in their DNS are probably the large-scale streaks even if these streaks are not studied by those authors.

(*a*)

(*b*)
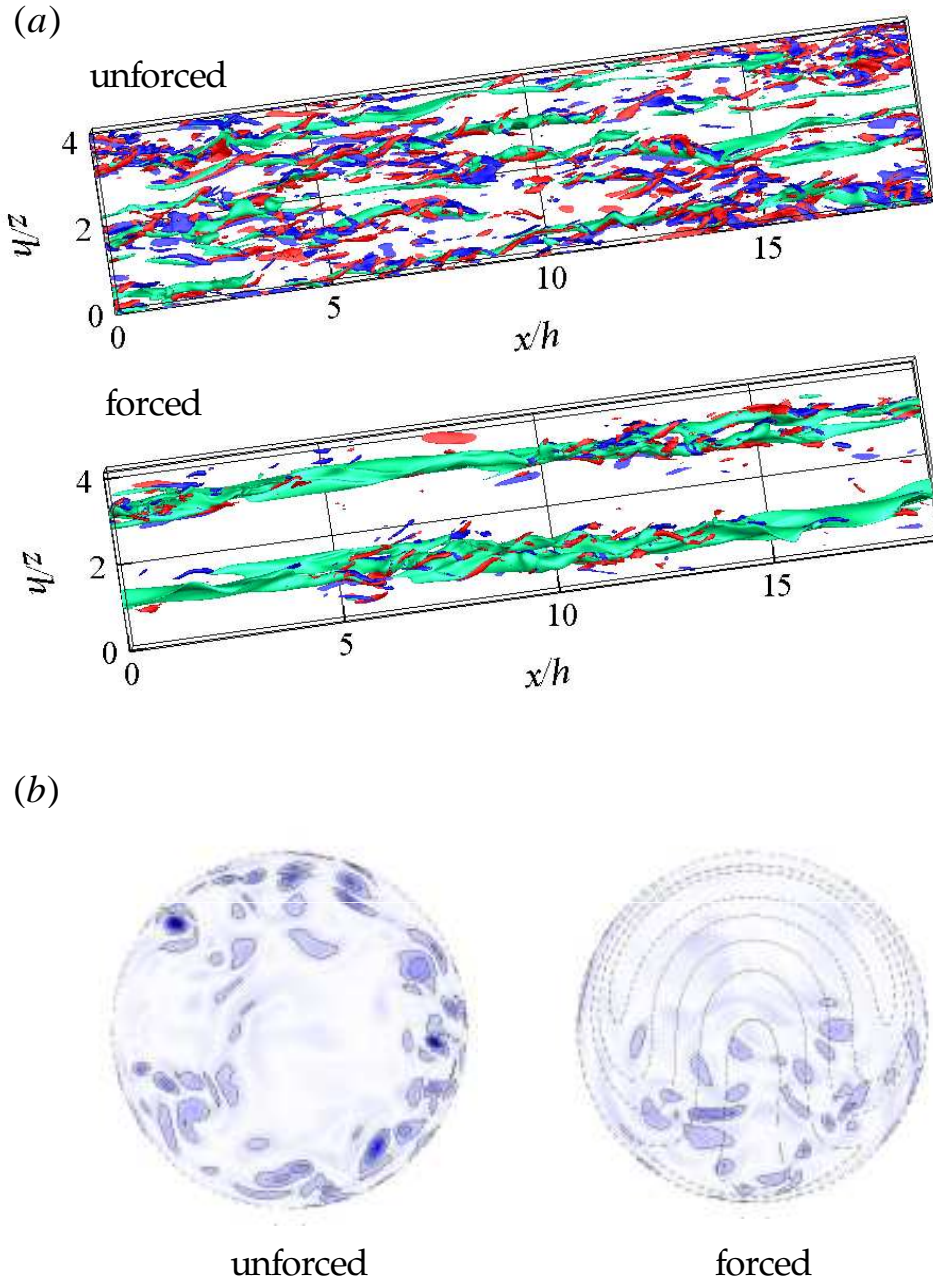
unforced   forced

Figure 5.7. Unforced and forced flow field in turbulent (*a*) channel and (*b*) pipe flows at $Re_\tau = 180$: (*a*) green is iso-surface of the streamwise velocity fluctuation with $u'/U_m = -0.11$, and red and blue denote streamwise vorticity fluctuation with $\omega_x' h/U_m = \pm 1.5$; (*b*) cross-streamwise view of instantaneous streamwise vorticity contour (blue/dark intense vorticity; white no vorticity) with iso-levels of the streamwise averaged velocity.

Moreover, the spanwise spacing of the vortices $L_z^+ \simeq 400$ in their study is roughly $L_z \simeq 2h$ at $Re_\tau = 180$, which almost coincides with the optimal spanwise spacing for streak amplification. However, in the present study, the effective large-scale forcing is predict to scale with the outer units instead of the inner units since the largest amplification are found at $\lambda_z = 2h$ for two different Reynolds numbers.

The results in the present study are limited to relatively low Reynolds numbers. However, if this outer-unit scaling property is confirmed at the high Reynolds numbers, this would represent a great benefit in developing 'practical' actuators because the outer length scale in boundary layer on the wings of commercial airplanes is $O(1cm)$. Reminding the typical size of the riblet $O(10\mu m)$, such control actuators would be much easier to develop. Moreover, the amplification ratio is also expected to increase with the Reynolds number, thus high efficiency may be achieved at the high Reynolds numbers where the practical engineering problem is often situated. These attractive features remains to be confirmed by the laboratory experiments in the future.

Chapter 6

Conclusion and outlook

The main goal of this thesis was to understand the origin and nature of large-scale streaky motions in wall-bounded turbulent flows. To achieve this goal, the work has been divided into distinct parts that are discussed below.

Linear non-normal amplification of coherent streaks

As a first step, we have extended the previous analyses of optimal temporal transient growth by del Álamo & Jiménez (2006), Pujals *et al.* (2009) and Cossu *et al.* (2009) to the computation of the optimal response to harmonic and stochastic forcing. Three cases have been considered: turbulent Couette flow at low Reynolds number, turbulent channel and pipe flows at high Reynolds numbers. The input-output analysis shows that streaks can be efficiently amplified by harmonic forcing, and stochastic excitation through the lift-up effect. Only streamwise-elongated perturbations ($\lambda_x \gtrsim \lambda_z$) are strongly amplified, and the maximum amplification is always found for streamwise uniform perturbations. While the optimal transient growth reveals two peaks in the spanwise wavelengths scaled by the outer and inner units, the responses to optimal and stochastic forcing are found to have such peaks in the responses premultiplied by the spanwise wavenumber and its square respectively. The spanwise spacings supporting the maximum amplification are found to be scaled by the outer units, and they show fair agreement with those of the large-scale streaky motions observed in the laboratory and numerical experiments. The secondary peak scaled by the inner units is also found at $\lambda_z^+ \simeq 80 \sim 100$ in the premultiplied curves. The associated optimal perturbations are similar to the typical near-wall structures. In the intermediate range between the outer and inner peaks, a power-law dependence is observed: $G_{\max} \sim \beta^0$, $R_{\max} \sim \beta^{-2}$ and $V \sim \beta^{-1}$. Such power-law dependence is originated from the geometrically similar nature of the optimal perturbations in the logarithmic layer.

The input-output analysis using the present linear model may be improved quantitatively by introducing more realistic models for the turbulent stresses. However, we believe that the qualitative conclusion found in the present study will not change if more refined models are used. Interpretation of the input-output analysis requires caution because studying the lift-up effect seems to provide only the spanwise length-scale selection. The spanwise power-spectral densities obtained from stochastic responses shows an encouraging agreement with those of real flows. However, this kind of approach may not be valid for the streamwise spectra because the streamwise length-scale selection is probably dominated by the streak instability or secondary transient growth process.

Secondary instability of finite-amplitude coherent streaks

The stability analysis of the amplified large-scale streaks for turbulent Couette and Poiseulle flows has been performed using a crude model that used the eddy viscosity associated with the spanwise homogeneous mean flow. The base flow is computed by solving a two-dimensional eddy-viscosity simulation. As the amplitude of initial optimal vortices increases, the amplitude of streaks also increases. It is shown that sufficiently amplified streaks become secondarily unstable with a most amplified fundamental sinuous mode. The critical streak amplitudes of the onset of instability are found to be lower than those in laminar flows. However, this does not mean that the streak instability in turbulent flows can be more easily triggered than that in laminar flows because initial vortices in turbulent flows are also found to be more energetic to drive streak instability than those in laminar flows.

In spite of the crudeness of the considered assumptions, the streamwise wavelengths attaining the maximum growth rate show good agreement with the streamwise length scale of the experimentally observed large-scale motions. The longest wavelengths revealing the marginal stability also corresponds well to the typical streamwise lengths of the very large-scale streaky structures in the outer region.

There is plenty of room to improve the stability analysis of the finite amplified streaks. Maybe the most important future goal is to find the evidences of the streak instability from laboratory and numerical experiments. A promising way is to introduce the streak through the external forcing as in chapter 5, and to seek statistical evidences of the large-scale streak instability. This kind of approach has been used to study the streak instability in laminar flows (Elosfsson *et al.*, 1999; Andersson *et al.*, 2001). The streamwise instability wavelength of the streaky structures in the logarithmic layer could also be a interesting issue to be studied. Similarly to the streaks in the near-wall region and transitional flows (Schoppa & Hussain, 2002; Hœpffner *et al.*, 2005; Cossu *et al.*, 2007), investigating the secondary transient growth of the large-scale streaks may also be a good idea.

Self-sustaining process at large scale

Even if the existence of a coherent lift-up effect and instability of streaks at large scale has been proven, the current wisdom is that large-scale outer motions are sustained by the bottom-up process where smaller-scale coherent structures merge and grow to form the large-scale ones. We have asked the questions: can large-scale outer motions sustain in the absence of any bottom-up process? We have therefore designed a conceptual numerical experiment with the static Smagorinsky model to quench the small-scale energetic eddies populating the near-wall and logarithmic regions. As the Smagorinksy constant is increased, the eddies in the near-wall and logarithmic regions are gradually quenched. We have found that the large-scale outer structures can indeed sustain without the presence of the small-scale near-wall and logarithmic-layer eddies. The 'surviving' structures consists of two modes: the detached part of the large-scale motions and the long streaky structures. The detached part of the large-scale motions is aligned at the top of the streaky structures in the sinuous manner, suggesting that it is a reflection of sinuous mode of the streak instability. The long streaky motions are mainly located at $y/h \lesssim 0.2$ and they strongly penetrate into the near-wall region. However, they do not carry the Reynolds stress in the near-wall region, and therefore they essentially remain to be 'inactive' in there. The minimal computational box size sustaining such outer structures is found to be $L_x \times L_z \approx 3h \times 1.5h$, corresponding well to the typical spatial size of the large-

scale motions. The dynamics in the minimal box shows that the self-sustaining process of the large-scale streaky structures bears some similarity to the near-wall self-sustaining cycle.

Probably, the most important finding in this thesis is the discovery of this self-sustaining cycle supported only at large scale. The natural extension of the present study is probably to look for the nonlinear traveling waves (Waleffe, 1998, 2001, 2003; Faisst & Eckhardt, 2003; Wedin & Kerswell, 2004) and the unstable periodic orbits (Kawahara & Kida, 2001; Jiménez *et al.*, 2005) embedded in this *turbulent* process. Also, since two similar self-sustaining process have been found in the near-wall and outer regions, the next focus should be taken for the structures scaled by the length scales of the logarithmic layer. The logarithmic layer has been thought as the place where the merger and growth of hairpin vortices occur in a self-similar way (Perry *et al.*, 1986; Tomkins & Adrian, 2003; Adrian, 2007). However, the discovery of an independent self-sustaining cycle in the outer regions now challenges this argument. Recalling the self-similarity of the logarithmic region, assuming the presence of self-sustaining cycles in this region is not a crude approximation. This idea also begins to be supported very recently by Flores & Jiménez (2010), where the bursting process of the logarithmic-layer structures is found. However, more evidences need to be accumulated and this remains for the future studies.

Turbulent skin-friction drag reduction by artificially driven streaks

To verify the predictions of the linear theory, the amplification of the linear optimal forcing has been computed in a direct numerical simulation. As the forcing amplitude is increased, the large amplitude streaks are clearly observed. At two different Reynolds numbers $Re_\tau = 100$ and $Re_\tau = 180$, the most amplified spanwise spacing is found at $\lambda_z \simeq 2h$ which agrees well with that of the large-scale streaky structures. The driven large-scale streaks are found to attenuate the near-wall streamwise vortices with the same mechanism deserved by Schoppa & Hussain (1998), and this results in up to 10.3% of skin-friction drag reduction. The largest amplification involving the significant amount of drag reduction seems to be scaled by the outer units. Also, the examination the control efficiency, which was not addressed in Schoppa & Hussain (1998), shows that the power spent by the forcing is less than 1% of the total drag. This clearly suggests that driving large-scale streaks could be promising method to reduce the skin friction for high Reynolds number turbulent flows. The large amplification of the streaks found here is also applicable to many engineering situations in which the efficient modulation of base or mean flows in the spanwise direction is useful to manipulate flows.

Appendix

Appendix

1 Numerical simulations

The work of the present thesis has required to perform stability analyses, direct numerical simulations, and large-eddy simulations of the incompressible Navier-Stokes equation. The followings are the details of the numerical methods used for the present work. The choice has been, where possible, to use already existing codes.

1.1 The channel flow code

The `channelflow` code is used to conduct direct numerical simulations at low Reynolds numbers in chapter 2 and 5. The code is originally developed by J. F. Gibson (Gibson *et al.*, 2008), and the further details are found in `http://www.channelflow.org/dokuwiki/doku.php`. The code solves the Navier-Stokes equation with the base flow $U(x_2)$ and the rotational form of nonlinear term:

$$\frac{\partial u_i}{\partial x} = 0, \tag{1a}$$

$$\frac{\partial u_i}{\partial t} + \nabla q = \nu \frac{\partial^2 u_i}{\partial x_j \partial x_j} - N_i + G_i, \tag{1b}$$

where

$$N_i \equiv \epsilon_{ijk}(\epsilon_{jik}\frac{\partial u_k}{\partial x_i})u_k + U\frac{\partial u_i}{\partial x_2} + u_2\frac{dU}{dx_2}\delta_{i1}, \tag{1c}$$

$$G_i \equiv (\nu\frac{d^2U}{dx_2^2} - \frac{dP}{dx_1})\delta_{i1} + f_i, \tag{1d}$$

$$q \equiv \frac{p}{\rho} + \frac{1}{2}u_i u_i. \tag{1e}$$

Here, dP/dx_1 is the mean pressure gradient that drives the flow in the channel and f_i is the body forcing term. It has been necessary to implement the body force in the code because the feature is not available in the distributed version. For the spatial discretization, the Fourier-Galerkin method is used for the streamwise and spanwise directions and the Chebyshev-tau method is used for the wall-normal direction. Dealiasing is implemented in the streamwise and spanwise directions using with the 2/3 rule. Time integration is conducted semi-implicitly using a third-order backwards-differentiation time-stepping method. During the simulation, the time step is chosen by keeping the CFL number between 0.2 and 0.4.

1.2 The diablo code

The `diablo` code has been used to carry out large-eddy simulations described in chapter 4, and it has been originally developed by T. R. Bewley and J. Taylor (Bewley *et al.*, 2001). This code integrates the conservative form of the filtered Navier-Stokes equation with the the static Smagorinsky model:

$$\frac{\partial \overline{u}_i}{\partial x} = 0, \tag{2a}$$

$$\frac{\partial \overline{u}_i}{\partial t} + \frac{\partial \overline{u}_i \overline{u}_j}{\partial x_j} = \nu \frac{\partial^2 \overline{u}_i}{\partial x_j \partial x_j} - \frac{\partial \overline{\tau}_{ij}}{\partial x_j} + \frac{1}{\rho} \frac{\partial \overline{q}}{\partial x_i}, \tag{2b}$$

where

$$\overline{q} \equiv \overline{p} + \frac{1}{3} \overline{\tau}_{ij}, \tag{2c}$$

$$\overline{\tau}_{ij} - \frac{\delta_{ij}}{3} \overline{\tau}_{kk} = -2\nu_t \overline{S}_{ij}, \quad \text{with } \nu_t = D(C_S \overline{\Delta})^2 \overline{\mathcal{S}}. \tag{2d}$$

Here, the overbar denotes the filtering action, $\overline{\mathcal{S}} = (2\overline{S}_{ij} \overline{S}_{ij})^{1/2}$, $\overline{\Delta} = (\overline{\Delta}_1 \overline{\Delta}_2 \overline{\Delta}_3)^{1/3}$ is the average length scale of the filter and C_S is the Smagorinsky constant. The van Driest damping function $D = 1 - e^{-(y^+/A^+)^3}$ with $A^+ = 25$ is also imposed to describe the proper physical behavior near the wall.

The filtered flow variables are discretized on the staggered grid system to avoid mesh-related instabilities. The Fourier-Galerkin method is used for the streamwise and span-wise directions and the second-order central difference is used for the wall-normal direction. Dealiasing is implemented in the streamwise and spanwise directions with the 2/3 rule. The wall-normal coordinate is stretched using hyperbolic tangent so that the near-wall region are sufficiently resolved. The filtering is implicitly implemented by the numerical truncation. Therefore, the spectral cut-off filter is applied to the streamwise and spanwise directions, and the box filter is adopted to the wall-normal direction.

Time integration is semi-implicitly conducted using the fractional step method in Kim & Moin (1985). All the terms with the wall-normal derivative are implicitly integrated using the second-order Crank-Nicolson method, and the rest of terms are advanced using the third-order Runge-Kutta method. The CFL number is chosen as 0.5, which ensures the numerical accuracy and stability.

All the numerical simulations are conducted by imposing the constant mass flux across the channel. The constant mass is kept by updating the desired mean pressure gradient dP/dx_1 at each Runge-Kutta substep in the following manner:

$$\frac{dP}{dx_1} = \frac{1}{L_x \times L_z} \int_0^{L_z} \int_0^{L_x} \tau_w \, dxdz + \kappa \left(\frac{1}{V} \int_V \rho u_1 dV - Q_{target} \right), \tag{3}$$

where Q_{target} is the desired mass flux, and κ is the proportional feedback gain. By several trial and error, the proportional gain is chosen as $\kappa = 1.5$.

2 The optimal amplification

The optimal perturbations are efficiently computed by combining the methods described in Schmid & Henningson (2001). The wall-normal direction of the generalized Orr-Sommerfeld-Squire system is discretized using the Chebyshev-collocation method (Weideman & Reddy,

2000) in which the differentiation matrices implicitly includes the boundary conditions. The discretized eigenvalue problem is solved using the `LAPACK` library. The code has been validated in the laminar case (e.g. Lauga & Cossu, 2005).

For the optimal transient growth and harmonic responses, the optimization problems are solved by projecting the physical space solution onto $\mathbb{S}_N = \text{span}\{\mathbf{C}\breve{\mathbf{q}}_1, \mathbf{C}\breve{\mathbf{q}}_2, ..., \breve{\mathbf{q}}_N\}$, where $\breve{\mathbf{q}}_1, \breve{\mathbf{q}}_2, ..., \breve{\mathbf{q}}_N$ are the eigenfunctions of the generalized Orr-Sommerfeld-Squire operator. Therefore, the general solution is constructed as

$$\hat{\mathbf{u}}(t) = \mathbf{C}\mathbf{X}\mathbf{a}(t), \tag{4}$$

where $\mathbf{X} \equiv [\breve{\mathbf{q}}_1, \breve{\mathbf{q}}_2, ..., \breve{\mathbf{q}}_N]$ and $\mathbf{a} = [a_1, a_2, ..., a_N]^T$ is the set of the expansion coefficients.

2.1 Optimal transient growth

The solution for any initial condition $\hat{\mathbf{u}}_0$ is given as $\hat{\mathbf{u}}(t) = \mathbf{C}\mathbf{X}e^{t\Lambda}\mathbf{a}_0$ where $\mathbf{a}_0$ is the projection of the initial condition onto $\mathbb{S}_N$. Using the standard procedure, the optimization problem (2.10) is then converted into the following eigenvalue problem:

$$(\rho \mathbf{X}^H \mathbf{C}^H \mathbf{M} \mathbf{C} \mathbf{X} - \mathbf{X}^H \mathbf{C}^H e^{t\Lambda^H} \mathbf{M} e^{t\Lambda} \mathbf{C} \mathbf{X}) \mathbf{a}_0 = 0. \tag{5}$$

Here, $\mathbf{M}$ is the weight matrix for the numerical integral in the wall-normal direction, and ρ is the eigenvalue corresponding to the Lagrange multiplier. The maximum transient growth $G(t)$ is then given by the largest eigenvalue ρ in (5), and the corresponding eigenvector $\mathbf{a}_0$ becomes the optimal initial condition projected onto $\mathbb{S}_N$. The largest eigenvalue in (5) is found using the power iteration, which significantly reduces the computational cost compared with the singular value decomposition. The code for solving this optimization problem has been validated by Lauga & Cossu (2005), Pujals *et al.* (2009) and Cossu *et al.* (2009).

2.2 Optimal harmonic forcing

The response to harmonic forcing $\hat{\mathbf{f}}(t) = \breve{\mathbf{f}}e^{i\omega_f t}$ is obtained as $\hat{\mathbf{u}}(t) = \mathbf{C}\mathbf{X}(i\omega_f - \Lambda)^{-1}\mathbf{a}_f e^{i\omega_f t}$, where $\mathbf{a}_f$ is the projection of $\breve{\mathbf{f}}$ onto $\mathbb{S}_N$. Similarly to the optimal transient growth, the computation of the optimal harmonic response becomes the following eigenvalue problem:

$$(\rho \mathbf{X}^H \mathbf{C}^H \mathbf{M} \mathbf{C} \mathbf{X} - \mathbf{X}^H \mathbf{C}^H [(i\omega_f - \Lambda)^{-1}]^H \mathbf{M} [(i\omega_f - \Lambda)^{-1}] \mathbf{C} \mathbf{X}) \mathbf{a}_f = 0. \tag{6}$$

The optimal harmonic response $R_{\max}$ is obtained as the largest eigenvalue ρ, and the corresponding eigenvector $\mathbf{a}_f$ is the optimal harmonic forcing projected onto $\mathbb{S}_N$. The eigenvalue problem (6) is also solved using the power iteration. The code for this case has also been developed priori to this thesis, but it has been validated in this thesis by comparing the results of Reddy & Henningson (1993).

2.3 Stochastic forcing

The stochastic responses are computed by directly solving the dual algebraic Lyapunov equations with the discretized operators:

$$\mathbf{A}\mathbf{X}_\infty + \mathbf{X}_\infty \mathbf{A}^\dagger + \mathbf{B}\mathbf{B}^\dagger = 0, \tag{7a}$$

$$\mathbf{A}^\dagger \mathbf{Y}_\infty + \mathbf{Y}_\infty \mathbf{A} + \mathbf{C}^\dagger \mathbf{C} = 0. \tag{7b}$$

The solutions of these algebraic Lyapunov equations are solved using the `lyap` function in `matlab`. The adjoint operators are defined with the standard inner product $(\hat{\mathbf{u}}, \hat{\mathbf{v}}) = \int_{-h}^{h} \hat{\mathbf{u}}^H \hat{\mathbf{v}} dy$, and they are given as follows:

$$\mathbf{A}^\dagger = \left[\begin{array}{cc} \Delta^{-1} \mathcal{L}_{OS}^\dagger & i\beta U' \\ 0 & \mathcal{L}_{SQ}^\dagger \end{array} \right], \quad \mathbf{B}^\dagger = \left[\begin{array}{cc} -i\alpha \mathcal{D} \Delta^{-1} & -i\beta \\ -ik^2 \Delta^{-1} & 0 \\ -i\beta \mathcal{D} \Delta^{-1} & i\alpha \end{array} \right], \tag{8a}$$

$$\mathbf{C}^\dagger = \frac{1}{k^2} \left[\begin{array}{ccc} i\alpha \mathcal{D} & k^2 & i\beta \mathcal{D} \\ i\beta & 0 & -i\alpha \end{array} \right],$$

with

$$\mathcal{L}_{OS}^\dagger = i\alpha U \Delta + 2i\alpha U' \mathcal{D} + \nu_T \Delta^2 + 2\nu_T' \Delta \mathcal{D} + \nu_T{''}(\mathcal{D}^2 + k^2), \tag{8b}$$

$$\mathcal{L}_{SQ}^\dagger = i\alpha U + \nu_T \Delta + \nu_T' \mathcal{D}. \tag{8c}$$

The code for computing the stochastic response has been entirely developed and validated by the author. In particular, the results have been validated by comparing with the ones of Jovanović & Bamieh (2005).

3 Stability of finite amplitude streaks

3.1 Two-dimensional eddy-viscosity simulation

A two-dimensional eddy-viscosity simulation code has been written by the author to compute the finite amplitude streaks used as base flow in chapter 3. The code solves the incompressible Reynolds-averaged Navier-Stokes equation with the eddy viscosity dependent only on wall-normal direction, and it is written in the following form of wall-normal velocity and vorticity:

$$\frac{\partial}{\partial t} \left(\frac{\partial^2 u_2}{\partial x_k \partial x_k} \right) = h_v + \frac{\partial^2}{\partial x_k \partial x_k} \left(\frac{\partial}{\partial x_j} \nu_T \left(\frac{\partial u_2}{\partial x_j} + \frac{\partial u_j}{\partial x_2} \right) \right), \tag{9a}$$

$$\frac{\partial \omega_2}{\partial t} = h_{\omega_y} + \nu_T \frac{\partial^2 \omega_2}{\partial x_j \partial x_j} + \frac{\partial \nu_T}{\partial x_2} \frac{\partial \omega_2}{\partial x_2}, \tag{9b}$$

where

$$h_v = \left(\frac{\partial^2}{\partial x_1 \partial x_1} + \frac{\partial^2}{\partial x_3 \partial x_3} \right) H_2 - \frac{\partial}{\partial x_2} \left(\frac{\partial H_1}{\partial x_1} + \frac{\partial H_3}{\partial x_3} \right), \tag{9c}$$

$$h_{\omega_y} = \frac{\partial H_1}{\partial x_3} - \frac{\partial H_3}{\partial x_1} \tag{9d}$$

with

$$H_i = \epsilon_{ijk} \epsilon_{ijk} U_j \omega_k + u_j \Omega_k + \epsilon_{ijk} u_j \omega_k. \tag{9e}$$

Here, u_i the perturbation velocity, ω_i the perturbation vorticity, $U_i = (U(y), 0, 0)$ the base flow and Ω_i is the vorticity related to base flow. The spatial discretization of (9) is conducted using the Fourier-Galerkin method for the streamwise and spanwise directions and the Chebyshev-collocation method for the wall-normal direction. Dealiasing is implemented in the streamwise and spanwise directions with the 3/2 rule. Time-integration is performed using the third-order Runge-Kutta method. The code is carefully validated in the laminar case ($\nu_T = \nu$) by comparing the results with those by the `channelflow` code and it also shows very good agreement with the results in Reddy *et al.* (1998).

3.2 Stability of the streaks

The stability of the nonlinearly developed streaks is studied using the code developed in Cossu & Brandt (2004). The code computes the temporal eigenvalue ω of the following linearized Navier-Stokes equation for the perturbation $(\hat{u}(y,z), \hat{v}(y,z), \hat{w}(y,z))e^{i(\alpha x - \omega t)}$ around the streaky base flow $(U(y,z), 0, 0)$:

$$(-i\omega + i\alpha U)\nabla^2\hat{v} + i\alpha(U_{zz} - U_{yy} + 2U_z\partial_z)\hat{v} - 2i\alpha(U_z\partial_y + U_{yz})\hat{w} \tag{10a}$$
$$-\nu_T\nabla^4\hat{v} - 2\nu_T'\nabla^2\partial y + \nu_T"(\nabla^2 - 2\partial_y^2)\hat{v} = 0,$$

$$(-i\omega + i\alpha U)\hat{\eta} + (U_y\partial_z + U_{yz} - U_z\partial_y)\hat{v} + U_{zz}\hat{w} - (\nu_T\nabla^2 + \nu_T'\partial_y)\hat{\eta} = 0, \tag{10b}$$

$$(\alpha^2 - \partial_z^2)\hat{w} = i\alpha\eta + \partial_y\partial_z\hat{v}, \tag{10c}$$

where $\nabla^2 = \partial_y^2 + \partial_z^2 - \alpha^2$, $\hat{v}$ the wall-normal velocity, and $\hat{\eta}$ is the wall-normal vorticity. If the streaky base flow is periodic in the spanwise direction, the Floquet theory is applied to (10). Then, the following expansion is admitted with the periodicity $\lambda_z = 2\pi/\beta_0$ of the base flow for the fundamental varicose mode:

$$\hat{v}(y,z) = \sum_{n=0}^{N_z} \tilde{v}_n(y)\cos n\beta_0 z, \quad \hat{\eta}(y,z) = \sum_{n=0}^{N_z} \tilde{\eta}_n(y)\sin n\beta_0 z. \tag{11}$$

Similarly, the fundamental sinuous mode is expanded as

$$\hat{v}(y,z) = \sum_{n=0}^{N_z} \tilde{v}_n(y)\sin n\beta_0 z, \quad \hat{\eta}(y,z) = \sum_{n=0}^{N_z} \tilde{\eta}_n(y)\cos n\beta_0 z. \tag{12}$$

For the subharmonic case, the same consideration is applicable, but the spanwise periodicity of the disturbances should be twice that of base flow. Therefore, the subharmonic varicose mode is written as

$$\hat{v}(y,z) = \sum_{n=0}^{N_z} \tilde{v}_n(y)\cos\left(\frac{n+1}{2}\right)\beta_0 z, \quad \hat{\eta}(y,z) = \sum_{n=0}^{N_z} \tilde{\eta}_n(y)\sin\left(\frac{n+1}{2}\right)\beta_0 z, \tag{13}$$

while the sinuous mode becomes as

$$\hat{v}(y,z) = \sum_{n=0}^{N_z} \tilde{v}_n(y)\sin\left(\frac{n+1}{2}\right)\beta_0 z, \quad \hat{\eta}(y,z) = \sum_{n=0}^{N_z} \tilde{\eta}_n(y)\cos\left(\frac{n+1}{2}\right)\beta_0 z. \tag{14}$$

In order to solve the temporal eigenvalue problem (10) numerically, the Chebyshev series expansion is used for the wall-normal direction. Also, the terms requiring convolution in the spanwise spectral space are computed in the physical space. Finally, the resulting matrix eigenvalue problem is solved using `ARPACK` library, which implements the implicitly restarted Arnoldi method.

Bibliography

ADRIAN, R. J. 2007 Hairpin vortex organization in wall turbulence. *Phys. Fluids.* **19**, 041301.

ADRIAN, R. J., MEINHART, C. D. & TOMKINS, C. D. 2000 Vortex organization in the outer region of the turbulent boundary layer. *J. Fluid. Mech.* **422**, 1–54.

DEL ÁLAMO, J.C. & JIMÉNEZ, J. 2003 Spectra of the very large anisotropic scales in turbulent channels. *Phys. Fluids* **15**, L41.

DEL ÁLAMO, J. C. & JIMÉNEZ, J. 2006 Linear energy amplification in turbulent channels. *J. Fluid Mech.* **559**, 205–213.

DEL ÁLAMO, J. C., JIMÉNEZ, J., ZANDONADE, P. & MOSER, R. D. 2004 Scaling of the energy spectra of turbulent channels. *J. Fluid Mech.* **500**, 135–144.

DEL ÁLAMO, J. C., JIMÉNEZ, J., ZANDONADE, P. & MOSER, R. D. 2006 Self-similar vortex clusters in the turbulent logarithmic region. *J. Fluid Mech.* **561**, 329–358.

ANDERSSON, P., BRANDT, L., BOTTARO, A. & HENNINGSON, D. 2001 On the breakdown of boundary layers streaks. *J. Fluid Mech.* **428**, 29–60.

BAILEY, S. C. C. & SMITS, A. J. 2010 Experimental investigation of the structure of large- and very large-scale motions in turbulent pipe flow. *J. Fluid Mech.* **651**, 339–356.

BALAKUMAR, B. J. & ADRIAN, R. J. 2007 Large- and very-large-scale motions in channel and boundary layer flows. *Phil. Trans. R. Soc. A* **365**, 665–681.

BALCKWELDER, R. F. & KOVASZNAY, L. S. G. 1972 Time scales and correlations in a turbulent boundary layer. *Phys. Fluids.* **15**, 1545–1554.

BAMIEH, B. & DAHLEH, M. 2001 Energy amplification in channel flows with stochastic excitation. *Phys. Fluids* **13**, 3258–69.

BEWLEY, T. R., MOIN, P. & TEMAM, R. 2001 Dns-based predictive control of turbulence: an optimal benchmark for feedback algorithms. *J. Fluid Mech.* **447**, 179–225.

BULLOCK, K. J., COOPER, R. E., & ABERNATHY, F. H. 1978 Structural similarity in radial correlations and spectra of longitudinal velocity fluctuations in pipe flow. *J. Fluid Mech.* **88**, 585–608.

BUTLER, K. M. & FARRELL, B. F. 1992 Three-dimensional optimal perturbations in viscous shear flow. *Phys. Fluids A* **4**, 1637–1650.

BUTLER, K. M. & FARRELL, B. F. 1993 Optimal perturbations and streak spacing in wall-bounded turbulent shear flow. *Phys. Fluids* **5**, 774–777.

CESS, R. D. 1958 A survey of the literature on heat transfer in turbulent tube flow. Research Report 8–0529–R24. Westinghouse.

CHOI, H., MOIN, P. & KIM, J. 1993 Direct numerical simulation of turbulent flow over riblets. *J. Fluid Mech.* **255**, 503–539.

CHOI, H., MOIN, P. & KIM, J. 1994 Active turbulence control for drag reduction in wall-bounded flows. *J. Fluid Mech.* **262**, 75–110.

CORRSIN, S. & KISTLER, A. L. 1954 The free-stream boundaries of turbulent flows. *Technical Note* **3133**, 120–130.

COSSU, C. & BRANDT, L. 2002 Stabilization of Tollmien-Schlichting waves by finite amplitude optimal streaks in the Blasius boundary layer. *Phys. Fluids* **14**, L57–L60.

COSSU, C. & BRANDT, L. 2004 On Tollmien–Schlichting waves in streaky boundary layers. *Eur. J. Mech./B Fluids* **23**, 815–833.

COSSU, C., CHEVALIER, M. & HENNINGSON, D.S. 2007 Optimal secondary energy growth in a plane channel flow. *Phys. Fluids* **19**, 058107.

COSSU, C., PUJALS, G. & DEPARDON, S. 2009 Optimal transient growth and very large scale structures in turbulent boundary layers. *J. Fluid Mech.* **619**, 79–94.

DUGUET, Y., WILLIS, A. P. & KERSWELL, R. R. 2008 Transition in pipe flow: the saddle structure on the boundary of turbulence. *J. Fluid Mech.* **613**, 255–274.

ECKHARDT, B., SCHNEIDER, T.M., HOF, B. & WESTERWEEL, J. 2007 Turbulence Transition in Pipe Flow. *Ann. Rev. Fluid Mech.* **39**, 447.

ELLINGSEN, T. & PALM, E. 1975 Stability of linear flow. *Phys. Fluids* **18**, 487.

ELOSFSSON, P. A., KAWAKAMI, M. & ALFREDSSON, P. H. 1999 Experiments on the stability of streamwise streaks in plane poiseuille flow. *Phys. Fluids* **11**, 915.

FAISST, H. & ECKHARDT, B. 2003 Travelling waves in pipe flow. *Phys. Rev. Lett.* **91**, 224502.

FALCO, R. E. 1977 Coherent motions in the outer region of turbulent boundary layers. *Phys. Fluids* **20**, S124–S132.

FARRELL, B. F. & IOANNOU, P. J. 1993*a* Optimal excitation of three-dimensional perturbations in viscous constant shear flow. *Phys. Fluids* **5**, 1390–1400.

FARRELL, B. F. & IOANNOU, P. J. 1993*b* Stochastic forcing of the linearized Navier-Stokes equation. *Phys. Fluids A* **5**, 2600–9.

FARRELL, B. F. & IOANNOU, P. J. 1994 Variance maintained by the stochastic forcing of non-normal dynamical systems associated with linearly stable shear flows. *Phys. Rev. Lett.* **72**, 1188–1191.

FARRELL, B. F. & IOANNOU, P. J. 1996 Generalized stability theory. *J. Atmos. Sci.* **53**, 2025–2053.

FARRELL, B. F. & IOANNOU, P. J. 1998 Perturbation structure and spectra in turbulent channel flow. *Theoret. Comput. Fluid Dyn.* **11**, 237–250.

FLORES, O. & JIMÉNEZ, J. 2006 Effect of wall-boundary disturbances on turbulent channel flows. *J. Fluid Mech.* **566**, 357–376.

FLORES, O. & JIMÉNEZ, J 2010 Hierarchy of minimal flow units in the logarithmic layer. *Phys. Fluids* **22**, 071704.

FLORES, O., JIMÉNEZ, J. & DEL ÁLAMO, J.C. 2007 Vorticity organization in the outer layer of turbulent channels with disturbed walls. *J. Fluid Mech.* **591**, 145–154.

FRANSSON, J., BRANDT, L., TALAMELLI, A. & COSSU, C. 2004 Experimental and theoretical investigation of the non-modal growth of steady streaks in a flat plate boundary layer. *Phys. Fluids* **16**, 3627–3638.

FRANSSON, J., BRANDT, L., TALAMELLI, A. & COSSU, C. 2005 Experimental study of the stabilisation of Tollmien-Schlichting waves by finite amplitude streaks. *Phys. Fluids* **17**, 054110.

FRANSSON, J., TALAMELLI, A., BRANDT, L. & COSSU, C. 2006 Delaying transition to turbulence by a passive mechanism. *Phys. Rev. Lett.* **96**, 064501.

GIBSON, J. F., HALCROW, J. & CVITANOVIC, P. 2008 Visualizing the geometry of state space in plane Couette flow. *J. Fluid Mech.* **611**, 107–130.

GIBSON, J. F., HALCROW, J. & CVITANOVIC, P. 2009 Equilibrium and traveling-wave solutions of plane couette flow. *J. Fluid Mech.* **638**, 243–266.

GUALA, M., HOMMEMA, S. E. & ADRIAN, R. J. 2006 Large-scale and very-large-scale motions in turbulent pipe flow. *J. Fluid Mech.* **554**, 521–541.

HAMILTON, J.M., KIM, J. & WALEFFE, F. 1995 Regeneration mechanisms of near-wall turbulence structures. *J. Fluid Mech* **287**, 317–348.

HÄRTEL, C. & KLEISER, L. 1998 Analysis and modelling of subgrid-scale motions in near-wall turbulence. *J. Fluid Mech* **356**, 327–352.

HEAD, M. R. & BANDYOPADHAY, P. 1981 New aspects of turbulent boundary-layer structure. *J. Fluid Mech* **107**, 297–338.

HŒPFFNER, J., BRANDT, L. & HENNINGSON, D. S. 2005 Transient growth on boundary layer streaks. *J. Fluid Mech.* **537**, 91–100.

HOYAS, S. & JIMÉNEZ, J. 2006 Scaling of the velocity fluctuations in turbulent channels up to $re_\tau = 2003$. *Phys. Fluids* **18**, 011702.

HUNT, J. C. R. & MORRISON, J. F. 2000 Eddy structure in turbulent boundary layer. *Eur. J. Mech. B* **19**, 673–694.

HUTCHINS, N. & MARUSIC, I. 2007a Evidence of very long meandering features in the logarithmic region of turbulent boundary layers. *J. Fluid Mech.* **579**, 1–28.

HUTCHINS, N. & MARUSIC, I. 2007b Large-scale influences in near-wall turbulence. *Phil. Trans. R. Soc. A* **365**, 647–664.

HWANG, Y. & COSSU, C. 2010a Amplification of coherent streaks in the turbulent Couette flow: an input-output analysis at low Reynolds number. *J. Fluid Mech.* **643**, 333–348.

HWANG, Y. & COSSU, C. 2010b Linear non-normal energy amplification of harmonic and stochastic forcing in the turbulent channel flow. *J. Fluid Mech.* In press.

HWANG, Y. & COSSU, C. 2010c Self-sustained process at large scales in turbulent channel flow. *Phys. Rev. Lett.* **105**, 044505.

IUSO, G., ONORATO, M., SPAZZINI, P. G. & DI CICCA, G. M. 2002 Wall turbulence manipulation by large-scale streamwise vortices. *J. Fluid Mech.* **473**, 23–58.

JIMÉNEZ, J. 1998 The largest scales of turbulent wall flows. Annual research briefs. Center for Turbulence Research, Stanford University.

JIMÉNEZ, J. 2007 Recent developments on wall-bounded turbulence. *Rev. R. Acad. Cien. Serie A Mat.* **101**, 187–203.

JIMÉNEZ, J., DEL ÁLAMO, J.C. & FLORES, O. 2004 The large-scale dynamics of near-wall turbulence. *J. Fluid Mech.* **505**, 179–199.

JIMÉNEZ, J. & HOYAS, S. 2008 Turbulent fluctuations above the buffer layer of wall-bounded flows. *J. Fluid Mech.* **611**, 215–236.

JIMÉNEZ, J., KAWAHARA, G., SIMENS, M. P., NAGATA, M. & SHIBA, M. 2005 *Phys. Fluids* **17**, 015105.

JIMÉNEZ, J. & MOIN, P. 1991 The minimal flow unit in near-wall turbulence. *J. Fluid Mech.* **225**, 213–240.

JIMÉNEZ, J. & PINELLI, A. 1999 The autonomous cycle of near-wall turbulence. *J. Fluid Mech.* **389**, 335–359.

JIMÉNEZ, J. & SIMENS, M. P. 2001 Low-dimensional dynamics of a turbulent wall flow. *J. Fluid Mech.* **435**, 81–91.

JOVANOVIĆ, M. R. & BAMIEH, B. 2005 Componentwise energy amplification in channel flow. *J. Fluid Mech.* **543**, 145–83.

VON KÁRMÁN, T. 1930 Mechanische aehnlichkeit und turbulenz. *Nachr. Ges. Wiss. Göttingen, Math. Phys. KL.* pp. 58–68, english translation NACA TM 611.

KAWAHARA, G. & KIDA, S. 2001 Periodic motion embedded in plane Couette turbulence: regeneration cycle and burst. *J. Fluid Mech.* **449**, 291–300.

KENDALL, J. M. 1985 Experimental study of disturbances produced in a pre-transitional laminar boundary layer by weak free-stream turbulence. *AIAA Paper* **85**, 1695.

KIM, J. & MOIN, P 1985 Application of a fractional-step method to incompressible navier-stokes equations. *J. Comp. Phys.* **59**, 308–323.

KIM, J., MOIN, P. & MOSER, R. D. 1987 Turbulence statistics in fully developed channel flow at low reynolds number. *J. Fluid Mech.* **177**, 133–166.

KIM, K. C. & ADRIAN, R. 1999 Very large-scale motion in the outer layer. *Phys. Fluids* **11** (2), 417–422.

KITOH, O., NAKABAYASHI, K. & NISHIMURA, F. 2005 Experimental study on mean velocity and turbulence characteristics of plane Couette flow: low-Reynolds-number effects and large longitudinal vortical structures. *J. Fluid Mech.* **539**, 199.

KITOH, O. & UMEKI, M. 2008 Experimental study on large-scale streak structure in the core region of turbulent plane Couette flow. *Phys. Fluids* **20**, 025107.

KLINE, S. J., REYNOLDS, W. C., SCHRAUB, F. A. & RUNSTADLER, P. W. 1967 The structure of turbulent boundary layers. *J. Fluid Mech.* **30**, 741–773.

KOMMINAHO, J., LUNDBLADH, A. & JOHANSSON, A. V. 1996 Very large structures in plane turbulent Couette flow. *J. Fluid Mech.* **320**, 259–285.

KOVASZNAY, L. S. G., KIBENS, V. & BLACKWELDER, R. F. 1970 Large-scale motion in the intermittent region of a turbulent boundary layer. *J. Fluid Mech.* **41**, 283–325.

KRAVCHENKO, A. G., CHOI, H. & MOIN, P. 1993 On the relation of near-wall streamwise vortices to wall skin friction in turbulent boundary layers. *Phys. Fluids A* **5**, 3307.

LANDAHL, M. T. 1980 A note on an algebraic instability of inviscid parallel shear flows. *J. Fluid Mech.* **98**, 243–251.

LANDAHL, M. T. 1990 On sublayer streaks. *J. Fluid Mech.* **212**, 593–614.

LAUGA, E. & COSSU, C. 2005 A note on the stability of slip channel flows. *Phys. Fluids* **17**, 088106.

LUNDBLADH, A., HENNINGSON, D. S. & JOHANSSON, A. V. 1992 An efficient spectral integration method for the solution of the Navier–Stokes equations. *Tech. Rep.*. FFA, the Aeronautical Research Institute of Sweden.

MATHIS, R., HUTCHINS, N. & MARUSIC, I. 2009 Large-scale amplitude modulation of the small-scale structures in turbulent boudnary layers. *J. Fluid. Mech.* **628**, 311–337.

MATSUBARA, M. & ALFREDSSON, P. H. 2001 Disturbance growth in boundary layers subjected to free stream turbulence. *J. Fluid. Mech.* **430**, 149–168.

MCKEON, B. J., ZAGAROLA, M. V. & SMITS, A. J. 2005 A new friction factor relationship for fully developed pipe flow. *J. Fluid Mech.* **538**, 429–443.

MILLIKAN, C.B. 1938 A critical discussion of turbulent flows in channels and circular tubes. In *Proceedings of the Fifth International Congress of Applied Mechanics*.

MOFFATT, H. K. 1967 The interaction of turbulence with strong wind shear. In *Proc. URSI-IUGG Coloq. on Atoms. Turbulence and Radio Wave Propag.* (ed. A.M. Yaglom & V. I. Tatarsky), pp. 139–154. Moscow: Nauka.

MONTY, J. P., HUTCHINS, N., NG, H. C. H., MARUSIC, I. & CHONG, M. S. 2009 A comparison of turbulent pipe, channel and boundary layer flows. *J. Fluid Mech.* **632**, 431442.

MORRISON, W. R. B. & KRONAUER, R. E. 1969 Structural similarity for fully developed turbulence in smooth tubes. *J. Fluid Mech.* **39**, 117–141.

MURLIS, J., TAI, H. M. & BRADSHAW, P. 1982 The structure of turbulent boundary layers at low reynolds numbers. *J. Fluid Mech.* **122**, 13–56.

NAGATA, M. 1990 Three-dimensional finite-amplitude solutions in plane Couette flow: bifurcation from infinity. *J. Fluid Mech.* **217**, 519–527.

NICKELS, T. B. 2010 On the three dimensional structure of the turbulent boundary layer. In *Workshop on Turbulent Boundary Layer*. Stockholm, Sweden, April 6-29.

ORSZAG, S. A. 1971 Accurate solution of the Orr–Sommerfeld stability equation. *J. Fluid Mech.* **50**, 689–703.

PANTON, R.L. 2001 Overview of the self-sustaining mechanisms of wall turbulence. *Progress in Aerospace Sciences* **37** (4), 341–384.

PARK, J., HWANG, Y. & COSSU, C. 2010 On the stability of large-scale streaks in the turbulent Couette and Poiseulle flows. *submitted to C. R. Mècanique* .

PATEL, V. C. & HEAD, R. 1969 Some observations on skin friction and velocity profiles in fully developed pipe and channel flows. *J. Fluid Mech.* **38**, 181–201.

PERRY, A. E. & CHONG, M. S. 1982 On the mechanism of turbulence. *J. Fluid Mech.* **119**, 173–217.

PERRY, A. E., HENBEST, S. & CHONG, M. S. 1986 A theoretical and experimental study of wall turbulence. *J. Fluid Mech.* **165**, 163–199.

PERRY, A. E. & MARUSIC, I. 1995 A wall-wake model for the turbulence structure of boundary layers. part 1. extension of the attached eddy hypothesis. *J. Fluid Mech.* **298**, 361–388.

PUJALS, G., COSSU, C. & DEPARDON, S. 2010*a* Forcing large-scale coherent streaks in a zero pressure gradient turbulent boundary layer. *J. Turb.* **11** (25), 1–13.

PUJALS, G., DEPARDON, S. & COSSU, C. 2010*b* Drag reduction of a 3D bluff body using coherent streamwise streaks. *Exp. Fluids* In press.

PUJALS, G., GARCÍA-VILLALBA, M., COSSU, C. & DEPARDON, S. 2009 A note on optimal transient growth in turbulent channel flows. *Phys. Fluids* **21**, 015109.

REDDY, S. C. & HENNINGSON, D. S. 1993 Energy growth in viscous channel flows. *J. Fluid Mech.* **252**, 209–238.

REDDY, S. C., SCHMID, P. J., BAGGETT, J. S. & HENNINGSON, D. S. 1998 On the stability of streamwise streaks and transition thresholds in plane channel flows. *J. Fluid Mech.* **365**, 269–303.

REDDY, S. C., SCHMID, P. J. & HENNINGSON, D. S. 1993 Pseudospectra of the Orr-Sommerfeld operator. *SIAM J. Appl. Math.* **53**, 1547.

REYNOLDS, W. C. & HUSSAIN, A. K. M. F. 1972 The mechanics of an organized wave in turbulent shear flow. Part 3. Theoretical models and comparisons with experiments. *J. Fluid Mech.* **54** (02), 263–288.

REYNOLDS, W. C. & TIEDERMAN, W. G. 1967 Stability of turbulent channel flow, with application to Malkus's theory. *J. Fluid Mech.* **27** (02), 253–272.

ROBINSON, S. K. 1991 Coherent motions in the turbulent boundary layer. *Ann. Rev. Fluid Mech.* **23**, 601–639.

ROMANOV, V. A. 1973 Nonlinear global modes in three-dimensional boundary layers. *Translated in Funktional Anal. Applics.* **137-146**.

SAGAUT, P. 1998 *Large eddy simulation for incompressible flows: an introduction.* Springer.

SCHMID, P.J. 2007 Nonmodal stability theory. *Annu. Rev. Fluid Mech.* **39**, 129–162.

SCHMID, P.J. & HENNINGSON, D. S. 1994 Optimal energy density growth in Hagen–Poiseuille flow. *J. Fluid Mech.* **277**, 197–225.

SCHMID, P. J. & HENNINGSON, D. S. 2001 *Stability and Transition in Shear Flows.* New York: Springer.

SCHNEIDER, T. M., ECKHARDT, B. & YORKE, J. A. 2007 Turbulence transition and the edge of chaos in pipe flow. *Phys. Rev. Lett.* **99**, 034502.

SCHOPPA, S. & HUSSAIN, F. 1998 A large-scale control strategy for drag reduction in turbulent boundary layers. *Phys. Fluids* **10**, 1049.

SCHOPPA, W. & HUSSAIN, F. 2002 Coherent structure generation in near-wall turbulence. *J. Fluid Mech.* **453**, 57–108.

SMAGORINSKY, J. 1963 General circulation experiments with the primitive equations: I. the basic equations. *Mon. Weather Rev.* **91**, 99–164.

SMITH, J. R. & METZLER, S. P. 1983 The characteristics of low-speed streaks in the near-wall region of a turbulent boundary layer. *J. Fluid Mech.* **129**, 27–54.

TENNEKES, H. & LUMLEY, J. L. 1967 *A first course in turbulence.* MIT Press.

TOH, S. & ITANO, T. 2005 Interaction between a large-scale structure and near-wall structures in channel flow. *J. Fluid Mech.* **524**, 249–262.

TOMKINS, C. D. & ADRIAN, R. J. 2003 Spanwise structure and scale growth in turbulent boundary layers. *J. Fluid Mech.* **490**, 37–74.

TOMKINS, C. D. & ADRIAN, R. J. 2005 Energetic spanwise modes in the logarithmic layer of a turbulent boundary layer. *J. Fluid Mech.* **545**, 141–162.

TOWNSEND, A. 1976 *The structure of turbulent shear flow*. Cambridge U. Press.

TREFETHEN, L. N., TREFETHEN, A. E., REDDY, S. C. & DRISCOLL, T. A. 1993 A new direction in hydrodynamic stability: Beyond eigenvalues. *Science* **261**, 578–584.

TSUKAHARA, T., , IWAMOTO, K. & KAWAMURA, H. 2007 POD analysis of large-scale structures through DNS of turbulence Couette flow. In *Advances in Turbulence XI.*, pp. 245–247. Springer.

TSUKAHARA, T., KAWAMURA, H. & SHINGAI, K. 2006 Dns of turbulent Couette flow with emphasis on the large-scale structure in the core region. *J. Turbulence.* **42**.

VISWANATH, D. 2007 Recurrent motions within plane couette turbulence. *J. Fluid Mech.* **580**, 339–358.

VISWANATH, D. 2009 The dynamics of transition to turbulence in plane couette flow. *Phil. Trans. Roy. Soc.* **367**, 561–576.

WALEFFE, F. 1995 Hydrodynamic stability and turbulence: Beyond transients to a self-sustaining process. *Stud. Appl. Math.* **95**, 319–343.

WALEFFE, F. 1997 On a self-sustaining process in shear flows. *Phys. Fluids* **9**, 883–900.

WALEFFE, F. 1998 Three-dimensional coherent states in plane shear flows. *Phys. Rev. Lett.* **81**, 4140–4143.

WALEFFE, F. 2001 Exact coherent structures in channel flow. *J. Fluid Mech.* **435**, 93–102.

WALEFFE, F. 2003 Homotopy of exact coherent structures in plane shear flows. *Phys. Fluids* **15**, 1517–1534.

WALSH, M. J. 1983 Riblets as a viscous drag reduction technique. *AIAA J.* **21** (4), 485–486.

WEDIN, H. & KERSWELL, R.R. 2004 Exact coherent structures in pipe flow: travelling wave solutions. *J. Fluid Mech.* **508**, 333–371.

WEIDEMAN, J. A. C. & REDDY, S. C. 2000 A MATLAB Differentiation Matrix Suite. *ACM Trans. Math. Soft.* **26**, 465–519.

WILLIS, A. P., HWANG, Y. & COSSU, C. 2010 Optimally amplified large-scale streaks and drag reduction in the turbulent pipe flow. *Phys. Rev. E* In press.

WILLIS, A. P. & KERSWELL, R. R. 2008 Coherent structures in local and global pipe turbulence. *Phys. Rev. Lett.* **100**, 124501.

ZANG, T. A. 1991 Numerical simulation of the dynamics of turbulent boundary layers: Perspectives of a transition simulator. *Phil. Trans. R. Soc. Lond. A* **336**, 95–102.

ZHOU, J., ADRIAN, R. J., BALACHANDAR, S. & KENDALL, T. M. 1999 Mechanisms for generating coherent packets of hairpin vortices in channel flow. *J. Fluid. Mech.* **387**, 353–396.

ZHOU, K., DOYLE, J.C. & GLOVER, K. 1996 *Robust and Optimal Control*. New York: Prentice Hall.

Articles

1

Article 1

Amplification of coherent streaks in the turbulent Couette flow: an input–output analysis at low Reynolds number

YONGYUN HWANG AND CARLO COSSU†

Laboratorie d'Hydrodynamique (LadHyX), CNRS-École Polytechnique, F-91128 Palaiseau, France

We compute the optimal response of the turbulent Couette mean flow to initial conditions, harmonic and stochastic forcing at $Re = 750$. The equations for the coherent perturbations are linearized near the turbulent mean flow and include the associated eddy viscosity. The mean flow is found to be linearly stable but it has the potential to amplify steamwise streaks from streamwise vortices. The most amplified structures are streamwise uniform and the largest amplifications of the energy of initial conditions and of the variance of stochastic forcing are realized by large-scale streaks having spanwise wavelengths of $4.4h$ and $5.2h$ respectively. These spanwise scales compare well with the ones of the coherent large-scale streaks observed in experimental realizations and direct numerical simulations of the turbulent Couette flow. The optimal response to the harmonic forcing, related to the sensitivity to boundary conditions and artificial forcing, can be very large and is obtained with steady forcing of structures with larger spanwise wavelength ($7.7h$). The optimal large-scale streaks are furthermore found proportional to the mean turbulent profile in the viscous sublayer and up to the buffer layer.

1. Introduction

Streamwise streaks, i.e. narrow regions where the streamwise velocity is larger or smaller than the average, are ubiquitous in wall-bounded turbulent flows. Kline *et al.* (1967) observed them in the near-wall region of turbulent boundary layers where they have a characteristic spanwise spacing of about one hundred wall units (Moin & Kim 1982; Smith & Metzler 1983). These streaks are now understood as a part of self-sustained processes playing a key role in the production of near-wall turbulence and skin friction (Jang, Benney & Gran 1986; Jiménez & Moin 1991; Hamilton, Kim & Waleffe 1995; Waleffe 1995; Schoppa & Hussain 2002). Further investigations have revealed the existence of coherent large-scale streaks extending in the outer layer and scaling with outer units. The turbulent Couette flow is one of the first cases where these large-scale streaks have been observed. Lee & Kim (1991) found large-scale quasi-steady coherent streaks in the direct numerical simulation (DNS) of the fully

† Email address for correspondence: carlo.cossu@ladhyx.polytechnique.fr

developed turbulent Couette flow at $Re = 3000$ (where Re is based on the channel half-width h and half of the velocity difference between the walls). These streaks, of spanwise wavelength $\lambda_z \approx 4h$, occupied half of the spanwise size ($L_z = 8\pi h/3$) of the computational domain and its whole streamwise extension ($L_x = 4\pi h$). The existence of these large-scale streaks was then confirmed by the experiments of Tillmark & Alfredsson (1994). In order to understand whether the characteristics of these large-scale structures were affected by the size of the computational box, Komminaho, Lundbladh & Johansson (1996) repeated the computations in a large domain ($L_x = 28\pi/h$ and $L_z = 8\pi h$) at $Re = 750$. They found large-scale coherent streaks with the same spanwise wavelength ($\approx 4h$) of those of Lee & Kim (1991) but more unsteady and extending more than $30h$ in the streamwise direction. They also found that resolving these large-scale structures is essential to obtain accurate turbulent statistics. Kitoh, Nakabayashi & Nishimura (2005), Tsukahara, Kawamura & Shingai (2006), Tsukahara, Iwamoto & Kawamura (2007) and Kitoh & Umeki (2008) also found large-scale streaky structures at higher Reynolds numbers with typical size $\lambda_z \approx 4.2h$–$5h$. Large-scale coherent streaks have also been observed in the turbulent pipe (Kim & Adrian 1999), in the turbulent plane Poiseuille flow (del Álamo & Jiménez 2003) and in the turbulent boundary layer (Tomkins & Adrian 2003, 2005; Hutchins & Marusic 2007*a*). At high Reynolds numbers, these large-scale structures dominate the streamwise turbulent kinetic energy throughout the logarithmic region (Tomkins & Adrian 2003, 2005), and modulate the cycles of near-wall structures (Hutchins & Marusic 2007*b*).

In free shear layers, the appearance of large-scale coherent structures has been related to the linear inflectional instability of the turbulent mean profile (Ho & Huerre 1984). This explanation is, however, not applicable to the large-scale coherent streaks observed in wall-bounded turbulent shear flows, such as the Couette, Poiseuille and boundary layer flows, because the mean velocity profiles of these flows are all linearly stable. For all these flows, the related mechanism observed in the laminar case is the 'lift-up' effect (Moffatt 1967; Ellingsen & Palm 1975; Landahl 1980, 1990), by which low-energy streamwise vortices are converted into high-energy streaks in the presence of shear. The growth of the streaks by lift-up is algebraic and unbounded in inviscid flows, but is only transient in viscous flows (Gustavsson 1991). The streaks transient growth is related to the non-normality of the Navier–Stokes operator and can be maximized by using optimal vortices as initial conditions (see e.g. Trefethen *et al.* 1993; Farrell & Ioannou 1996; Schmid & Henningson 2001). Streaks of large enough amplitude undergo inflectional instabilities (Waleffe 1995; Reddy *et al.* 1998; Andersson *et al.* 2001) playing a crucial role in subcritical transition to turbulence. The optimal perturbations leading to the largest growth of streaks have been computed for virtually all canonical laminar shear flows such as the Couette, Poiseuille or Blasius solutions (Butler & Farrell 1992; Reddy & Henningson 1993; Trefethen *et al.* 1993; Schmid & Henningson 1994).

Butler & Farrell (1993) transposed the computation of optimal perturbations to turbulent flows using the turbulent mean flow profile as base flow and the molecular viscosity in the equations for the perturbations. For the turbulent Poiseuille flow, they found an optimal spanwise wavelength $\lambda_z = 3h$ close to the one found in the laminar case. They were able to retrieve the optimal spanwise wavelength $\lambda_z^+ \approx 100$ typical of the near-wall streaks by constraining the optimization time to an appropriate value. The use of the molecular viscosity and the subsequent necessary enforcement of characteristic time scales also appear in the investigations of the response to stochastic forcing by Farrell & Ioannou (1993*a*, 1998). Later, del Álamo & Jiménez

(2006) and Pujals *et al.* (2009) have recomputed the optimal growths sustained by the turbulent Poiseuille flow including an effective turbulent viscosity in the linearized equation according to the approach used by Reynolds & Hussain (1972). Without any additional constraint on the optimization time, they find that at sufficiently high Reynolds numbers two locally optimal spanwise wavelengths exist respectively scaling with outer and inner units. The maximum growth was obtained for $\lambda_z = 4h$, in good agreement with the observations of large-scale streaks. The secondary maximum of the growth was found to scale in inner units and it was reached for $\lambda_z^+ = 92$, which corresponds well to the spanwise spacing of the near-wall streaks. These findings suggest that a strong relation exists between the large-scale streaks patterns selected by the optimal transient energy growth and those observed in turbulent wall-bounded shear flows. Considering turbulent boundary layer profiles, Cossu, Pujals & Depardon (2009) have also found the two peaks of energy amplification respectively related to near-wall and large-scale streaks. However, in that case the spanwise wavelength optimizing the energy growth of large-scale streaks was found to be larger than the one of the large-scale coherent streaks actually observed.

No investigation of the optimal energy amplifications sustained by the turbulent Couette flow is currently available, even if the presence of large-scale coherent streaks with a spanwise spacing of 4*h*–5*h* is a well-established feature of this flow. Furthermore, del Álamo & Jiménez (2006), Cossu *et al.* (2009) and Pujals *et al.* (2009) have only considered the optimal temporal energy growth whereas the optimal response to harmonic and stochastic forcing may be equally relevant and their computation is now routine for the canonical laminar flows (Farrell & Ioannou 1993*a*,*b*; Bamieh & Dahleh 2001; Jovanović & Bamieh 2005; Fontane, Brancher & Fabre 2008). In this respect, some relevant questions are still unanswered: What are the streamwise and spanwise scales most amplified by the turbulent Couette flow in the initial value and in the harmonic and stochastic forcing problems? How do they compare between them and with analogous results found in laminar flows? What is the shape of the corresponding optimal perturbations? How do these structures relate to the large-scale coherent structures observed in experiments and DNS? Do their spanwise scales relate well to the most energetic ones, as found in the turbulent Poiseuille flow, or are they larger, as found in the turbulent boundary layer?

In order to answer these questions, we have conducted an input–output analysis of the turbulent Couette mean flow by considering its optimal response to an initial condition and to harmonic forcing, and its response to stochastic forcing. In the latter case, the structures that contribute most to the variance of the response have also been computed. The turbulent mean flow is computed by DNS. Our results have been obtained at the low Reynolds number $Re = 750$ corresponding to $Re_\tau \approx 52$, which is a well-documented case with respect to both the large scale structures characteristics and the convergence of the mean profile with respect to the size of the computational box. Well converged, but less documented, results from DNS are currently only available for $Re_\tau \lesssim 200$, which is well below the regime ($Re_\tau \gtrsim 500$ according to Pujals *et al.* 2009) where the primary and secondary peaks begin to be well separated and where well-defined asymptotic scalings in Re_τ can be obtained. There is therefore not great advantage in considering slightly larger Reynolds numbers.

The paper is organized as follows: In §2, we briefly introduce the mathematical problem to be solved and describe the tools used to numerically solve it. The main results are reported and compared with previous findings in §3. A summary of the main findings and a discussion of their implications are given in §4.

2. Background

2.1. *Turbulent mean flow and eddy viscosity*

We consider the plane Couette flow of a viscous fluid of kinematic viscosity ν and constant density ρ between two parallel plates located at $y = \pm h$, where we denote by x, y and z the streamwise, wall-normal and spanwise coordinates respectively. The plates move in opposite directions with velocity $(\pm U_w, 0, 0)$. For sufficiently high values of the Reynolds number $Re = hU_w/\nu$, the flow is turbulent. DNS is used to compute the turbulent mean velocity profile $U(y)$ that is obtained by averaging the instantaneous fields in space (over horizontal planes in the computational box) and in time. Once that $U(y)$ is known, it is straightforward to compute the mean shear stress at the wall $\tau_w/\rho = \nu dU/dy|_w$, the friction velocity $u_\tau = \sqrt{\tau_w/\rho}$ and the friction Reynolds number $Re_\tau = u_\tau h/\nu$. Since the mean pressure gradient is zero in the Couette flow, the mean shear stress $\tau = -\rho \overline{u'v'} + \rho \nu dU/dy$ (where u' and v' are the streamwise and the wall-normal velocity fluctuations, respectively) is constant and equal to its value at the wall τ_w. By introducing the eddy viscosity $\nu_t(y) = -\overline{u'v'}/(dU/dy)$, it is found that

$$\left[\frac{\nu_t(y)}{\nu} + 1 \right] \frac{d(U/u_\tau)}{d(y/h)} = Re_\tau. \tag{2.1}$$

The (total) effective viscosity is then defined as $\nu_T = \nu_t + \nu$.

2.2. *Generalized Orr–Sommerfeld–Squire equations*

Following the approach of Reynolds & Hussain (1972), del Álamo & Jiménez (2006), Cossu *et al.* (2009) and Pujals *et al.* (2009), we consider the linearized equations satisfied by *small coherent* perturbations in the presence of the associated effective viscosity $\nu_T(y)$:

$$\nabla \cdot \boldsymbol{u} = 0, \tag{2.2a}$$

$$\frac{\partial \boldsymbol{u}}{\partial t} + \nabla \boldsymbol{u} \cdot \boldsymbol{U} + \nabla \boldsymbol{U} \cdot \boldsymbol{u} = -\frac{1}{\rho} \nabla p + \nabla \cdot [\nu_T(\nabla \boldsymbol{u} + \nabla \boldsymbol{u}^T)] + \boldsymbol{f}, \tag{2.2b}$$

where $\boldsymbol{U} = (U, 0, 0)$ and $\boldsymbol{u} = (u, v, w)$ are the mean and the perturbation velocities respectively, p is the perturbation pressure and $\boldsymbol{f} = (f_u, f_v, f_w)$ is a forcing term. The streamwise and spanwise homogeneity of the problem allow to consider separately each in-plane Fourier mode $\hat{\boldsymbol{u}}(y, t; \alpha, \beta)e^{i(\alpha x + \beta z)}$ and $\hat{\boldsymbol{f}}(y, t; \alpha, \beta)e^{i(\alpha x + \beta z)}$, where α and β are the streamwise and spanwise wavenumbers respectively. The following generalized Orr–Sommerfeld–Squire system is obtained from (2.2):

$$\frac{\partial}{\partial t} \begin{bmatrix} \hat{v} \\ \hat{\eta} \end{bmatrix} = \underbrace{\begin{bmatrix} \Delta^{-1}\mathscr{L}_{OS} & 0 \\ -i\beta U' & \mathscr{L}_{SQ} \end{bmatrix}}_{A} \begin{bmatrix} \hat{v} \\ \hat{\eta} \end{bmatrix}$$

$$+ \underbrace{\begin{bmatrix} -i\alpha\Delta^{-1}\mathscr{D} & -k^2\Delta^{-1} & -i\beta\Delta^{-1}\mathscr{D} \\ i\beta & 0 & -i\alpha \end{bmatrix}}_{B} \begin{bmatrix} \hat{f}_u \\ \hat{f}_v \\ \hat{f}_w \end{bmatrix}, \tag{2.3a}$$

with the generalized Orr–Sommerfeld–Squire operators, given by (e.g. Reynolds & Hussain 1972; Cossu *et al.* 2009; Pujals *et al.* 2009):

$$\mathscr{L}_{OS} = -i\alpha(U\Delta - U'') + \nu_T\Delta^2 + 2\nu_T'\Delta\mathscr{D} + \nu_T''(\mathscr{D}^2 + k^2),$$
$$\mathscr{L}_{SQ} = -i\alpha U + \nu_T\Delta + \nu_T'\mathscr{D}. \tag{2.3b}$$

Here, $\mathscr{D}$ and $'$ denote $\partial/\partial y$, $\Delta = \mathscr{D}^2 - k^2$, $k^2 = \alpha^2 + \beta^2$ and $\hat{\eta}$ is the wall-normal vorticity Fourier mode. The system is completed by the initial condition $\hat{\boldsymbol{u}}|_{t=0} = \hat{\boldsymbol{u}}_0$ and homogeneous boundary conditions for the velocity perturbations on the walls, which result in $\hat{v}(y = \pm h) = 0$, $\mathscr{D}\hat{v}(\pm h) = 0$ and $\hat{\eta}(\pm h) = 0$. The velocity components can be retrieved from the wall-normal variables with

$$\begin{bmatrix} \hat{u} \\ \hat{v} \\ \hat{w} \end{bmatrix} = \frac{1}{k^2} \underbrace{\begin{bmatrix} \mathrm{i}\alpha\mathscr{D} & -\mathrm{i}\beta \\ k^2 & 0 \\ \mathrm{i}\beta\mathscr{D} & \mathrm{i}\alpha \end{bmatrix}}_{C} \begin{bmatrix} \hat{v} \\ \hat{\eta} \end{bmatrix}. \tag{2.4}$$

2.3. *Optimal perturbations*

We consider the optimal response of the system (2.3) to initial conditions, harmonic forcing and stochastic forcing. The definition of these optimals, briefly recalled below, is quite standard and can be found, for example, in the monographs by Farrell & Ioannou (1996) and Schmid & Henningson (2001). The optimal temporal energy growth of (α, β) modes is found by optimizing over the shape of the initial condition the ratio of the energy of the response at a given time t to the energy of the initial condition:

$$G(t; \alpha, \beta) \equiv \max_{\hat{\boldsymbol{u}}_0 \neq \boldsymbol{0}} \frac{\|\hat{\boldsymbol{u}}(t; \alpha, \beta)\|^2}{\|\hat{\boldsymbol{u}}_0(\alpha, \beta)\|^2}, \tag{2.5}$$

where $\|\hat{\boldsymbol{u}}\|^2 = \int_{-h}^{h} \hat{\boldsymbol{u}}^H \hat{\boldsymbol{u}} \, \mathrm{d}y = \int_{-h}^{h} |\hat{u}|^2 + |\hat{v}|^2 + |\hat{w}|^2 \mathrm{d}y$. The maximum growth is defined by further maximizing in time $G_{max}(\alpha, \beta) \equiv \max_t G(t; \alpha, \beta)$ and it is attained at $t = t_{max}$.

When harmonic forcing $\hat{\boldsymbol{f}}(y, t) = \tilde{\boldsymbol{f}}(y)\mathrm{e}^{-\mathrm{i}\omega_f t}$ is applied with frequency ω_f, the response $\hat{\boldsymbol{u}}(y, t) = \tilde{\boldsymbol{u}}(y)\mathrm{e}^{-\mathrm{i}\omega_f t}$ is observed after the switch-on transients have decayed, assuming that the system is stable. In this case, the optimal response is the one having the maximum ratio of the energy of the response to the energy of the forcing:

$$R(\omega_f; \alpha, \beta) = \max_{\tilde{f} \neq \boldsymbol{0}} \frac{\|\tilde{\boldsymbol{u}}(\omega_f; \alpha, \beta)\|^2}{\|\tilde{\boldsymbol{f}}(\omega_f; \alpha, \beta)\|^2}. \tag{2.6}$$

The optimal response $R(\omega_f)$ is given by the norm of the resolvent operator along the imaginary axis $\zeta = -\mathrm{i}\omega_f$ (e.g. Trefethen *et al.* 1993). The maximum response $R_{max}(\alpha, \beta) = \max_{\omega_f} R(\omega_f; \alpha, \beta)$ is obtained with $\omega_{f,max}$, and is also referred to as H_∞ norm of the transfer function relating the forcing to the response (Zhou, Doyle & Glover 1996).

The response to the stochastic forcing $\hat{\boldsymbol{f}}(t, y)\mathrm{e}^{\mathrm{i}(\alpha x + \beta z)}$ with Gaussian probability distribution and zero mean value $\langle \hat{\boldsymbol{f}} \rangle = \boldsymbol{0}$ is finally considered. The forcing is assumed to be delta-correlated in time: $\langle \hat{\boldsymbol{f}}(y, t) \otimes \hat{\boldsymbol{f}}^*(y', t') \rangle = \boldsymbol{R}\delta(t - t')$ where * denotes complex conjugation and $\delta(t)$ is the Dirac's delta function. We also assume, without loss of generality, that $\boldsymbol{R} = \boldsymbol{I}$. The variance of the response, $V(\alpha, \beta) = \langle \|\hat{\boldsymbol{u}}\|^2 \rangle$, also referred to as H_2 norm of the transfer function relating the forcing to the output (Zhou *et al.* 1996), is given by

$$V(\alpha, \beta) = trace(\boldsymbol{C}\boldsymbol{X}_\infty \boldsymbol{C}^\dagger), \tag{2.7}$$

where the superscript † denotes the adjoint with respect to the standard inner product (after discretization $\boldsymbol{C}^\dagger$ would simply be the Hermitian of $\boldsymbol{C}$). $\boldsymbol{X}_\infty$ is the solution of the following algebraic Lyapunov equation:

$$\boldsymbol{A}\boldsymbol{X}_\infty + \boldsymbol{X}_\infty \boldsymbol{A}^\dagger + \boldsymbol{B}\boldsymbol{B}^\dagger = \boldsymbol{0}. \tag{2.8}$$

Since $C X_\infty C^\dagger$ is a self-adjoint operator, it has real eigenvalues σ_j and a set of mutually orthogonal eigenfunctions that are usually referred to as 'empirical orthogonal functions' (EOF) or Karhunen–Loève (KL) or 'proper orthogonal decomposition' (POD) modes. The variance being $V = \sum \sigma_j$, the ratio σ_j/V represents the contribution of the jth mode to the (total) variance. The mode corresponding to the largest σ_j is the optimal one in the sense that it contributes most to the total variance of the system. The part of the stochastic forcing accounting for that optimal mode is computed by solving the dual Lyapunov problem. For further details, the interested reader is referred to the papers by Farrell & Ioannou (1993*a*,*b*), Zhou *et al.* (1996), Bamieh & Dahleh (2001) and Jovanović & Bamieh (2005) and Schmid (2007).

2.4. *Numerical tools*

The DNS of the turbulent channel flow, necessary to compute the mean flow, has been performed using the `channelflow` code (Gibson, Halcrow & Cvitanovic 2008) that integrates the incompressible Navier–Stokes equation using a spectral method based on the Fourier–Galerkin discretization in the streamwise and spanwise directions, and the Chebyshev-tau discretization in the wall-normal direction. The solution is advanced in time using a third-order semi-implicit time-stepping. Dealiasing with the 2/3 rule is implemented in the streamwise and spanwise directions.

The generalized Orr–Sommerfeld–Squire system (2.3) is discretized using a Chebyshev-collocation method with N_y collocation points in the wall-normal direction. The differentiation operators are discretized using the Chebyshev differentiation matrices of Weideman & Reddy (2000) that include the appropriate boundary conditions for $\hat{v}$ and $\hat{\eta}$. The optimal transient growth and the optimal harmonic response are computed using standard methods described, for example, in Schmid & Henningson (2001) which are implemented in the well validated code used in the channel and boundary layer computations of Pujals *et al.* (2009) and Cossu *et al.* (2009). The Lyapunov equation (2.8), discretized by the same method, was solved using the `lyap` function in `matlab`. The algorithms used to compute the optimal harmonic and stochastic responses have been validated by comparing the results obtained for laminar Couette and Poiseulle flows with those of Reddy & Henningson (1993), Schmid & Henningson (2001) and Jovanović & Bamieh (2005). The results in the present study are obtained with $N_y = 257$. We have verified, for some selected case, that the results do not change in any appreciable way if the number of collocation points is doubled to $N_y = 513$.

3. Results

3.1. *Turbulent mean flow and the Reynolds stress*

The turbulent mean flow and the associated Reynolds shear stress computed by DNS at $Re = 750$ are reported in figure 1. To obtain well-converged results we have used the same computational box ($L_x \times L_y \times L_z = 28\pi h \times 2h \times 8\pi h$) and resolution ($N_x \times N_y \times N_z = 340 \times 55 \times 170$ after dealiasing) used by Komminaho *et al.* (1996). The turbulent flow is allowed to develop up to $t = 800h/U_w$ and then the mean quantities are obtained by averaging in the symmetric horizontal planes $\pm y$ and in time for $t \in [800, 1500]h/U_w$. Re_τ converges to the same $Re_\tau = 52$ found by Komminaho *et al.* (1996) and shows also good agreement with the experimental value $Re_\tau = 50$ reported by Kitoh *et al.* (2005). The mean shear rate at the centreline $\mathrm{d}(U/U_w)/\mathrm{d}(y/h)|_{y=0} = 0.1865$ is also in good accordance with the 0.18 value found
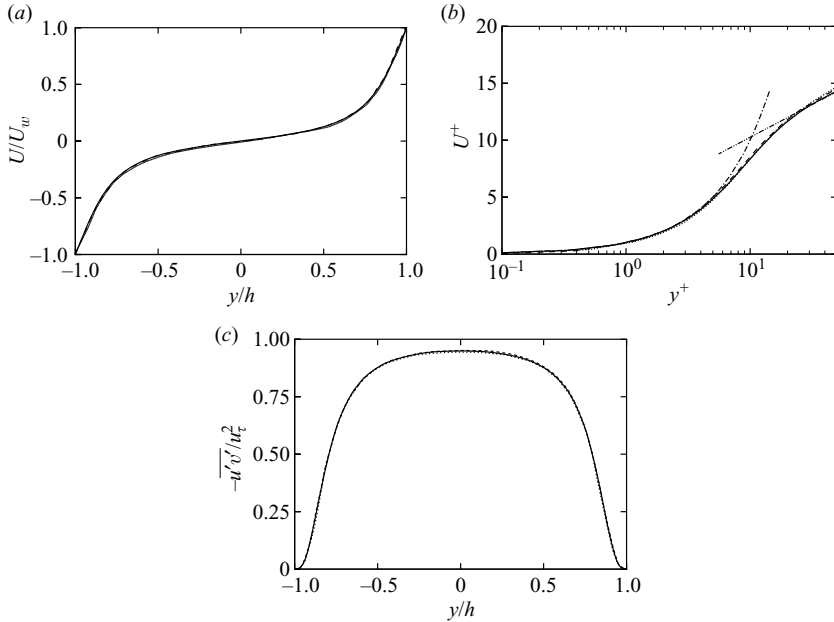
FIGURE 1. Turbulent mean velocity profile and shear stress from DNS. (*a*) Mean velocity profile expressed in outer units: present DNS (———) compared with the profiles found by Komminaho *et al.* (1996) (– – – –) and Tsukahara *et al.* (2006) (·········); the curves are almost undistinguishable. (*b*) Same profile from the DNS (———) expressed in inner units $U^+ \equiv (U + U_w)/u_\tau$ and $y^+ = (y + h)u_\tau/\nu$ and compared to the curves $U^+ = y^+$ (—·—·—) and $U^+ = (1/0.4) \log y^+ + 4.5$ (–··–··–). (*c*) Turbulent mean shear stress $-\overline{u'v'}/u_\tau^2$ from the present DNS (———) and from the data of Komminaho *et al.* (1996) (– – – –) and Tsukahara *et al.* (2006) (·········); the curves are almost undistinguishable.

by Komminaho *et al.* (1996) and the experimental value of 0.2 (Tillmark 1995; Kitoh *et al.* 2005). As shown in figure 1, the computed mean flow and the associated Reynolds shear stress are almost undistinguishable from from the ones computed by Komminaho *et al.* (1996) and by Tsukahara *et al.* (2006).

3.2. *Optimal response to initial conditions, harmonic and stochastic forcing*

As a preliminary step, the eigenvalues of the Orr–Sommerfeld–Squire operator equation (2.3) have been computed and found to be stable. The optimal response to initial condition, harmonic and stochastic forcing have then been computed for a set of wavenumbers α and β ranging from 0 to $5/h$ and from 0 to $20/h$ respectively. The optimal temporal energy growths $G(t, \alpha, \beta)$ are computed up to $t = 100h/U_w$ with the resolution $\Delta t = 0.05h/U_w$ allowing the extraction of the respective $G_{max}(\alpha, \beta)$ reported in figure 2. Only elongated structures, roughly the ones with $\alpha < \beta$, are significantly amplified, the most amplified ones being streamwise uniform ($\alpha = 0$ i.e. $\lambda_x = \infty$). The energy growths G_{max} are not very large, attaining a maximum value of 6.49. For streamwise uniform perturbations, the most amplified spanwise wavenumber is $\beta = 1.43/h$ corresponding to the spanwise wavelength $\lambda_z = 4.4h$. As α increases, the most amplified β slightly increases: e.g. $\beta = 1.46/h$ ($\lambda_z = 4.3h$) for $\alpha = 0.1/h$ ($\lambda_x = 63h$), $\beta = 1.57/h$ ($\lambda_z = 4.0h$) for $\alpha = 0.25/h$ ($\lambda_x = 25h$) and $\beta = 1.75/h$ ($\lambda_z = 3.6h$) for $\alpha = 0.5/h$ ($\lambda_x = 12.5h$).
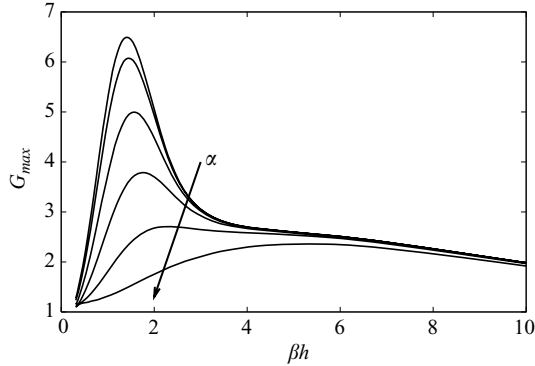
FIGURE 2. Dependence of the maximum temporal energy growth G_{max} on the dimensionless spanwise wavenumber βh for selected streamwise wavenumbers (top to bottom: $\alpha h = 0, 0.1, 0.25, 0.5, 1, 2$).
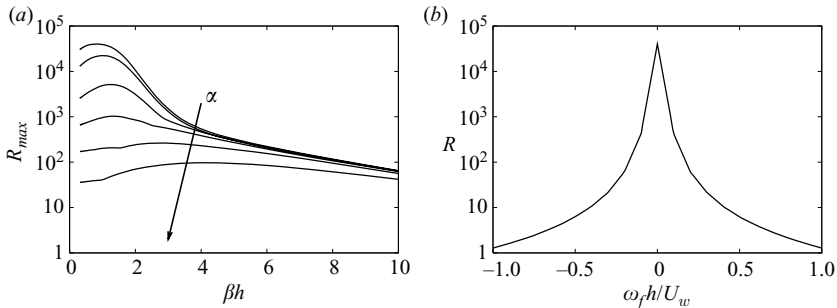

FIGURE 3. (*a*) Dependence of the maximum energy amplification of harmonic forcing R_{max} on the dimensionless spanwise wavenumber βh for selected streamwise wavenumbers α (top to bottom: $\alpha h = 0, 0.1, 0.25, 0.5, 1, 2$). (*b*) Dependence of the optimal energy amplification R on the dimensionless harmonic forcing frequency $\omega_f h/U_w$ for the optimal wavenumbers ($\alpha = 0$, $\beta h = 0.82$).

The optimal response to harmonic forcing $R(\omega_f, \alpha, \beta)$ is computed for the same set of wavenumbers. A set of forcing frequencies ω_f ranging from $-10U_w/h$ to $10U_w/h$ with resolution $\Delta\omega_f = 0.1U_w/h$ is considered, and the maximum response $R_{max}(\alpha, \beta)$ extracted from these data is reported in figure 3(*a*). Similarly to the optimal transient growth, only elongated structures are appreciably amplified. For streamwise uniform structures, the largest response ($R_{max} = 40269$) is obtained for $\beta = 0.82/h$ (corresponding to $\lambda_z = 7.7h$). The dependence of the optimal response on the forcing frequency is shown in figure 3(*a*) for the most amplified wavenumbers ($\alpha = 0$, $\beta = 0.82/h$). From this figure it is seen that the largest response is obtained when the forcing is steady ($\omega_{f,max} = 0$) and that the frequency response is strongly concentrated near $\omega_f = 0$. This indicates that the system behaves like a strongly selective low-pass frequency filter.

Finally, the variance $V(\alpha, \beta)$ of the response maintained by the stochastic forcing is computed, always for the same set of wavenumbers and it is shown in figure 4(*a*). The selection of elongated structures appears also in this case. The maximum amplification of the variance ($V = 377$) is obtained with streamwise uniform structures and the spanwise wavenumber $\beta = 1.21/h$ (corresponding to $\lambda_{zmax} = 5.2h$). The structures with the largest contribution to the variance are then identified using the

Flow	Optimal λ_z/h			Re
	G_{max}	R_{max}	V	
Turbulent Couette	$4.4^{(*)}$	$7.7^{(*)}$	$5.2^{(*)}$	750
Laminar Couette	$3.9^{(a)}$	$5.3^{(a)}$	$4.5^{(b)}$	$Re \gg 1$
Turbulent Poiseulle	$4.0^{(c)}$	—	—	$Re \gg 1$
Laminar Poiseulle	$3.1^{(a)}$	$3.9^{(a)}$	$3.5^{(b)}$	$Re \gg 1$

TABLE 1. Optimal spanwise wavenumbers of the maximum responses to initial perturbation, harmonic forcing, and stochastic excitation. Results from: (*) the present investigation, (*a*) Trefethen *et al.* (1993), (*b*) Jovanović & Bamieh (2005) and (*c*) Pujals *et al.* (2009).
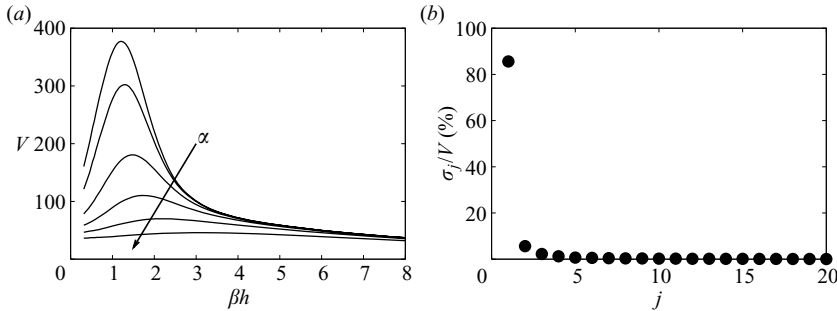

FIGURE 4. (*a*) Dependence of the variance V of the response to stochastic forcing on the dimensionless spanwise wavenumber βh for selected streamwise wavenumbers α (same values as in figures 2 and 3: top to bottom $\alpha h = 0, 0.1, 0.25, 0.5, 1, 2$). (*b*) Contribution of the leading 20 Karhunen–Loève modes to the total variance.

Karhunen–Loève decomposition. The twenty largest ratios σ_j/V, representing the contribution of the jth mode to the total variance, are reported in figure 4(*b*) for the wavenumbers associated to the largest variance ($\alpha = 0$, $\beta = 1.21/h$). We find that the most energetic mode contributes to 85 % of the total maintained energy variance, implying that a unique coherent structure strongly dominates the stochastic response in this case.

3.3. *Comparison with previous results*

The fact that for all the three types of response, the maximum energy amplification is obtained by streamwise uniform structures ($\alpha = 0$) is in accordance with the similar analyses of other turbulent and laminar flows except possibly only the maximum temporal growth of the laminar Couette flow that is obtained with perturbations non-streamwise uniform, but having a very large streamwise wavelength ($\lambda_x = 180h$). The most amplified spanwise wavelength is not the same for the different types of problem: The largest ($\lambda_z = 7.7h$) is found for the harmonic forcing whereas the shortest ($\lambda_z = 4.4h$) is found for the initial value problem, the stochastic forcing one being located in between ($\lambda_z = 5.2h$). The same ordering of spanwise optimal wavelengths is observed for the laminar Couette and Poiseuille flows (see table 1). Moreover, the spanwise wavelength maximizing G_{max} in the turbulent Couette case is slightly larger than the one found for the laminar case. This is also in accordance with what is observed, for example, for the turbulent Poiseuille flow (as reported in table 1).

At the very low Reynolds number considered here ($Re_\tau = 52$), the small temporal energy growths that we find ($G_{max} \leqslant 6.5$) are not surprising if compared, for example,
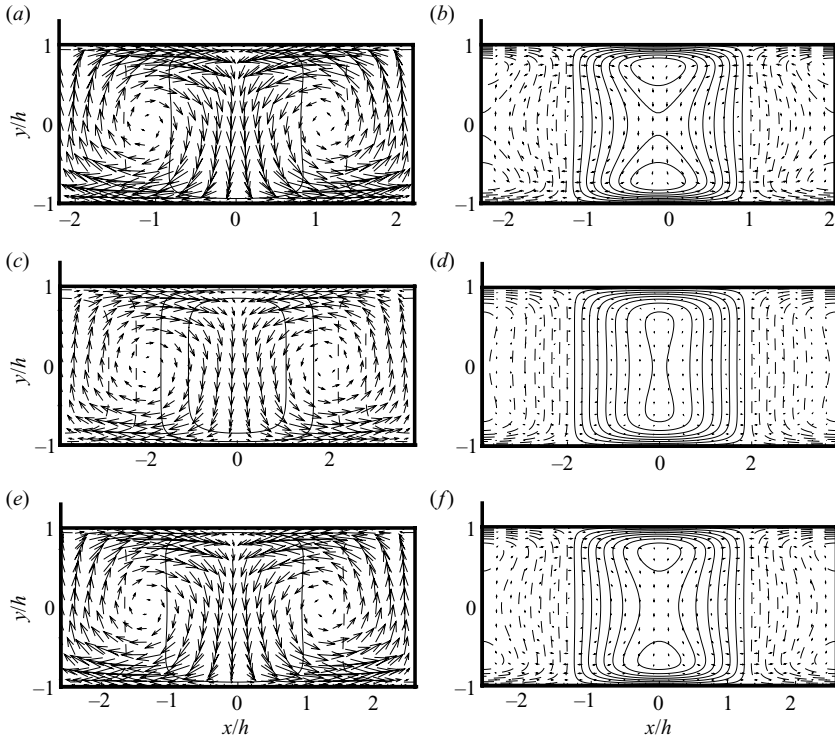
FIGURE 5. Cross-stream (y–z plane) view of the optimal input (a, c, e) and output (b, d, f) perturbation fields of the initial value problem (a, b), the response to harmonic (c, d) and stochastic (e, f) forcing problems. Each field corresponds to the respective optimal wavenumbers $\alpha = 0$ and $\beta h = 1.43$ ($\lambda_z = 4.4h$) for the initial value problem $\beta h = 0.82$ ($\lambda_z = 7.7h$) for the response to harmonic forcing, and $\beta h = 1.21$ ($\lambda_z = 5.2h$) for the response to stochastic forcing. In all the plots the solid and dashed contours denote respectively positive and negative values of the streamwise component (with increment of 0.1 the maximum value of the output) while the cross-stream components are represented as vectors (same scales in input and output plots).

to the turbulent Poiseulle flow case where a maximum growth of the order of 10 is observed for $Re_\tau = 500$ (Pujals *et al.* 2009). The low Reynolds number also explains that the G_{max} curves do not show any sign of the secondary peak associated with near-wall structures with $\lambda_z^+ \approx 90 - 100$, contrary to what is found by del Álamo & Jiménez (2006) and Pujals *et al.* (2009) for the plane Poiseuille flow. In these studies, the secondary peak appeared separated from the primary peak only for sufficiently large Reynolds numbers (typically Re_τ larger than ≈ 500), i.e. when the inner and outer scales are sufficiently separated. The two scales are not separated in the present case ($Re_\tau = 52$) where the expected inner peak value $\lambda_z^+ \approx 100$ corresponds to $\lambda_z \approx 2h$, which is well in the range of the primary peak.

3.4. *Spatial structure of the optimal input and output perturbations*

The optimal inputs and outputs respectively associated to the maximum energy amplification in time and to the maximum response to harmonic and stochastic forcing are shown in figure 5. The optimals displayed are all uniform in the streamwise direction but their spanwise wavelength is not the same. The physical meaning of each input or output is also different. For the case of the optimal temporal energy

growth the input (figure 5*a*) is the optimal initial condition (it is a velocity field) given at $t=0$ and the optimal output (figure 5*b*) is the velocity field of maximum energy obtained at t_{max} (here $t_{max} = 22.8h/U_w$). For the harmonic forcing problem, the input (figure 5*c*) is the optimal harmonic forcing term $\boldsymbol{f}$ while the output (figure 5*d*) is the velocity field of the corresponding harmonic response at the same frequency in the permanent regime. As here the optimal frequency is $\omega_f = 0$, only a plot of the input and of the output is needed, as they do not change in time. Finally, for the stochastic forcing problem, the optimal input (figure 5*e*) and output (figure 5*f*) are respectively the forcing term and the associated response corresponding to the most energetic Karhunen–Loève mode representing 85 % of total variance of the stochastically forced system. What is however similar in these three different cases is that for all the considered outputs most of the energy lies in the streamwise velocity component while for all the input fields most of the energy is in the cross-stream components. This implies that the dominant physical mechanism at work in the three cases is the lift-up effect by which streamwise vortices efficiently induce streamwise streaks. This is also in accordance with previous results such as, e.g. the ones of Gustavsson (1991) and Butler & Farrell (1992) for the optimal temporal response, Trefethen *et al.* (1993) and Reddy & Henningson (1993) for the optimal harmonic response (including complex frequencies) and Farrell & Ioannou (1993*b*) and Jovanović & Bamieh (2005) for the optimal stochastic response of laminar channel flows (see also e.g. Schmid & Henningson 2001; Schmid 2007, for a review), and the results of del Álamo & Jiménez (2006) and Pujals *et al.* (2009) for the optimal temporal response of the turbulent Poiseuille flow.

The wall-normal Fourier components ($\hat{v}$ and $\hat{f}_v$) of the optimal inputs and the streamwise Fourier component ($\hat{u}$) of the optimal outputs shown in figure 5 are reported in figures 6(*a*) and 6(*b*) respectively. The wall-normal components of the optimal inputs have almost the same shape (figure 6*a*). The streak shapes of the corresponding optimal outputs show two maxima at $y/h = \pm 0.72$ for the optimal temporal response, $y/h = \pm 0.68$ for the leading KL mode while the streaks corresponding to the (deterministic) harmonic forcing are almost uniform in the bulk region ($|y/h| \lesssim 0.5$).

In the case of the turbulent Poiseuille and boundary layer flows, Pujals *et al.* (2009) and Cossu *et al.* (2009) have found that the optimal streaks (output) of the initial value problem are proportional to the mean velocity profile $U^+(y^+)$ in the near-wall region up to the overlap region ($y^+ \lesssim 100$) for large Reynolds numbers (typically larger than $Re_\tau = 500$ for the turbulent Poiseuille flow). In the present study, this extension to the outer layer cannot be observed due to the low Reynolds number considered here $Re_\tau = 52$ (the channel centreline corresponds to $y^+ = 52$). We anyway replot in inner units (in figure 6*c*) the profile of the optimal streaks of the temporal problem but also those of the harmonic and stochastic forcing problems already reported in figure 6(*b*). All the optimal output streaks profiles are proportional to the mean velocity profile U up to the buffer layer ($y^+ \lesssim 8 - 10$). This partially extends to the optimal large-scale streaks of the forced problems the similitude observed for optimal large-scale streaks of the initial value problem.

4. Summary and discussion

In the present study, we have computed the optimal energy amplifications of coherent structures sustained by the turbulent Couette mean flow at $Re = 750$. The turbulent mean flow has been obtained by DNS and the dynamics of the coherent
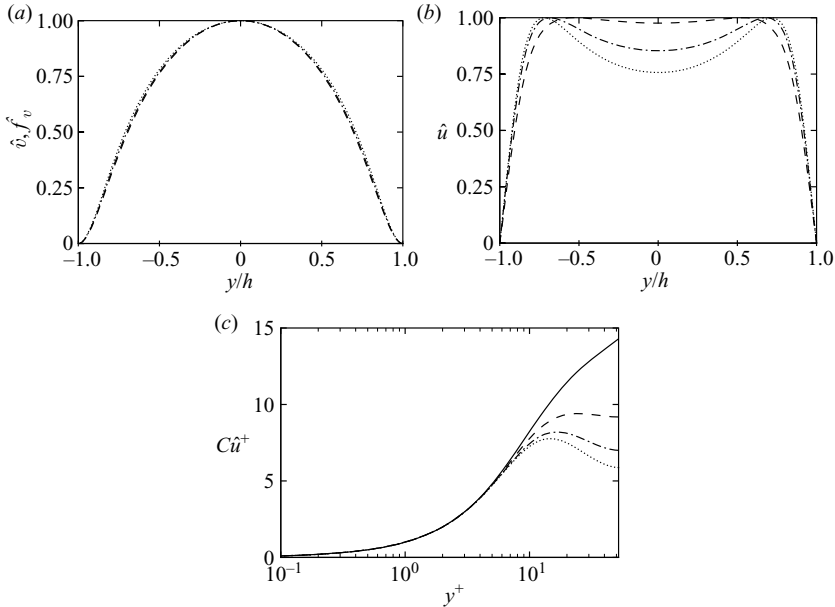
FIGURE 6. Wall-normal dependence of (*a*) the wall-normal Fourier component $\hat{v}(y/h)$, $\hat{f}_y(y/h)$ corresponding to the optimal input fields (figure 5*a,c,e*) and of (*b*) the streamwise Fourier component $\hat{u}(y/h)$ corresponding to the optimal output velocity fields (figure 5*b,d,f*). (*c*) Same as in (*a*) but in wall units: $C\hat{u}^+(y^+)$ with the constant C chosen so as to match the mean velocity field $U^+(y^+)$ reported in the same figure (———). In (*a*) and (*b*), the maximum values have been normalized to 1 to allow for comparison. Data from the initial value problem (·········) and from the stochastic (−·−·−) and harmonic (− − − −) forcing problems.

perturbations has been modelled with the Orr–Sommerfeld–Squire system generalized to include the variable eddy viscosity following Reynolds & Hussain (1972), del Álamo & Jiménez (2006), Pujals *et al.* (2009) and Cossu *et al.* (2009). The main results are as follows:

(*a*) The computed turbulent mean flow at $Re = 750$ is well converged for averaging times of the order of $700h/U_w$ where it displays $Re_\tau = 52$. The mean velocity profile and the associated turbulent shear stress show good agreement with previous results of Komminaho *et al.* (1996) and Kitoh *et al.* (2005).

(*b*) The turbulent mean flow is asymptotically stable (it has stable eigenvalues).

(*c*) The maximum temporal energy growth is small (less than 6.5 at this low Reynolds number) but the responses to the external forcing are larger. The energy amplification of the optimal deterministic forcing is two orders of magnitude larger than the maximum amplification of the variance induced by stochastic forcing.

(*d*) In the case of stochastic forcing with the wavenumbers inducing maximum variance, almost 85 % of the variance is due to the first Karhunen–Loève mode.

(*e*) Only structures elongated in the streamwise direction are significantly amplified, and the most amplified ones are streamwise uniform ($\alpha = 0$, $\lambda_x = \infty$).

(*f*) For streamwise uniform perturbations, the spanwise wavelength maximizing the temporal energy growth is $\lambda_z = 4.4h$, the one maximizing the amplification of the variance of stochastic forcing is $\lambda_z = 5.2h$ while the maximum amplification of harmonic forcing is obtained for the larger spanwise wavelength $\lambda_z = 7.7h$ and with steady forcing ($\omega_f = 0$).

(*g*) For all the three types of input–output problems, the optimal output velocity fields have a dominant streamwise component (streaks) while the input has dominant cross-stream components (streamwise vortices).

(*h*) The wall-normal profile of the wall-normal component of the three considered optimal inputs is essentially the same, even if the physical significance of each input is different from the others.

(*i*) The profiles of the optimal (output) large-scale streaks pertaining to the three considered problems are proportional to the turbulent mean profile up to buffer layer ($y^+ \lesssim 8 - 10$ for this very low Reynolds number).

These results are consistent with previous input–output analyses of laminar and turbulent wall-bounded flows. In particular: (i) the maximum growths G_{max} sustained by the turbulent mean flow are small compared to the ones sustained by the laminar flow at the same Re; the associated optimal λ_z in the turbulent case is larger than the optimal value in the laminar case. (ii) Only streamwise elongated structures are amplified with the optimal output given by streaks and the optimal input by streamwise vortices indicating that in all three cases (initial value problem, stochastic and harmonic forcing) a 'mean' lift-up mechanism is responsible for the energy amplifications. (iii) The ordering of the optimal spanwise wavelengths (the largest optimal corresponding to harmonic forcing, the shortest to the initial value problem with the one corresponding to the stochastic forcing lying in between) is also consistent with previous findings in laminar flows (no result is currently available for any other turbulent flow). (iv) The proportionality of the optimal large-scale streak profiles to the mean velocity profile near the wall is consistent with previous findings for the initial value problem in the turbulent Poiseuille and boundary layer flows. We prove that this feature also extends to the responses to harmonic and stochastic forcing.

The scales of the optimal streamwise uniform structures having the largest response to initial conditions ($\lambda_z = 4.4h$) and stochastic forcing ($\lambda_z = 5.2h$) show good agreement with those of the most energetic coherent structures observed in the numerical simulations of Komminaho *et al.* (1996) ($\lambda_z = 4.2h$ and $\lambda_x > 30h$ at $Re = 750$), Tsukahara *et al.* (2006) ($\lambda_z = 4.2 - 5h$ and $\lambda_x \approx 42 - 64h$ at $Re = 750$ and 2150) and in the experiments of Tillmark & Alfredsson (1994), Tillmark (1995) ($\lambda_z \approx 4 - 5h$ and $\lambda_x > 30h$ at $Re = 3300$) and Kitoh & Umeki (2008) ($\lambda_z = 4h$ and $\lambda_x \approx 40 - 60h$ at $Re = 3750$). Furthermore, Tsukahara *et al.* (2006) have found that at $Re = 750$ the most energetic POD modes have scales $\lambda_z = 4.2 - 5.1h$ and $\lambda_x \approx 45h$. These most energetic POD modes show a striking resemblance with the most energetic mode of the response to stochastic forcing reported in our figure 6(*f*); the position of the peak in the *u* response, at $y^+ = 15 - 20$, is also similar. In all these cases, the observed coherent streaks were not artificially forced, so that it is not surprising that the relevant scales come from the response to stochastic forcing and to initial conditions if one assumes that the effect of the nonlinear terms and of the small-scale fluctuations can be treated either as a stochastic forcing or as random initial conditions.

From the viewpoint of flow control and sensitivity to boundary conditions, where the forcing is deterministic and correlated over all times, then, the relevant scales should come from the harmonic forcing analysis. In this case, the present results indicate that the optimal response is obtained with the spanwise spacing $\lambda_z = 7.7h$, larger than the one arising in the (unforced) observed large-scale coherent streak ($\lambda_z = 4h$–$5h$). Furthermore, the very large response to harmonic forcing indicates good controllability of the large-scale structures even at low Reynolds numbers. This extreme sensitivity of the turbulent Couette flow to steady forcing has also been reported by Kitoh *et al.* (2005) and confirmed by Kitoh & Umeki (2008) who

artificially forced the large-scale streaks using vortex generators. If such a strong sensitivity of large-scale streaks to deterministic forcing is confirmed, then one could imagine to use them to modify the mean flow properties with specific targets. This kind of approach has already proven successful in the laminar boundary layer where optimal laminar streaks have been used to stabilize Tollmien–Schlichting waves and delay transition (Cossu & Brandt 2002; Fransson *et al.* 2006).

Our results confirm the strong relation between the optimally amplified streaks and the large-scale coherent streaks measured in experiments and in DNS already reported for the turbulent Poiseuille flow (del Álamo & Jiménez 2006; Pujals *et al.* 2009). The reasons of this strong correlation might however be more complex than they appear. In fact, the optimal perturbation approach provides a measure of the maximum amplification of streaks with given streamwise and spanwise scales but this amplification is only part of more complicated processes leading to the 'refuelling' of the vortices that induce the streaks. Mechanisms like the secondary instability of the streaks (Waleffe 1995; Reddy *et al.* 1998) or the transient amplification of streak bending (Schoppa & Hussain 2002) are primordial to generate streamwise non-uniform perturbations leading to the refuelling of the quasi-streamwise vortices in the models of self-sustained turbulent cycles. These additional processes select particular streamwise and spanwise scales in the flow. The self-sustained scales that are actually observed, are therefore selected by the different mechanisms embedded in the self-sustained process. The correspondence, observed in the turbulent Couette and Poiseuille flows, of the scales of the large-scale streaks in the actual turbulent flows with the scales most amplified by the mean lift-up probably means that the scale selection from the additional processes is weak. It is important to remind that this situation could be not general. For instance, Cossu *et al.* (2009) found that in the turbulent boundary layers the optimal scale ($\lambda_z \approx 8\delta$) selected by the initial value problem is larger than the scale ($\lambda_z \approx \delta$) actually observed for the coherent large-scale streaks (e.g. Jiménez *et al.* 2007). The search for self-sustained cycles of the large-scale coherent structures in turbulent wall-bounded flows and the investigation of the mechanisms selecting their scales are the subject of current intensive investigation.

REFERENCES

DEL ÁLAMO, J. C. & JIMÉNEZ, J. 2003 Spectra of the very large anisotropic scales in turbulent channels. *Phys. Fluids* **15**, L41.

DEL ÁLAMO, J. C. & JIMÉNEZ, J. 2006 Linear energy amplification in turbulent channels. *J. Fluid Mech.* **559**, 205–213.

ANDERSSON, P., BRANDT, L., BOTTARO, A. & HENNINGSON, D. 2001 On the breakdown of boundary layers streaks. *J. Fluid Mech.* **428**, 29–60.

BAMIEH, B. & DAHLEH, M. 2001 Energy amplification in channel flows with stochastic excitation. *Phys. Fluids* **13**, 3258–3269.

BUTLER, K. M. & FARRELL, B. F. 1992 Three-dimensional optimal perturbations in viscous shear flow. *Phys. Fluids* A **4**, 1637–1650.

BUTLER, K. M. & FARRELL, B. F. 1993 Optimal perturbations and streak spacing in wall-bounded turbulent shear flow. *Phys. Fluids* **5**, 774–777.

COSSU, C. & BRANDT, L. 2002 Stabilization of Tollmien–Schlichting waves by finite amplitude optimal streaks in the Blasius boundary layer. *Phys. Fluids* **14**, L57–L60.

Cossu, C., Pujals, G. & Depardon, S. 2009 Optimal transient growth and very large scale structures in turbulent boundary layers. *J. Fluid Mech.* **619**, 79–94.

Ellingsen, T. & Palm, E. 1975 Stability of linear flow. *Phys. Fluids* **18**, 487–488.

Farrell, B. F. & Ioannou, P. J. 1993a Optimal excitation of three-dimensional perturbations in viscous constant shear flow. *Phys. Fluids* **5**, 1390–1400.

Farrell, B. F. & Ioannou, P. J. 1993b Stochastic forcing of the linearized Navier-Stokes equation. *Phys. Fluids* A **5**, 2600–2609.

Farrell, B. F. & Ioannou, P. J. 1996 Generalized stability theory. *J. Atmos. Sci.* **53**, 2025–2053.

Farrell, B. F. & Ioannou, P. J. 1998 Perturbation structure and spectra in turbulent channel flow. *Theor. Comput. Fluid Dyn.* **11**, 237–250.

Fontane, J., Brancher, P. & Fabre, D. 2008 Stochastic forcing of the Lamb–Oseen vortex. *J. Fluid Mech.* **613**, 233–254.

Fransson, J., Talamelli, A., Brandt, L. & Cossu, C. 2006 Delaying transition to turbulence by a passive mechanism. *Phys. Rev. Lett.* **96**, 064501.

Gibson, J. F., Halcrow, J. & Cvitanovic, P. 2008 Visualizing the geometry of state space in plane Couette flow. *J. Fluid Mech.* **611**, 107–130.

Gustavsson, L. H. 1991 Energy growth of three-dimensional disturbances in plane Poiseuille flow. *J. Fluid Mech.* **224**, 241–260.

Hamilton, J. M., Kim, J. & Waleffe, F. 1995 Regeneration mechanisms of near-wall turbulence structures. *J. Fluid Mech.* **287**, 317–348.

Ho, C. M. & Huerre, P. 1984 Perturbed shear layers. *Annu. Rev. Fluid Mech.* **16**, 365–424.

Hutchins, N. & Marusic, I. 2007a Evidence of very long meandering features in the logarithmic region of turbulent boundary layers. *J. Fluid Mech.* **579**, 1–28.

Hutchins, N. & Marusic, I. 2007b Large-scale influences in near-wall turbulence. *Phil. Trans. R. Soc*. A **365**, 647–664.

Jang, P. S., Benney, D. J. & Gran, D. L. 1986 On the origin of streamwise vortices in a turbulent boundary layer. *J. Fluid Mech.* **169**, 109–123.

Jiménez, J. 2007 Recent developments on wall-bounded turbulence. *Rev. R. Acad. Cien. Ser.* A *Mat.* **101**, 187–203.

Jiménez, J. & Moin, P. 1991 The minimal flow unit in near-wall turbulence. *J. Fluid Mech.* **225**, 213–240.

Jovanović, M. R. & Bamieh, B. 2005 Componentwise energy amplification in channel flow. *J. Fluid Mech.* **543**, 145–83.

Kim, K. C. & Adrian, R. 1999 Very large-scale motion in the outer layer. *Phys. Fluids* **11** (2), 417–422.

Kitoh, O., Nakabayashi, K. & Nishimura, F. 2005 Experimental study on mean velocity and turbulence characteristics of plane Couette flow: low-Reynolds-number effects and large longitudinal vortical structures. *J. Fluid Mech.* **539**, 199.

Kitoh, O. & Umeki, M. 2008 Experimental study on large-scale streak structure in the core region of turbulent plane Couette flow. *Phys. Fluids* **20**, 025107.

Kline, S. J., Reynolds, W. C., Schraub, F. A. & Runstadler, P. W. 1967 The structure of turbulent boundary layers. *J. Fluid Mech.* **30**, 741–773.

Komminaho, J., Lundbladh, A. & Johansson, A. V. 1996 Very large structures in plane turbulent Couette flow. *J. Fluid Mech.* **320**, 259–285.

Landahl, M. T. 1980 A note on an algebraic instability of inviscid parallel shear flows. *J. Fluid Mech.* **98**, 243–251.

Landahl, M. T. 1990 On sublayer streaks. *J. Fluid Mech.* **212**, 593–614.

Lee, M. J. & Kim, J. 1991 The structure of turbulence in a simulated plane Couette flow. In *Eighth Symp. on Turbulent Shear Flow*, pp. 5.3.1–5.3.6. Technical University of Munich, Munich, Germany.

Moffatt, H. K. 1967 The interaction of turbulence with strong wind shear. In *Proceedings of URSI-IUGG Colloquium on Atomspheric Turbulence and Radio Wave Propagation* (ed. A. M. Yaglom & V. I. Tatarsky), pp. 139–154. Nauka.

Moin, P. & Kim, J. 1982 Numerical investigation of turbulent channel flow. *J. Fluid Mech.* **118**, 341–377.

PUJALS, G., GARCÍA-VILLALBA, M., COSSU, C. & DEPARDON, S. 2009 A note on optimal transient growth in turbulent channel flows. *Phys. Fluids* **21**, 015109.

REDDY, S. C. & HENNINGSON, D. S. 1993 Energy growth in viscous channel flows. *J. Fluid Mech.* **252**, 209–238.

REDDY, S. C., SCHMID, P. J., BAGGETT, J. S. & HENNINGSON, D. S. 1998 On the stability of streamwise streaks and transition thresholds in plane channel flows. *J. Fluid Mech.* **365**, 269–303.

REYNOLDS, W. C. & HUSSAIN, A. K. M. F. 1972 The mechanics of an organized wave in turbulent shear flow. Part 3. Theoretical models and comparisons with experiments. *J. Fluid Mech.* **54** (02), 263–288.

SCHMID, P. J. 2007 Nonmodal stability theory. *Annu. Rev. Fluid Mech.* **39**, 129–162.

SCHMID, P. J. & HENNINGSON, D. S. 1994 Optimal energy density growth in Hagen–Poiseuille flow. *J. Fluid Mech.* **277**, 197–225.

SCHMID, P. J. & HENNINGSON, D. S. 2001 *Stability and Transition in Shear Flows*. Springer.

SCHOPPA, W. & HUSSAIN, F. 2002 Coherent structure generation in near-wall turbulence. *J. Fluid Mech.* **453**, 57–108.

SMITH, J. R. & METZLER, S. P. 1983 The characteristics of low-speed streaks in the near-wall region of a turbulent boundary layer. *J. Fluid Mech.* **129**, 27–54.

TILLMARK, N. 1995 Experiments on transition and turbulence in plane Couette flow. PhD thesis, Department of Mechanics, Royal Institute of Technology (KTH), Stockholm.

TILLMARK, N. & ALFREDSSON, H. 1994 Structures in turbulent plane Couette flow obtained from correlation measurements. In *Advances in Turbulences V* (ed. R. Benzi), pp. 502–507. Kluwer.

TOMKINS, C. D. & ADRIAN, R. J. 2003 Spanwise structure and scale growth in turbulent boundary layers. *J. Fluid Mech.* **490**, 37–74.

TOMKINS, C. D. & ADRIAN, R. J. 2005 Energetic spanwise modes in the logarithmic layer of a turbulent boundary layer. *J. Fluid Mech.* **545**, 141–162.

TREFETHEN, L. N., TREFETHEN, A. E., REDDY, S. C. & DRISCOLL, T. A. 1993 A new direction in hydrodynamic stability: beyond eigenvalues. *Science* **261**, 578–584.

TSUKAHARA, T., IWAMOTO, K. & KAWAMURA, H. 2007 POD analysis of large-scale structures through DNS of turbulence Couette flow. In *Advances in Turbulence XI* (ed. J. M. L. M. Palma & A. Silva Lopes) pp. 245–247. Springer.

TSUKAHARA, T., KAWAMURA, H. & SHINGAI, K. 2006 DNS of turbulent Couette flow with emphasis on the large-scale structure in the core region. *J. Turbul.* **7**, 19.

WALEFFE, F. 1995 Hydrodynamic stability and turbulence: beyond transients to a self-sustaining process. *Stud. Appl. Math.* **95**, 319–343.

WEIDEMAN, J. A. C. & REDDY, S. C. 2000 A MATLAB differentiation matrix suite. *ACM Trans. Math. Softw.* **26**, 465–519.

ZHOU, K., DOYLE, J. C. & GLOVER, K. 1996 *Robust and Optimal Control*. Prentice Hall.

2

Article 2

Linear non-normal energy amplification of harmonic and stochastic forcing in the turbulent channel flow

YONGYUN HWANG[1]† AND CARLO COSSU[2,3]

[1]Laboratorie d'Hydrodynamique (LadHyX), CNRS–École Polytechnique,
F-91128 Palaiseau, France

[2]CNRS–Institut de Mécanique des Fluides de Toulouse (IMFT),
Allée du Professeur Camille Soula, F-31400 Toulouse, France

[3]Département de Mécanique, École Polytechnique, F-91128 Palaiseau, France

The linear response to stochastic and optimal harmonic forcing of small coherent perturbations to the turbulent channel mean flow is computed for Reynolds numbers ranging from $Re_\tau = 500$ to $20\,000$. Even though the turbulent mean flow is linearly stable, it is nevertheless able to sustain large amplifications by the forcing. The most amplified structures consist of streamwise-elongated streaks that are optimally forced by streamwise-elongated vortices. For streamwise-elongated structures, the mean energy amplification of the stochastic forcing is found to be, to a first approximation, inversely proportional to the forced spanwise wavenumber while it is inversely proportional to its square for optimal harmonic forcing in an intermediate spanwise wavenumber range. This scaling can be explicitly derived from the linearized equations under the assumptions of geometric similarity of the coherent perturbations and of logarithmic base flow. Deviations from this approximate power-law regime are apparent in the pre-multiplied energy amplification curves that reveal a strong influence of two different peaks. The dominant peak scales in outer units with the most amplified spanwise wavelength of $\lambda_z \approx 3.5h$, while the secondary peak scales in wall units with the most amplified $\lambda_z^+ \approx 80$. The associated optimal perturbations are almost independent of the Reynolds number when, respectively, scaled in outer and inner units. In the intermediate wavenumber range, the optimal perturbations are approximatively geometrically similar. Furthermore, the shape of the optimal perturbations issued from the initial value, the harmonic forcing and the stochastic forcing analyses are almost indistinguishable. The optimal streaks corresponding to the large-scale peak strongly penetrate into the inner layer, where their amplitude is proportional to the mean-flow profile. At the wavenumbers corresponding to the large-scale peak, the optimal amplifications of harmonic forcing are at least two orders of magnitude larger than the amplifications of the variance of stochastic forcing and both increase with the Reynolds number. This confirms the potential of the artificial forcing of optimal large-scale streaks for the flow control of wall-bounded turbulent flows.

Key words: turbulent boundary layers, turbulence theory

---

† Email address for correspondence: yongyun.hwang@ladhyx.polytechnique.fr

1. Introduction

The understanding of the dynamics of wall-bounded turbulent flows is an interesting topic in its own right, but it is also relevant for applications ranging from flow control to atmospheric dynamics. For these applications, the high-Reynolds-number regime is of particular interest. In this regime, it is generally accepted that the dissipation of energy is associated with structures at very small scales, while there is much less consensus on the mechanisms by which energy is extracted from the mean flow and injected in the turbulent motions. In this respect, much attention is currently given to the dynamics of streamwise streaks which are narrow regions, elongated in the streamwise direction, of excess or deficit of streamwise velocity. There is a growing body of numerical and experimental evidence of the existence of streamwise streaks ranging from small to very large scales. It has been known for a while that streaky motions with a mean spanwise spacing of about 100 wall units exist in the buffer layer (Kline *et al.* 1967; Smith & Metzler 1983). These streaky motions have been shown to be able to self-sustain even in the absence of outer-layer motions and to substantially contribute to the production of turbulent kinetic energy in the near-wall region (Jiménez & Moin 1991; Jiménez & Pinelli 1999). The self-sustained mechanism is now understood to be based on the strong amplification of the streaks from quasi-streamwise vortices followed by the breakdown of the streaks leading to the 'refuelling' of the quasi-streamwise vortices (Hamilton, Kim & Waleffe 1995; Waleffe 1995; Schoppa & Hussain 2002).

Streaky motions also exist at larger scales and have been observed recently in most wall-bounded flows such as plane Couette flow (Komminaho, Lundbladh & Johansson 1996; Kitoh, Nakabayashi & Nishimura 2005), pipes (Kim & Adrian 1999; Guala, Hommema & Adrian 2006), plane Poiseuille flow (Jiménez 1998; del Álamo & Jiménez 2003; del Álamo *et al.* 2004) and flat-plate boundary layers (Tomkins & Adrian 2003, 2005; Hutchins & Marusic 2007*a,b*). These streaky motions, called 'very large-scale motion' or 'global mode' or 'superstructure', extend up to a few outer length units, h, in the spanwise direction, and they carry a significant amount of the turbulent kinetic energy and Reynolds stress in the outer region (Komminaho *et al.* 1996; Tomkins & Adrian 2005; Guala *et al.* 2006). Moreover, the influence of these energetic structures is felt even in the buffer layer, leading to the modulation of the near-wall cycles (Hunt & Morrison 2000; Hutchins & Marusic 2007*b*; Mathis, Hutchins & Marusic 2009).

The understanding of the physical mechanism by which energy could be extracted from the turbulent mean flow and, in particular, the mechanism leading to the amplification of the streaks, has long been elusive because the mean velocity profiles of the wall-bounded turbulent flows are linearly stable (Malkus 1956; Reynolds & Tiederman 1967). However, in the more tractable case of laminar base flows, it has been shown that large shear can support the strong amplification of streamwise vortices into streamwise streaks via the lift-up effect (Moffatt 1967; Ellingsen & Palm 1975; Landahl 1980, 1990). This amplification is associated with the non-normality of the linearized Navier–Stokes operator (for a review see e.g. Trefethen *et al.* 1993; Farrell & Ioannou 1996; Schmid & Henningson 2001). In the initial-value problem framework, of interest for the understanding of subcritical transition, the optimal amplification of streaks has been shown to be proportional to the square of the Reynolds number (Gustavsson 1991) and has been computed for virtually all the canonical laminar shear flows (Butler & Farrell 1992; Reddy & Henningson 1993; Schmid & Henningson 1994).

It is tempting to transpose the lift-up mechanism to the case of turbulent flows. In this case, however, one has to deal with the unsteadiness and randomness of the local shear promoting the lift-up. Progress has been made by considering the Reynolds-averaged Navier–Stokes equations linearized in the neighbourhood of the turbulent mean flow. These equations rule the dynamics of small-amplitude coherent perturbations, while all the effects of the other perturbations, which have a zero statistical average, are captured by the Reynolds shear-stress tensor. Reynolds & Hussain (1972) have shown that a formulation where the Reynolds shear stress is modelled with an eddy viscosity is much better adapted to the description of the motion of small-amplitude coherent perturbations than the one where the Reynolds shear stress is simply neglected. Del Álamo & Jiménez (2006) and Pujals *et al.* (2009) have adopted this modelling for the computation of the optimal temporal transient growths supported by the turbulent channel flow. They find that only streamwise-elongated structures are noticeably amplified. For these structures, at sufficiently high Reynolds numbers, two locally optimal spanwise wavelengths exist that, respectively, scale in outer and inner units. The global maximum growth is associated to the main peak at $\lambda_z \approx 4\,h$, in fair agreement with the spanwise spacing of large-scale streaky motions in the outer region. The secondary peak of the growth was found at $\lambda_z^+ \approx 100$, which corresponds well to the average spanwise spacing of the buffer-layer streaks. These results strongly suggest that a 'coherent lift-up' mechanism plays a crucial role in the selection of the spanwise scales of streaky structures in turbulent flows.

In turbulent flows, structures of a given scale are permanently forced by structures of different scales via nonlinear interactions. In this context, a modelling of the streaks' amplification based on the response to stochastic forcing would seem more appropriate than the optimal initial-value problem considered in previous investigations. Furthermore, in the perspective of flow control, it is also of interest to compute the optimal response of the turbulent flow to deterministic forcing. In the case of laminar flows the computation of the response to optimal harmonic (deterministic) forcing (Reddy & Henningson 1993; Reddy, Schmid & Henningson 1993; Trefethen *et al.* 1993) and to stochastic forcing (Farrell & Ioannou 1993*a*,*b*, 1996; Bamieh & Dahleh 2001; Jovanović & Bamieh 2005) is routine, but this is not the case for turbulent flows.

In this study, we compute the response of the turbulent channel flow to both stochastic and optimal harmonic forcing for Reynolds numbers ranging from $Re_\tau = 500$ to $20\,000$. We anticipate that the amplification of the forcing is found to always decrease with the scale of the forced structures, contrary to what has been found for the optimal growth of initial perturbations. In particular, we show that for streamwise uniform and geometrically similar structures living in the log layer, the energy amplification of stochastic forcing and of harmonic forcing scale like β^{-1} and β^{-2}, respectively, where β is their spanwise wavenumber. This scaling is actually found to approximatively apply to the numerical results in an intermediate wavenumber range. The use of pre-multiplied energy amplifications allows us then to analyse the deviations from the β-power-law behaviour and to identify the spanwise scales associated to the most amplified structures in the near wall and at large scales. Previous similar investigations have not detected the approximate β-power scaling of the amplifications of log-layer structures, either because the molecular viscosity instead of the turbulent eddy viscosity was used in the linearized equations (Farrell & Ioannou 1998) or because a too low Reynolds number was considered (Hwang & Cossu 2010).

This paper is organized as follows: in §2, we briefly introduce the considered turbulent mean base flow, the associated eddy viscosity and the equations satisfied by small coherent perturbations to the base flow. We then recall the standard framework adopted for the computation of the response to stochastic forcing and for the optimal response to harmonic forcing. The amplifications of the forcing computed for $Re_\tau = 10\,000$ are analysed in §3 and their dependence on the Reynolds number is detailed in §4. The scaling with the wavenumber of the amplification of geometrically similar log-layer structures is derived from the linear model in §5 with some of the details reported in the Appendix. The results are discussed in §6, while the main findings are summarized in §7.

2. Background

2.1. *Linear model for the evolution of small-amplitude coherent structures*

We consider a pressure-driven turbulent channel flow of incompressible viscous fluid with density ρ, kinematic viscosity ν and mean centreline velocity U_e between two infinite parallel walls located at $y = \pm h$. Here, we denote streamwise, wall-normal and spanwise coordinates by x, y and z, respectively. In the following, we will also use the distance from the wall scaled in wall (inner) units and defined as $y^+ = (y + h)u_\tau/\nu$ when the lower wall is considered. Following Reynolds & Hussain (1972), del Álamo & Jiménez (2006) and Pujals *et al.* (2009) and others, we introduce the linearized equations for 'small coherent perturbations' in the presence of the total eddy viscosity $\nu_T(y) = \nu + \nu_t(y)$

$$\nabla \cdot \boldsymbol{u} = 0, \tag{2.1a}$$

$$\frac{\partial \boldsymbol{u}}{\partial t} + \nabla \boldsymbol{u} \cdot \boldsymbol{U} + \nabla \boldsymbol{U} \cdot \boldsymbol{u} = -\frac{1}{\rho}\nabla p + \nabla \cdot [\nu_T(\nabla \boldsymbol{u} + \nabla \boldsymbol{u}^T)] + \boldsymbol{f}, \tag{2.1b}$$

where $\boldsymbol{U}$ is the base mean velocity, $\boldsymbol{u} = (u, v, w)$ and p are the coherent perturbation velocity and pressure, respectively, and $\boldsymbol{f} = (f_u, f_v, f_w)$ is the forcing term. These equations can be derived from the Reynolds-averaged Navier–Stokes equations by the standard, if crude, modelling of the Reynolds stress term with an isotropic eddy viscosity and by a linearization near the base flow $\boldsymbol{U}$. The base flow should be understood as the turbulent mean flow obtained for $\boldsymbol{f} = \boldsymbol{0}$ in the absence of any statistically correlated initial condition. In that case, the temporal and horizontal statistical invariance of the mean solution gives $\boldsymbol{U} = (U_b(y), 0, 0)$. In the following we will refer to 'coherent perturbation' as a perturbation $\boldsymbol{u}$ of the base flow $\boldsymbol{U}$ that has a non-zero ensemble average. Note that $\boldsymbol{u}$ does not need to be steady or spatially uniform. In an experiment or a direct numerical simulation (DNS) these coherent perturbations would typically be realized using artificial forcing (see e.g. Reynolds & Hussain 1972), ensuring that their spatial and temporal phases are always the same in each realization or by locating and tracking (with same phase) the same kind of event over multiple realizations. The linearized equations (2.1) apply to these coherent perturbations if their amplitude is sufficiently small, which does not seem too unreasonable. Indeed, the amplitudes of natural or artificially forced output streaks are typically not larger than $\approx O(10^{-1}U_e)$. Furthermore, as the input–output energy amplifications are typically large, the amplitude of the optimal input vortices needed to force streaks at the observed small amplitudes are even smaller. This supports the idea that an optimal coherent lift-up process mainly acts at small perturbation amplitude levels, where the linear approximation applies.

For the total eddy viscosity, we adopt the semi-empirical expression proposed by Cess (1958), as reported by Reynolds & Tiederman (1967):

$$\nu_T(\eta) = \frac{\nu}{2}\left\{1 + \frac{\kappa^2 Re_\tau^2}{9}(1-\eta^2)^2(1+2\eta^2)^2 \times \{1 - \exp[(|\eta|-1)Re_\tau/A]\}^2\right\}^{1/2} + \frac{\nu}{2},$$
(2.2)

where $\eta = y/h$ and $Re_\tau = u_\tau h/\nu$ is the Reynolds number based on the friction velocity u_τ. We set the von Kármán constant $\kappa = 0.426$ and the constant $A = 25.4$ as in del Álamo & Jiménez (2006) and Pujals *et al.* (2009). Note that these values were obtained from fits based on a DNS performed at $Re_\tau = 2000$ (Hoyas & Jiménez 2006), thus they may not be reliable far from this Reynolds number. The mean velocity profile is obtained by integrating $\mathrm{d}U_b^+/\mathrm{d}\eta = -Re_\tau\eta/\nu_T^+(\eta)$, where $\nu_T^+ = \nu_T/\nu$. Since the mean flow is homogeneous in the streamwise and spanwise directions, we consider the plane Fourier modes $\hat{\boldsymbol{u}}(y,t;\alpha,\beta)\mathrm{e}^{\mathrm{i}(\alpha x+\beta z)}$ and $\hat{\boldsymbol{f}}(y,t;\alpha,\beta)\mathrm{e}^{\mathrm{i}(\alpha x+\beta z)}$ of streamwise and spanwise wavenumbers α and β for which the following system is obtained (Pujals *et al.* 2009; Hwang & Cossu 2010) from (2.1):

$$\frac{\partial\hat{\boldsymbol{q}}}{\partial t} = \boldsymbol{A}\hat{\boldsymbol{q}} + \boldsymbol{B}\hat{\boldsymbol{f}}.$$
(2.3a)

The state vector is formed with the wall-normal components of the velocity and vorticity Fourier modes $\hat{\boldsymbol{q}} = [\hat{v}, \hat{\omega}_y]^\mathrm{T}$. The operators $\boldsymbol{A}$ and $\boldsymbol{B}$ are defined as

$$\boldsymbol{A} = \begin{bmatrix} \Delta^{-1}\mathscr{L}_{O\mathscr{S}} & 0 \\ -\mathrm{i}\beta U' & \mathscr{L}_{\mathscr{S}\mathscr{Q}} \end{bmatrix}, \quad \boldsymbol{B} = \begin{bmatrix} -\mathrm{i}\alpha\Delta^{-1}\mathscr{D} & -k^2\Delta^{-1} & -\mathrm{i}\beta\Delta^{-1}\mathscr{D} \\ \mathrm{i}\beta & 0 & -\mathrm{i}\alpha \end{bmatrix}, \quad (2.3b)$$

with the generalized Orr–Sommerfeld and Squire operators:

$$\mathscr{L}_{O\mathscr{S}} = -\mathrm{i}\alpha(U\Delta - U'') + \nu_T\Delta^2 + 2\nu_T'\Delta\mathscr{D} + \nu_T''(\mathscr{D}^2 + k^2),$$
(2.3c)

$$\mathscr{L}_{\mathscr{S}\mathscr{Q}} = -\mathrm{i}\alpha U + \nu_T\Delta + \nu_T'\mathscr{D}.$$
(2.3d)

Here, $\Delta = \mathscr{D}^2 - k^2$, $k^2 = \alpha^2 + \beta^2$, $\mathscr{D}$ and $'$ denote $\partial/\partial y$. Homogeneous boundary conditions are enforced on both walls: $\hat{v}(\pm h) = \mathscr{D}\hat{v}(\pm h) = \hat{\omega}_y(\pm h) = 0$. Otherwise, when it is not specified, we will assume that homogeneous initial conditions $\hat{\boldsymbol{u}}_0 = \boldsymbol{0}$ are used for the system. The velocity can be obtained from the state vector with

$$\hat{\boldsymbol{u}} = \boldsymbol{C}\hat{\boldsymbol{q}}, \quad \boldsymbol{C} = \frac{1}{k^2}\begin{bmatrix} \mathrm{i}\alpha\mathscr{D} & -\mathrm{i}\beta \\ k^2 & 0 \\ \mathrm{i}\beta\mathscr{D} & \mathrm{i}\alpha \end{bmatrix}, \quad (2.3e)$$

and *vice versa*

$$\hat{\boldsymbol{q}} = \boldsymbol{D}\hat{\boldsymbol{u}}, \quad \boldsymbol{D} = \begin{bmatrix} 0 & 1 & 0 \\ \mathrm{i}\beta & 0 & -\mathrm{i}\alpha \end{bmatrix}.$$
(2.3f)

The forcing term $\boldsymbol{f}$ driving the system will be referred to as 'input' and the driven motions $\boldsymbol{u}$ as 'output'.

2.2. *Optimal harmonic and stochastic energy amplification*

When an harmonic forcing $\hat{\boldsymbol{f}}(y,t) = \tilde{\boldsymbol{f}}(y)\mathrm{e}^{\mathrm{i}\omega_f t}$ of real frequency ω_f drives the linearly stable system (2.3), for sufficiently large times, the response is $\hat{\boldsymbol{u}}(y,t) = \tilde{\boldsymbol{u}}(y)\mathrm{e}^{\mathrm{i}\omega_f t}$. Making use of (2.3) it is easily found that $\tilde{\boldsymbol{u}} = \boldsymbol{H}\tilde{\boldsymbol{f}}$, where the transfer function is

$\boldsymbol{H} = \boldsymbol{C}(\mathrm{i}\omega_f \boldsymbol{I} - \boldsymbol{A})^{-1}\boldsymbol{B}$. In this case, the optimal harmonic amplification is defined by optimizing the ratio of the energy of the output to the energy of the input and coincides with the square of the norm of the transfer function, i.e. the pseudospectrum evaluated on the imaginary axis (see e.g. Reddy *et al.* 1993; Trefethen *et al.* 1993)

$$R(\omega_f; \alpha, \beta) = \max_{\tilde{f} \neq \mathbf{0}} \frac{\|\tilde{\boldsymbol{u}}\|^2}{\|\tilde{\boldsymbol{f}}\|^2} = \|\boldsymbol{H}\|^2, \qquad (2.4)$$

where the standard energy norm is used, $\|\hat{\boldsymbol{u}}\|^2 = \int_{-h}^{h} \hat{\boldsymbol{u}}^H \hat{\boldsymbol{u}} \, \mathrm{d}y$. The maximum response $R_{max}(\alpha, \beta) = \max_{\omega_f} R(\omega_f; \alpha, \beta)$, obtained with $\omega_{f,max}$, is also referred to as the H_∞ norm of the transfer function (Zhou, Doyle & Glover 1996).

When a stochastic forcing drives the system (2.3), the response is also stochastic, and we are interested in its variance $V = \langle \|\hat{\boldsymbol{u}}\| \rangle$, where $\langle \cdot \rangle$ is the ensemble average. The variance can also be retrieved as the trace of the covariance tensor $\langle \hat{\boldsymbol{u}}\hat{\boldsymbol{u}}^H \rangle$. We follow previous investigations in considering a zero-mean ($\langle \hat{\boldsymbol{f}} \rangle = \mathbf{0}$) delta-correlated forcing with Gaussian probability density distribution which, for convenience, we also assume to be isotropic $\langle \hat{\boldsymbol{f}}(t)\hat{\boldsymbol{f}}^H(t') \rangle = \boldsymbol{I}\delta(t - t')$. In this case the variance can be obtained in the frequency or in the temporal domain as

$$V(\alpha, \beta) = \frac{1}{2\pi} \int_{-\infty}^{\infty} \mathrm{trace}(\boldsymbol{H}\boldsymbol{H}^\dagger) \mathrm{d}\omega = \mathrm{trace}(\boldsymbol{C}\boldsymbol{X}_\infty \boldsymbol{C}^\dagger), \qquad (2.5)$$

where the adjoints † are defined with respect to the inner product $(\hat{\boldsymbol{u}}, \hat{\boldsymbol{v}}) = \int_{-h}^{h} \hat{\boldsymbol{u}}^H \hat{\boldsymbol{v}} \, \mathrm{d}y$. The variance represents the H_2 norm of the transfer function (Zhou *et al.* 1996). Following the temporal domain approach, one has to compute the solution $\boldsymbol{X}_\infty$ of the algebraic Lyapunov equation:

$$\boldsymbol{A}\boldsymbol{X}_\infty + \boldsymbol{X}_\infty \boldsymbol{A}^\dagger + \boldsymbol{B}\boldsymbol{B}^\dagger = 0. \qquad (2.6)$$

The covariance of the response is then retrieved as $\langle \hat{\boldsymbol{u}}\hat{\boldsymbol{u}}^H \rangle = \boldsymbol{C}\boldsymbol{X}_\infty \boldsymbol{C}^\dagger$. The covariance is self-adjoint and has real eigenvalues σ_j with $V = \sum \sigma_j$, and a set of mutually orthogonal eigenfunctions often referred to as 'empirical orthogonal functions', Karhunen–Loève (KL) or 'proper orthogonal decomposition' (POD) modes. The ratio σ_j/V represents the contribution of the jth mode to the variance, and the corresponding eigenfunction provides the associated spatial structure in the response. The eigenfunction corresponding to the largest σ_j is the optimal mode in the sense that it contributes most to the variance. The forcing profiles associated with each KL mode are obtained by solving the dual Lyapunov problem. For further details, the reader is referred to Farrell & Ioannou (1993*a,b*), Zhou *et al.* (1996), Bamieh & Dahleh (2001), Jovanović & Bamieh (2005) and Schmid (2007).

The response to optimal harmonic forcing and the variance maintained by stochastic forcing are computed based on the generalized Orr–Sommerfeld-Squire system (2.3). A Chebyshev-collocation method is used to discretize the above equations in the wall-normal direction. The discretized differentiation operators of Weideman & Reddy (2000), which include the appropriate boundary conditions, are used, and standard methods described in Schmid & Henningson (2001), for example, are used to compute the optimal harmonic response. The stochastic response is obtained by solving the Lyapunov equation (2.6) with the lyap function in MATLAB. The codes for computing the optimal harmonic and stochastic responses have been validated in Hwang & Cossu (2010). The results in this study are obtained by using from 129 to 513 collocation points as in Pujals *et al.* (2009).
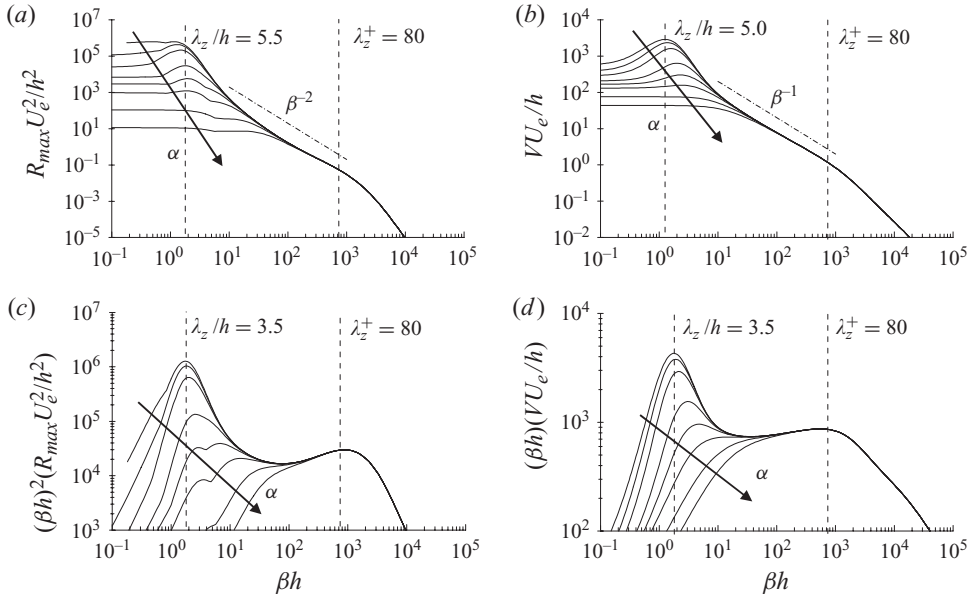
FIGURE 1. Energy amplifications and corresponding pre-multiplied energy amplifications of optimal harmonic and stochastic forcing at $Re_\tau = 10\,000$: (*a*) $R_{max}(\alpha, \beta)$, (*b*) $V(\alpha, \beta)$, (*c*) $\beta^2 R_{max}(\alpha, \beta)$ and (*d*) $\beta V(\alpha, \beta)$. Here, $\alpha h = 0.0, 0.1, 0.2, 0.5, 1.0, 2.0, 5.0, 10.0$, outer to inner curves.

3. Energy amplifications at $Re_\tau = 10\,000$

3.1. *Wavenumber dependence of the energy amplifications*

We begin by considering the single Reynolds number $Re_\tau = 10\,000$. R_{max} and V have been computed for a set of selected streamwise and spanwise wavenumbers and are reported in figures 1(*a*) and 1(*b*), respectively. In both cases, the largest amplifications are reached for streamwise uniform perturbations ($\alpha = 0$). Only streamwise-elongated perturbations ($\alpha \leqslant \beta$) are significantly amplified. R_{max} and V have a peak at $\beta = 1.25/h$ ($\lambda_z = 5.0h$) and $\beta = 1.14/h$ ($\lambda_z = 5.5h$), respectively, and they monotonously decrease as β increases, with a noticeable change of slope near $\lambda_z^+ \approx 80$. For spanwise wavenumbers roughly in the range $15 < \beta h < 400$ (and for $\alpha \ll \beta$), however, both R_{max} and V show an approximate linear dependence on β in log–log coordinates denoting a power-law dependence. A best fit in this range reveals a β^{-2} scaling for R_{max} and a β^{-1} scaling for V. A detailed discussion of these scalings is deferred to §5, where we will show that they are associated to geometrical similarity of optimal structures in the log layer. The deviations from the approximate β^{-2} and β^{-1} scalings are revealed by a pre-multiplication of R_{max} and V with β^2 and β, respectively. The pre-multiplied amplification curves, reported in figures 1(*c*) and 1(*d*), reveal the same double-peaked structure already observed for the optimal transient growth by del Álamo & Jiménez (2006) and Pujals *et al.* (2009). For both R_{max} and V, the peak associated with the streamwise uniform large-scale structures is found at $\beta h \simeq 1.8$ ($\lambda_z/h \simeq 3.5$), while that associated with near-wall streaks is found at $\beta^+ \simeq 0.079$ ($\lambda_z^+ \simeq 80$). These two optimal wavelengths delimit the range where the approximate power law can apply. From figures 1(*c*) and 1(*d*), it is also seen how, however, even at this very large Re_τ, the influence of the inner and outer scales is also felt well inside the intermediate wavenumber range.
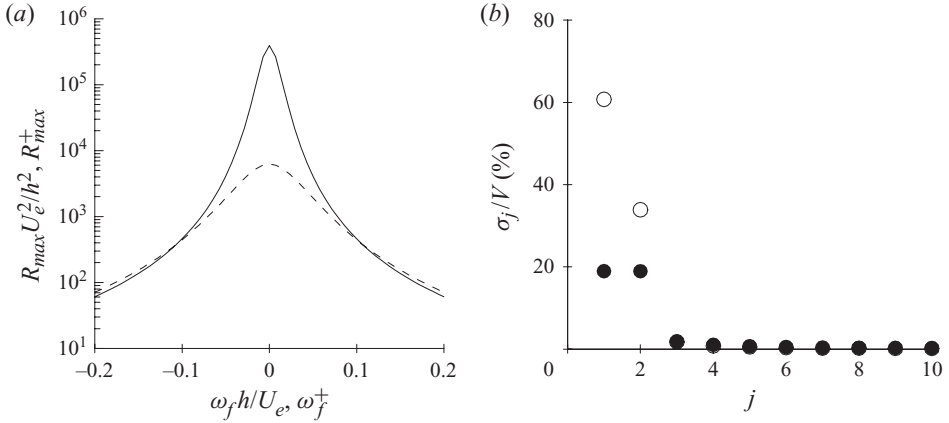
FIGURE 2. (*a*) Optimal harmonic amplification, R, plotted versus the forcing frequency, ω_f, in correspondence to the outer peak at $\lambda_z = 3.5h$ and to the inner peak at $\lambda_z^+ = 80$. (*b*) Contributions σ_j/V of the first 10 KL modes to the variance of the stochastic response in correspondence to the outer peak at $\lambda_z = 3.5h$ (○) and to the inner peak at $\lambda_z^+ = 80$ (●). Streamwise uniform perturbations ($\alpha = 0$) are considered.

3.2. *Optimal structures*

In figure 2, we analyse the 'selectivity' of the amplifications obtained in correspondence to the outer and inner peaks of the pre-multiplied amplifications for $\lambda_x = \infty$ ($\alpha = 0$), $\lambda_z = 3.5h$ and $\lambda_z^+ = 80$. For the structures associated to both the inner and the outer peak, the system behaves like a low-pass frequency filter, as seen from figure 2(*a*), where the dependence of the optimal response R on the forcing frequency ω_f is reported. The maximum amplification is reached with steady forcing ($\omega_{f,max} = 0$); the corresponding optimal structures are reported in figures 3(*a*) and 3(*c*), respectively. As expected, the optimal forcing represents streamwise vortices, while the optimal responses are streamwise streaks. The structures associated with the near-wall peak are located in the buffer layer, where they have a maximum amplitude at $y^+ \approx 10$, as for the experimentally observed near-wall streaks. The optimal forcing associated with the outer peak extends to the whole channel width and induces alternated high- and low-speed streamwise streaks on both walls.

The most energetic KL (POD) modes have been computed to seek the structures with the largest contribution to the variance V of the stochastic response in correspondence to the inner and outer peaks. From figure 2(*b*), where the contributions of the first 10 KL modes are reported, we see that for the outer peak, the dominant mode contributes to 64 % of the total variance. This mode fills the whole wall-normal domain (see figure 3*b*). For the wavenumbers associated to the inner peak, two dominant modes are found, each contributing to 23 % of the total variance. These two modes are associated to identical near-wall structures, respectively, located on the upper and the lower walls (see also figure 3*d*). Each mode can be obtained by the other one via a $y \rightarrow -y$ transformation.

The optimal perturbations reported in figure 3, corresponding to harmonic and stochastic forcing, respectively, are very similar. We further examine this resemblance by comparing in figure 4 their optimal inputs and outputs for wall-normal profiles. We also include, for comparison, the optimal perturbations computed by Pujals *et al.* (2009) for the initial-value problem. The optimal inputs and outputs of the three
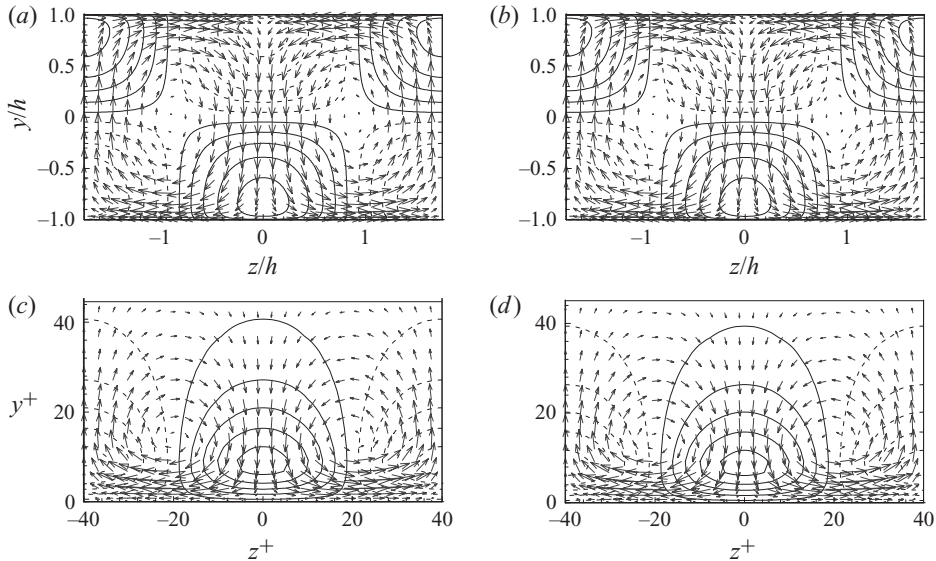
FIGURE 3. Cross-stream (y–z plane) view of the normalized optimal forcing and the corresponding response for spanwise wavenumbers corresponding to (a, b) the outer peak ($\lambda_z = 3.5h$) and (c, d) inner peak ($\lambda_z^+ = 80$) for harmonic forcing (a, c) and stochastic forcing (b, d). The solid and dashed contours denote the positive and negative streamwise velocity of the responses with increment of 0.2 from -0.9 to 0.9, respectively, and the vectors represent the cross-streamwise fields of the forcing. The perturbations are streamwise uniform ($\alpha = 0$).

different problems are almost identical. The optimal wall-normal input components (vortices) associated to the outer peaks have their maxima at the channel centre (figure 4a), and those associated to the inner peaks have their maxima at $y^+ \simeq 15$ (figure 4c). The maxima of the output streaks for the outer peaks are located at $|y/h| = 0.8$ (i.e. at a distance of 0.2h from the walls, figures 4b and 4d), while those for the inner peaks reach a maximum amplitude at $y^+ \simeq 10$ (figures 4b and 4d).

The resemblance of the optimal harmonic and stochastic forcing optimals is also observed for spanwise wavenumbers situated in the intermediate range between the two peaks of the pre-multiplied amplification curves reported in figures 4(b) and 4(e). The wall-normal maxima of these optimals are situated in the log layer (between $y^+ \approx 50$ and $y \approx 0.2h$) and their amplitude is negligible in the outer layer.

For the initial-value problem, del Álamo & Jiménez (2006) have found that, in the intermediate range, the optimal structures are, to a first approximation, geometrically similar. We have therefore plotted their profiles in the similarity variable $y^+/\lambda_z^+ = (y + h)/\lambda_z$ for three representative wavenumbers in the intermediate range. From figures 4(b) and 4(e), we see that the optimal input and output for the stochastic and harmonic forcing are, to a first approximation, geometrically similar. Their re-scaled shape is also not very different from that of the buffer-layer structures if those ones are re-scaled on their wavelength $\lambda_z^+ = 80$.

The results found for streamwise uniform structures ($\alpha = 0$) extend to the $\alpha \ll \beta$ case with only minor modifications. When $\alpha \neq 0$, the optimal forcing frequency is different from zero in the harmonic forcing case, and the real and imaginary part of the optimal perturbations display a slight tilting in the streamwise direction reminiscent of the Orr effect for purely two-dimensional perturbations (see e.g. Butler & Farrell 1992;
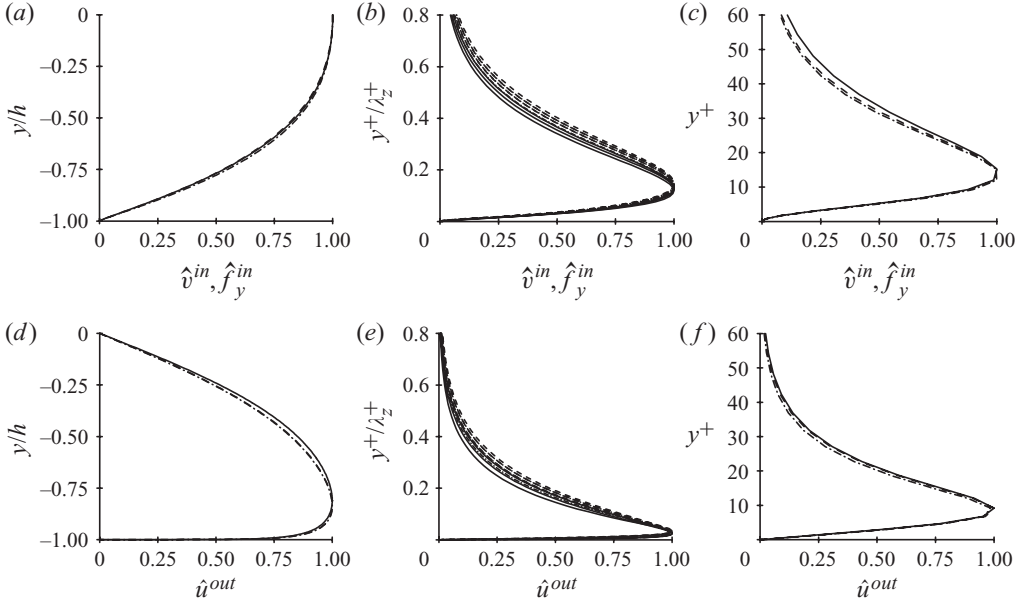
FIGURE 4. Profiles of streamwise uniform ($\alpha = 0$) optimal modes corresponding to the outer peak (a, d), the intermediate wavenumber range (b, e) and the inner peak (c, f) of the pre-multiplied amplifications. (a–c) Wall-normal components of the input (initial condition $\hat{v}^{in}(y)$ for transient growth and forcing $\hat{f}_y^{in}(y)$ for harmonic and stochastic forcing); (d–f) streamwise components of the corresponding outputs $\hat{u}^{out}(y)$. Here, ——, optimal transient growth; - - - -, optimal harmonic forcing; —·—·—, stochastic excitation. The outer and inner peaks correspond, respectively, to $\lambda_z = 4h$ and $\lambda_z^+ = 92$ for transient growth (see also Pujals *et al.* 2009), $\lambda_z = 3.5h$ and $\lambda_z^+ = 80$ for harmonic and stochastic forcing. In the intermediate β range between the outer and inner peaks, the wavenumbers $\beta^+ = 0.01/h, 0.005/h, 0.003/h$ ($\lambda_z^+ = 628, 1257, 2094$) are chosen. In ($b$, d), the profiles are plotted versus y/λ_z to account for the geometrical similarity of log-layer structures.

Schmid & Henningson 2001). However, the wall-normal amplitude of the optimal perturbations changes only slightly with respect to the streamwise uniform case, as shown in figure 5 where wavelengths typical of experimental observations ($\lambda_z = 3.5h$, $\lambda_x = 20h$) and ($\lambda_z^+ = 100$, $\lambda_x^+ = 600$) are considered. Also in this case, the optimal inputs and outputs obtained with the three different analyses (initial value, harmonic forcing and stochastic forcing) are almost indistinguishable (not shown).

4. Dependence on the Reynolds number

The optimal amplifications have been computed for selected values of Re_τ ranging from 500 to 20 000. For the Re_τ considered, it is found that the streamwise uniform ($\alpha = 0$) perturbations are the most amplified ones (not shown). The respective inner and outer scaling of the inner and outer peaks for both the response to harmonic and to stochastic forcing is clearly seen in figure 6, where the pre-multiplied optimal amplifications for $\alpha = 0$ are reported versus the spanwise wavenumber β scaled in outer and inner units. The maximum amplifications associated with the outer peak clearly increases with Re_τ, as already found by Pujals *et al.* (2009) and Cossu, Pujals & Depardon (2009) in the optimal transient growth case. The amplifications
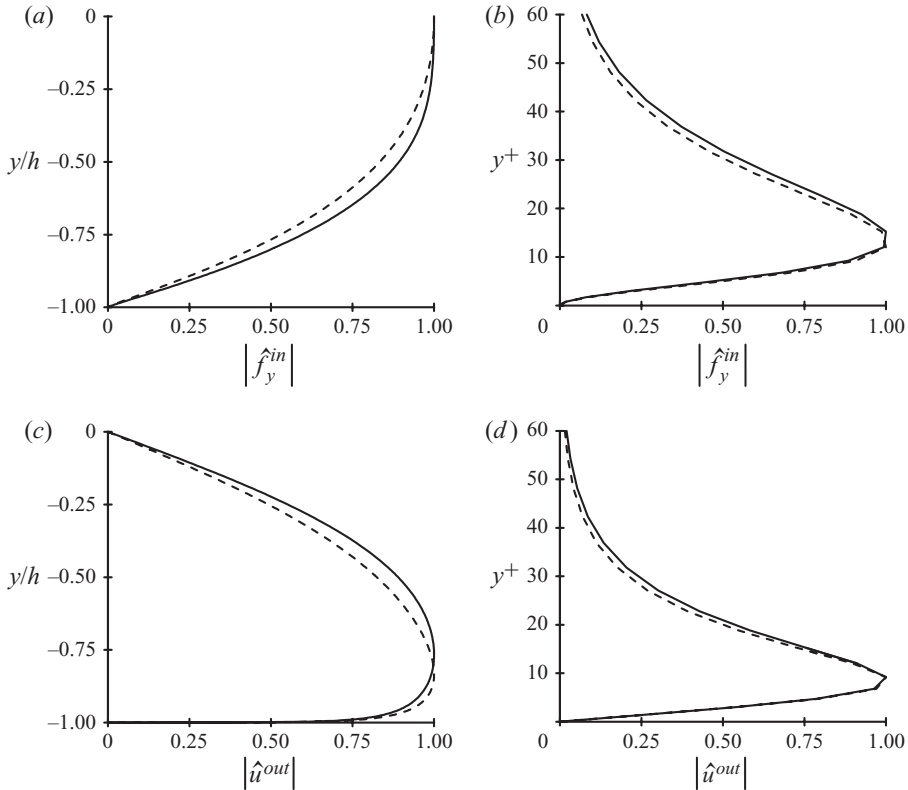
FIGURE 5. Solid lines: profiles of optimal modes with $\lambda_x \approx 6\lambda_z$ ($\alpha = 0.167\beta$) for (a, c) wavelengths in the neighbourhood of the outer peak ($\lambda_z = 3.5h$, $\lambda_x = 20h$) and (b, d) wavelengths in the neighbourhood of the inner peak ($\lambda_z^+ = 100$, $\lambda_x^+ = 600$). (a, b) Wall-normal components of the optimal input $|\hat{f}_y^{in}|(y)$ amplitude for harmonic forcing; (c, d) streamwise components of the amplitude of the corresponding output $|\hat{u}|(y)$. The streamwise uniform perturbations ($\alpha = 0$, $\lambda_x = \infty$) with the same spanwise wavelength are also reported for comparison as dashed lines. Only the perturbations for the optimal harmonic forcing are reported; those for the optimal initial-value problem and for stochastic forcing are almost indistinguishable.

associated with the inner peak do not sensibly change with Re_τ, when re-scaled in inner units.

The shape of the optimal input and output harmonic forcing profiles for, respectively, the inner and outer peaks already reported in figure 4 are re-plotted in figure 7 for the considered Reynolds numbers Re_τ ranging from 500 to 20 000. From this figure, it is apparent that their shape does not change with the Reynolds number when it is plotted in, respectively, inner and outer units. This extends to the harmonic forcing case the results for the initial-value problem found by Pujals *et al.* (2009) for the turbulent channel and by Cossu *et al.* (2009) in the turbulent boundary layer. Exactly the same results are found when considering the maximum energy KL (POD) modes for the stochastic forcing case. Pujals *et al.* (2009) and Cossu *et al.* (2009) also observed that when the wall-normal profile $\hat{u}(y)$ of the optimal streaks corresponding to the outer peak are scaled in inner units, they coincide in the inner layer ($y < \approx 0.1h$), where they are proportional to the mean-flow profile $U_b(y)$. Here, we find that the same applies to the optimal responses to forcing, as can be seen
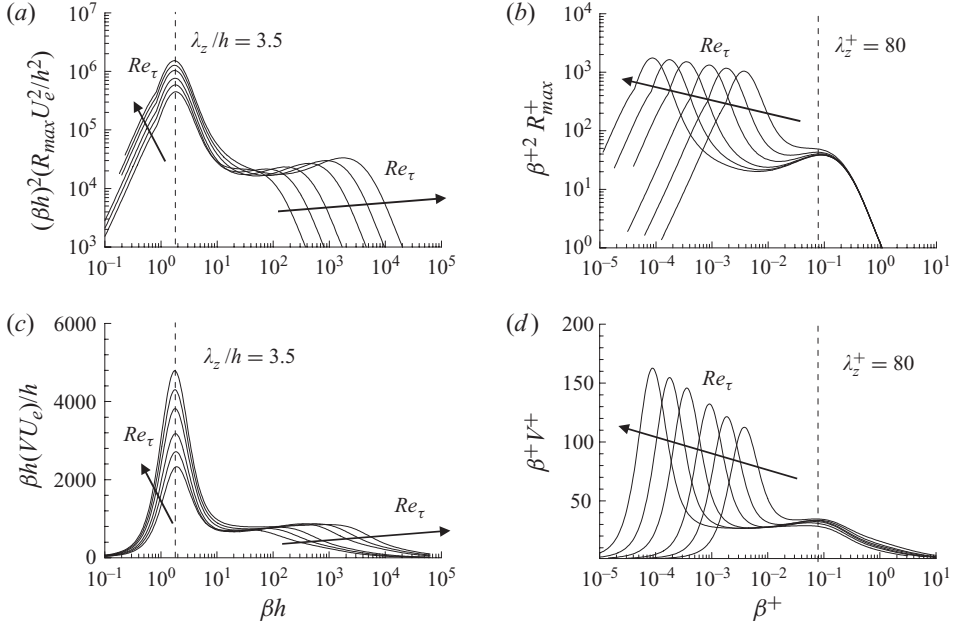
FIGURE 6. Pre-multiplied responses to (a, b) optimal harmonic forcing and (c, d) stochastic excitation with respect to the spanwise wavenumber for the Reynolds numbers $Re_\tau = 500, 1000, 2000, 5000, 10\,000$ and $20\,000$: (a, c) scaling in the outer units; (b, d) scaling in the inner units.
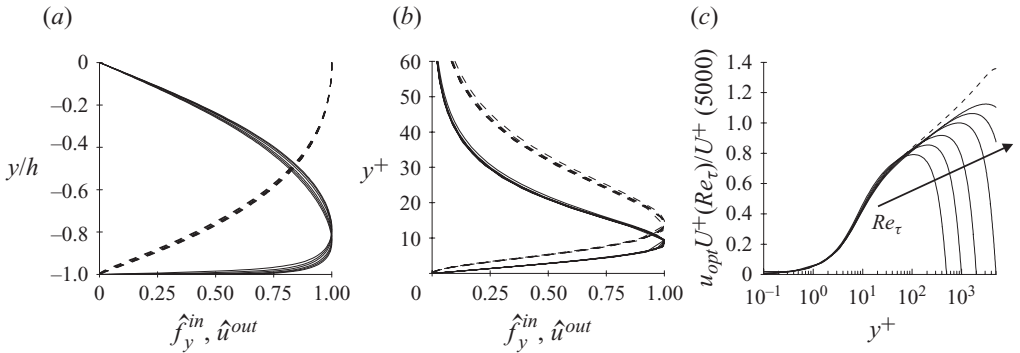

FIGURE 7. Profiles of the wall-normal component $\hat{f}_y^{in}(y)$ of the optimal harmonic forcing and the streamwise component $\hat{u}^{out}(y)$ of its response at (a) the outer peak $(\alpha h = 0, \beta h = 1.8)$ and (b) the inner peak $(\alpha^+ = 0, \beta^+ = 0.079)$ for $Re_\tau = 500, 1000, 2000, 5000, 10\,000$ and $20\,000$. Note that all the curves are almost indistinguishable. Here, $----$, $\hat{f}_y^{in}$; ———, $\hat{u}^{out}$. (c) Outer peak streamwise velocity response $\hat{u}^{out}(y)$ scaled with a factor $U_e^+(Re_\tau)/U_e^+(5000)$ for the selected Reynolds numbers. The re-scaled mean flow profile at $Re_\tau = 5000$ (dashed line) is also shown for comparison.

in figure 7(c) where the optimal outer-peak streak amplitudes $\hat{u}$ are plotted in inner units. From figure 7(c), it is also seen that the optimal streaks associated to the outer peak deeply penetrate into the buffer layer; as in the optimal transient growth case, the streaks at $y^+ = 12$ still exhibit half of their maximum amplitude.

5. Scaling of optimal amplifications of geometrically similar log-layer structures

The numerical results reported in §3 have shown that the amplifications R_{max} and V of the most amplified streamwise-elongated perturbations ($\alpha \ll \beta$) exhibit an approximate β^{-2} and β^{-1} scaling, respectively, in the intermediate β range. The data reported in figures 4(b) and 4(e) also show that the associated optimal input and outputs are, to first order, geometrically similar, consistent with the previous findings of del Álamo & Jiménez (2006). Furthermore, these optimal perturbations have maximum amplitude in the log layer, and have negligible amplitudes in the outer layer. In §5, we show that the observed β^{-2} and β^{-1} scalings can be directly deduced from the generalized Orr–Sommerfeld–Squire model (2.3) under the assumptions of log-layer behaviour of the base-flow profile and of geometric similarity of the perturbations. We consider streamwise uniform ($\alpha = 0$) perturbations that, besides being the most amplified ones, are also easily tractable.

Spanwise periodic, geometrically similar streamwise uniform velocity and forcing fields are identical in the variables $y^+/\lambda_z^+ = (y+h)/\lambda_z$, $z^+/\lambda_z^+ = z/\lambda_z$. As a consequence, their Fourier amplitudes at different λ_z are given by the same function of the re-scaled wall-normal coordinate $\check{y} = \bar{\beta}(y+h)$ with $\bar{\beta} = (\beta/\check{\beta})$ so that $(y+h)/\lambda_z = \check{y}/\check{\lambda}_z$, where the reference spanwise wavenumber $\check{\beta}$ can be arbitrarily chosen. The re-scaled state vector is defined as $\check{q} = [\hat{v}, \hat{\omega}_y/\bar{\beta}]^T(\check{y}, t)$. The re-scaling of the wall-normal vorticity is due to the fact that, for streamwise uniform perturbations, $\hat{\omega}_y = i\beta\hat{u}$, and therefore the similarity is obtained on $\hat{\omega}_y/\beta$ instead of $\hat{\omega}_y$. In the Appendix we detail how, assuming a logarithmic behaviour for the base flow and reformulating system (2.3) in terms of re-scaled variables, the following system is obtained: $\partial\check{q}/\partial t = \bar{\beta}\check{A}\check{q} + \check{B}\hat{f}$, with $\hat{u} = \check{C}\check{q}$ and for the initial conditions $\check{q}_0 = \check{D}\hat{u}_0$. The operators $\check{A}$, $\check{B}$, $\check{C}$ and $\check{D}$ are obtained by simply evaluating A, B, C and D at the reference $\check{\beta}$ and $\alpha = 0$. These operators therefore do not depend on β.

The solution of the initial-value problem without forcing $\partial\check{q}/\partial t = \bar{\beta}\check{A}\check{q}$ is $\check{q} = e^{t\bar{\beta}\check{A}}\check{q}_0$ and depends on time only via $\bar{\beta}t$. We therefore define the re-scaled time $\bar{t} = \bar{\beta}t$ and rewrite the system as

$$\frac{\partial\check{q}}{\partial\bar{t}} = \check{A}\check{q} + \bar{\beta}^{-1}\check{B}\hat{f}. \tag{5.1}$$

In the case of the initial-value problem without forcing, the solution in terms of velocity is $\hat{u} = \check{C}e^{\bar{t}\check{A}}\check{D}\hat{u}_0$. The optimal energy growth is $G = \max_{\hat{u}_0} \|\hat{u}\|^2/\|\hat{u}_0\|^2 = \|\check{C}e^{\bar{t}\check{A}}\check{D}\|^2$. The dependence of the optimal growth on β appears only through the re-scaled time and therefore

$$G(\beta, t) = G(\check{\beta}, \bar{t}\check{\beta}/\beta). \tag{5.2}$$

The optimal growth for a given β is given by the optimal growth computed at the reference $\check{\beta}$ re-scaled in time with a factor $\check{\beta}/\beta$. The time at which the maximum growth is attained, $t_{max} = \bar{t}_{max}\check{\beta}/\beta$, is therefore proportional to the wavelength λ_z of the perturbation, while the maximum growth $G_{max} = \max_t G(t)$ does not depend on β. These properties have indeed been observed in the computations of optimal transient growth (del Álamo & Jiménez 2006; Cossu *et al.* 2009; Pujals *et al.* 2009) for the range of spanwise wavenumbers associated with log-layer structures.

In the case of harmonic forcing, the re-scaled forcing frequency $\bar{\omega}_f = \omega_f/\bar{\beta}$ can be defined such that $\omega_f t = \bar{\omega}_f\bar{t}$. From (5.1) it then follows that the harmonic response $\hat{u} = \tilde{u}\,e^{i\bar{\omega}_f\bar{t}}$ to the harmonic forcing $\hat{f} = \tilde{f}\,e^{i\bar{\omega}_f\bar{t}}$ is $\tilde{u} = \bar{\beta}^{-1}\check{H}\tilde{f}$, where

$\check{\boldsymbol{H}} = \check{\boldsymbol{C}}(i\bar{\omega}_f \boldsymbol{I} - \check{\boldsymbol{A}})^{-1}\check{\boldsymbol{B}}$. The optimal amplification is $R = \bar{\beta}^{-2}\|\check{\boldsymbol{H}}\|^2$ which implies that

$$R(\beta, \omega_f) = \left(\frac{\check{\beta}}{\beta}\right)^2 R(\check{\beta}, \bar{\omega}_f \beta/\check{\beta}). \qquad (5.3)$$

The maximum optimal harmonic amplification R_{max} therefore scales like β^{-2} and is found for $\omega_{f,max} = \bar{\omega}_{f,max}\beta/\check{\beta}$. These predictions agree with what is observed, to a first approximation, for the optimal harmonic amplification in the intermediate wavenumber regime.

Finally, the variance V of the response to stochastic forcing can be obtained in the frequency domain as $V = (1/2\pi)\int_{-\infty}^{\infty} \text{trace}(\boldsymbol{HH}^{\dagger})\,d\omega$. Under the assumptions of §5, $\boldsymbol{H} = \bar{\beta}^{-1}\check{\boldsymbol{H}}$ so that, changing the integration variable to $\omega = \bar{\beta}\bar{\omega}$, it is found that $V = (\bar{\beta}^{-1}/2\pi)\int_{-\infty}^{\infty} \text{trace}[(\check{\boldsymbol{H}}\check{\boldsymbol{H}}^{\dagger})]\,d\bar{\omega}$ and therefore

$$V(\beta) = \left(\frac{\check{\beta}}{\beta}\right) V(\check{\beta}). \qquad (5.4)$$

The variance therefore scales like β^{-1}, as found from the numerical results reported in §3.

6. Discussion

6.1. *Remarks on the scaling of geometrically similar log-layer perturbations*

The numerical results reported in §3 have shown that in an intermediate β range, the optimal perturbations exhibit an approximate geometrical similarity in the log layer, which is completely compatible with the concept of geometrically similar 'attached' eddies proposed by Townsend (1976) and further developed in the theory of Perry & Chong (1982) and many others, and with the experimental findings of Morrison & Kronauer (1969).

In the intermediate β range, where the approximate geometrical similarity is observed, the amplification of the optimal harmonic and stochastic forcing displays an approximate β^{-2} and β^{-1} scaling. Exactly the same β scalings are predicted by assuming geometrically similar perturbations and a log-layer form for the base flow and the associated eddy viscosity in the generalized Orr–Sommefeld–Squire operators, as shown in §5. The examination of the pre-multiplied amplification curves, however, reveals that the power-law dependence is only a first-order approximation and that the influence of the outer and inner scales is important even in the intermediate wavenumber regime, where a sort of plateau would be expected. A possible explanation for this, among others, is that the considered Reynolds numbers are not sufficiently high for a well-defined plateau to exist. The examination of figure 6 reveals that, actually, a sort of plateau seems to develop when the Reynolds number is increased, even if no definite conclusion can be drawn from these results. However, an order of magnitude of the minimum Reynolds number necessary to observe the hypothetical plateau, can be evaluated from the existing data. From figure 4(e) it is seen that in the geometrically similar regime the optimal response (streaks) amplitude $\hat{u}(y)$ becomes negligible for $y^+ > \approx 0.6\lambda_z^+$, while it is maximum at $y^+ \approx 0.05\lambda_z^+$. Let us assume that the log layer extends from $y^+ \approx 50$ to $(y + h) \approx 0.2h$. If the maximum of the geometrically similar streaks has to be in the log layer then $0.05\lambda_z^+ > 50$, i.e. $\lambda_z^+ > \lambda_{z,min}^+ = 1000$ and in outer units $\lambda_{z,min} = 1000h/Re_\tau$. If it is further required that the streak amplitude is negligible outside the log layer

then $0.6\lambda_z < 0.2h$, i.e. $\lambda_z < \lambda_{z,max} = h/3$. The condition $\lambda_{z,max}/\lambda_{z,min} > 1$ leads to the requirement $Re_\tau > O(10^3)$. If it is required that a plateau exist on at least two wavelength (or wavenumber) decades then the condition is $Re_\tau > O(10^5)$, which suggests that the considered Reynolds numbers may not be sufficiently high to observe a well-defined plateau in the pre-multiplied amplification curves. However, other possible explanations for the absence of a well-defined plateau may exist, such as a structural lack of exact similarity of the log-layer structures even at large Re_τ. This issue therefore has to be considered unsolved.

6.2. *Non-normality and the large influence of large-scale optimal perturbations on the near-wall velocity field*

A noteworthy feature of the optimal streaks at large scale is that, even if they scale in outer units, they strongly penetrate into the inner layers where they still posses a large fraction of their maximum amplitude (as seen e.g. in figures 4*d*, 5*c*, 7*a* and 7*c*). These optimal output streaks are induced by optimal inputs (initial condition or forcing) that are located essentially in the outer layer (see e.g. figures 4*a*, 5*a* and 7*a*). The forcing of optimal input vortices in the outer layer therefore leads to a large response in the inner layer. This is the case even when the input g is not optimal. The input can, indeed, be decomposed in a part parallel to the optimal input and another part orthogonal to it as $g = A f^{(opt)} + g^\perp$ (where parallel and orthogonal are meant in the sense of the inner product used to define the energy norm, $f^{(opt)}$ is normalized to unit energy and A is the amplitude of the projection of g on $f^{(opt)}$). As the system is linear, the response to g is the sum of the responses to $A f^{(opt)}$ and $g^\perp$, respectively. As the response to $f^{(opt)}$ is very large, the global output streak will have a large component proportional to the optimal large-scale streak, except in the very special case where A is negligible. As, furthermore, the maximum amplification associated to the peak scaling in outer units increases with the Reynolds number Re_τ, the influence of the outer-layer motions on the inner-layer streamwise velocity is predicted to increase with Re_τ. This is what is observed in the real turbulent flows.

The fact that outer-layer motions can influence the near-wall region has been known at least since the seminal study of Townsend (1976). This influence has usually been interpreted 'kinematically' in terms of the velocity field directly induced by the outer motions. What is revealed by this study, and the previous ones in the same spirit, is that the large influence of outer-layer motions on the near-wall streamwise velocity is mainly 'dynamic', and based on the strong non-normality of the underlying linearized operator. The increase of the outer-layer influence with the Reynolds number is also naturally embedded in this non-normal dynamic mechanism. This interpretation also predicts that, when an integral over all spanwise wavelengths is performed, the total streamwise variance near the wall does not scale only in inner units, when components from motions at large scale are considered, and that an inner units scaling will be less and less accurate when Re_τ is increased. These qualitative predictions are compatible with the observations of De Graaff & Eaton (2000), Hunt & Morrison (2000), Metzger & Klewicki (2001), del Álamo *et al.* (2004) and Hutchins & Marusic (2007*a*). However, note that recent studies reveal that large-scale outer motions are also able to modulate the amplitude of the near-wall cycle (see, e.g. Hutchins & Marusic 2007*b*; Mathis *et al.* 2009). This effect, which is probably nonlinear, is not taken into account by the present linear analysis.
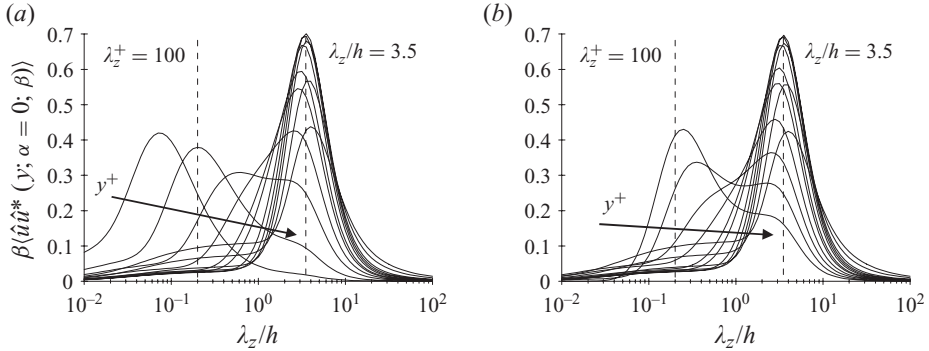
FIGURE 8. Pre-multiplied spectral density at each wall-normal location for the streamwise uniform case $\beta\hat{u}\hat{u}^*(y; \alpha = 0, \beta)$ based on the response to stochastic forcing (a) without wall-damping function and (b) with wall-damping function $f_d(y) = 1 - \exp(-(y^+/A^+)^3)$, where $A^+ = 25$. Here, the wall-normal location is chosen to be $y^+ = 5, 15, 29, 48, 71, 98, 155, 202, 309, 402, 500$ and each pre-multiplied spectral density is normalized by its area to emphasize its contents in spanwise wavenumbers. The considered Reynolds number is $Re_\tau = 500$ to allow comparison with Jiménez (1998).

6.3. *Relevance of the stochastic forcing analysis*

When trying to relate the results of the present analysis to experimental observations of unforced turbulent flows, considering stochastic forcing is probably more relevant than considering harmonic forcing. In the spirit of Farrell & Ioannou (1994) and Farrell & Ioannou (1998), the stochastic forcing can be assumed to be a surrogate for the nonlinear terms that are neglected in the linearized model. The distribution $V(\alpha, \beta)$ would then represent the linear amplification of the variance of the nonlinear terms, where the whole variance integrated in the wall-normal direction is considered. More detailed information can, however, be extracted from the operator $\boldsymbol{CX}_\infty\boldsymbol{C}^\dagger$, which gives the spatial spectral density amplification tensor of the correlations of $\hat{u}_i^*(y, t)\hat{u}_j(y', t)$. This tensor has been computed assuming that the forcing variance is uniform in y, which is not a realistic or even qualitatively correct assumption, especially near the wall. This can be seen in figure 8(a), where we report the normalized spanwise pre-multiplied spectra $\beta E_{uu}(\alpha = 0, \beta)$ at selected distances y from the wall for $Re_\tau = 500$. The agreement of these curves with those reported by Jiménez (1998) and based on DNS data (at $Re_\tau = 590$) is obviously only qualitative: the outer-layer spanwise peak predicted at $\lambda_z \approx 3.5h$ is found at 1.5–2h in the DNS. Furthermore, at $y^+ = 5$ the peak is found at values well below the expected $\lambda^+ \approx 100$. Upgrading the simple Gaussian probability distribution to something more refined would probably not have a large effect on the presented results, as only low-order statistics are considered. However, a better modelling of the wall-normal distribution of the forcing can probably improve the results. For instance, it is not likely that the nonlinear terms at $y^+ = 5$ have the same amplitude as, for instance, in the buffer layer, where the near-wall self-sustaining cycle is located. If, then, the operator $\boldsymbol{CX}_\infty\boldsymbol{C}^\dagger$ is recomputed, enforcing that the variance of the forcing decreases in the viscous sublayer, then the pre-multiplied amplification spectra at $y^+ = 5$ are improved, as shown in figure 8(b).

More realistic forcing distributions have not been considered, on purpose. Actually, the most relevant result of the presented stochastic response analysis is that, even with this extremely unrealistic input (Gaussian isotropic flat spectrum, uniform in

the wall-normal direction), the output displays properties observed in real turbulent flows (strongly anisotropic velocity field with a dominant streak component, strongly non-flat spectrum with spanwise scales in the range of those observed in the real flows, approximate geometric similarity for intermediate wavenumbers). The fact that qualitatively 'realistic' spanwise scales are selected by the non-normal linear amplification mechanism suggests that this mechanism plays an important role in the real turbulent flows. However, the linear theory alone probably does not say much about the scale selection in the streamwise direction. In self-sustained processes, both the linear amplification and the nonlinear refuelling of the amplification process are necessary to select specific structures. The modelling of these additional nonlinear processes is completely absent from the present investigation. The exploration of these additional processes in fully turbulent flows is the object of current intensive investigation.

6.4. *Relevance of the harmonic forcing analysis*

Even if information on the spatio-temporal energy spectral densities for stochastic forcing can be extracted from the operator $[\boldsymbol{HH}^{\dagger}](\alpha, \beta, \omega)$, the main use of the harmonic forcing analysis is in its prediction of the optimal response to deterministic forcing. The deterministic forcing analysis has, for instance, been recently used by McKeon (2008) to analyse the effect of 'dynamic roughness' at $Re_{\tau} = 500$.

Our results indicate that the largest response to forcing is expected for the steady or very-low-frequency forcing of large-scale structures with $\lambda_z \approx 2\text{--}6h$ and that the associated amplification can be very large, if compared to stochastic forcing, for example. A large sensitivity to steady forcing has indeed been observed in recent experiments on Couette and boundary layer flows (Kitoh *et al.* 2005; Kitoh & Umeki 2008; Pujals, Cossu & Depardon 2010*a*) where the large-scale streaky motions are artificially forced by passive devices.

The strong amplification of the harmonic forcing can be exploited to efficiently manipulate the turbulent mean flow. As the forced streaks must reach a finite amplitude in order to modify the mean flow at leading order, nonlinear effects must in principle be taken into account in the analysis. However, a series of previous investigations has shown that if the amplitude of the forced streaks is not too large ($\approx 10\text{--}15\,\%$ of U_e), the main nonlinear effects essentially reduce to a saturation of the streaks' amplitude, whose amplification, however, remains large. Indeed, Willis, Hwang & Cossu (2009, 2010) have forced large-scale linearly optimal $\alpha = 0$ vortices, computed with the same approach used in this study, in a DNS of the turbulent pipe flow. A large amplification of the forcing is observed and the induced large-scale finite-amplitude streaks modify the flow at leading order and induce a reduction of the turbulent drag consistently with the results of Schoppa & Hussain (1998) (plane channel flow, DNS) and Iuso *et al.* (2002) (boundary layer, experimental results).

The above results more generally confirm the conclusions obtained in related studies, where the framework is spatial transient growth, that the large amplifications associated with the coherent lift-up effect can be successfully exploited for flow control applications. In the experiments of Fransson *et al.* (2004), finite-amplitude streamwise streaks with the optimal spanwise wavelength predicted by the linear optimal spatial transient growth analysis of Andersson, Berggren & Henningson (1999) have been artificially forced in the laminar Blasius boundary layer. These streaks display large spatial amplifications, with amplitudes up to $\approx 13\,\%$ of U_e, and the leading-order effect on the base flow is instrumental in improving its stability with respect to Tollmien–Schlichting waves (Cossu & Brandt 2002, 2004; Fransson *et al.* 2005) and in delaying

transition to turbulence (Fransson *et al.* 2006). In a similar way, Pujals *et al.* (2010*a*) have forced steady large-scale coherent streamwise streaks in the flat-plate turbulent boundary layer, also showing that in this case the large-scale coherent streaks display a non-normal amplification at finite amplitude. Furthermore, Pujals *et al.* (2010*a*) show that the most amplified spanwise wavelengths correspond well to the optimal values predicted in the optimal transient growth analysis of Cossu *et al.* (2009) despite the fact that this latter prediction is based on a temporal analysis (for $\alpha = 0$) and not on a spatial analysis. Pujals, Depardon & Cossu (2010*b*) have used the same type of forcing of Pujals *et al.* (2010*a*) to induce coherent streaks on the roof of an Ahmed body, which is relevant for industrial applications. In this latter case the forced streaks are no more optimal and the base flow is strongly non-parallel, but nevertheless the streaks are sufficiently amplified to modify the base flow at leading order. This mean flow modification has been shown to suppress the separation on the rear end of the Ahmed body.

7. Summary and conclusions

The main objective of the present investigation was to understand how small coherent perturbations to the turbulent channel flow respond to stochastic and deterministic forcing. Following Reynolds & Hussain (1972), del Álamo & Jiménez (2006), Pujals *et al.* (2009), Cossu *et al.* (2009) and Hwang & Cossu (2010), we have used a linear model including eddy viscosity for the dynamics of coherent perturbations. The main results are as follows.

(*a*) Only structures elongated in the streamwise direction are significantly amplified, and the most amplified ones are streamwise uniform ($\alpha = 0$; $\lambda_x = \infty$). The optimal outputs are strongly anisotropic, with a dominant streamwise component (streaks), while the optimal inputs have dominant cross-stream components (streamwise vortices).

(*b*) The energy amplification by the optimal harmonic forcing is more than two orders of magnitude larger than the amplification of the variance induced by stochastic forcing.

(*c*) The amplification of the optimal harmonic and stochastic forcing of streamwise uniform structures are found to approximatively scale with the spanwise wavenumber as β^{-2} and β^{-1}, respectively, in an intermediate β range where the optimal structures are found to be, to a first approximation, geometrically similar.

(*d*) We show that the numerically observed β^{-2} and β^{-1} approximate scalings can be formally derived from the linearized system assuming geometric similarity for the coherent perturbations and a logarithmic base flow. Following this approach, it is also shown that, in the same regime, the optimal transient growth of initial perturbation does not depend on β and that the time of maximum growth scales linearly with λ_z.

(*e*) To detect the deviations from the log-layer regime, the optimal harmonic (R_{max}) and stochastic (V) amplifications obtained for $\alpha = 0$ have been pre-multiplied by β^2 and β, respectively. The pre-multiplied amplification curves clearly show two peaks. For both the harmonic and the stochastic forcing cases, the dominant (outer) peak scales in outer units with a most-amplified wavelength of $\lambda_z = 3.5h$, while the secondary peak scales in inner units with an optimal wavelength of $\lambda^+ = 80$.

(*f*) The amplifications associated with the outer (dominant) peak increase with the Reynolds number, while those associated with the inner (secondary) peak and those in the log-layer scaling region are almost independent of the Reynolds number if scaled in inner units.

(*g*) The shapes of the optimal input and outputs associated to the outer and inner peaks of the pre-multiplied amplifications are almost independent from the Reynolds number when plotted in outer and inner units, respectively. Furthermore, the optimal inputs and outputs of the three different optimal frameworks (harmonic forcing, stochastic forcing, initial-value problems) all have the same shapes. The profiles of the streak amplitude $\hat{u}(y)$ corresponding to the outer peak are proportional to the turbulent mean flow profile in the inner layer.

These results extend and complete the previous analyses of del Álamo & Jiménez (2006) and Pujals *et al.* (2009), which considered the optimal response to initial conditions in the turbulent channel. In accordance with these studies we find that the optimal inputs and outputs are streamwise uniform and are quasi-geometrically similar in the intermediate β range where they scale with their spanwise wavelength, which is also in accordance with the idea of geometrically similar attached eddies proposed by Townsend (1976). The two peaks in the 'pre-multiplied' amplification curves are also found at wavelengths $\lambda_z^+ \approx 80$–100 and $\lambda_z/h \approx 3$–4 very similar to those found for the optimal initial-value problem. Optimal growths and perturbations with $\alpha \ll \beta$ are very similar to those found for $\alpha = 0$. The optimal structures associated to the inner and outer peaks (possibly with $\alpha \ll \beta$) correspond qualitatively, in size and shape, to the most energetic streamwise streaks, respectively, observed in the buffer layer (Kline *et al.* 1967; Smith & Metzler 1983; Robinson 1991) and at very large scales in the channel (del Álamo *et al.* 2004; Jiménez 2007), as already discussed by del Álamo & Jiménez (2006) for example. This correspondence can only be qualitative because of the crude assumptions used in the present analysis, like the linear approximation, or the modelling of the Reynolds stress with an isotropic eddy viscosity.

The near-coincidence of the optimal perturbations pertaining to the three different analyses (initial-value problem, harmonic and stochastic forcing) is, however, unexpected and currently unexplained. This issue certainly deserves further investigation to understand whether this result is general and to provide a sound explanation for it.

The most important difference between the three different linear input–output analyses comes from the different scaling of the optimal amplifications in the intermediate β range: β^{-2} for the optimal harmonic forcing, β^{-1} for the stochastic forcing and β^0 (no dependence) for the initial-value problem. We have shown how this different behaviour directly stems from the β scaling of the whole linear generalized Orr–Sommerfeld–Squire operator obtained when perturbations are assumed to be geometrically similar and a base flow profile and eddy viscosity with log-layer properties are assumed. The same arguments explain the proportionality to λ_z of the time of maximum temporal growth of log-layer structures observed by del Álamo & Jiménez (2006) and Pujals *et al.* (2009).

Appendix. Re-scaled operators in the log-layer approximation

The Fourier amplitudes of spanwise periodic, geometrically similar streamwise uniform fields are given by the same function of the re-scaled wall-normal coordinate

$\check{y} = \bar{\beta}(y + h)$, where $\check{\beta}$ is taken as the reference spanwise wavenumber, and the wavenumber re-scaling factor is defined by $\bar{\beta} = (\beta/\check{\beta})$. The chain rule immediately gives $\mathscr{D} = \bar{\beta}\check{\mathscr{D}}$ with $\check{\mathscr{D}} = \partial/\partial\check{y}$, and therefore $\Delta = \bar{\beta}^2\check{\Delta}$ and $\Delta^{-1} = \bar{\beta}^{-2}\check{\Delta}^{-1}$ with $\check{\Delta} = \check{\mathscr{D}}^2 - \check{\beta}^2$.

As in the log layer the shear of the base flow is $U' = u_\tau/\kappa(y + h) = \bar{\beta}u_\tau/\kappa\check{y}$, we assume that $U' = \bar{\beta}\check{U}'$, where $\check{U}' = \check{\mathscr{D}}U(\check{y})$. Furthermore, in the log region the Reynolds stress is to a first approximation constant and equal to u_τ^2, which gives for the eddy viscosity introduced in §2 $\nu_T(y) = u_\tau\kappa(y + h) = \bar{\beta}^{-1}u_\tau\kappa\check{y}$. We therefore also assume that $\nu_T = \bar{\beta}^{-1}\check{\nu}_T$, where $\check{\nu}_T = \nu_T\check{y}$. From the above assumptions replaced in system (2.3) and further assuming $\alpha = 0$, the following re-scaled system is found:

$$\frac{\partial\check{q}}{\partial t} = \bar{\beta}\check{A}\check{q} + \check{B}\hat{f}, \qquad (A\,1a)$$

where $\check{q} = [\check{v}, \check{\omega}_y]^T$ with $\check{v} = \hat{v}$, $\check{\omega}_y = \hat{\omega}_y/\bar{\beta}$. As already mentioned in §2.1, the wall-normal vorticity had been re-scaled with $\bar{\beta}$ to preserve the self-similarity on the velocity field u when β is changed. The operators $\check{A}$ and $\check{B}$ are

$$\check{A} = \begin{bmatrix} \check{\Delta}^{-1}\check{\mathscr{L}}_{OS} & 0 \\ -i\check{\beta}\check{U}' & \check{\mathscr{L}}_{SQ} \end{bmatrix}, \qquad \check{B} = \begin{bmatrix} 0 & -\check{\beta}^2\check{\Delta}^{-1} & -i\check{\beta}\check{\Delta}^{-1}\check{\mathscr{D}} \\ i\check{\beta} & 0 & 0 \end{bmatrix}, \qquad (A\,1b)$$

with

$$\check{\mathscr{L}}_{OS} = \check{\nu}_T\check{\Delta}^2 + 2\check{\nu}_T'\check{\Delta}\check{\mathscr{D}} + \check{\nu}_T''(\check{\mathscr{D}}^2 + \check{\beta}^2), \qquad (A\,1c)$$

$$\check{\mathscr{L}}_{SQ} = \check{\nu}_T\check{\Delta} + \check{\nu}_T'\check{\mathscr{D}}. \qquad (A\,1d)$$

The velocity components are obtained from the wall-normal variables with

$$\hat{u} = \check{C}\check{q}, \qquad \check{C} = \frac{1}{\check{\beta}^2}\begin{bmatrix} 0 & -i\check{\beta} \\ \check{\beta}^2 & 0 \\ i\check{\beta}\check{\mathscr{D}} & 0 \end{bmatrix}. \qquad (A\,1e)$$

The re-scaled state vector $\check{q}$ can also be obtained from the velocity with

$$\check{q} = \check{D}\hat{u}, \qquad \check{D} = \begin{bmatrix} 0 & 1 & 0 \\ i\check{\beta} & 0 & 0 \end{bmatrix}. \qquad (A\,1f)$$

The operators $\check{A}$, $\check{B}$, $\check{C}$, $\check{D}$ and $\check{\mathscr{L}}_{OS}$, $\check{\mathscr{L}}_{SQ}$ do not depend on $\bar{\beta}$ (and β), but only on the reference value $\check{\beta}$.

REFERENCES

DEL ÁLAMO, J. & JIMÉNEZ, J. 2003 Spectra of the very large anisotropic scales in turbulent channels. *Phys. Fluids* **15**, L41.

DEL ÁLAMO, J. C. & JIMÉNEZ, J. 2006 Linear energy amplification in turbulent channels. *J. Fluid Mech.* **559**, 205–213.

DEL ÁLAMO, J. C., JIMÉNEZ, J., ZANDONADE, P. & MOSER, R. D. 2004 Scaling of the energy spectra of turbulent channels. *J. Fluid Mech.* **500**, 135–144.

ANDERSSON, P., BERGGREN, M. & HENNINGSON, D. 1999 Optimal disturbances and bypass transition in boundary layers. *Phys. Fluids* **11** (1), 134–150.

BAMIEH, B. & DAHLEH, M. 2001 Energy amplification in channel flows with stochastic excitation. *Phys. Fluids* **13**, 3258–3269.

BUTLER, K. M. & FARRELL, B. F. 1992 Three-dimensional optimal perturbations in viscous shear flow. *Phys. Fluids* A **4**, 1637–1650.

CESS, R. D. 1958 A survey of the literature on heat transfer in turbulent tube flow. *Res. Rep.* 8-0529-R24. Westinghouse.

COSSU, C. & BRANDT, L. 2002 Stabilization of Tollmien–Schlichting waves by finite amplitude optimal streaks in the Blasius boundary layer. *Phys. Fluids* **14**, L57–L60.

COSSU, C. & BRANDT, L. 2004 On Tollmien–Schlichting waves in streaky boundary layers. *Eur. J. Mech.* B/ *Fluids* **23**, 815–833.

COSSU, C., PUJALS, G. & DEPARDON, S. 2009 Optimal transient growth and very large scale structures in turbulent boundary layers. *J. Fluid Mech.* **619**, 79–94.

ELLINGSEN, T. & PALM, E. 1975 Stability of linear flow. *Phys. Fluids* **18**, 487.

FARRELL, B. F. & IOANNOU, P. J. 1993a Optimal excitation of three-dimensional perturbations in viscous constant shear flow. *Phys. Fluids* **5**, 1390–1400.

FARRELL, B. F. & IOANNOU, P. J. 1993b Stochastic forcing of the linearized Navier–Stokes equation. *Phys. Fluids* A **5**, 2600–2609.

FARRELL, B. F. & IOANNOU, P. J. 1994 Variance maintained by the stochastic forcing of non-normal dynamical systems associated with linearly stable shear flows. *Phys. Rev. Lett.* **72**, 1188–1191.

FARRELL, B. F. & IOANNOU, P. J. 1996 Generalized stability theory. *J. Atmos. Sci.* **53**, 2025–2053.

FARRELL, B. F. & IOANNOU, P. J. 1998 Perturbation structure and spectra in turbulent channel flow. *Theor. Comput. Fluid Dyn.* **11**, 237–250.

FRANSSON, J., BRANDT, L., TALAMELLI, A. & COSSU, C. 2004 Experimental and theoretical investigation of the non-modal growth of steady streaks in a flat plate boundary layer. *Phys. Fluids* **16**, 3627–3638.

FRANSSON, J., BRANDT, L., TALAMELLI, A. & COSSU, C. 2005 Experimental study of the stabilisation of Tollmien–Schlichting waves by finite amplitude streaks. *Phys. Fluids* **17**, 054110.

FRANSSON, J., TALAMELLI, A., BRANDT, L. & COSSU, C. 2006 Delaying transition to turbulence by a passive mechanism. *Phys. Rev. Lett.* **96**, 064501.

DE GRAAFF, D. & EATON, J. 2000 Reynolds-number scaling of the flat-plate turbulent boundary layer. *J. Fluid Mech.* **422**, 319–346.

GUALA, M., HOMMEMA, S. E. & ADRIAN, R. J. 2006 Large-scale and very large-scale motions in turbulent pipe flow. *J. Fluid Mech.* **554**, 521–541.

GUSTAVSSON, L. H. 1991 Energy growth of three-dimensional disturbances in plane Poiseuille flow. *J. Fluid Mech.* **224**, 241–260.

HAMILTON, J., KIM, J. & WALEFFE, F. 1995 Regeneration mechanisms of near-wall turbulence structures. *J. Fluid Mech.* **287**, 317–348.

HOYAS, S. & JIMÉNEZ, J. 2006 Scaling of the velocity fluctuations in turbulent channels up to $Re_\tau = 2003$. *Phys. Fluids* **18**, 011702.

HUNT, J. C. R. & MORRISON, J. F. 2000 Eddy structure in turbulent boundary layer. *Eur. J. Mech.* B **19**, 673–694.

HUTCHINS, N. & MARUSIC, I. 2007a Evidence of very long meandering features in the logarithmic region of turbulent boundary layers. *J. Fluid Mech.* **579**, 1–28.

HUTCHINS, N. & MARUSIC, I. 2007b Large-scale influences in near-wall turbulence. *Phil. Trans. R. Soc.* A **365**, 647–664.

HWANG, Y. & COSSU, C. 2010 Amplification of coherent streaks in the turbulent Couette flow: an input–output analysis at low Reynolds number. *J. Fluid Mech.* **643**, 333–348.

IUSO, G., ONORATO, M., SPAZZINI, P. G. & DI CICCA, G. M. 2002 Wall turbulence manipulation by large-scale streamwise vortices. *J. Fluid Mech.* **473**, 23–58.

JIMÉNEZ, J. 1998 The largest scales of turbulent wall flows. In *CTR Annual Research Briefs*, pp. 943–945. Center for Turbulence Research, Stanford University.

JIMÉNEZ, J. 2007 Recent developments on wall-bounded turbulence. *Rev. R. Acad. Cien. Ser.* A *Mat.* **101**, 187–203.

JIMÉNEZ, J. & MOIN, P. 1991 The minimal flow unit in near-wall turbulence. *J. Fluid Mech.* **225**, 213–240.

JIMÉNEZ, J. & PINELLI, A. 1999 The autonomous cycle of near-wall turbulence. *J. Fluid Mech.* **389**, 335–359.

JOVANOVIĆ, M. R. & BAMIEH, B. 2005 Componentwise energy amplification in channel flow. *J. Fluid Mech.* **543**, 145–83.

KIM, K. C. & ADRIAN, R. 1999 Very large-scale motion in the outer layer. *Phys. Fluids* **11** (2), 417–422.

KITOH, O., NAKABAYASHI, K. & NISHIMURA, F. 2005 Experimental study on mean velocity and turbulence characteristics of plane Couette flow: low-Reynolds-number effects and large longitudinal vortical structures. *J. Fluid Mech.* **539**, 199.

KITOH, O. & UMEKI, M. 2008 Experimental study on large-scale streak structure in the core region of turbulent plane Couette flow. *Phys. Fluids* **20**, 025107.

KLINE, S. J., REYNOLDS, W. C., SCHRAUB, F. A. & RUNSTADLER, P. W. 1967 The structure of turbulent boundary layers. *J. Fluid Mech.* **30**, 741–773.

KOMMINAHO, J., LUNDBLADH, A. & JOHANSSON, A. V. 1996 Very large structures in plane turbulent Couette flow. *J. Fluid Mech.* **320**, 259–285.

LANDAHL, M. T. 1980 A note on an algebraic instability of inviscid parallel shear flows. *J. Fluid Mech.* **98**, 243–251.

LANDAHL, M. T. 1990 On sublayer streaks. *J. Fluid Mech.* **212**, 593–614.

MALKUS, W. V. R. 1956 Outline of a theory of turbulent shear flow. *J. Fluid Mech.* **1**, 521–539.

MATHIS, R., HUTCHINS, N. & MARUSIC, I. 2009 Large-scale amplitude modulation of the small-scale structures in turbulent boundary layers. *J. Fluid. Mech.* **628**, 311–337.

MCKEON, B. J. 2008 A model for 'dynamic' roughness in turbulent channel flow. In *Proceedings of the Summer Program*, pp. 399–410. Center for Turbulence Research, Stanford University.

METZGER, M. M. & KLEWICKI, J. C. 2001 A comparative study of near-wall turbulence in high and low Reynolds number boundary layers. *Phys. Fluids* **13**, 692–701.

MOFFATT, H. K. 1967 The interaction of turbulence with a strong wind shear. In *Proceedings URSI-IUGG International Colloquium on Atmospheric Turbulence and Radio Wave Propagation*, pp. 139–154. Nauka.

MORRISON, W. R. B. & KRONAUER, R. E. 1969 Structural similarity for fully developed turbulence in smooth tubes. *J. Fluid Mech.* **39**, 117–141.

PERRY, A. E. & CHONG, M. S. 1982 On the mechanism of turbulence. *J. Fluid Mech.* **119**, 173–217.

PUJALS, G., COSSU, C. & DEPARDON, S. 2010*a* Forcing large-scale coherent streaks in a zero pressure gradient turbulent boundary layer. *J. Turbulence* **11** (25), 1–13.

PUJALS, G., DEPARDON, S. & COSSU, C. 2010*b* Drag reduction of a 3D bluff body using coherent streamwise streaks. *Exp. Fluids* (in press).

PUJALS, G., GARCÍA-VILLALBA, M., COSSU, C. & DEPARDON, S. 2009 A note on optimal transient growth in turbulent channel flows. *Phys. Fluids* **21**, 015109.

REDDY, S. C. & HENNINGSON, D. S. 1993 Energy growth in viscous channel flows. *J. Fluid Mech.* **252**, 209–238.

REDDY, S. C., SCHMID, P. J. & HENNINGSON, D. S. 1993 Pseudospectra of the Orr–Sommerfeld operator. *SIAM J. Appl. Math.* **53**, 1547.

REYNOLDS, W. C. & HUSSAIN, A. K. M. F. 1972 The mechanics of an organized wave in turbulent shear flow. Part 3. Theoretical models and comparisons with experiments. *J. Fluid Mech.* **54** (2), 263–288.

REYNOLDS, W. C. & TIEDERMAN, W. G. 1967 Stability of turbulent channel flow, with application to Malkus's theory. *J. Fluid Mech.* **27** (2), 253–272.

ROBINSON, S. K. 1991 Coherent motions in the turbulent boundary layer. *Annu. Rev. Fluid Mech.* **23**, 601–639.

SCHMID, P. 2007 Nonmodal stability theory. *Annu. Rev. Fluid Mech.* **39**, 129–162.

SCHMID, P. & HENNINGSON, D. S. 1994 Optimal energy density growth in Hagen–Poiseuille flow. *J. Fluid Mech.* **277**, 197–225.

SCHMID, P. J. & HENNINGSON, D. S. 2001 *Stability and Transition in Shear Flows*. Springer.

SCHOPPA, S. & HUSSAIN, F. 1998 A large-scale control strategy for drag reduction in turbulent boundary layers. *Phys. Fluids* **10**, 1049.

SCHOPPA, W. & HUSSAIN, F. 2002 Coherent structure generation in near-wall turbulence. *J. Fluid Mech.* **453**, 57–108.

SMITH, C. R. & METZLER, S. P. 1983 The characteristics of low-speed streaks in the near-wall region of a turbulent boundary layer. *J. Fluid Mech.* **129**, 27–54.

TOMKINS, C. D. & ADRIAN, R. J. 2003 Spanwise structure and scale growth in turbulent boundary layers. *J. Fluid Mech.* **490**, 37–74.

TOMKINS, C. D. & ADRIAN, R. J. 2005 Energetic spanwise modes in the logarithmic layer of a turbulent boundary layer. *J. Fluid Mech.* **545**, 141–162.

TOWNSEND, A. 1976 *The Structure of Turbulent Shear Flow*, 2nd edn. Cambridge University Press.

TREFETHEN, L. N., TREFETHEN, A. E., REDDY, S. C. & DRISCOLL, T. A. 1993 A new direction in hydrodynamic stability: beyond eigenvalues. *Science* **261**, 578–584.

WALEFFE, F. 1995 Hydrodynamic stability and turbulence: beyond transients to a self-sustaining process. *Stud. Appl. Math.* **95**, 319–343.

WEIDEMAN, J. A. C. & REDDY, S. C. 2000 A MATLAB Differentiation Matrix Suite. *ACM Trans. Math. Softw.* **26**, 465–519.

WILLIS, A. P., HWANG, Y. & COSSU, C. 2009 Optimal harmonic forcing and drag reduction in pipe flow. *Bull. Am. Phys. Soc.* **54** (19), 227.

WILLIS, A. P., HWANG, Y. & COSSU, C. 2010 Optimally amplified large-scale streaks and drag reduction in the turbulent pipe flow. *Phys. Rev.* E (submitted).

ZHOU, K., DOYLE, J. & GLOVER, K. 1996 *Robust and Optimal Control*. Prentice-Hall.

3

Article 3

On the stability of large-scale streaks in turbulent Couette and Poiseulle flows

Sur la stabilité des streaks à grande échelle dans les écoulements de Couette et Poiseuille turbulents

Junho Park [a], Yongyun Hwang [a,*], Carlo Cossu [b,c]

[a] *Laboratoire d'hydrodynamique (LadHyX), École polytechnique, 91128 Palaiseau cedex, France*
[b] *CNRS – Institut de mécanique des fluides de Toulouse (IMFT), allée du Pr. Camille-Soula, 31400 Toulouse, France*
[c] *Département de mécanique, École polytechnique, 91128 Palaiseau cedex, France*

A R T I C L E   I N F O

A B S T R A C T

The linear secondary stability of large-scale optimal streaks in turbulent Couette flow at $Re_\tau = 52$ and Poiseuille flow at $Re_\tau = 300$ is investigated. The streaks are computed by solving the nonlinear two-dimensional Reynolds-averaged Navier–Stokes equations using an eddy-viscosity model. Optimal initial conditions leading the largest linear transient growth are used, and as the amplitude of the initial vortices increases, the amplitude of streaks gradually increases. Instabilities of the streaks appear when their amplitude exceeds approximately 18% of the velocity difference between walls in turbulent Couette flow and 21% of the centerline velocity in turbulent Poiseuille flow. When the amplitude of the streaks is sufficiently large, the instabilities attain significant growth rates in a finite range of streamwise wavenumbers that shows good agreement with the typical streamwise wavenumbers of the large-scale motions in the outer region.

© 2010 Académie des sciences. Published by Elsevier Masson SAS. All rights reserved.

R É S U M É

L'instabilité linéaire secondaire des streaks à grande échelle est étudiée dans les écoulements de Couette turbulent à $Re_\tau = 52$ et Poiseuille turbulent à $Re_\tau = 300$. Les streaks sont calculés en résolvant les équations de Navier–Stokes moyennées selon Reynolds en utilisant un modèle de viscosité turbulente. Les conditions initiales optimales, induisant la plus grande croissance transitoire, sont utilisées; quand l'amplitude des tourbillons optimaux initiaux est augmentée, l'amplitude des streaks augmente aussi. Les streaks deviennent instables quand leur amplitude est supérieure à environ 18% de la différence de vitesse entre les deux parois dans l'écoulement de Couette turbulent et 21% de la vitesse au centre du canal dans l'écoulement de Poiseuille turbulent. Quand l'amplitude des streaks est suffisamment élevée les instabilités atteignent des taux d'amplification significatifs dans une bande de longueurs d'onde qui est en bon accord avec les longueurs d'onde typiques observées dans les région externe.

© 2010 Académie des sciences. Published by Elsevier Masson SAS. All rights reserved.

---

* Corresponding author.
E-mail addresses: junho.park@ladhyx.polytechnique.fr (J. Park), yongyun@ladhyx.polytechnique.fr (Y. Hwang), carlo.cossu@imft.fr (C. Cossu).

1. Introduction

Understanding the dynamics of coherent motions is a central issue in the research on wall-bounded turbulent flows. In the near-wall region, streaks, i.e. spanwise alternating patterns of high- and low-momentum regions with mean spacing about one hundred wall units, have been found as the most prominent feature [1]. These streaks sustain independently of the turbulent motions in the outer region [2], and the corresponding process has been understood as a cycle involving amplification of streaks by vortices, breakdown of the streaks via instability and the subsequent nonlinear process generating new vortices [3,4]. Streaky motions, however, have been also found in the outer region, and they carry a significant fraction of turbulent kinetic energy and Reynolds stress [5,6]. The origin of these large-scale streaky motions is not clear yet, but nonmodal stability theory has predicted that they can be significantly amplified by lift-up mechanism [7–9]. This encouraging result suggests that a self-sustaining process similar to the buffer-layer cycle presumably exists in the outer region, as confirmed by recent results [10]. However, streaks maximally amplified are found to be uniform in the streamwise direction, whereas the streaky motions observed in experiments have the finite streamwise wavelengths and meander with vortex packets (also called large-scale motions) coherently aligned to them [5,6]. Currently, there is no sound explanation for these features, and only recently it has been conjectured that the vortex packets may be related to the instability of large-scale streaks [5]. The goal of the present study is to analyze the stability of large-scale streaks and to seek a relationship between the streamwise wavelengths of the instability and the length-scales of the coherent structures in the outer region. In order to theoretically track this issue, we consider an eddy-viscosity model for the organized waves [11] successfully used to study the transient growth of large-scale streaks [7–9], and conduct a secondary stability analysis of the most amplified streaks in the turbulent Couette flow and in the turbulent Poiseuille flow.

2. Background

We consider the turbulent flow of an incompressible fluid with the density ρ and kinematic viscosity ν in a channel with walls located at $\pm h$. Here, the streamwise, wall-normal and spanwise directions are denoted as x, y and z respectively. For Couette flow, the upper and the lower walls move in opposite directions with the same velocity U_w. The Poiseuille flow is driven by a constant pressure gradient across the channel and has centerline velocity U_{cl}. For both cases, the equation for organized waves in perturbation form around the mean flow ($U_i = (U(y, z), 0, 0)$) is written as [11,7–9]

$$\frac{\partial u_i}{\partial t} + u_j \frac{\partial U_i}{\partial x_j} + U_j \frac{\partial u_i}{\partial x_j} + u_j \frac{\partial u_i}{\partial x_j} = -\frac{1}{\rho} \frac{\partial p}{\partial x_i} + \frac{\partial}{\partial x_j} \left[\nu_T(y) \left(\frac{\partial u_i}{\partial x_j} + \frac{\partial u_j}{\partial x_i} \right) \right] \tag{1}$$

Here, $u_i = (u, v, w)$ is the velocity of the organized wave and $\nu_T(y) \equiv \nu + \nu_t(y)$, where $\nu_t(y)$ is the turbulent eddy viscosity. The streaky base flow is computed using a mean profile $U(y)$ issued from DNS for the Couette flow as in [9] and the Reynolds–Tiederman profile for the Poiseuille flow as in [8]. $\nu_T(y)$ is the total eddy viscosity in equilibrium with $U(y)$ and the solutions are assumed uniform in the streamwise direction. Once the streaky base flow $u_s(y, z)$ is computed, the secondary base flow is defined as $U_b(y, z) \equiv U(y) + u_s(y, z)$. The stability of $U_b(y, z)$ is then studied by linearizing (1) with the secondary perturbations $u'_i(x, y, z, t)$. Under the assumption that the base flow $U_b(y, z)$ is periodic in the spanwise direction, the Floquet theory allows the linearized equation to have the following normal-mode solution:

$$u'_i(x, y, z, t) = e^{i\alpha x - i\omega t} \sum_{n=-\infty}^{\infty} \hat{u}_i^n(y) e^{i(n+\epsilon)\beta_0 z} + c.c. \tag{2}$$

where α is the streamwise wavenumber, ω the complex frequency, β_0 the spanwise wavenumber related to the fundamental period of the base flow, and $0 \leqslant \epsilon \leqslant 1/2$ is the detuning parameter. According to the values of ϵ, the solutions (2) are classified into 'fundamental' ($\epsilon = 0$) and 'subharmonic' ($\epsilon = 1/2$) modes. Also, the modes with even and odd symmetries about base flows are called 'sinuous' and 'varicose' respectively. For further details on the classification of the modes, the readers are referred to [12]. In the present study, we focus only on the fundamental sinuous mode, found as the most unstable one for all the cases considered.

Eq. (1) is discretized using Chebyshev polynomials and Fourier series in the wall-normal and spanwise directions respectively. The time integration used to compute $U_b(y, z)$ is conducted using the Runge–Kutta third-order method. For the Floquet analysis, the same spatial discretization is applied to the linear operators. The resulting numerical eigenvalue problem is then solved using the implicitly restarted Arnoldi method (for further details, see [12]). All the computations here are carried out with $N_y \times N_z = 65 \times 32$.

3. Results

We consider a turbulent Couette flow at $Re_\tau = 52$ and a Poiseuille flow at $Re_\tau = 300$. The computation of the streaky base flows is carried out by using the optimal initial conditions, that consist of pairs of the counter-rotating streamwise vortices computed in [8,9] (see also Fig. 2). The spanwise spacing is chosen as $\lambda_z = 4h$ ($\beta_0 h = \pi/2$), which is very near the optimal value [8,9]. The spanwise size of computational box is set to as $L_z = \lambda_z$, so that a single pair of optimal initial
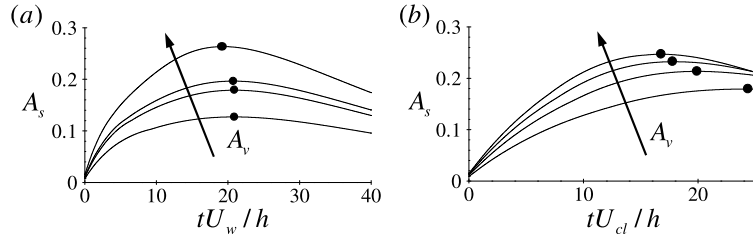
Fig. 1. Evolution of the streak amplitude in time: (a) Couette flow with $A_v = 0.08, 0.11, 0.12, 0.16$; (b) Poiseulle flow with $A_v = 0.06, 0.078, 0.09, 0.1$. Here, • denotes the maximum of A_s at $t = t_{max}$.
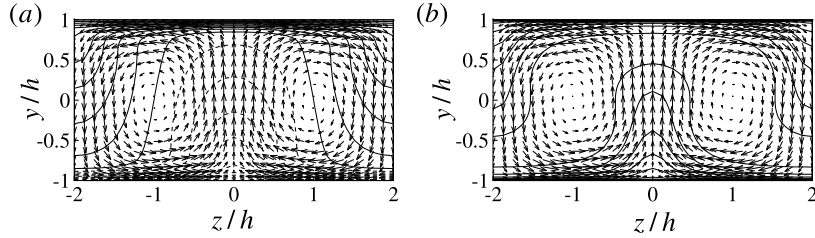

Fig. 2. Cross-stream (y–z) view of streaky base flow extracted at $t = t_{max}$ and optimal initial vortices: (a) Couette flow with $A_s = 26\%$ and (b) Poiseulle flow with $A_s = 25\%$. Here, the solid and dashed contour lines respectively denote positive and negative parts of the streaky base flow with the increment 0.1 of its maximum, and the vectors represent the initial vortices.
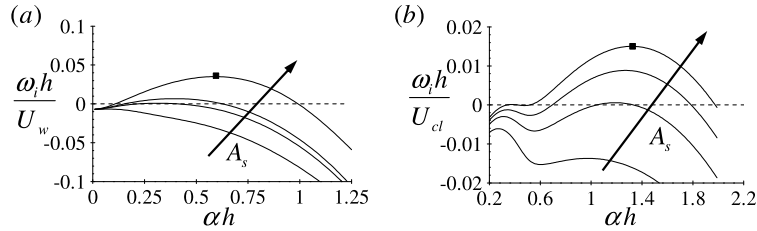
Fig. 3. Growth rate of fundamental sinuous mode with the streamwise wavenumber α for streaky base flows corresponding to • in Fig. 1: (a) Couette flow with $A_s = 13, 18, 20, 26\%$; (b) Poiseulle flow with $A_s = 18, 21, 23, 25\%$. Here, ■ indicates the location of maximum ω_i of the largest amplitude of streaks considered.

vortices is driven. The amplitude of the initial vortices is defined as $A_v = [(2/V) \int_V (u^2 + v^2 + w^2)dV]^{1/2}$. The amplitude of the streaks induced by these vortices is defined [14] as

$$A_s = \frac{[\max_{y,z} \Delta U(y,z) - \min_{y,z} \Delta U(y,z)]}{2\, U_{ref}} \qquad (3)$$

where $\Delta U(y,z) \equiv u_s(y,z)$. Here, $U_{ref} = 2U_w$ and $U_{ref} = U_{cl}$ for Couette and Poiseulle flows respectively.

Fig. 1 shows the temporal evolution of the streak amplitude for several amplitudes A_v of the optimal initial vortices. Both Couette and Poiseulle flows exhibit large transient amplifications of the streaks through the coherent lift-up effect. As A_v increases, the amplitude of the streaks also increases. However, the ratio of the amplification slightly decays with increasing A_v, and the time for A_s to reach its maximum (t_{max}) also becomes shorter. Typical cross-stream views of the initial vortices and streaks at $t = t_{max}$ are reported in Fig. 2. It is seen that the low-momentum regions where the fluid is ejected from the wall by the vortices (($y > 0$, $z \simeq \pm 2h$) and ($y < 0$, $z \simeq 0$) in Fig. 2) are narrow and intense, and this tendency generally becomes stronger for larger streak amplitudes.

The Floquet stability analysis is performed for the fundamental modes using the streaky base flows extracted at $t = t_{max}$. Fig. 3 shows the growth rate ω_i of sinuous modes versus the streamwise wavenumber α for several A_s. Both Couette and Poiseulle flows are stable for sufficiently low amplitudes of the streaks ($\omega_i < 0$). As the amplitude of streak A_s increases, the growth rate gradually increases. Then instability begins to appear ($\omega_i > 0$) when A_s reaches the value: $A_{s,c} = 18\%$ at $\alpha_c h = 0.3$ for Couette flow (Fig. 3a) and $A_{s,c} = 21\%$ at $\alpha_c h = 1.2$ for Poiseulle flow (Fig. 3b). When $A_s > A_{s,c}$, a finite interval of the streamwise wavenumbers is unstable with maximum growth at $\alpha_{max} h \simeq 0.6$ in Couette flow (Fig. 3a) and $\alpha_{max} h \simeq 1.4$ in Poiseulle flow (Fig. 3b). We have verified that varicose modes are less unstable than sinuous modes in this range of A_v–A_s.

Fig. 4 shows the spanwise velocity component w of the streak-instability eigenfunction and the line where the mean velocity is the same as the phase speed c_r of instability wave ($c_r = 0$ in Couette flow while $c_r = 0.87U_{cl}$ in Poiseulle flow). The w-component of the eigenfunction is concentrated in the lifted low-momentum region for both Couette and Poiseulle
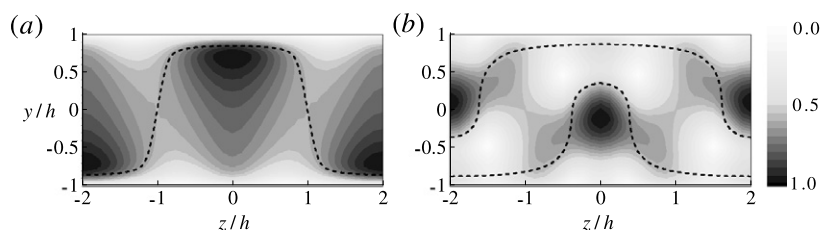
Fig. 4. Cross-stream (y–z) view of the absolute value of the spanwise velocity eigenfunction corresponding to ■ in Fig. 3: (a) Couette flow; (b) Poiseulle flow. Here, the contour is normalized by its maximum and the thick dashed line denotes the velocity of streaky base flow which is the same with the phase speed of the streak instability.

flows. In Couette flow the amplitude of the eigenfunction is appreciable even close to the opposite wall, whereas in Poiseulle flow it is mainly concentrated on the center of the channel, which is reminiscent of the unstable modes found in the laminar case.

4. Discussion

We have investigated the instability of finite amplitude streaks in the framework of an eddy viscosity of turbulent Couette and Poiseulle flows. The nature of the streak instability we find bears same similarity the one observed in the laminar flows: the instability appears for the high amplitude streaks and it is dominated by the fundamental sinuous mode. An interesting point is that the critical streak amplitudes in the present model are lower than those in laminar flows: for example, our own computations in laminar Couette and Poiseulle flows at $Re_h = 500$ give $A_{s,c} \simeq 23\%$ and $A_{s,c} \simeq 28\%$ respectively (see also [13]), whereas for the turbulent Couette and Poiseulle flows it is found $A_{s,c} \simeq 18\%$ and $A_{s,c} \simeq 21\%$ respectively at $Re_\tau = 52$ and $Re_\tau = 300$. However, this does not mean that the streak instability in turbulent flows can be more easily triggered than in laminar flows because as the optimal turbulent transient growth is smaller than the laminar one [8,9], initial vortices in turbulent flows should be more energetic to drive streak instability than those in laminar flows. For example, in the laminar Poiseulle flow, $A_{v,c} \sim O(10^{-3})$ is required to trigger streak instability [13], but the amplitude of initial vortices in the present model of Poiseulle flow is almost two order of magnitude larger (i.e. $A_{v,c} \simeq 0.08$).

In the outer region of the turbulent Poiseulle flow, the streamwise length scale of the large-scale motions has been associated with the peak near the high wavenumber boundary of the α^{-1} regime in the spectra of the outer region at $\alpha h = 1 \sim 2$ ($\lambda_x = 3.1 \sim 6.3h$), and that is clearly visible for $0 < |y| < 0.6h$ [15,16]. The range of unstable streamwise wavenumbers in the present study is also obtained at $\alpha h = 0.8 \sim 1.8$ ($\lambda_x = 3.5 \sim 7.9h$; see Fig. 3b), showing good agreement with the location of the peak in the streamwise spectra. Moreover, the eigenfunctions obtained here have significant values in $0 < |y| < 0.6h$, also comparable to the spectra. For the turbulent Couette flow, the streamwise wavenumber having the maximum growth rate ($\alpha h \simeq 0.6$; $\lambda_x \simeq 10.5h$; see Fig. 3a) also corresponds well to the location of the peak in the streamwise spectra at the channel center ($\alpha h \simeq 0.63$; $\lambda_x \simeq 10h$) [17]. This good correlation in the length-scale comparison implies that the large-scale motion could be formed by instability of much longer streaky motions in the outer region. However, as the Reynolds numbers considered here are fairly low, this conclusion remains to be confirmed at larger Re. Also, alternative scenario based on the secondary transient growth as in [18] may also be relevant, and is currently under active investigation.

References

[1] S.J. Kline, W.C. Reynolds, F.A. Schraub, P.W. Runstadler, The structure of turbulent boundary layers, J. Fluid Mech. 30 (1967) 741–773.
[2] J. Jiménez, A. Pinelli, The autonomous cycle of near-wall turbulence, J. Fluid Mech. 389 (1999) 335–359.
[3] J.M. Hamilton, J. Kim, F. Waleffe, Regeneration mechanisms of near-wall turbulence structures, J. Fluid Mech. 287 (1995) 317–348.
[4] F. Waleffe, On a self-sustaining process in shear flows, Phys. Fluids 9 (1997) 883–900.
[5] M. Guala, S.E. Hommema, R.J. Adrian, Large-scale and very-large-scale motions in turbulent pipe flow, J. Fluid Mech. 554 (2006) 521–541.
[6] N. Hutchins, I. Marusic, Evidence of very long meandering features in the logarithmic region of turbulent boundary layers, J. Fluid Mech. 579 (2007) 1–28.
[7] J.C. del Álamo, J. Jiménez, Linear energy amplification in turbulent channels, J. Fluid Mech. 559 (2006) 205–213.
[8] G. Pujals, M. García-Villalba, C. Cossu, S. Depardon, A note on optimal transient growth in turbulent channel flows, Phys. Fluids 21 (015109) (2009) 1–6.
[9] Y. Hwang, C. Cossu, Amplification of coherent streaks in the turbulent Couette flow: an input–output analysis at low Reynolds number, J. Fluid Mech. 643 (2010) 333–348.
[10] Y. Hwang, C. Cossu, On a self-sustained process at large scales in the turbulent channel flow, Phys. Rev. Lett. 105 (2010) 044505.
[11] W.C. Reynolds, A.K.M.F. Hussain, The mechanics of an organized wave in turbulent shear flow. Part 3. Theoretical models and comparisons with experiments, J. Fluid Mech. 54 (1972) 263–288.

[12] C. Cossu, L. Brandt, On Tollmien–Schlichting waves in streaky boundary layers, Eur. J. Mech./B Fluids 23 (2004) 815–833.

[13] S.C. Reddy, P.J. Schmid, J.S. Baggett, D.S. Henningson, On the stability of streamwise streaks and transition thresholds in plane channel flows, J. Fluid Mech. 365 (1998) 269–303.

[14] P. Andersson, L. Brandt, A. Bottaro, D. Henningson, On the breakdown of boundary layers streaks, J. Fluid Mech. 428 (2001) 29–60.

[15] B.J. Balakumar, R.J. Adrian, Large- and very-large-scale motions in channel and boundary layer flows, Phil. Trans. R. Soc. A 365 (1852) (2001) 665–681.

[16] J.P. Monty, N. Hutchins, H.C.H. Ng, I. Marusic, M.S. Chong, A comparison of turbulent pipe, channel and boundary layer flows, J. Fluid Mech. 632 (2009) 431–442.

[17] T. Tsukahara, H. Kawamura, K. Shingai, DNS of turbulent Couette flow with emphasis on the large-scale structure in the core region, Journal of Turbulence 7 (19) (2006).

[18] W. Schoppa, F. Hussain, Coherent structure generation in near-wall turbulence, J. Fluid Mech. 453 (2002) 57–108.

4

Article 4

P H Y S I C A L   R E V I E W   L E T T E R S

Self-Sustained Process at Large Scales in Turbulent Channel Flow

Yongyun Hwang[*]

LadHyX, CNRS-École Polytechnique, 91128 Palaiseau, France

Carlo Cossu[†]

IMFT-CNRS, Allée du Professeur Camille Soula, 31400 Toulouse, France
and Département de Mécanique, École Polytechnique, 91128 Palaiseau, France

Large-scale motions, important in turbulent shear flows, are frequently attributed to the interaction of structures at smaller scales. Here we show that, in a turbulent channel at $\mathrm{Re}_\tau \approx 550$, large-scale motions can self-sustain even when smaller-scale structures populating the near-wall and logarithmic regions are artificially quenched. This large-scale self-sustained mechanism is not active in periodic boxes of width smaller than $L_z \approx 1.5h$ or length shorter than $L_x \approx 3h$ which correspond well to the most energetic large scales observed in the turbulent channel.

Understanding the mechanisms by which turbulence self-sustains in wall-bounded turbulent shear flows is still an open challenge that is relevant for applications ranging from atmospheric dynamics to the design of low drag vehicles. One of the most robust features of these flows is the presence of streamwise streaks, i.e., narrow streamwise regions where the streamwise velocity is larger or smaller than the mean velocity at the same distance from the wall. The existence of streaks in the buffer layer with a characteristic average spanwise scale $\lambda_z^+ \approx 100$, in wall units, has been revealed by early experimental observations [1,2]. Numerical experiments furthermore reveal that turbulence is not sustained in periodic domains smaller than this spacing [3]. There is now a large consensus that these near-wall structures are generated via a self-sustained process [4,5] based on the amplification of streaks from the vortices via the lift-up effect [6], followed by the breakdown of the streaks [7,8] and the regeneration of the vortices. This buffer-layer process survives when turbulent structures are artificially removed from the outer layers [9].

Coherent structures, however, exist at larger scales. It has long been known that streamwise velocity correlations are important up to lengths of the order of the outer length scale h of the flow (e.g. the channel half-width, the pipe radius, or the boundary layer thickness), and have been related to the presence of "bulges" or "large-scale motions" [10]. Recently, it has also been realized that coherent streaks exist at even larger scales, with typical spanwise and streamwise scales $\lambda_z \approx O(h)$ and $\lambda_x \approx O(10h)$, respectively [11–15]. These very-large-scale streaks, also referred to as very-large-scale motions or global modes or superstructures, are important because they carry a very significant fraction of the turbulent kinetic energy and of the turbulent Reynolds stress [12,13,15,16], contradicting the early view that the motions at very large scales are essentially inactive [17].

The fundamental question in which we are interested here is as follows: What is the origin of the streaky motions at very large scales? It has been conjectured that these motions could result from the concatenation of large-scale motions [13,16]. These large-scale motions are, in turn, made of the aggregation of a huge number of hairpin vortices of smaller scales [12,18]. Even from a different perspective, further numerical experiments [19] support the idea that very-large-scale motions can be directly forced and can interact with near-wall structures, at much smaller scales, via a cosupporting cycle. In this mechanism, while the near-wall cycle would continue to exist even in the absence of large-scale structures, the reverse would not happen.

The current wisdom is therefore that large- and very-large-scale motions would not exist in the absence of smaller-scale structures. An alternative way of thinking is, however, emerging from recent findings that extend recent hydrodynamic stability methodologies to fully developed turbulent flows. It has recently been theoretically predicted that very-large-scale streamwise streaks can be amplified by a coherent lift-up effect which is able to extract energy from the mean flow at very large scales, without the mediation of coherent structures at smaller scales [20–24]. The existence of the coherent lift-up has been confirmed in experiments where very-large-scale coherent streaks have been artificially induced by forcing coherent streamwise vortices [25–27]. It is therefore tempting to conjecture that the very-large-scale motions could result from a self-sustained mechanism bearing some similarity to the processes observed in the buffer layer and in transitional flows (see, e.g., the discussions in [13,22,28]). The goal of the present study is to verify whether or not this conjecture is true.

We proceed by designing a "conceptual" numerical experiment where we gradually remove the smaller scales

from the flow while still taking into account the associated dissipation. The ideal tool to perform such an experiment is the large eddy simulation (LES), which also has the advantage of keeping the computations in very-large domains manageable at high Reynolds numbers. In LES the very-small-scale motions are not resolved by the grid, and the residual stress tensor associated with these small-scale filtered motions is modeled with an eddy viscosity $\tau_{ij} - \tau_{kk}\delta_{ij}/3 = -2\nu_T \bar{S}_{ij}$, where $\bar{S}_{ij}$ is the symmetric part of the filtered velocity gradient. From the adopted perspective it is important to avoid any backward spectral energy transfer from the smaller to the larger scales. Therefore, we consider the "static" Smagorinsky model [29], where the eddy viscosity is simply modeled as $\nu_T = D(C_S\bar{\Delta})^2\bar{S}$, with $\bar{S} = (2\bar{S}_{ij}\bar{S}_{ij})^{1/2}$ being a measure of the local shear and $C_S\bar{\Delta}$ the local mixing length, given by the product of the filtering scale $\bar{\Delta}$ to the Smagorinsky constant C_S. The van Driest damping function $D = 1 - e^{-(y^+/A^+)^3}$ is also used to enforce a physical behavior near the wall (for further details on properties of the Smagorinsky model, the reader may refer, e.g., to [30,31]). Dynamic Smagorinsky models, which are known to perform better for engineering applications, are not used here because we want to avoid backscatter. The simulations are performed using the public domain code DIABLO [32] which implements the fractional-step method based on a semi-implicit time integration scheme and a mixed finite-difference and Fourier discretization in space. The computational domain is chosen large enough ($L_z = 6h$) to contain three to four large-scale streaks in the spanwise direction and long enough ($L_x = 56h$) to contain the longest observed streamwise wavelengths of the very-large-scale motions. The grid size of $384 \times 65 \times 96$ points in, respectively, the streamwise (x), wall-normal (y), and spanwise (z) directions is set up so as to resolve the near-wall cycle properly in the reference simulations [33]. A grid stretching is applied in the wall-normal direction with the first grid point at $y^+ = 1.8$ and a maximum spacing $\Delta_y^+ = 40$ at the channel center.

The simulations are performed by enforcing a constant mass flux corresponding to the constant $Re_m = 20\,133$, where $Re_m = U_m 2h/\nu$ is the Reynolds number based on the bulk velocity $U_m = (1/2h)\int_{-h}^{h} U dy$, the kinematic viscosity ν, and the channel half-height h. The reference case is first considered by choosing the Smagorinsky constant $C_S = 0.05$ which was shown to provide the best accordance with statistics of direct numerical simulations [30]. The reference solution exhibits an average friction-based Reynolds number $Re_\tau = 550$, where $Re_\tau = hu_\tau/\nu$ and u_τ is the friction velocity. The mean streamwise velocity profile and the turbulence intensities agree well with those from direct numerical simulations at the same Re_τ [34] as reported in Fig. 1. A snapshot of the streamwise velocity fluctuation in the reference case is reported in Fig. 2(a). The structure of this field is very similar to the
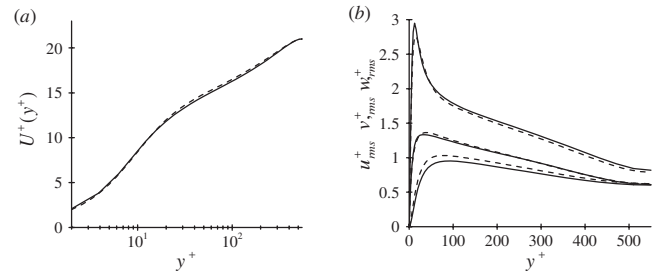

FIG. 1. Comparison of mean statistics of the reference case ($C_S = 0.05$) with data from the direct numerical simulations in Ref. [34] at the same $Re_\tau = 550$: (a) mean streamwise velocity profile $U(y^+)$; (b) turbulence intensity profiles $u_{\mathrm{rms}}(y^+)$, $v_{\mathrm{rms}}(y^+)$, and $w_{\mathrm{rms}}(y^+)$.

one obtained from direct numerical simulations, with large-scale streaks embedded in clouds of smaller-scale structures (see, e.g., [28]). The premultiplied spanwise and streamwise velocity spectra $k_z E_{uu}(k_z)$ and $k_x E_{uu}(k_x)$ corresponding to the reference case, reported in Figs. 3(a) and 3(c), respectively, are also in qualitatively good accordance with those from direct numerical simulation at simi-
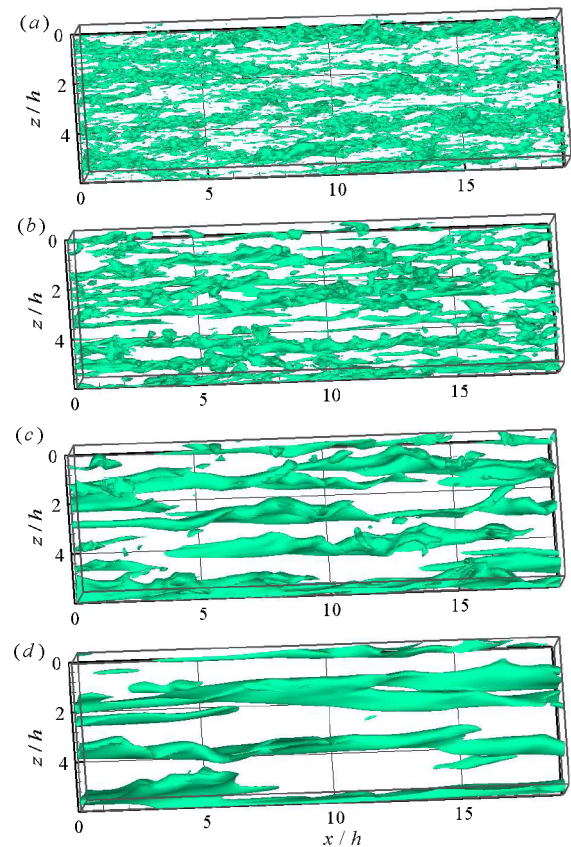

FIG. 2 (color online). Isosurface ($u^+ = -2$) of the instantaneous streamwise velocity fluctuation for the reference simulation with $C_S = 0.05$ (a) and for simulations performed with increasing artificial dissipation of the small scales with $C_S = 0.1$ (b), $C_S = 0.2$ (c), and $C_S = 0.3$ (d).
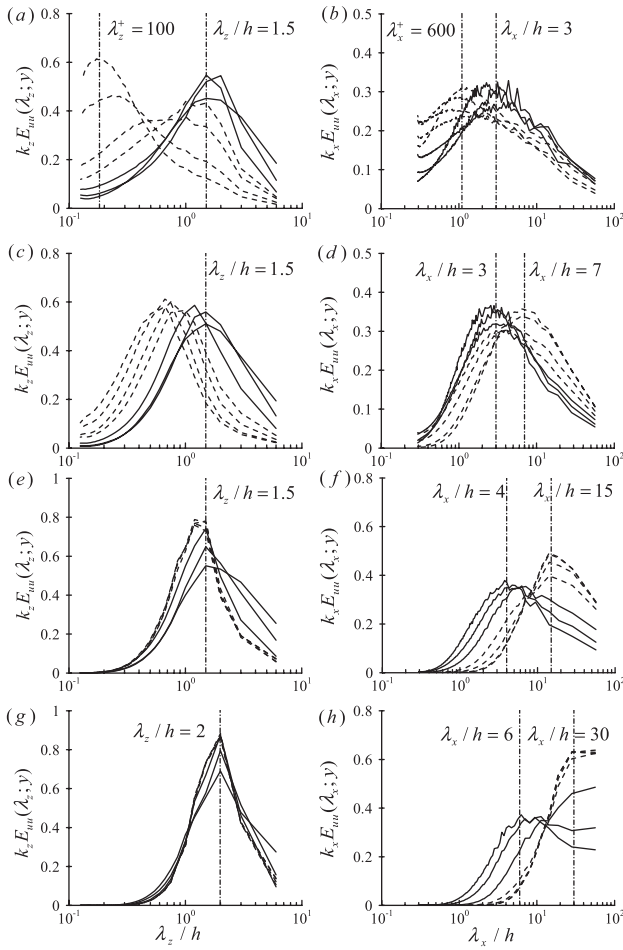
FIG. 3. Spanwise premultiplied power spectrum $k_z E_{uu}(\lambda_z)$ [(a), (c), (e), and (g)] and streamwise premultiplied power spectrum $k_x E_{uu}(\lambda_x)$ [(b), (d), (f), and (h)] for, respectively, the reference simulation with $C_S = 0.05$ [(a) and (b)] and for the cases $C_S = 0.1$ [(c) and (d)], $C_S = 0.2$ [(e) and (f)], and $C_S = 0.3$ [(g) and (h)]. The premultiplied spectra are extracted in the inner layer ($y^+ = 16, 30, 70, 108$; dashed lines) and in the outer layer ($y/h = 0.38, 0.65, 1$; solid lines).

lar Re_τ [11]. In particular, in the premultiplied spectra, the scales of the buffer-layer cycle $\lambda_z^+ \approx 100$ and $\lambda_x^+ \approx 600$ are observed for $y^+ < 30$, while in the outer region the peaks corresponding to the large-scale motions are observed at $\lambda_z/h \approx 1.5$–2 and $\lambda_x/h \approx 3$–4 with long tails in the range of $\lambda_x/h > 3$–4 that represent the very-large-scale motions [16,35,36].

To test if the large-scale structures can survive even in the absence of smaller scales, we progressively damp the small-scale structures by simply repeating the simulations with larger values of the Smagorinsky constant C_S, which only affects the diffusion term and not the nonlinear advective terms. In these additional simulations the Reynolds number is kept at its reference value $\mathrm{Re}_m = 20\,133$. The friction-based Reynolds number is not strongly affected by

the change in C_S: $\mathrm{Re}_\tau = 494$ is found for $C_S = 0.1$, $\mathrm{Re}_\tau = 518$ for $C_S = 0.2$, and $\mathrm{Re}_\tau = 560$ for $C_S = 0.3$.

For increasing C_S values, the small-scale coherent motions are increasingly damped, as can be seen from the instantaneous streamwise velocity fluctuation fields reported in Fig. 2. Only large- and very-large-scale streaky motions survive for $C_S \approx 0.3$ [Fig. 2(d)]; also, these motions are quenched for $C_S = 0.4$. The effects observed on the instantaneous velocity fields are confirmed by the analysis of the premultiplied spectra reported in Fig. 3. For $C_S = 0.1$, the buffer-layer peak $\lambda_z^+ \approx 100$ in the spanwise premultiplied spectrum $k_z E_{uu}(\lambda_z)$ has been quenched, meaning that the near-wall cycle has been suppressed. However, structures with almost constant λ_z/y survive in the log layer for $C_S = 0.1$, as seen in Fig. 3(c). For larger C_S, these structures are also quenched. Only one peak survives with $\lambda_z \approx 1.5h$ for $C_S = 0.2$ and $\lambda_z = 2h$ for $C_S = 0.3$, with λ_z corresponding well to the large- and very-large-scale motions [$\lambda_z \approx (1.5$–$2)h$] apparent in Fig. 3(a) and observed in numerical simulations and experiments [11,15].

The analysis of the streamwise premultiplied spectra $k_x E_{uu}(\lambda_x)$ confirms this scenario. For $C_S = 0.1$ the $\lambda_x^+ \approx 600$ peak has been replaced by much longer structures ($\lambda_x \approx 7h$). In the channel center, structures with $\lambda_x \approx 3h$ dominate, like in the reference simulation. The typical streamwise scales in the inner layer, no longer masked by the near-wall cycle, are now longer than in the outer layer. These scales grow longer when C_S is further increased [see Figs. 3(d), 3(f), and 3(h)]. The streamwise scales surviving for $C_S = 0.3$ are larger by a factor of 2 when compared to the "natural" large-scale and very-large-scale motions, which can probably be attributed to the very important artificial dissipation enforced at this C_S. The analysis of the wall-normal structure of the modes associated with these scales reveals that the modes associated with longer λ_x, when compared to shorter λ_x ones, (a) have turbulence intensity peaks nearer to the wall, (b) penetrate more to the wall with a larger turbulence intensity, and (c) have a smaller ratio of the wall-normal to the streamwise turbulence intensity. These structures remain essentially outer-layer structures even for the longest λ_x. We have verified that the results described above do not depend on the details of the damping of the small-scale motions by repeating the simulations with a different form of artificial extra dissipation.

These findings, especially for the case $C_S = 0.1$, are in accordance with recent numerical experiments, where it was shown that large-scale motions in the outer layers are almost independent of the buffer-layer processes [37,38]. Even more importantly, these results prove that large- and very-large-scale motions in the turbulent channel do not necessarily rely on the existence of smaller-scale structures like buffer-layer streaks and vortices or hairpin vortices. This is a strong indication that an independent self-

sustained process at large scales exists in the turbulent channel and probably in the other turbulent canonical shear flows such as the pipe and the boundary layer, as was previously conjectured [13,20,22].

The self-sustained process at large scales is associated with coherent large-scale streaks that undergo sinuous oscillations and break down in an apparently random way. This phenomenology is similar to what is observed in minimal box realizations of the buffer-layer self-sustained process and in the subcritical laminar-turbulent transition in the channel [3,4,7,39]. In these situations, the process can self-sustain only in periodic boxes sufficiently large for the streaks to grow by the lift-up effect and sufficiently long to allow the sinuous streak oscillations to develop. We have therefore repeated the simulations for $C_S = 0.3$ in smaller horizontally periodic boxes. A constant spatial resolution $(\Delta x, \Delta z)$ is used so as to maintain the LES filter width, unchanged. A detailed analysis of numerous box combinations reveals that the large-scale process is sustained only if the streamwise and spanwise box sizes are larger than the minimal values $L_{x,\min} \approx 3h$ and $L_{z,\min} \approx 1.5h$, respectively. These values are in very good agreement with the spatial length scales of the most energetic outer-layer motions [11,15,20,35]. This similarity of the minimal box sizes to the characteristic scales of the most energetic structures observed in the "natural" turbulent flows is also observed for buffer-layer structures [3], The minimal spanwise size $L_{z,\min}$ is also well in the range of scales where streaks are strongly amplified by the coherent lift-up effect in turbulent channels [20,21].

The analysis of the power input and dissipation, $I(t)$ and $D(t)$, in the minimal box $L_{x,\min} \times L_{z,\min}$ for $C_S = 0.3$ reveals pseudoperiodic oscillations with time period $T \approx (13$–$15)h/U_b$ associated with sinuous oscillations of the low speed streaks in the whole channel. These oscillations are typically followed, in an intermittent way, by a large excursion in the drag and dissipation that is very similar to the "bursting" observed in the buffer-layer process [3].

From the minimal box results we also conclude that the existence of motions at very large scales $(\lambda_x > 3h)$ is not necessary for the survival of the motions at large scales $(\lambda_x \approx 3h)$. Whether the motions with $\lambda_x > 3h$ are active or are passively forced by the process at $\lambda_x \approx 3h$ is still an open question that is currently under scrutiny.

*yongyun@ladhyx.polytechnique.fr
†carlo.cossu@imft.fr

[1] S. J. Kline, W. C. Reynolds, F. A. Schraub, and P. W. Runstadler, J. Fluid Mech. **30**, 741 (1967).
[2] J. R. Smith and S. P. Metzler, J. Fluid Mech. **129**, 27 (1983).
[3] J. Jiménez and P. Moin, J. Fluid Mech. **225**, 213 (1991).
[4] J. Hamilton, J. Kim, and F. Waleffe, J. Fluid Mech. **287**, 317 (1995).
[5] F. Waleffe, Phys. Fluids **9**, 883 (1997).
[6] M. T. Landahl, J. Fluid Mech. **212**, 593 (1990).
[7] F. Waleffe, Stud. Appl. Math. **95**, 319 (1995).
[8] W. Schoppa and F. Hussain, J. Fluid Mech. **453**, 57 (2002).
[9] J. Jiménez and A. Pinelli, J. Fluid Mech. **389**, 335 (1999).
[10] L. S. G. Kovasznay, V. Kibens, and R. F. Blackwelder, J. Fluid Mech. **41**, 283 (1970).
[11] J. Jiménez, Annual Research Briefs, Center for Turbulence Research, Stanford University (1998).
[12] C. D. Tomkins and R. J. Adrian, J. Fluid Mech. **490**, 37 (2003).
[13] M. Guala, S. E. Hommema, and R. J. Adrian, J. Fluid Mech. **554**, 521 (2006).
[14] N. Hutchins and I. Marusic, J. Fluid Mech. **579**, 1 (2007).
[15] B. J. Balakumar and R. J. Adrian, Phil. Trans. R. Soc. A **365**, 665 (2007).
[16] K. C. Kim and R. Adrian, Phys. Fluids **11**, 417 (1999).
[17] A. Townsend, *The Structure of Turbulent Shear Flow* (Cambridge University Press, Cambridge, England, 1976).
[18] X. Wu and P. Moin, J. Fluid Mech. **630**, 5 (2009).
[19] S. Toh and T. Itano, J. Fluid Mech. **524**, 249 (2005).
[20] J. C. del Álamo and J. Jiménez, J. Fluid Mech. **559**, 205 (2006).
[21] G. Pujals, M. García-Villalba, C. Cossu, and S. Depardon, Phys. Fluids **21**, 015109 (2009).
[22] C. Cossu, G. Pujals, and S. Depardon, J. Fluid Mech. **619**, 79 (2009).
[23] Y. Hwang and C. Cossu, J. Fluid Mech. **643**, 333 (2010).
[24] Y. Hwang and C. Cossu, J. Fluid Mech. (to be published).
[25] O. Kitoh and M. Umeki, Phys. Fluids **20**, 025107 (2008).
[26] G. Pujals, C. Cossu, and S. Depardon, in *Sixth Symposium on Turbulence and Shear Flow Phenomena* (Seoul National University, Seoul, Korea, 2009).
[27] G. Pujals, C. Cossu, and S. Depardon, J. Turbul. (to be published).
[28] J. Jiménez, Rev. R. Acad. Cien. Serie A Mat. **101**, 187 (2007).
[29] J. Smagorinsky, Mon. Weather Rev. **91**, 99 (1963).
[30] C. Härtel and L. Kleiser, J. Fluid Mech. **356**, 327 (1998).
[31] C. Meneveau and J. Katz, Annu. Rev. Fluid Mech. **32**, 1 (2000).
[32] T. R. Bewley, P. Moin, and R. Temam, J. Fluid Mech. **447**, 179 (2001).
[33] T. A. Zang, Phil. Trans. R. Soc. A **336**, 95 (1991).
[34] J. del Álamo and J. Jiménez, Phys. Fluids **15**, L41 (2003).
[35] J. C. del Álamo, J. Jiménez, P. Zandonade, and R. D. Moser, J. Fluid Mech. **500**, 135 (2004).
[36] J. P. Monty, N. Hutchins, H. C. H. Ng, I. Marusic, and M. S. Chong, J. Fluid Mech. **632**, 431 (2009).
[37] O. Flores and J. Jiménez, J. Fluid Mech. **566**, 357 (2006).
[38] O. Flores, J. Jiménez, and J. del Álamo, J. Fluid Mech. **591**, 145 (2007).
[39] S. C. Reddy, P. J. Schmid, J. S. Baggett, and D. S. Henningson, J. Fluid Mech. **365**, 269 (1998).

5

Article 5

Optimally amplified large-scale streaks and drag reduction in turbulent pipe flow

Ashley P. Willis[*] and Yongyun Hwang[†]

Laboratoire d'Hydrodynamique (LadHyX), École Polytechnique, 91128 Palaiseau, France

Carlo Cossu[‡]

Institut de Mécanique des Fluides de Toulouse (IMFT), 31400 Toulouse, France and Département de Mécanique,
École Polytechnique, 91128 Palaiseau, France

(Received 10 June 2009; revised manuscript received 3 July 2010; published 28 September 2010)

The optimal amplifications of small coherent perturbations within turbulent pipe flow are computed for Reynolds numbers up to one million. Three standard frameworks are considered: the optimal growth of an initial condition, the response to harmonic forcing and the Karhunen-Loève (proper orthogonal decomposition) analysis of the response to stochastic forcing. Similar to analyses of the turbulent plane channel flow and boundary layer, it is found that streaks elongated in the streamwise direction can be greatly amplified from quasistreamwise vortices, despite linear stability of the mean flow profile. The most responsive perturbations are streamwise uniform and, for sufficiently large Reynolds number, the most responsive azimuthal mode is of wave number $m=1$. The response of this mode increases with the Reynolds number. A secondary peak, where m corresponds to azimuthal wavelengths $\lambda_\theta^+ \approx 70-90$ in wall units, also exists in the amplification of initial conditions and in premultiplied response curves for the forced problems. Direct numerical simulations at Re $=5300$ confirm that the forcing of $m=1,2$ and $m=4$ optimal structures results in the large response of coherent large-scale streaks. For moderate amplitudes of the forcing, low-speed streaks become narrower and more energetic, whereas high-speed streaks become more spread. It is further shown that drag reduction can be achieved by forcing steady large-scale structures, as anticipated from earlier investigations. Here the energy balance is calculated. At Re $=5300$ it is shown that, due to the small power required by the forcing of optimal structures, a net power saving of the order of 10% can be achieved following this approach, which could be relevant for practical applications.

I. INTRODUCTION

The nature of laminar-turbulent transition, and of the structure of turbulence in pipe flow, is a subject that has interested generations of fluid dynamicists since the pioneering work of Reynolds [1]. Laminar pipe flow (the Hagen-Poiseuille flow solution) is linearly stable, but subcritical transition to turbulence is observed at Reynolds numbers as low as ≈ 2000. A key mechanism in the transition process is played by the lift-up effect [2,3] consisting of the strong amplification of the energy of streamwise streaks that evolve from streamwise vortices. These streaks are narrow elongated regions where the streamwise velocity is larger or smaller that the average at the same distance from the wall. The large amplification of the streaks by the lift-up mechanism is related to the strong non-normality of the linearized Navier–Stokes operator [4–6]. Optimal perturbations, which maximize the energy amplifications, have been computed for most of the canonical laminar shear flows, where it is found that streamwise uniform structures are the most amplified. The maximum amplification of initial conditions, and responses to harmonic and stochastic forcing have been found to scale such as Re^2, Re^4, and Re^3, respectively [6–9]. For laminar pipe flow, the most amplified streamwise uniform

modes are those of azimuthal wave number $m=1$ [10–12], decreasing monotonically with increasing m, and the resulting streaks are significantly unstable when of sufficient amplitude [13].

Coherent streaky motions also exist in the turbulent pipe. The existence of streaks in the buffer layer with a mean spanwise spacing of ≈ 100 wall units has been well documented for the boundary layer [14–16] and for pipe flows [17,18]. Coherent streaky structures exist also at much larger scales, of the order of several pipe radii, R. Recently it has been realized that these structures can be very long (at least $\approx 8R$ to 16R), and contribute to half of the total turbulent kinetic energy and Reynolds stress [19,20]. Contrary to other canonical turbulent flows, for the case of the turbulent pipe relatively little is known on the spanwise (azimuthal) structure of these coherent large-scale structures.

While early computations of optimal growths and responses to stochastic forcing [21–23] have considered the turbulent mean flow as a base flow, the molecular viscosity was included in the equations for the coherent perturbations. An externally imposed eddy turnover time had to be included in the optimization process. More recent analyses of the turbulent plane channel flow [24–26], boundary layer [27] and Couette flow [28] have included the effect of the eddy viscosity in the linearized equations, in the spirit of Ref. [29]. In this approach the eddy turnover time need not be enforced, but is an output of the optimization process. Following this approach, two preferred spanwise wavelengths are found for the amplification of streamwise uniform streaks, for sufficiently high Reynolds numbers. The first ($\lambda_z \approx 3h$ to $4h$ for

─────────────
[*]willis@ladhyx.polytechnique.fr
[†]yongyun@ladhyx.polytechnique.fr
[‡]carlo.cossu@imft.fr

plane channel flow) scales in outer units (i.e., with the channel half-width h), and the maximum amplifications increase with the Reynolds number. The second preferred spanwise length, which scales in inner (wall) units, is found at $\lambda^+ \approx 100$, in good accordance with the scales of the buffer layer cycles. Here milder energy amplification of initial conditions is found. These results strongly suggest that the mean lift-up effect is involved as an essential part of the mechanisms that permit the sustenance of turbulent coherent structures.

When streaks are of finite amplitude they may support the amplification of secondary perturbations [30,31] that lead to their breakdown, and to the refueling of streamwise vorticity necessary to sustain the streaks [32,33]. This self-sustained process is christened in the emergence of nonlinear saddle solutions [34,35] and unstable periodic orbits [36]. Many unstable nonlinear solutions have also been found for pipe flow [37,38], where a positive Lyapunov exponent is displayed in the turbulent regime [39]. These "exact" solutions [40], which are believed to provide a structure to the subcritical transition process [41], typically have few unstable eigenvalues and associated modes, while they are attracting in all other directions in phase space. It has therefore been conjectured that transitional flow spends significant periods of time in the neighborhood of a few of these nonlinear solutions, and that therefore the lowest order statistics could be retrieved by averaging over the exact solutions. This rational framework has been boosted by the experimental observation of the velocity field bearing resemblance to exact nonlinear traveling wave solutions [42]. Exciting phase space portraits of the transitional regime are becoming available for the plane Couette flow [43].

It is currently not clear how to extend the dynamical systems approach into the régime of developed turbulence. At large Reynolds numbers, exact solutions typically have high wave numbers, implying an unrealistic number of repetitions of the structure in space. Progress is being made with respect to this spatial dependence, with the discovery of localized counterparts to the infinitely extended solutions [44]. Other periodic solutions have been continued to high Reynolds numbers [45]. A different but serious problem is that, while capturing the typical features of turbulence near the wall, exact solutions do not exhibit the large dissipation of turbulence in the central region of the flow. It is this dissipation that leads to flattened mean profiles of the flow and strong deceleration of the core region for pipe flow. This slow core is clearly present in the observations of [42]. While dissipation occurs on small scales in the central region, however, coherent streaks certainly are present. A myriad of solutions exhibiting streaks is now available for pipe flow [46], but it is not yet clear how to determine which best characterize turbulence. Toward this end, in the present study the eddy viscosity is invoked to help reveal on which length scales the most important structures occur, those associated with energy production through amplification, and who's presence may otherwise be masked by the dissipative eddies.

In addition to its potential relevance for understanding the structure of turbulent flows, the analysis of optimal energy amplifications is also relevant for flow control. In the laminar boundary layer, for instance, the forcing of nearly optimal streaks has been used to stabilize the base flow to Tollmien-

Schlichting waves [47–49] and delay transition to turbulence [50]. That large-scale coherent streaks can be effectively amplified in the turbulent boundary layer [51,52] has opened the way for their use in separation control in industrial applications [53]. Furthermore, a few studies [54,55] have shown that by forcing large-scale streamwise vortices, viscous drag can be reduced in the plane channel flow. However, in these studies the cost of the control action has not been evaluated, and it is therefore unclear if a net power saving can be achieved. In this study, the advantage of forcing optimal structures is that the energy required for the forcing is minimized, reducing the cost of the control.

The scope of the present investigations is therefore to answer the following questions: what are the optimal energy amplifications and responses to forcing sustained by the mean turbulent flow in a pipe? Structures of which wavelengths are most amplified? And, how do these amplifications and their structure change with Reynolds number? Despite its ubiquity in practical applications, these results are not yet available for turbulent pipe flow. A linear model is presented in Sec. II. Linear results (Sec. III), based on the eddy-viscosity model, here and for the planar geometries, are yet to be compared with simulations of "real" turbulence, i.e., in full resolved simulation (Sec. IV). In other words, do the optimal streaks predicted by the linear eddy-viscosity model compare well to artificially forced streaks computed in direct numerical simulation? As simulations in the presence of turbulence are inherently nonlinear, what is the effect of finite amplitude forcing on these coherent streaks? Finally, we are interested in the influence of artificially forced finite amplitude streaks on the drag. Can the mean drag be reduced in the presence of large amplitude streaks? Is a net power saving, including the cost of the control, achievable, and if so, what is the best performance?

II. BACKGROUND

A. Turbulent base flow and eddy viscosity

Consider the incompressible flow of a viscous fluid of kinematic viscosity ν in a circular pipe of radius R. The bulk velocity U_b (mean streamwise speed) is assumed constant. Lengths are nondimensionalized by R and velocities by $U_{cl}^{lam} = 2U_b$, the center-line speed for laminar flow of the same bulk velocity [12,38,56,57]. The usual Reynolds number based on the mass flux is defined as $Re = 2U_b R/\nu$. At sufficiently large Reynolds numbers the flow is turbulent and the turbulent mean flow profile preserves invariance in the spanwise direction θ, the streamwise direction x, and in time t. The mean flow velocity is written $\boldsymbol{U} = U(y)\boldsymbol{e}_x$, where $y = 1 - r$ is the dimensionless distance from the boundary wall and r is the radial coordinate. In complement to this "outer" scaling, convenient for measuring large-scale properties, to describe near-wall structure it is commonplace to also define units via the friction velocity $u_\tau^2 = \nu \partial_y U|_{y=0}$, based on the shear near the wall. The wall units of length and time are then ν/u_τ and ν/u_τ^2, respectively. Variables nondimensionalized on this "inner" scaling bare the superscript + in the following, and the wall-Reynolds number is defined $Re_\tau = u_\tau R/\nu$.

If, as a first approximation, the Boussinesq eddy viscosity is used to model the turbulent Reynolds-stresses, then the streamwise component of the Reynolds-averaged momentum conservation reads

$$\frac{1}{\text{Re}}\left(\frac{1}{r}+\partial_r\right)(\nu_T\partial_r U)=\partial_x P, \tag{1}$$

where the total effective viscosity is $\nu_T(y)=1+E(y)$ and $E(y)$ is the eddy-viscosity, normalized such that at the wall $\nu_T(0)=1$, i.e., the kinematic value is attained. We denote by $B=-\partial_x P$, the averaged streamwise pressure gradient necessary to maintain the prescribed mass flux.

For $E(y)$ we use the convenient expression originally suggested for pipe flow by Cess [58], later used for channel flows by Reynolds and Tiederman [59], then by many others [21,24,25]:

$$E(y)=\frac{1}{2}\left\{1+\frac{\kappa^2\hat{R}^2\hat{B}}{9}[2y-y^2]^2(3-4y+2y^2)^2\right.$$
$$\left.\times\left[1-\exp\left(\frac{-y\hat{R}\sqrt{\hat{B}}}{A^+}\right)\right]^2\right\}^{1/2}-\frac{1}{2}. \tag{2}$$

The mean streamwise velocity $U(y)$ in equilibrium with this radially dependent eddy viscosity [Eq. (2)] is easily inverted from the mean averaged momentum Eq. (1), and matches very well experimental observations. Here, $\hat{R}=\text{Re}/2$, $\hat{B}=2B$. The fitting parameters $A^+=27$ and $\kappa=0.42$ have been updated to improve the match with recent observations in [60].

B. Equations for the small coherent perturbations to the turbulent base flow

We now take the state $\boldsymbol{\Phi}=(U,P)$, solution of Eq. (1), as a (steady) base flow and consider small coherent (correlated when ensemble-averaged) perturbations, $\boldsymbol{\varphi}=(\boldsymbol{u},p)$, to $\boldsymbol{\Phi}$ in the presence of a coherent (correlated) force $\boldsymbol{f}$ and/or coherent initial conditions $\boldsymbol{u}_0$. Note that $\boldsymbol{\Phi}$ is understood to be the turbulent mean state for $\boldsymbol{f}=\boldsymbol{0}$ and $\boldsymbol{u}_0=\boldsymbol{0}$.

The equations governing the coherent perturbations require modeling of the Reynolds stresses to be closed. Reynolds and Hussain [29] discussed the eddy viscosity as a simple closure model, finding that it compared well for small-amplitude perturbations. Linearizing the closed equations, following [24–29], the equation governing small-amplitude coherent perturbations is

$$\partial_t\boldsymbol{u}+u_r\partial_r U\boldsymbol{e}_x+U\partial_x\boldsymbol{u}=-\boldsymbol{\nabla}p+\frac{1}{\text{Re}}\boldsymbol{\nabla}\cdot[\nu_T(y)(\nabla\boldsymbol{u}+\nabla\boldsymbol{u}^T)]$$
$$+\boldsymbol{f}. \tag{3}$$

These perturbations also satisfy continuity, $\boldsymbol{\nabla}\cdot\boldsymbol{u}=0$. The explicit components for the viscous term are given in Appendix A.

Exploiting the rotational and the streamwise translational invariance of the system, one may expand the perturbations in Fourier modes $\boldsymbol{\varphi}(r,\theta,x;t)=\Sigma_{\alpha m}\hat{\boldsymbol{\phi}}_{\alpha m}(r;t)\text{e}^{\text{i}(\alpha x+m\theta)}$, where α and m are the streamwise and azimuthal wave number respectively. Substitution into Eq. (3) gives

$$\partial_t\hat{\boldsymbol{\phi}}_{\alpha m}(r;t)=\boldsymbol{L}_{\alpha m}(\boldsymbol{\Phi})\hat{\boldsymbol{\phi}}_{\alpha m}+\hat{\boldsymbol{f}}_{\alpha m}(r;t), \tag{4}$$

where $\boldsymbol{L}_{\alpha m}$ is the linear operator acting on the Fourier mode $\hat{\boldsymbol{\phi}}_{\alpha m}(r)$. The problem may be considered for each mode independently, and the subscript α,m is dropped in the following. The spanwise and streamwise wavelengths for each perturbation are given by $\lambda_\theta=2\pi/m$ and $\lambda_x=2\pi/\alpha$ respectively in units of R.

C. Optimal growth and response to forcing

Three properties of the linearized system are now examined. They are the optimised growth of initial conditions, the optimised response to harmonic forcing, and the response to stochastic forcing. Standard definitions (see, e.g., [6,61]) are briefly restated below for the present context.

Optimal growth in time over all possible nonzero initial conditions $\hat{\boldsymbol{u}}_0$, for a particular α,m mode, is given by the function

$$G(\alpha,m;t)\equiv\max_{\hat{\boldsymbol{u}}_0\neq\boldsymbol{0}}\frac{\|\hat{\boldsymbol{u}}(t)\|^2}{\|\hat{\boldsymbol{u}}_0\|^2}, \tag{5}$$

and the maximum achieved over all times is $G_{\max}(\alpha,m)\equiv\max_t G(\alpha,m;t)$. Here $\hat{\boldsymbol{f}}=\boldsymbol{0}$, and the energy norm used is $\|\hat{\boldsymbol{u}}\|^2\equiv(1/V)\int_V\boldsymbol{u}\cdot\boldsymbol{u}\,\text{d}V$.

For harmonic forcing, $\hat{\boldsymbol{f}}=\tilde{\boldsymbol{f}}\text{e}^{\text{i}\Omega_f t}$, and accompanying response, $\hat{\boldsymbol{u}}=\tilde{\boldsymbol{u}}\text{e}^{\text{i}\Omega_f t}$, the optimal response is given by

$$R(\alpha,m;\Omega_f)\equiv\max_{\tilde{\boldsymbol{f}}\neq\boldsymbol{0}}\frac{\|\tilde{\boldsymbol{u}}\|^2}{\|\tilde{\boldsymbol{f}}\|^2}. \tag{6}$$

The maximum over all frequencies Ω_f is $R_{\max}(\alpha,m)=\max_{\Omega_f}R(\alpha,m;\Omega_f)$.

Finally, the response to a stochastic force is usually considered in the discretized form (here radially). Let $\hat{\boldsymbol{f}}(t)$ be the discretized stochastic force vector, and $\langle\cdot\rangle$ denote ensemble averaging. Following analyses [9,22,61–64], the forcing is assumed to have Gaussian probability density with zero average (i.e., $\langle\hat{\boldsymbol{f}}\rangle=\boldsymbol{0}$), isotropic (equal variance on all the three components) and delta-correlated in space and time, $\langle\hat{\boldsymbol{f}}(t)\hat{\boldsymbol{f}}^H(t')\rangle=\boldsymbol{I}\delta(t-t')$, where the superscript H denotes the Hermitian transpose. The amplification of the stochastic forcing is then measured by the variance of the response:

$$V(\alpha,m)\equiv tr\{\boldsymbol{C}_\infty\}, \tag{7}$$

where $\boldsymbol{C}_\infty=\langle\hat{\boldsymbol{u}}\hat{\boldsymbol{u}}^H\rangle$ is the covariance matrix for the response in the limit $t\rightarrow\infty$. This covariance matrix is computed by solving an algebraic Lyapunov equation (see Appendix B). The eigenfunction decomposition of the Hermitian matrix $\boldsymbol{C}_\infty$ is known as the Karhunen-Loève (KL) or proper orthogonal decomposition (POD). The ratio of its real and positive eigenvalues, σ_n, to the variance $V=\Sigma_n\sigma_n$ represent the relative contribution to the variance from each orthogonal mode. The eigenfunction corresponding to the leading eigenvalue thus contributes most to the variance V. For details see [9,22,62–65].

D. Numerical methodology

The linear operator appearing in Eq. (3) must be discretized in order to compute the optimal growths and the responses described above. Some attention must be paid to difficulties introduced by the cylindrical geometry, and full details of the methods are given in Appendix B. Here we note the general approach and convergence of the results.

A Chebyshev-collocation method on up to $N=250$ radial points was used to calculate up to $2N-3$ eigenvectors and eigenvalues for the linear system [Eq. (3)]. The optimal growth code, which requires only these eigenvectors, eigenvalues and weights for calculating norms, is a well validated code used for several previous studies [25,27,28,66]. Results for the optimal growth and the response to steady forcing were also verified by direct time stepping. At the largest $Re=10^6$ the power spectral drop-off for the optimal modes was of eight orders of magnitude.

Responses from the linear model are compared with direct numerical simulations of the original Navier-Stokes equations. The pipe flow code described in [67] has been used for simulation of full turbulence subject to a forcing f. This time stepping code also uses a Fourier decomposition in θ and x, but finite differences on a nonequispaced radial (y) nine-point stencil. Time steps are controlled using information from a second-order predictor-corrector method. For most simulations presented, the radial spacings are $\delta r_{min}^+ = 0.11$, $\delta r_{max}^+ = 4.4$ (wall units ν/u_τ). With dealiasing, $\delta_\theta^+ = 5.9$, $\delta_x^+ = 9.4$ at the boundary, in a domain $L=15(R)$, $L^+ = 2700$. Verification of these results is performed by calculation where the spacings above are respectively 0.08, 4.0, 3.9, 6.3 for $L=20$. Simulations enforce a fixed mass flux, consistent with previous analyses [54,68].

III. LINEAR AMPLIFICATION OF COHERENT STRUCTURES

A. Wave number dependence

We first consider the dependence of the optimal amplifications on the streamwise and azimuthal wave numbers at the very large flux-Reynolds number of $Re=10^6$ corresponding to $Re_\tau = 19\,200$. Figure 1 shows the dependence of G_{max}, R_{max} and V on m for the selected $\alpha = 0, 1, 10, 100, 1000$. It is clear from all plots that streamwise elongated structures, where $\lambda_x > \lambda_\theta$, are significantly amplified. The greatest growths are found for axially independent modes ($\alpha=0$), for which the curve provides an envelope over the results for nonzero α. The maxima on the $\alpha=0$ curves are for $m=1$ azimuthal symmetry. The inset to Fig. 1(b) shows that steady forcing is optimal for axially independent harmonic forcing, $\alpha=0$, while for streamwise nonuniform perturbations, a nonzero forcing frequency is optimal. For the stochastic forcing at the optimal value $\alpha=0$, $m=1$, it is found that the leading Karhunen-Loève mode dominates, representing 93% of the contribution to the total variance, as reported in the inset to Fig. 1(c).

A secondary peak occurs in G_{max} at a larger m corresponding to an azimuthal wavelength of $\lambda_\theta^+ = 92$ (wall units ν/u_τ). Contrary to the optimal growth of initial conditions,
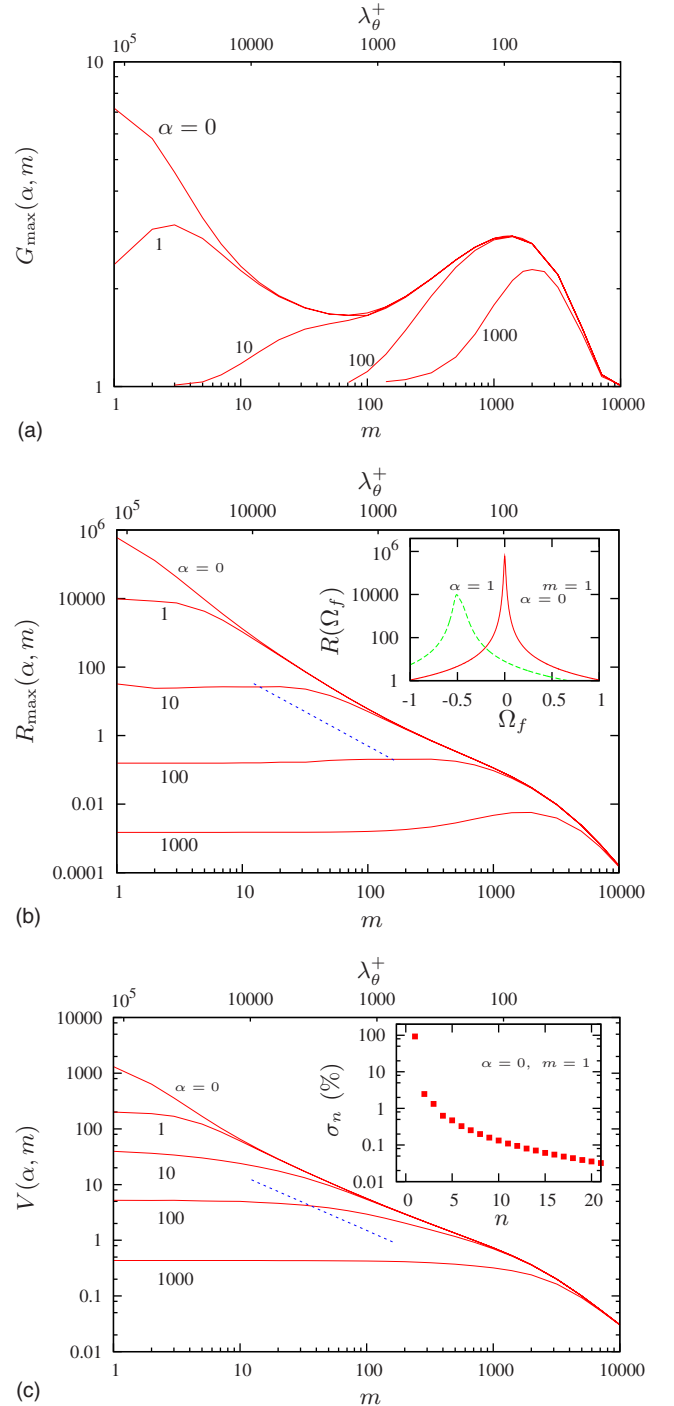

FIG. 1. (Color online) Optimal energy growth of initial conditions G_{max} (a), optimal response to harmonic forcing R_{max} (b) and variance of the response to stochastic forcing V (c) for $Re_\tau = 19200$. Dependence on azimuthal wave number m, with corresponding wavelength in wall units λ_θ^+ (top axis), for selected values of the dimensionless streamwise wave number α. Reference slopes m^{-2} and m^{-1} (dotted lines) are shown in subfigures (b) and (c) respectively. The dependence of the optimal harmonic forcing amplification $R(\alpha, m=1; \Omega_f)$ on the forcing frequency Ω_f is reported in the insert of subfigure (b) for $\alpha=0$ and $\alpha=1$; $R_{max} = \max_{\Omega_f} R$. The percentage contribution to the variance, $100\sigma_j/V(0,1)$, of the response to stochastic forcing contained in the first 20 Karhunen-Loève modes is reported in the insert of subfigure (c).
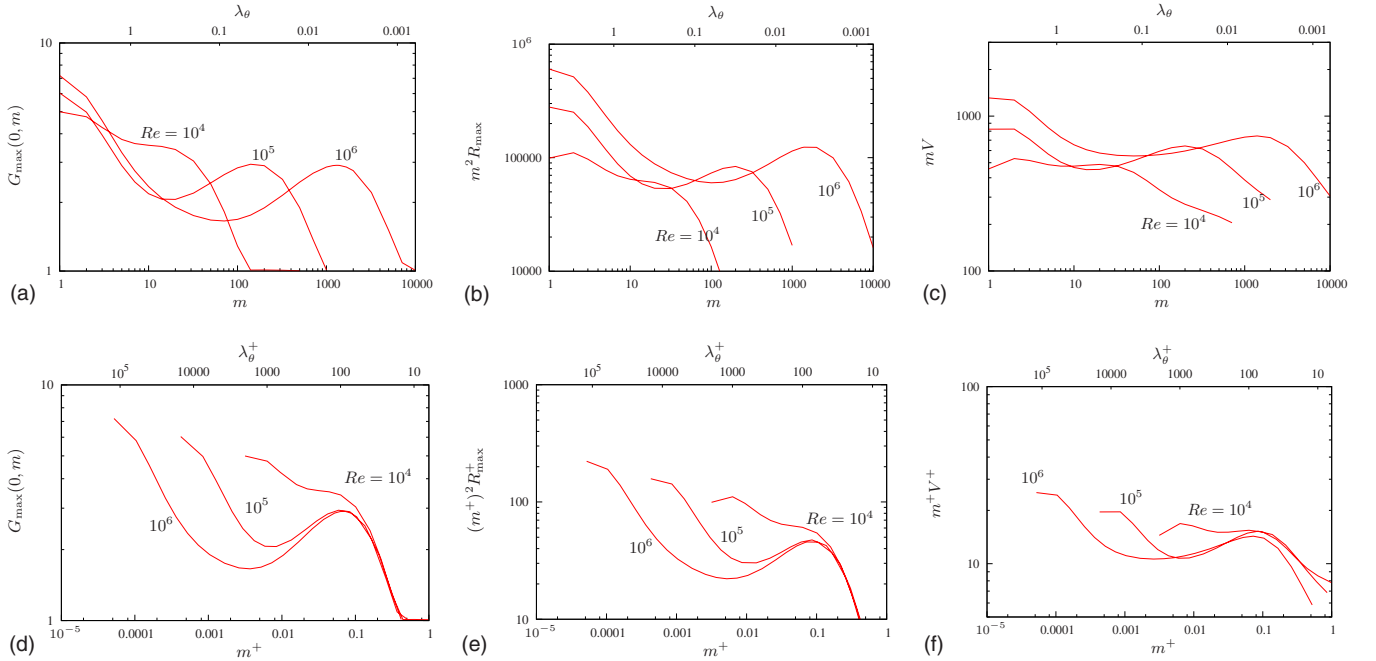
FIG. 2. (Color online) Dependence on the azimuthal wave number m and the corresponding azimuthal wavelength (top axis) of: the optimal energy amplification of initial condition $G_{\max}$ [(a) and (d)], the premultiplied optimal response to harmonic forcing $m^2 R_{\max}$ [(b) and (e)] and of the premultiplied variance of the response stochastic forcing mV [(b) and (e)]. Streamwise uniform ($\alpha=0$) perturbations are considered for the selected Reynolds numbers Re=10^4, 10^5 and 10^6 corresponding to Re$_\tau$=317, 2830, and 19200. The responses, wave numbers and wavelengths are scaled in outer units on the upper row [(a), (b), and (c)] and in inner units in the lower row [(d), (e), and (f)].

no secondary peak is found in the optimal response to forcing. A closer examination of Figs. 1(b) and 1(c) reveals that the $R_{\max}$ and V curves corresponding to $\alpha=0$ scale approximatively like m^{-2} and m^{-1}, respectively, for intermediate values of m. A noticeable change of slope is found for values of m corresponding to $\lambda_\theta^+ \approx 100$. In plane channel flow, this power-law dependence has been explicitly related to the behavior of geometrically similar optimal structures in the log-layer [26]. In the case of the response to forcing, primary and secondary peaks occur in the deviations from this power-law behavior [26]. This can be seen by considering the premultiplied responses $m^2 R_{\max}$ and mV. A secondary peak at $\lambda_\theta^+ = 73$ is found in the premultiplied response curves for $\alpha=0$, shown in Figs. 2(b) and 2(c).

B. Reynolds number dependence

The spanwise optimal wave numbers, corresponding to the primary and to the secondary peak, do not change with Re when, respectively, scaled with outer and inner units. This can be seen in Fig. 2, where $G_{\max}$ and the premultiplied

$m^2 R_{\max}$, mV computed for Re=10^4, 10^5, and 10^6 (corresponding to Re$_\tau$=317, 2380, and 19 200, respectively) for $\alpha=0$ are reported. While the premultiplied response to steady forcing is useful for showing deviations from the $R_{\max} \sim m^{-2}$ trend, the premultiplied stochastically forced case is arguably more representative of turbulence. When m is presented on a log scale, equal area under the curve mV implies equal contribution to the total variance. Here, where the spanwise wave number is integer for pipe flow, all the primary peaks are reached for $m=1$ except for the premultiplied stochastic response at lower Re$_\tau$; for Re$_\tau$=10^4, $m=2$ is preferred and the selection of m is very weak in mV for Re =10^4 and lower. The secondary peak is always found at $\lambda_\theta^+ \approx 70$–$90$ for all the premultiplied responses. The primary and the secondary peaks, however, are not yet separated at Re$_\tau$=10^4, while they are for Re$_\tau$=10^5 and higher, in good accordance with the turbulent plane channel [24–26] the boundary layer [27].

The maximum responses, associated with the primary peak ($\alpha=0$, $m=1$) increase with the Reynolds number, while those associated with the secondary peak remain almost constant. The structure of the leading modes corresponding to
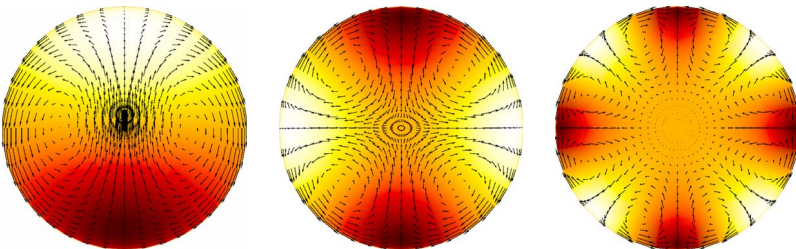

FIG. 3. (Color online) Linear optimal responses to steady forcing for $\alpha=0$ and $m =1,2,4$; Re$_\tau$=19200. Vectors: cross-stream components of the input vector field. (Colored) contour levels: streamwise component of the output field (streaks). White fast-streaks, red/dark slow streaks.
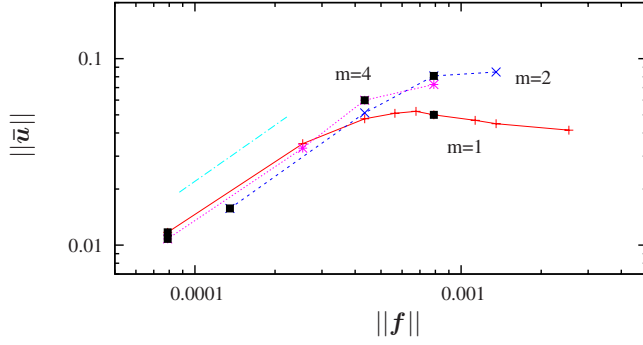
FIG. 4. (Color online) Response to forcing in full simulation showing the linear régime and nonlinear saturation. $\|f\|$ is the rms value. The isolated line is of slope 1 and squares correspond to the plots of Fig. 5.

the primary peak for optimal growth, for the response to steady and stochastic forcing, appear to be almost identical and remain the same over the entire range of Reynolds numbers. Plotted in Fig. 3 are the leading modes for $m = 1, 2, 4$ (data from the optimal harmonic forcing case at Re $= 10^6$). The optimal input consists of the expected large-scale streamwise vortices and the optimal output of large-scale streamwise streaks. Note that in this geometry, only modes of $m = 1$ can exhibit flow across the axis. The structures corresponding to the secondary peak, which scale in inner units, are almost indistinguishable from those found in the plane channel and the boundary layer [25–27] and are therefore not reported here.

IV. SIMULATION OF FORCED FINITE AMPLITUDE COHERENT STREAKS

A. Response to finite amplitude optimal steady forcing

The optimal response predictions, described in the previous section, were based on two main simplifying assumptions: (a) the effect of the uncorrelated motions was modeled with an isotropic eddy-viscosity and (b) coherent perturbations were assumed small. We now test the level of approxi-

mation implied in these assumptions by computing in full DNS the effective responses of the predicted optimal perturbations. In particular, we consider the response to the optimal steady large-scale forcing, the mode which is the most amplified, and potentially the most relevant for passive flow control applications. The forcing term f is taken to be proportional to the mode $\widetilde{f}$ that optimizes $R_{\max}$, obtained from the above linear analysis, for $\alpha = 0$ and a given m. As the considered optimal forcing is steady, time averages can be easily calculated and the statistical convergence readily checked. The magnitude of the steady forcing $\|f\|$ is measured by the rms value, as before. The response of the flow in simulations is given by $\bar{u}(r, \theta) = \langle u \rangle_{x,t} - \bar{U}(r)\hat{x}$, where $\bar{U}(r) = \langle u \rangle_{\theta,x,t}$ is the mean flow in the absence of forcing. $\langle \cdot \rangle_s$ indicates averaging over the subscripted variables. Averages are taken over at least $2800 R / U_{\mathrm{cl}}^{\mathrm{lam}}$ time units. The DNSs are performed at Re $= 5300$, for which Re$_\tau = 180$.

From Fig. 4 it is seen that the amplitude of the responses $\|\bar{u}\|$ depends linearly on the forcing for small forcing amplitudes $\|f\|$. Small forcing can lead to large responses, in agreement with the linear eddy-viscosity model and, in the linear régime, the leading mode is $m = 1$, as expected. The response predicted by the linear eddy-viscosity model is $R_{\max} = 276^2$ for $m = 1$ at this Re, while in the simulations, $\|\bar{u}\| / \|f\|$ is a factor 2 smaller than expected in the linear range. As the time-averaged mean flow for the unforced case, obtained from DNS, deviates very little from that given by Eqs. (2) and (1), this difference is most likely attributed to the isotropic eddy-viscosity assumption. Similar considerations apply to the observation that the $m = 4$ mode is slightly more responsive than the $m = 2$ mode in the linear regime.

For larger forcing amplitude, the amplitude of response saturates. For the $m = 1$ mode, this saturation begins when the amplitude A_S of the associated coherent streaks is near to 19% of the center-line speed, where $A_S = \frac{1}{2}(\max \bar{u}_x - \min \bar{u}_x)$ [69]. The responses to higher order optimal modes ($m = 2$ and $m = 4$) saturate at larger forcing amplitudes $\|f\|$, and therefore contain more energy $\|\bar{u}\|^2$ than the $m = 1$ mode, for sufficiently large forcing amplitudes.

In Fig. 5, we report the finite amplitude coherent vortices and streaks induced by the steady forcing for, respectively,
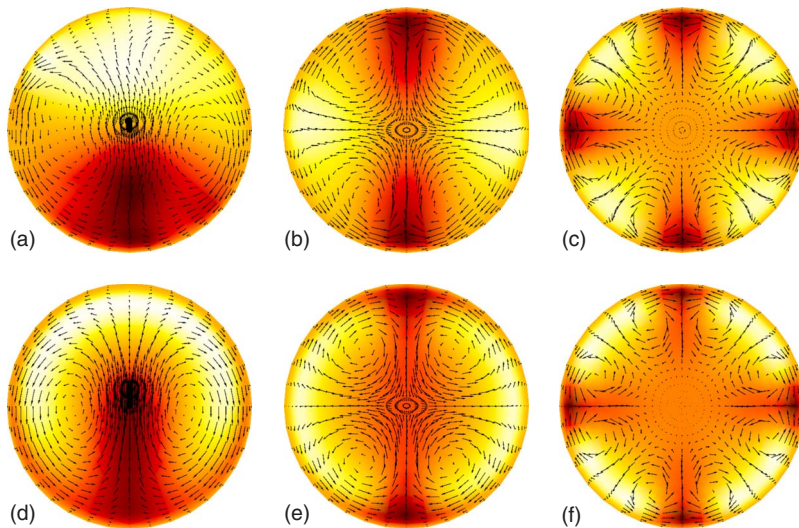

FIG. 5. (Color online) Nonlinear responses to finite amplitude forcing for $\alpha = 0$ and $m = 1, 2, 4$ from direct numerical simulation at Re$_\tau = 180$. Small forcing amplitude (upper row) and moderate forcing (lower row), corresponding to the marked squares in Fig. 5. (a) $m = 1$, $\|f\| = 8.0\,10^{-5}$; (b) $m = 2$, $\|f\| = 1.4\,10^{-5}$; (c) $m = 4$, $\|f\| = 8.0\,10^{-5}$; (d) $m = 1$, $\|f\| = 8.0\,10^{-4}$; (e) $m = 2$, $\|f\| = 8.0\,10^{-4}$; (f) $m = 4$, $\|f\| = 2.5\,10^{-4}$. Vectors: cross-stream components of the forced velocity field. (Colored) contour levels: streamwise component of the output field (streaks). White fast-streaks, red/dark slow-streaks.
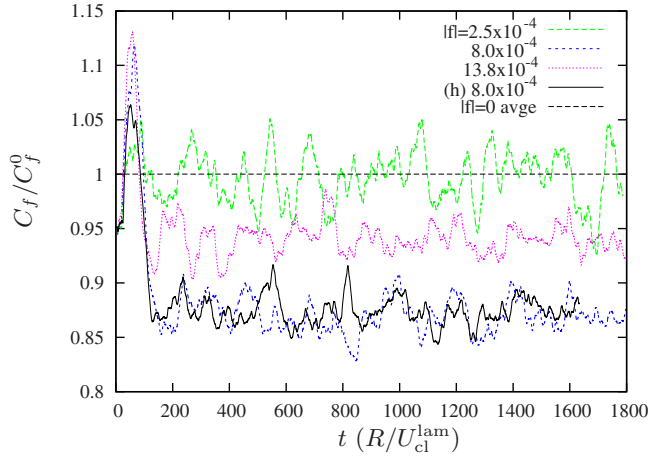
FIG. 6. (Color online) Relative drag for several levels of steady forcing of the $m=1$ mode from direct numerical simulation. At intermediate levels of forcing the drag is reduced, falling below the average of the unforced case (horizontal straight line). The forcing can reduce the drag. The solid line is a higher resolution check at $\|f\|=8.010^{-4}$.

low and moderate forcing amplitudes for the three azimuthal modes $m=1$, $m=2$, and $m=4$. From these figures, and by comparing them with the linear optimals reported in Fig. 3, it is seen how, for increasing forcing amplitude, the low-speed streaks are more and more spatially concentrated, while high-speed streaks have a tendency to widen.

B. Influence on the drag

We now examine the influence of the forced finite amplitude streaks on the drag, always at Re=5300 (corresponding to Re$_\tau$=180). Figure 6 shows time series for the instantaneous $C_f=2(u_\tau/U_b)^2$ in full DNS for three levels of optimal steady forcing of the $m=1$, $\alpha=0$ mode. In wall units, the spanwise wavelength of the forced streaks for $m=1$ is $\lambda_\theta^+ \approx 1130$, which extends by a factor greater than 2 the spacings considered in earlier investigations of the plane channel flow [54,55]. The horizontal line in Fig. 6 represents the baseline (time averaged) C_f in the absence of forcing. From this figure we see that indeed average drag reductions can be obtained also in the turbulent pipe flow. We have verified the accuracy of this result, in particular that no loss of the observed drag occurs (solid line), by performing an additional calculation at higher resolution (more than doubling the number of grid points, see Sec. II D).

In Fig. 7, the relative change for time averaged C_f is reported versus the forcing amplitude for the $m=1$, $m=2$, and $m=4$ modes. Drag reduction is obtainable over a range of forcing amplitudes covering approximately one order of magnitude. Selecting the best forcing amplitude, the maximum drag reduction achieved is 12.8% when forcing the $m=1$ mode. It is reduced for higher modes, e.g., 10.4% for $m=2$ ($\lambda_\theta^+ \approx 565$) and 4% for the mode $m=4$ ($\lambda_\theta^+ \approx 280$). Forcing streaks at the near-wall peak mean spacing ($\lambda_\theta^+=100$, corresponding to $m \approx 12$) results in increased drag.

For this control strategy to be interesting for applications, the net power saved must be considered. The power con-
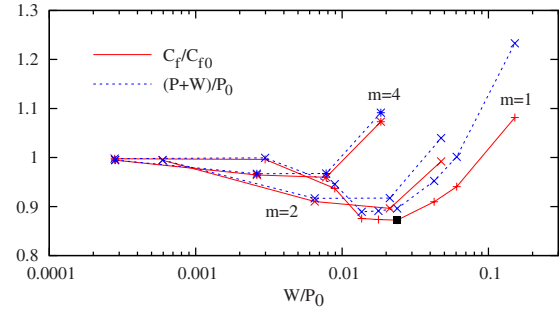

FIG. 7. (Color online) Effect of forcing on the mean skin friction, relative to the unforced case (solid). Relative net power consumption including the work done by the force (dashed). Black square corresponds to $\|f\|=8.010^{-4}$.

sumption (per unit length) spent to maintain the desired constant volume flux of the turbulent flow is $P=\frac{\pi}{8}C_f$ in units $\rho U_{cl}^{lam3}R$, and the control power spent (per unit length) to maintain the vortices is $W=\frac{1}{L}\int u \cdot f dV$. The drag relative to the unforced case is then given by $C_f/C_{f0}=P/P_0$, and the total relative net power consumption by $(P+W)/P_0$. The percentage net power saving is thus $100[1-(P+W)/P_0]$. From Fig. 7, where the relative drag and net power consumption are shown versus the forcing power, it is seen that the best net power saving corresponds to 11.1% and is obtained for the $m=1$ mode. For this case, W is only 1.4% of P_0. The response to forcing the large-scale mode is large, and as a result little energy is required to generate the prominent large-scale slow streak which affects the drag at the walls. The forcing of higher optimal modes results in smaller net power savings (e.g., at best 8.3% for $m=2$ and 3.3% for $m=4$).

The drag reducing mechanism appears to be consistent with that observed in plane channel flow [54,55]. Figure 8(a) shows a snapshot of streamwise vorticity field in the absence of forced streaks. Intense small-scale quasistreamwise vortices with $\lambda_\theta^+ \approx 100$ appear irregularly but in the whole azimuthal domain. These vortices, largely responsible for the turbulent skin friction [70], are weakened when large-scale streaks are artificially forced, and are almost suppressed from the high-speed streak region as seen in Figs. 8(b) and 8(c). In
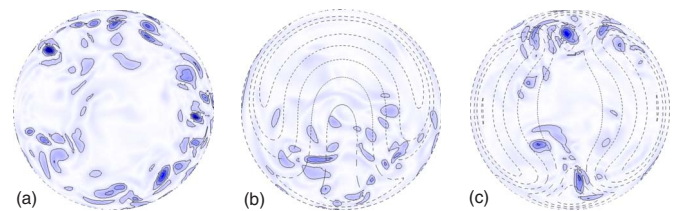

FIG. 8. (Color online) Snapshots of the cross-stream distribution of the streamwise vorticity ω_x field at a selected streamwise station from direct numerical simulation. (a) Streamwise vorticity in the absence of forcing. (b,c) Weakened and localized streamwise vorticity in the presence of the $m=1,2$ steady forcing, corresponding to optimal drag reduction. Blue/dark intense vorticity, white no vorticity. Same color scales are used on all the subplots. Contour lines denote isolevels of the streamwise averaged velocity (the forced streaks).

the absence of this mechanism the drag would only increase due to distortion of the mean flow by the forcing. This drag, however, only appears to be large for moderate to large amplitudes of the forcing, leading to the observed drag reduction for intermediate forcing.

V. SUMMARY AND CONCLUSIONS

The first part of this investigation was dedicated to the computation of the optimal linear energy amplifications of coherent structures supported by the turbulent pipe mean flow. The problem formulation and the tools used in the analysis follow those of investigations of the turbulent plane channel flow [24–26], Couette flow [28], and boundary layer flow [27]. In accordance with these investigations it is found that, despite the turbulent mean flow is linearly stable, it can support the energy amplification of initial conditions and of harmonic and stochastic forcing. These energy amplifications have the expected characteristics of the lift-up effect, where vortices amplify streaks and the most amplified perturbations are streamwise uniform ($\alpha=0$). For these streamwise uniform structures, at sufficiently large Re, the maximum energy amplifications are obtained for the $m=1$ azimuthal mode. Furthermore, this large amplification increases with the Reynolds number. As observed in the Couette and plane channel flow [26,28], for the three different calculations, the initial value problem, response to harmonic forcing and most energetic Karhunen-Loève mode for stochastic forcing, the optimal inputs and outputs almost coincide.

A secondary peak is found in the $G_{max}(m, \alpha=0)$ curves for the azimuthal mode corresponding to an azimuthal wave number $\lambda_\theta^+=92$, but only a change of slope in the $R_{max}(m, \alpha=0)$, $V(m, \alpha=0)$ curves is noticeable at this λ_θ^+. The responses R_{max} and V of optimal harmonic and stochastic forcing, for $\alpha=0$ decrease with the azimuthal wave number, with an approximate scaling of m^{-2} and m^{-1} respectively for intermediate m. For the plane channel flow, this inverse power dependence on the spanwise wave number has been related to the amplification of geometrically similar structures in the log-layer [26]. To highlight the departure of the optimal responses from the power-law trend, the premultiplied responses $m^2 R_{max}$ and mV have been considered. A secondary peak is then found at $\lambda_\theta^+=73$. This peak wavelength and the corresponding responses do not change with Reynolds number, provided that they are scaled in inner units, and that the Reynolds number is sufficiently large, so as to allow for a well defined inner-outer scale separation. The corresponding structures consist of streamwise uniform buffer-layer streaks and vortices.

The linear formulations we have used allowed a relatively straightforward computation of the linear optimal energy amplifications. The advantage of this model, based on the turbulent eddy viscosity, is therefore its simplicity, while quantitatively accurate predictions could be made with more sophisticated models. It is however important to verify that the predictions of the model, such as the order of magnitude of the growth of structures at large scale, or the fact that they more amplified than small-scale structures, are at least qualitatively verified. We have therefore reported the results of direct numerical simulations, where coherent structures have been artificially forced at the moderate $Re_\tau=180$. The optimal steady forcing of large-scale structures ($m=1$, $m=2$, and $m=4$) has been considered as these structures are the most responsive, and therefore are not only easier to detect, but are potentially most interesting for control purposes. The main predictions of the linear model are qualitatively observed in the DNS: the low-m optimal perturbations show a very large response in the amplitude of induced streaks. For sufficiently small forcing amplitudes, the response to forcing is linear and the azimuthal symmetries of the forced modes are well preserved in the response. In this linear regime, the $m=1$ mode is the most responsive. The agreement between the amplifications predicted by the linear model and the one observed in the DNS is only qualitative. The quantitative differences can probably be attributed to the very eddy-viscosity assumption and could probably be reduced by using a more realistic modeling of the Reynolds stresses. As coherent structures are strongly elongated in the streamwise direction, the isotropic eddy viscosity is gives only a first order approximation. At finite amplitudes of the coherent motions, the neglected interactions with the mean flow and the random turbulent field clearly become important [71]. For larger forcing amplitudes, a saturation in the amplitude of the forced response is observed. The $m=1$ mode is the first to saturate, at a considerable amplitude of almost 20% of the centerline velocity. For increasing amplitudes, the symmetry between the high and low-speed streaks is progressively lost. Low speed streaks concentrate in smaller spanwise extensions, with slightly larger amplitude, while high-speed streaks widen and slightly decrease in amplitude. This asymmetry recalls the observed "real" unforced turbulent flows [72].

The exact relation existing between optimally amplified streaks and the coherent structures populating the "natural" (unforced) turbulent pipe flow requires consideration. In the plane channel and Couette flows, the similarity of the spanwise scales selected by the linear mechanism and those observed in the actual turbulent flow is probably explained by the requirement that significant amplification is necessary for energetic turbulent processes to be self-sustained. What is currently not clear, because of the lack of experimental or numerical data, is if $m=1$ is the dominating coherent mode at sufficiently large Re. Most of the investigations of large- and very-large scale coherent motions in the pipe flow [19,20,73,74], have rather focused on the streamwise scales of these motions. If these motions arise through a self-sustaining process, then the streamwise scales of the motion would be selected by processes related to the breakdown of the streaks. This process is missing in the present analysis. What can be said with the model, however, is which azimuthal modes are most amplified for a streamwise scale selected by other stochastic processes. For instance, if one considers streamwise wavelengths ranging from $\lambda_x=16(R)$ ($\alpha \approx 0.4$) to $\lambda_x=6$ ($\alpha \approx 1$), then the most amplified structures vary from $m=2$ to $m=5$ modes at sufficiently large Re in the stochastic response. However, at even moderately low Reynolds number (e.g., $Re=10^4$ corresponding to $Re_\tau=317$), the azimuthal selection is weak and modes ranging from $m=1$ to $m=10$ all exhibit a comparable variance [see Fig. 2(c)] in the

integrated response. These predictions are compatible with recent results from direct numerical simulations at $Re_\tau = 150$ [75] where the most energetic POD modes are found for the streamwise wavelength $\lambda_x = 20(R)$ (the computational box size) and for azimuthal modes ranging from $m=2$ to $m=7$. Additional simulations or experiments would be highly desirable to examine the azimuthal structure of the most energetic modes at larger Re.

One of the most relevant applications of the optimal perturbations of the turbulent mean flows probably resides in flow control. The direct numerical simulations confirm that energy can be greatly amplified in a turbulent flow. An objective of both theoretical and practical relevance is the reduction of the power required to drive the constant mass flux through the pipe. Using optimal forcing, less than 2% of the power required to pump the (unforced) flow, is required to induce modifications in the mean flow of the order of 20% of the centerline mean velocity. Previous numerical [54] and experimental [55] studies have shown that it is possible to reduce the mean turbulent drag in the plane channel flow by forcing large-scale vortices with spanwise wavelength of ≈ 400–500 wall units. Here we have extended this result to pipe flow, where $\lambda_\theta^+ \approx 1200$ wall units for $m=1$. Mean drag reductions of $\approx 13\%$ are achieved by forcing this $m=1$ mode, while the drag reduction is reduced for reduced spanwise spacing. In [54] the observed drag reduction was attributed to the mean weakening of the circulation of quasistreamwise coherent vortices. This effect on the quasistreamwise vortices is found in the present turbulent pipe flow. Our visualizations show that the quasistreamwise vortices of the "natural" buffer layer cycle are packed in the low-speed streak region, while they are essentially removed from the high-speed streak region.

At present it is not clear why the drag reduction reduces as the spanwise spacing is reduced. It is possible that for $m=2$ ($\lambda_\theta^+ \approx 600$) the reduced scale separation from that of the naturally occurring streaks ($\lambda_\theta^+ \approx 100$) causes the drag-reduction effect to be reduced. At spanwise separations greater than those possible at this Re_τ, where clear scale separation occurs, a plateau in the drag reduction is possible for separations greater than $\lambda_\theta^+ \approx 1200$. However, if the greatest reduction continues to be observed for the largest possible spacing, here $m=1$, it may be conjectured that, rather than scaling in inner units, the mode that most reduces drag has an upper limit that depends on the geometry. Additional simulations or new experiments at much larger Re_τ could confirm or reject these conjectures.

We have also extended earlier investigations by computing the net power saving obtained by forcing the optimal coherent streaks. As these streaks are optimal, the power required to force them is already almost minimized. Even at the considered low Reynolds number, the controlling streaks are forced with less than 2% of the power necessary to maintain the base flow, and a net power saving of $\approx 11\%$ is achieved with the $m=1$ mode. For useful implementation of the method proposed in this study, the induction of rolls need not be efficient. For example, efficiency of 50%, still using only 4% of the driving energy, might be acceptable. Note also that, as the amplification of the forcing is expected to increase with increasing Re, the percentage of total power used to force the streaks is predicted to *decrease* for increasing Re. In practice, induction of large-scale rolls is possible via passive actuators in laminar [49,50,76] and turbulent flows [51–53]. Although neither would reproduce the precise details of forcing used here, linear optimals are known to be robust to perturbations of the system, and responses close to those seen here can be expected. An experimental verification of the proposed control strategy would of course be very welcome.

APPENDIX A: RADIALLY-DEPENDENT VISCOSITY

For the radially dependent effective viscosity, $\nu_T(r)$, the viscous terms in Eq. (3) are given by

$$\boldsymbol{\nabla} \cdot [\nu_T(r)(\boldsymbol{\nabla u} + \boldsymbol{\nabla u}^T)] = \nu_T \boldsymbol{\nabla}^2 \boldsymbol{u}$$
$$+ \partial_r \nu_T \cdot \begin{bmatrix} 2\partial_r u_r \\ \partial_r u_\theta - \dfrac{1}{r} u_\theta + \dfrac{1}{r}\partial_\theta u_r \\ \partial_x u_r + \partial_r u_x \end{bmatrix}, \tag{A1}$$

where

$$\boldsymbol{\nabla}^2 \boldsymbol{u} = \begin{bmatrix} \nabla^2 u_r - \dfrac{2}{r^2}\partial_\theta u_\theta - \dfrac{u_r}{r^2} \\ \nabla^2 u_\theta + \dfrac{2}{r^2}\partial_\theta u_r - \dfrac{u_\theta}{r^2} \\ \nabla^2 u_x \end{bmatrix}. \tag{A2}$$

APPENDIX B: NUMERICAL CONSIDERATIONS

Cumbersome differential operations in cylindrical coordinates, particularly given $\nu_T = \nu_T(r)$, mean that finding the Orr-Somerfield form for Eq. (B2) is not straight forward in this geometry. Instead, for this study the continuity equation together with Eq. (3) have been used directly in primitive variable form, giving the generalized eigenvalue problem

$$\mathbf{X}\hat{\phi} = -\sigma \mathbf{Y}\hat{\phi}, \tag{B1}$$

where $\phi(r;t) = \hat{\phi}(r)e^{\sigma t}$. Note that $\mathbf{Y}$ is singular, containing three zero boundary conditions and a zero right hand side for the continuity condition. Simplifications can be made by observing that $\mathbf{X}$ is invertible, and that, as the σ have real part strictly less than zero, Eq. (B1) can be written in the standard form, $(-1/\sigma)\hat{\psi} = (\mathbf{X}^{-1}\mathbf{Y})\hat{\psi}$. Standard LAPACK routines return the leading eigenvalues along with a predicable number of infinite eigenvalues that are easily filtered. Excellent numerical stability is observed.

The continuity equation together with the linearized Eq. (3) and no-slip boundary conditions can be written in the form

$$u = Vx,$$

$$\partial_t x = \Lambda x + Wf, \tag{B2}$$

where x is an alternative representation for the state space ϕ. Conversion between the representations is performed by the action of V and W. This form is again familiar through the Orr-Somerfield formulation of the governing equations. Here, however, the eigenfunction decomposition is employed. Matrix V has columns of eigenvectors $\hat{u}_n$ and $\Lambda = \text{diag}(\sigma_n)$, with the σ_n arranged in descending order. These matrices, along with the diagonal weight matrix M s.t. $\|u\|^2 \equiv u^H M u$, are sufficient to calculate optimally growing initial conditions.

Consider the norm for x given by $\|u\|^2 = x^H \hat{M} x \equiv \|x\|^2 = (x, x)$, where $\hat{M} = V^H M V$. The optimal initial condition x_0

for growth at time t satisfies $G(t) = (Ax_0, Ax_0)/(x_0, x_0) = (A^+ A x_0, x_0)/(x_0, x_0)$, where the transfer function for x is $A = e^{t\Lambda}$ and the adjoint can be shown in a few operations to be $A^+ = \hat{M}^{-1} A^H \hat{M}$. The growth and initial condition can be calculated by power iteration on the matrix $A^+ A$. This matrix is straight-forward to evaluate when Λ is diagonal.

Calculation of the optimal harmonic forcing requires only minor alterations to the above. In this case one uses $A = (i\Omega_f I - \Lambda)^{-1}$, which is again a diagonal matrix for Λ diagonal.

For the stochastic response, it can be shown [65] that $C_\infty = V G_\infty V^H$, where G_∞ solves the Lyapunov equation

$$\Lambda G_\infty + G_\infty \Lambda^H + W W^H = 0. \tag{B3}$$

For W one may take the Moore-Penrose pseudoinverse of V. (Singularity of Y leads to fewer columns of eigenvectors than rows in V.) MATLAB routines are then available to solve Eq. (B3).

[1] O. Reynolds, Proc. R. Soc. London **35**, 84 (1883).

[2] H. K. Moffatt, in *Proceedings of the URSI-IUGG Colloquium on Atomspheric Turbulence and Radio Wave Propagation*, edited by A. Yaglom and V. I. Tatarsky (Nauka, Moscow, 1967), pp. 139–154.

[3] M. T. Landahl, J. Fluid Mech. **98**, 243 (1980).

[4] S. C. Reddy and D. S. Henningson, J. Fluid Mech. **252**, 209 (1993).

[5] L. N. Trefethen, A. E. Trefethen, S. C. Reddy, and T. A. Driscoll, Science **261**, 578 (1993).

[6] P. J. Schmid and D. S. Henningson, *Stability and Transition in Shear Flows* (Springer, New York, 2001).

[7] L. H. Gustavsson, J. Fluid Mech. **224**, 241 (1991).

[8] K. M. Butler and B. F. Farrell, Phys. Fluids A **4**, 1637 (1992).

[9] B. F. Farrell and P. J. Ioannou, Phys. Fluids A **5**, 2600 (1993).

[10] L. Bergström, Stud. Appl. Math. **87**, 61 (1992).

[11] L. Bergström, Phys. Fluids A **5**, 2710 (1993).

[12] P. Schmid and D. S. Henningson, J. Fluid Mech. **277**, 197 (1994).

[13] O. Y. Zikanov, Phys. Fluids **8**, 2923 (1996).

[14] S. J. Kline, W. C. Reynolds, F. A. Schraub, and P. W. Runstadler, J. Fluid Mech. **30**, 741 (1967).

[15] J. R. Smith and S. P. Metzler, J. Fluid Mech. **129**, 27 (1983).

[16] J. C. Klewicki, M. M. Metzger, E. Kelner, and E. M. Thurlow, Phys. Fluids **7**, 857 (1995).

[17] M. K. Lee, L. D. Eckelman, and T. J. Hanratty (1974).

[18] B. U. Achia and D. W. Thompson, J. Fluid Mech. **81**, 439 (1977).

[19] K. C. Kim and R. Adrian, Phys. Fluids **11**, 417 (1999).

[20] M. Guala, S. E. Hommema, and R. J. Adrian, J. Fluid Mech. **554**, 521 (2006).

[21] K. M. Butler and B. F. Farrell, Phys. Fluids A **5**, 774 (1993).

[22] B. F. Farrell and P. J. Ioannou, Phys. Fluids **5**, 1390 (1993).

[23] B. F. Farrell and P. J. Ioannou, Theor. Comput. Fluid Dyn. **11**, 237 (1998).

[24] J. C. del Álamo and J. Jiménez, J. Fluid Mech. **559**, 205 (2006).

[25] G. Pujals, M. García-Villalba, C. Cossu, and S. Depardon, Phys. Fluids **21**, 015109 (2009).

[26] Y. Hwang and C. Cossu, J. Fluid Mech. (to be published).

[27] C. Cossu, G. Pujals, and S. Depardon, J. Fluid Mech. **619**, 79 (2009).

[28] Y. Hwang and C. Cossu, J. Fluid Mech. **643**, 333 (2010).

[29] W. C. Reynolds and A. K. M. F. Hussain, J. Fluid Mech. **54**, 263 (1972).

[30] F. Waleffe, Phys. Fluids **7**, 3060 (1995).

[31] W. Schoppa and F. Hussain, J. Fluid Mech. **453**, 57 (2002).

[32] J. Hamilton, J. Kim, and F. Waleffe, J. Fluid Mech. **287**, 317 (1995).

[33] F. Waleffe, Stud. Appl. Math. **95**, 319 (1995).

[34] M. Nagata, J. Fluid Mech. **217**, 519 (1990).

[35] F. Waleffe, Phys. Rev. Lett. **81**, 4140 (1998).

[36] G. Kawahara and S. Kida, J. Fluid Mech. **449**, 291 (2001).

[37] H. Faisst and B. Eckhardt, Phys. Rev. Lett. **91**, 224502 (2003).

[38] H. Wedin and R. Kerswell, J. Fluid Mech. **508**, 333 (2004).

[39] N. V. Nikitin, Fluid Dyn. **44**, 652 (2009).

[40] F. Waleffe, J. Fluid Mech. **435**, 93 (2001).

[41] B. Eckhardt, T. Schneider, B. Hof, and J. Westerweel, Annu. Rev. Fluid Mech. **39**, 447 (2007).

[42] B. Hof, C. van Doorne, J. Westerweel, F. Nieuwstadt, H. Faisst, B. Eckhardt, H. Wedin, R. Kerswell, and F. Waleffe, Science **305**, 1594 (2004).

[43] J. F. Gibson, J. Halcrow, and P. Cvitanovic, J. Fluid Mech. **611**, 107 (2008).

[44] T. M. Schneider, J. F. Gibson, and J. Burke, Phys. Rev. Lett. **104**, 104501 (2003).

[45] D. Viswanath, Philos. Trans. R. Soc. London, Ser. A **367**, 561 (2009).

[46] C. C. T. Pringle, Y. Duguet, and R. R. Kerswell, Philos. Trans. R. Soc. London, Ser. A **367**, 457 (2009).

[47] C. Cossu and L. Brandt, Phys. Fluids **14**, L57 (2002).

[48] C. Cossu and L. Brandt, Eur. J. Mech. B/Fluids **23**, 815 (2004).

[49] J. Fransson, L. Brandt, A. Talamelli, and C. Cossu, Phys. Fluids **17**, 054110 (2005).

[50] J. H. M. Fransson, A. Talamelli, L. Brandt, and C. Cossu, Phys. Rev. Lett. **96**, 064501 (2006).

[51] G. Pujals, C. Cossu, and S. Depardon, *Sixth Symposium on Turbulence and Shear Flow Phenomena* (Seoul National University, Seoul, Korea, 2009).

[52] G. Pujals, C. Cossu, and S. Depardon, J. Turbul. (to be published).

[53] G. Pujals, S. Depardon, and C. Cossu, Exp. Fluids (to be published).

[54] S. Schoppa and F. Hussain, Phys. Fluids **10**, 1049 (1998).

[55] G. Iuso, M. Onorato, P. G. Spazzini, and G. M. di Cicca, J. Fluid Mech. **473**, 23 (2002).

[56] S. A. Orszag and A. T. Patera, J. Fluid Mech. **128**, 347 (1983).

[57] M. Quadrio and S. Sibilla, J. Fluid Mech. **424**, 217 (2000).

[58] R. D. Cess, Westinghouse Research Report No. 8–0529–R24, 1958 (unpublished).

[59] W. C. Reynolds and W. G. Tiederman, J. Fluid Mech. **27**, 253 (1967).

[60] B. J. McKeon, M. V. Zagarola, and A. J. Smits, J. Fluid Mech. **538**, 429 (2005).

[61] B. F. Farrell and P. J. Ioannou, J. Atmos. Sci. **53**, 2025 (1996).

[62] B. Bamieh and M. Dahleh, Phys. Fluids **13**, 3258 (2001).

[63] M. R. Jovanović and B. Bamieh, J. Fluid Mech. **534**, 145 (2005).

[64] P. Schmid, Annu. Rev. Fluid Mech. **39**, 129 (2007).

[65] K. Zhou, J. Doyle, and K. Glover, *Robust and Optimal Control* (Prentice Hall, New York, 1996).

[66] E. Lauga and C. Cossu, Phys. Fluids **17**, 088106 (2005).

[67] A. P. Willis and R. R. Kerswell, Phys. Rev. Lett. **100**, 124501 (2008).

[68] A. P. Willis and R. R. Kerswell, J. Fluid Mech. **619**, 213 (2009).

[69] P. Andersson, L. Brandt, A. Bottaro, and D. Henningson, J. Fluid Mech. **428**, 29 (2001).

[70] A. G. Kravchenko, H. Choi, and P. Moin, Phys. Fluids A **5**, 3307 (1993).

[71] Y. Lifshitz, D. Degani, and A. Tumin, Flow, Turbul. Combust. **80**, 61 (2008).

[72] C. D. Tomkins and R. J. Adrian, J. Fluid Mech. **490**, 37 (2003).

[73] W. R. B. Morrison and R. E. Kronauer, J. Fluid Mech. **39**, 117 (1969).

[74] K. J. Bullock, R. E. Cooper, and F. H. Abernathy, J. Fluid Mech. **88**, 585 (1978).

[75] A. Duggleby, K. S. Ball, and M. Schwaenen, Philos. Trans. R. Soc. London, Ser. A **367**, 473 (2009).

[76] J. Fransson, L. Brandt, A. Talamelli, and C. Cossu, Phys. Fluids **16**, 3627 (2004).